Understanding the Mechanisms of Order Formation in Mesoporous Silica Synthesis

PhD Thesis

Tom Stavert

Supervisors: Miguel Jorge, Siddharth V. Patwardhan
Department of Chemical & Process Engineering
University of Strathclyde, Glasgow

May 16, 2025

This thesis is the result of the author's original research. It has been composed by the author and has not been previously submitted for examination which has led to the award of a degree.

Tom Stavert
May 2025

Abstract

Since their discovery over 30 years ago, ordered mesoporous silica (OMS) has been widely demonstrated to be an incredibly useful and valuable nanomaterial, in a variety of applications. Its usefulness is derived from its underlying structure, consisting of well-ordered mesopores, the size of which can be tuned by modifying the synthesis procedure used. This structure is determined early in the synthesis by the self-assembly of a surfactant template in the presence of a silica precursor. Therefore, understanding the mechanisms underpinning this self-assembly behaviour allows the properties of the final material to be more readily controlled. However, efforts to produce OMS on a larger scale have been unsuccessful due to several factors surrounding its laboratory synthesis route, which make it uneconomical and unsustainable at a commerical scale. While greener, more scalable synthesis routes for producing porous silica exist, they are unable to produce materials with the same degree of order as OMS, hampering their effectiveness in many applications. Understanding how the degree of order of OMS is determined and maintained during synthesis is therefore of utmost importance, in order to develop new, greener synthesis routes for this valuable class of nanomaterials.

In this thesis, the mechanisms which determine the degree of structural ordering in OMS are investigated in detail. Both computational and experimental approaches are utilized. In the computational work, multi-scale modelling is used to develop a coarse-grained model for the self-assembly of OMS. In the experimental work, the design of experiments approach is taken, allowing relationships between synthesis conditions and material properties to be established, with a particular focus on the degree of order of samples produced. This work also presents a rapid room-temperature synthesis route for producing OMS, demonstrating a greener pathway for producing these materials than the traditional synthesis method, which requires long reaction times and harsh conditions. In both approaches, the use of bio-inspired additives to aid in the synthesis of OMS is investigated, demonstrating that if correctly chosen, they may be used to improve the degree of order of materials obtained through this new synthesis route. The computational portion of the work is then expanded to study the pH-responsive surfactant, dodecylamine, showing how its self-assembly behaviour is strongly dictated by changes in the proportion of charged surfactant species, a behaviour that could be exploited to produce alternative routes for producing OMS.

This work identifies that two related, but distinct, stages of OMS synthesis are responsible for dictating the degree of order of the resultant material. The first of these is the self-assembly process, which is shown to be most strongly influenced by charge-matching behaviour between surfactant and silica species. This highlights the importance of carefully controlling the relative quantities of charged silica precursor, and charged surfactant species, which is strongly dependent on both the relative concentrations of these species in solution, and the system pH. The second stage of OMS synthesis which strongly influences the ordering of pores is the condensation of silica precursor species, which effectively locks in the structure formed by self-assembly. This work shows that when these condensation reactions proceed rapidly, the ordered structure is maintained, while slower reactions lead to disordering of the silica-surfactant mesophase before it can be locked in. Once again, system pH plays a strong role in this stage of the synthesis, since the kinetics of silica condensation is strongly dependent on it. In addition, if carefully selected, bio-inspired additives can aid in locking in the ordered structure by catalysing silica condensation reactions at the silica-surfactant interface. These findings demonstrate the effectiveness of computational modelling as a tool to better understand the complex mechanisms governing order formation in OMS.

Publications

Parts of the following chapters have been published in:

Chapter 2	T. Stavert, S. V. Patwardhan, R. Pilling, M. Jorge, “Unlocking the holy grail of sustainable and scalable mesoporous silica using computational modelling”, *RSC Sustainability* **2023**, *1*, 432–438
Chapter 4	T. Stavert, S. V. Patwardhan, M. Jorge, “Development of a coarse—grained model for the early stages of ordered mesoporous silica formation”, *Molecular Simulation* **2025**, *51*, 188–205
Chapter 5	T. Stavert, C. Brambila, S. V. Patwardhan, M. Jorge, “Computer—Aided Development of Bio—Inspired Routes to Highly Ordered Green Mesoporous Silica”, Submitted
Chapter 6	T. Stavert, M. Jorge, “Understanding the pH—responsive behaviour of alkylamine surfactants”, *Journal of Molecular Liquids* **2025**, *431*, 127656

Acknowledgements

In September 2001, my mother went to bed in the early hours of the morning, secure in the knowledge that her thesis had been completed, printed, and bound, ready for submission the next day. Unbeknownst to her, my sister and I decided to get up early that day, and finding the thesis, decided that it looked a little boring, and could use some illustration. Finding one's thesis decorated with crayons on the day of submission no doubt caused some degree of panic, and so my first acknowledgement must go to my mother, who inspired me to undertake a PhD, and has supported me throughout. Professor Jill Stavert has politely declined my invite to illustrate this thesis.

I'd also like to thank my other family members, my father, Andrew, his partner Pam, my sister, Harriet, and my grandmother, Wendy, for their support throughout my PhD, and their tireless attempts to try and understand what it is that I'm actually studying. Thanks to my friends Adair, Angus and Christiano for all the laughs and distractions from my studies, particularly when things were difficult, as well as all my other friends, who encouraged me, and gave me things to look forward to when my day's work was done. Thanks to my fellow PhD students: Nisha, Elliot, Robbie, Jordan, Stuart, Angharad, Chris and Jenny, to name a few, who I wish I could have spent more time with in the last few years, had I not been living so far away.

My deepest gratitude is given to my supervisor, Miguel Jorge, who helped me to secure funding for my PhD, provided endless support throughout my project, and encouraged me to push myself. I can't imagine having a better supervisor, and it's been a great pleasure to work with you. I'd also like to thank my second supervisor, Siddharth Patwardhan, for making me feel so welcome in the research group in Sheffield and continuing to support me after I left. Thanks to Gwen for showing me the ropes in the lab, and for being there to moan to when my experiments weren't going to plan. Thanks to Rob for our chats about research, which I always came away from with a new perspective. I'd also like to thank the academics I've met who have shown an interest in my work, for helping me to formulate my ideas and construct this thesis.

Last, but by no means least, thank you to my girlfriend, Lucy, for your endless support and encouragement, and for helping me to believe in myself. I don't know how I would have found my way through the last few months of my PhD without you, and without our adventures together.

Contents

List of Figures

List of Tables

Chapter 1

Introduction

The synthesis of ordered mesoporous silica (OMS) materials, such as MCM-41 [5] and SBA-15 [6], relies on the self-assembly of a surfactant mesophase around which silica precursor species aggregate. The structure of the material which forms, dictates its performance in a broad variety of applications, and is largely decided by this self-assembly process. Therefore, understanding the mechanisms underpinning surfactant self-assembly, particularly in the presence of silica precursor species, is of great importance to allow greater control over the structural properties of these materials. In particular, since the traditional routes for producing OMS rely on energy intensive and wasteful methods which are challenging to scale and have severe environmental impacts [7], it becomes increasingly important that these mechanisms are understood so that this knowledge can be transferred to design greener alternative synthesis routes for these materials in a more rational fashion. One promising avenue to producing porous silica in a more environmentally friendly way follows a bio-inspired approach, which adopts a rapid, room temperature synthesis route which may also be economically attractive due to low energy costs [8]. However, this synthesis is still relatively poorly understood from a mechanistic perspective [1].

Whilst experimental approaches have been applied to study OMS synthesis, in recent years computational modelling has been applied to great effect to study the self-assembly of OMS [9]. Whilst this has provided unprecedented insight into the OMS synthesis process, accurately modelling the self-assembly which takes place during synthesis remains a significant challenge. This is due to the relatively large time and length scales over which OMS synthesis takes place, making it inaccessible to traditional atomistic modelling approaches and necessitating the use of coarse-grained and multi-scale modelling. These techniques have also only been applied to study bio-inspired porous silica in a more limited capacity [10, 11].

In this work, a new model for OMS self-assembly is developed which takes advantage of the latest advances in modelling approaches, in particular a new atomistic force field for silicate species [12] and the Martini 3 coarse-grained force-field [13]. This model is used in conjunction with experimental synthesis and characterisation of OMS to provide new insight into the synthesis process. The incorporation of bio-inspired additives to enhance the synthesis of OMS is explored experimentally, supported by simulations which provide mechanistic insight into the potential of these additives in OMS synthesis. The same coarse-grained modelling technique is also applied to investigate the mechanisms of self-assembly for pH-switchable surfactants, providing a possible avenue for more environmentally friendly synthesis routes for OMS, as well as demontrating the effectiveness of this technique in modelling more complex self-assembly behaviour.

1.1 Prior Work

The basis for the synthesis procedure used in this work (see Chapter 5) resulted from an investigation by Dr Carlos Brambila in the Green Nanomaterials Research Group at the University of Sheffield, under the supervision of Prof. Siddharth Patwardhan. The specific details of this synthesis procedure are given in Chapter 5, Section 5.2.1. This synthesis procedure utilized the amino acid, arginine, which is frequently used as a bio-inspired additive in the synthesis of bio-inspired silica [14, 15], and resulted in well-ordered mesoporous silica being obtained at room temperature with a synthesis time of just 5 minutes and without hydrothermal treatment. This had previously not been reported in literature to the knowledge of the research group. The material was characterized by TEM imaging and gas adsorption. It displayed a narrow pore size distribution (see Figure 1.1) of well-ordered pores with a hexagonal arrangement (Figure

1.2). BET analysis also showed that the sample had a large surface area of 726 m^2 g^{-1}. However, the mechanism by which arginine could promote the formation of an ordered mesoporous material without a hydrothermal treatment step was not understood. This prompted the investigation into this synthesis route, which is explored in this work.

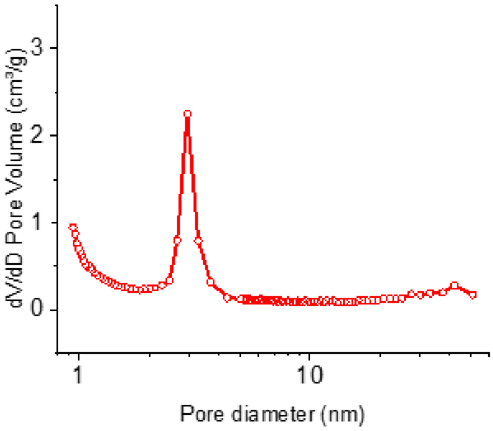

Figure 1.1: Pore size distribution of preliminary sample produced by Dr Carlos Brambila.

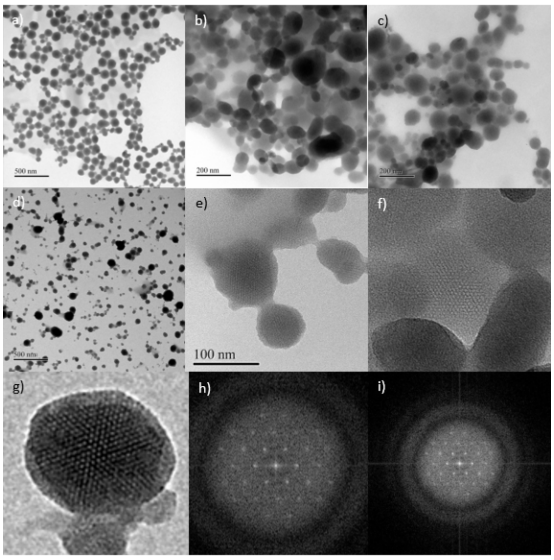

Figure 1.2: TEM imaging of preliminary sample produced by Dr Carlos Brambila. Image credit to Dr John Nutter, Henry Royce Institute, Sheffield.

1.2 Thesis Outline

This thesis is organised as follows. In Chapter 2, an overview of ordered mesoporous silica synthesis is provided, including currently understood mechanisms of self-assembly for these materials. Bio-inspired silica is introduced and synthesis methods are discussed. This is followed by a review of the most important computational modelling studies of porous silica synthesis. The chapter is concluded with a brief overview of silica and surfactant chemistry, focusing on the concepts that are most relevant to this work. In Chapter 3, the background methodology for both computational and experimental work is provided, with a focus on methods relevant to molecular dynamics and more specifically, coarse-grained molecular dynamics and the Martini force field, as well as experimental analysis methods used in this work. In Chapter 4, results are presented for the development of a coarse-grained model for molecular dynamics that is compatible with the Martini 3 force field. In Chapter 5, an experimental investigation following the Design of Experiments approach is presented in which links between synthesis conditions and material properties are estabished, supported by simulation results. In Chapter 6, the modelling methodology presented in Chapter 4 is applied to pH-responsive amine surfactants to study the phase behaviour of these surfactants in response to changes in the proportion of charged surfactant species present in the system. Chapters 4 to 6 are prefaced with an introduction which highlights specific literature relevant to that chapter, followed by a description of computational and experimental methods which are relevant specifically to that chapter. Finally, in Chapter 7, conclusions and proposals for possible directions for future work are given.

Chapter 2

Literature Review

2.1 Silica and Surfactant Chemistry

The synthesis of OMS relies on the formation of a supramolecular assembly, consisting of surfactant molecules and silica precursors. This assembly is frequently referred to as a "template" because it imparts its structure on to the final mesoporous material, meaning that a direct link can be drawn between the arrangement of the silica/surfactant mesophase and the final material's properties. This is an example of "bottom-up" synthesis, which stands in contrast to "top-down" synthesis methods such as electrochemical etching in which a structure is "carved out" of of an existing material. Due to this link between mesophase formation and material properties, an understanding of silica and surfactant chemistry is crucial to describing the formation of mesoporous silica from a mechanistic perspective and enabling tailored material design.

2.1.1 Chemistry of Silica

The formation of porous silica materials typically starts from a solution of small silica species that are soluble in water, the smallest being monosilicic acid ($Si(OH)_4$), which consists of a single silicon atom bonded to four oxygen atoms in a tetrahedral arrangement. The formation of large silica networks occurs via polymerization of these small species to form particles, which occurs above the solubility limit (approximately 100 ppm, 1 mM) [16]. This polymerization involves the condensation of the silanol (SiOH) groups of different silica molecules to form Si-O-Si bonds.

$$(\mathrm{OR})_3\mathrm{Si{-}OH} + \mathrm{HO{-}Si(OR)_3} \underset{\text{Hydrolysis}}{\overset{\text{Condensation}}{\rightleftharpoons}} (\mathrm{OR})_3\mathrm{Si{-}O{-}Si(OR)_3} + \mathrm{H_2O} \quad (2.1)$$

where R can be a hydroxyl group, or connected silica units in the case of condensation reactions between higher oligomers of silica. Through this condensation process, a range of small oligomers of silica are formed. These small orthosilicic acid oligomers have various structures, including cyclic trimers and cubic octamers (see Figure 2.1). The deprotonation equilibria for monomers and dimers can be written as:

$$\mathrm{SiO}_{i-1}(\mathrm{OH})_{5-i}^{(i-1)-} \overset{K_{\mathrm{m}}^{\mathrm{i}}}{\rightleftharpoons} \mathrm{SiO}_{i}(\mathrm{OH})_{4-i}^{i-} + \mathrm{H}^{+} \quad (2.2)$$

$$\mathrm{Si_2O}_{i}(\mathrm{OH})_{7-i}^{(i-1)-} \overset{K_{\mathrm{d}}^{\mathrm{i}}}{\rightleftharpoons} \mathrm{Si_2O}_{i+1}(\mathrm{OH})_{6-i}^{i-} + \mathrm{H}^{+} \quad (2.3)$$

where K_m^i and K_d^i are the equilibrium constants for monomers and dimers, respectively. Only very limited experimental data is available for the pKa values of small silicate species. The most comprehensive review on the topic gives the pKa values only for monomers and dimers [17] as 9.5 and 9.0, respectively. Notably, the pKa value of a silica surface (that is, the surface of a significantly condensed silica network) is 6.8 [18], much lower than the pKa of small oligomers. Generally, silicic acid molecules will condense so that the number of Si-O-Si bonds is maximised, meaning that cyclic species are more common in the early stages of condensation. As cyclic oligomers dominate, smaller oligomers (i.e. monomers, dimers) will react preferentially with cyclic species due to the higher density of ionized silanol groups [16]. These small species will continue to undergo condensation reactions, eventually forming small silica particles. Throughout particle growth, smaller silica particles dissolve and the silicic acid from these particles deposits on larger particles in a process known as Ostwald ripening. These particles then grow and become linked together to form branched chains, and then three-dimensional gel networks [19].

Close to neutral pH, particles will continue to grow until the negative surface charge causes them to repel one another. Salts and other charged species can screen the charge between particles, allowing them to aggregate and form more condensed networks. Under certain conditions, such as high pH, the reactivity of small silicate species is low and silica will remain present in solution as small oligomers.

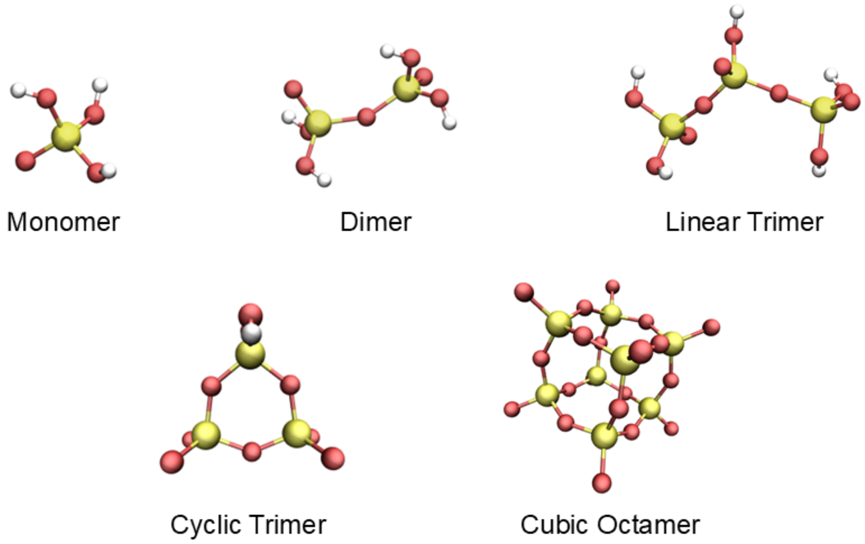

Figure 2.1: Selected examples of some forms of silicic acid, formed through polycondensation reactions.

2.1.2 Chemistry of Surfactants

Surfactants are molecules that are defined by their dual nature, comprising of a polar or hydrophilic head and a nonpolar or hydrophobic tail (see Figure 2.2). This structure gives surfactants interesting properties, which allows them to carry out important roles in biology and makes them useful in detergents and other consumer products. The amphiphilic nature of surfactants imparts on them two important behaviours: adsorption on surfaces or interfaces at low concentration, termed “surface activity”, and aggregation into micelles or liquid crystal phases at higher concentrations [20, 21]. The liquid crystal phases that form include lamellar, hexagonal and cubic phases, depending on both the properties of the surfactant molecules and the environment they are present in. This assembly into liquid crystal phases also gives rise to their use as templates in the synthesis of mesoporous materials [22].

The interactions between surfactant molecules that give rise to aggregation and the formation of structured phases are driven by relatively weak van der Waals, and stronger electrostatic interactions, in contrast to solid particles or rigid macromolecules which are held together by strong covalent or ionic bonds. This gives aggregate surfactant structures flexibility and causes them to be responsive to changes in their environment, critically factors such as pH and electrolyte concentration [20].

In aqueous solution above the critical micelle concentration (CMC), surfactant molecules will typically arrange into spherical micelles or bilayers. Surfactants with a single hydrophobic chain as a tail typically form micelles, whereas those with double-chains form bilayers (see Figure 2.3). This is due to the relative size of the hydrophilic and hydrophobic regions of the surfactant; surfactants with bulkier tails often cannot pack into smaller spherical micelles. Molecules arrange themselves in this way in order to minimise the surface area of the hydrophobic region with water. For this reason, bilayers will often arrange into spherical vesicles with aqueous regions contained both inside and outside the vesicles.

To understand how systems of surfactant molecules form aggregated structures in aqueous solution we must consider the relevant intermolecular interactions in general statistical thermodynamic terms. For these aggregates to form, the chemical potential of all identical surfactant molecules in different aggregates must be the same.

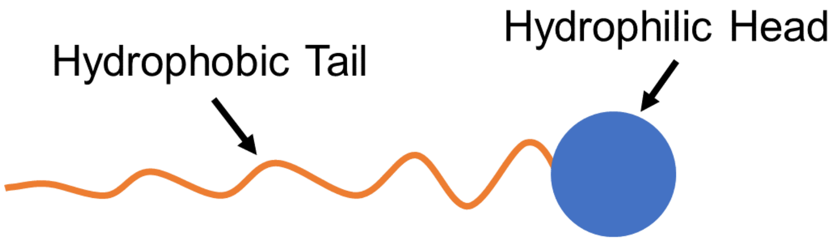

Figure 2.2: Simple diagram of a surfactant.

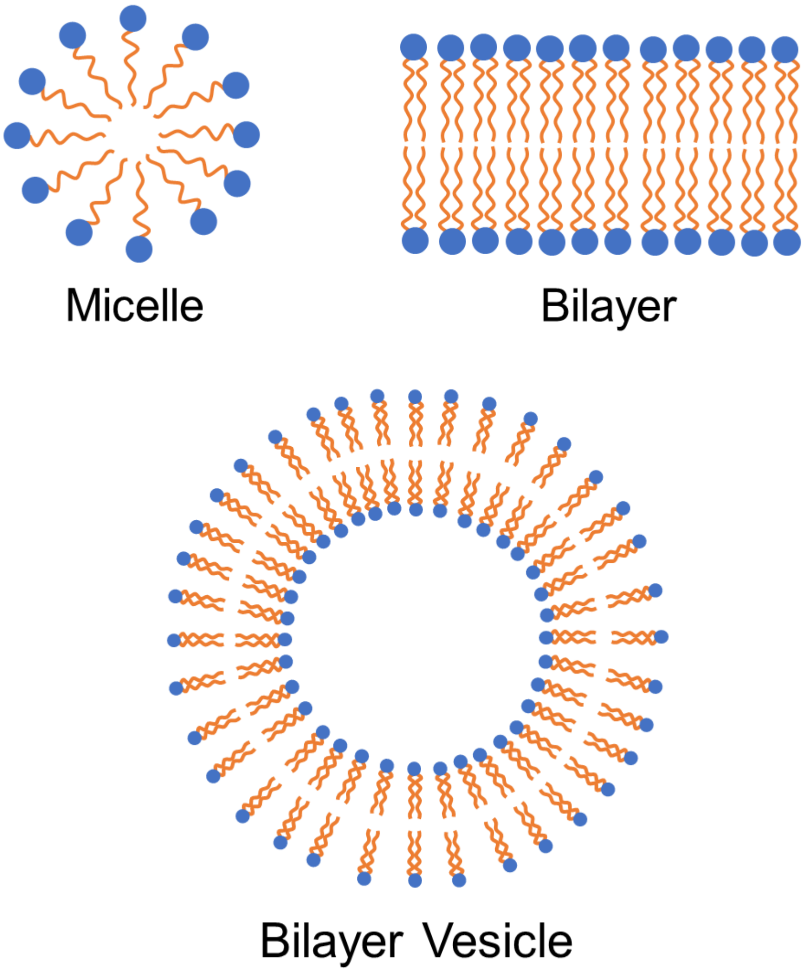

Figure 2.3: Diagram showing the arrangement of surfactant molecules in micelles, bilayers and spherical vesicles.

$$\mu = \mu_N = \mu_N^\circ + \frac{kT}{N} \log\left(\frac{X_N}{N}\right) = \text{constant}, \quad N = 1, 2, 3, ... \tag{2.4}$$

where μ_N is the mean chemical potential of a surfactant molecule in an aggregate with a number of molecules N (i.e. $N = 1$ refers to monomers or "free" surfactant molecules, $N = 2$ refers to dimers, $N = 3$ refers to trimers etc.), μ_N° is the mean interaction free energy per molecules in these aggregates and X_N is the concentration of molecules in these aggregates. Molecules form aggregates when the free energy of the aggregated states is less than the dispersed states. The value of μ_N° will remain constant if all different-sized aggregates experience the same interaction with their surroundings.

$$X_N = N X_1^N \quad \text{for} \quad \mu_1^\circ = \mu_2^\circ = \mu_3^\circ = ... = \mu_N^\circ \tag{2.5}$$

X_1, which corresponds to the isolated molecules (or monomers), must be < 1, meaning that $X_N \ll X_1$, so most molecules will be present as monomers. Therefore, for the formation of large stable aggregates to become probable, it must be the case that $\mu_N^\circ < \mu_1^\circ$. The relationship between μ_N° and N is therefore of great importance to determining the physical properties of aggregates. Importantly, depending on the functional form of this relationship, a number of different values of N may be stable for a given system, allowing for structurally different populations to coexist. The general functional form for the simplest shaped structures (e.g. rods, discs, spheres) is given by the following equation.

$$\mu_N^\circ = \mu_\infty^\circ + \alpha kT / N^p \tag{2.6}$$

where α is a positive constant which depends on the strength of interactions between surfactant molecules, and p is dependent on the shape or dimensionality of surfactant aggregates. From Eq. (2.6) it can be shown that:

$$X_N \approx N[X_1 e^\alpha]^N \tag{2.7}$$

At low monomer concentrations where $X_1 e^\alpha \ll 1$, then $X_1 > X_2 > X_3 > ...$ for any value of α. This means that most surfactant molecules will be present in the solution as free monomers and will therefore not form aggregates. However, as X_1 approaches $e^{-\alpha}$ it cannot increase any further since X_N cannot be greater than 1. This places a limit on the number of surfactant molecules that can be present as monomers, and above this concentration, aggregates must form. This concentration is known as the critical micelle concentration (CMC), a very important property of surfactants.

Above the CMC, the geometry of surfactant aggregates is dependent on the relative size of the surfactant's hydrophobic and hydrophilic parts. At the CMC, the types of aggregates that form can be predicted by calculating the critical packing parameter, p:

$$p = \frac{v}{a_o l_c} \tag{2.8}$$

where v is the volume of the hydrophobic tail, a_0 is the effective head group area and l_c is the length of the hydrophobic tail (see Figure 2.4). The expected shapes of aggregates that will form based on the value of the packing parameter are summarised in Table 2.1. However, this value of p is not fixed as concentration increases above the CMC and also changes in response to solutes in solution [23, 24]. Phase diagrams are often used to display the dependence of phase behaviour on various system conditions. Most commonly, two dimensional surfactant phase diagrams are constructed as a function of surfactant concentration and temperature (see Figure 2.5). Since the addition of further species such as oils, co-surfactants and acids may also induce phase transitions in some surfactants, ternary (isothermal) phase diagrams may also be constructed [21].

Table 2.1: Expected aggregation shape for surfactants based on the critical packing parameter, p.

p	**Shape**
$0 < p \leq 1/3$	Spherical micelles
$1/3 < p \leq 1/2$	Rod-like or hexagonal
$1/2 < p \leq 1$	Planar (sheet or bilayer)

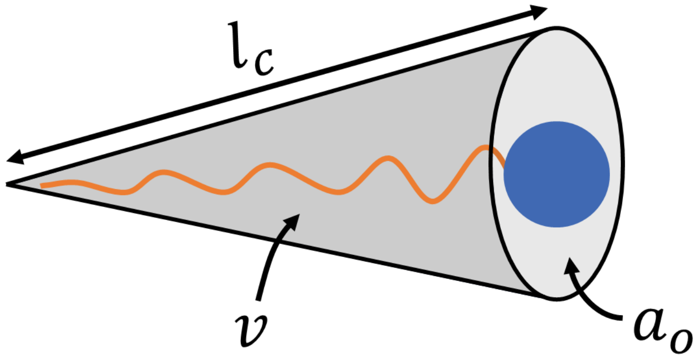

Figure 2.4: Diagram of a surfactant indicating parameters used to calculate the critical packing parameter, p.

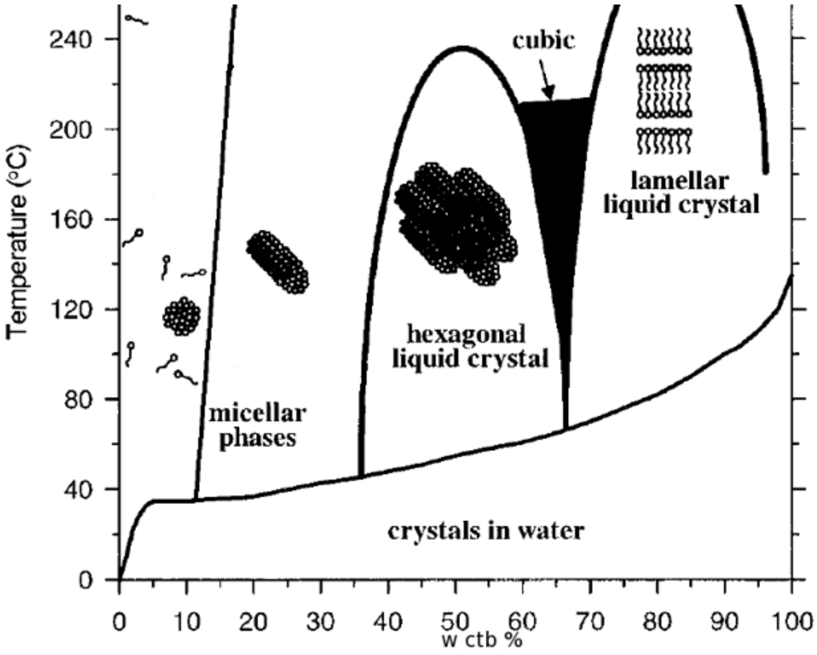

Figure 2.5: An example of a surfactant phase diagram for the surfactant cetyltrimethylammonium bromide (CTAB). Adapted from [25].

2.2 Ordered Mesoporous Silica

OMS materials were discovered in the 1990s by scientists at Mobil and in Japan [5, 26, 27]. This came about from investigations looking to identify new porous materials that could be used as catalysts and molecular sieves, focusing on combining what was known about zeolites and pillared layered materials. Zeolites were favoured for their stability, however they are limited to small pore sizes (less than 1.2 nm) [22]. Pillared layered materials possess mesopores, however they have a wide pore size distribution and are not thermally stable enough for many applications [28]. The theory proposed by a small group of researchers at Mobil was that zeolites that were formed via layered intermediates could be used to form pillared porous materials with zeolite character, a concept which eventually led to the discovery of materials such as MCM-22 [29]. Some of these attempts used long chain alkyltrimethylammonium surfactants at high pH in the presence of a reactive silica source which was then hydrothermally treated [28]. The materials formed showed strange properties, later discerned to be indicative of mesoporous structure, which included extremely high surface area and high hydrocarbon sorption capacities [30].

This material would eventually be named MCM-41 (MCM standing for Mobil Composition of Matter), representing a new family of mesoporous molecular sieves. MCM-41 possesses a hexagonal array of uniform mesopores that can be varied in size from 1.5-10 nm, depending on the chain length of surfactant used for synthesis [5]. Similar materials in this new M41S family, such as MCM-48 and MCM-50, were also discovered by studying the effect of changing the surfactant to silicate ratio [31]. These materials also showed order on the mesoscale but exhibited different structure, with MCM-48 exhibiting a cubic pore system and MCM-50 possessing a lamellar arrangement of pores.

Following the initial discovery of MCM-41, there was an explosion of research into this area in an attempt to identify new, useful, porous materials. The nature of the pore structure obtained is highly dependent on the surfactant used.

In the case of quaternary cationic surfactants such as cetyltrimethylammonium bromide (CTAB), it has been shown that varying the length of the alkyl chain will change the pore size of the MCM-41 obtained [5]. This can be used to create porous materials with tunable pore sizes, simply by changing the length of the surfactant used. By varying the ratio of surfactant to silicate concentration, MCM-48 and MCM-50 can be obtained which exhibit cubic and lamellar arrangements of pores, respectively. Cationic surfactants with large head groups, such as gemini or bolaform surfactants, are capable of forming cubic mesostructures, producing SBA-1 or SBA-6 depending on pH [32]. However, despite their effectiveness at producing ordered mesoporous materials, these surfactants are expensive and toxic, prompting researchers to investigate alternative, non-ionic structure directing agents.

Attard and co-workers produced ordered porous silica materials with a variety of mesostructures using the non-ionic surfactants octaethylene glycol monododecyl ether ($C_{12}EO_8$) and octaethylene glycol monohexadecyl ether ($C_{16}EO_8$), their form mimicking the organic mesophase of the surfactant used [33]. While this added an element of predictability in the synthesis of OMS, low pH values (pH 2) are required with the proposed mechanism, involving charge matching between positively charged silicate oligomers via an electrical triple layer. Another avenue that has been investigated is the use of block copolymers, appealing due to being readily available commercially, low in cost, biodegradable and non-toxic [22]. Zhao et al. used the triblock copolymer poly(ethylene oxide)-b-poly(propylene oxide)-b-poly(ethylene oxide) (PEO-PPO-PEO) to synthesise the mesoporous silica material SBA-15, which possesses highly ordered hexagonal pores up to 30 nm in diameter [6]. However, ordered silica structures are only formed under highly acidic conditions ($pH < 1$) while under neutral conditions only amorphous pores are obtained, once again necessitating harsh conditions to form ordered mesoporous silica.

The need for charged surfactant species and extreme pH results from the underlying intermolecular interactions taking place during the dynamic self-assembly of templating molecules. It is likely that in all cases where ordered mesoporous silica is produced, the formation of the supramolecular template is driven by strong electrostatic interactions. When non-ionic surfactants are employed under neutral pH, only relatively weaker hydrogen bonding interactions take place, which appear to be insufficient in promoting order in the supramolecular assembly, causing the resultant silica to possess only poorly ordered, amorphous pores. Contrary to this, a so-called “neutral templating route” has been proposed to describe the formation of hexagonal mesoporous silica, driven by hydrogen bonding interactions [34]. However, recent experimental and simulation work has determined that this does not in fact represent a viable description of the synthesis mechanism, and that the process is instead driven by the charge-matching of ionic interactions [11].

2.3 OMS Synthesis Method and Mechanism

Generally, mesoporous silica is synthesised following the “hydrothermal” method. A surfactant is dissolved in a solvent (typically water) followed by a silicate precursor, commonly tetraethyl orthosilicate; however other precursors such as silica gels or water glass (sodium silicates) may be used [22]. Water hydrolyses the silicate precursor, forming a sol of silicate oligomers. This process typically takes place under acidic or basic conditions, depending on the surfactant used, which catalyses the hydrolysis reaction of silicates. Silicates and surfactant molecules interact cooperatively, self-assembling into an arrangement that mimics the structure of the final silica material (see Figure 2.6). This is followed by hydrothermal treatment which allows polymerization and condensation of silicates, improving the mesoscopic regularity and stability of pores [35]. This process takes place at elevated temperatures (between 80 and 150°C) which must be maintained for a long period of time, often multiple days or even weeks [22]. This makes the synthesis process of OMS incredibly time-consuming. After hydrothermal treatment, the surfactant template must be removed in order to obtain the porous silica material. Calcination is the most common method employed for this, as it completely removes the template by thermal decomposition. This involves heating at very high temperatures (in the case of MCM-41, 550°C [5]) for several hours in order to fully break down the surfactant molecules, destroying the valuable template in the process. This method is both energy intensive and wasteful, but is frequently necessary due to the strong surfactant-silica interactions that govern the initial self-assembly process in

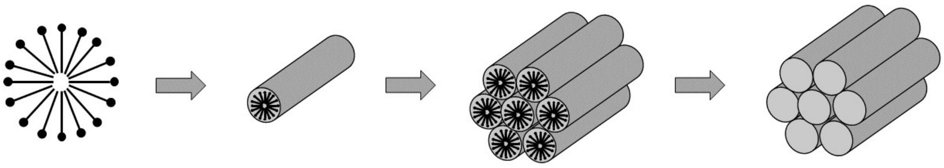

Figure 2.6: A simplified schematic of the templating mechanism that forms the ordered mesoporous material MCM-41. Initially, surfactant molecules form small micelles at the surfaces of which silica aggregates. These micelles fuse to form larger worm-like micelles and eventually a hexagonal mesostructure. The surfactant is removed (typically by calcination), leaving behind a porous silica structure.

the case of ordered materials, which make template removal by other methods challenging. Alternative methods for template removal have been proposed, however each presents its own issues, frequently resulting in incomplete template removal, disordering of pores or increased energy intensity [36, 37].

This initial mechanism of template formation is termed cooperative self-assembly and is accepted as by far the most common synthesis pathway for this class of materials. However, a different mechanism was proposed by the scientists who first synthesised MCM-41. In this mechanism, termed liquid-crystal templating (LCT), instead of being actively involved in the self-assembly of the surfactant mesostructure, the silicates simply condense around a preformed liquid crystalline surfactant phase. While this mechanism is now considered to be less common in the synthesis of OMS, mesoporous molecular sieves have also been synthesised that are believed to follow this alternative LCT route [33].

As the name suggests, cooperative self-assembly relies on cooperative interactions between the surfactant and silica species in order to form the supramolecular template. This is typically driven by electrostatic Coulomb forces, however mechanisms involving hydrogen bonding [34] and covalent bonding [38, 39] have also been proposed. The mechanisms most relevant to mesoporous silica synthesis are summarised in Table 2.2.

In the most straightforward mechanisms, S^+I^- and S^-I^+, the charged surfactant is paired with the inorganic precursor, which promotes assembly into a mesostructure, the interface of which is rich with inorganic species. This was described as the “direct”

Table 2.2: Summary of the interactions between surfactant and inorganic species that give rise to mesoporous materials. S are surfactants, I are inorganic species (often silica) and X are counter-ions.

Interaction	Type	Conditions	Example Materials	Reference
S^+I^-	Electrostatic	Basic	M41S	[5]
S^-I^+	Electrostatic	Basic/Acidic/Neutral	Mesoporous metal oxides	[40]
$S^+X^-I^+$	Electrostatic, double layer H bond	Acidic	SBA-1, SBA-2, SBA-3	[41]
$S^0H^+X^-I^+$	Electrostatic, double layer H bond	Acidic	SBA-15	[6]
S^0I^0	H bond	Neutral	HMS, MSU (disordered)	[34, 42]
$S^+ - I^-$	Covalent bond	Basic	Mesoporous silica	[38, 39]

pathway by Stucky and co-workers [40]. In some cases, the inorganic species promotes aggregation of the surfactant to form the mesophase template. An example of the S^+I^- pathway is the formation of the M41S family of materials, such as MCM-41. Through the use of *in situ* Si NMR measurements, Firouzi et al. demonstrated that at pH 13 silica is present primarily as double-four-ring (cubic octamers) with smaller quantities of monomers and double-three-ring species [43]. Thus, at the conditions under which mesoporous silica materials (such as MCM-41) are frequently synthesised, silica is initially present as small, negatively charged oligomeric species which interact strongly with the cationic surfactant template. In a similar manner, cationic oxide species may be used in conjunction with anionic surfactants to form mesoporous metal oxides (e.g. iron, aluminium and lead). Although the latter case is not relevant to mesoporous silica synthesis, it is included here for completeness.

Alternatively, interactions between surfactant and silica species are made possible by counter-ions in the "mediated" pathways, $S^+X^-I^+$ and $S^0H^+X^-I^+$. These occur at very low pH, where silica species are positively charged and must be mediated by anionic species (e.g. bromide, chloride, sulphate, nitrate). The mediating counter-ion allows for assembly of same-charge surfactant and inorganic species through a double-layer hydrogen bonding interaction.

The neutral templating mechanism, S^0I^0, was first proposed by Tanev and Pinnavaia in the synthesis of hexagonal mesoporous silica [34]. In this mechanism, the formation of the inorganic/surfactant mesophase is proposed to be driven entirely by hydrogen bonding interactions rather than interactions between charged species. This includes neutral amine surfactants and non-ionic surfactants. However, the computational study of Centi et al. demonstrated that this neutral templating mechanism does not represent a realistic description of the self-assembly behaviour, and instead demonstrates that the mesoscale structure must be formed via charge-matching interactions between the amine surfactant and silicate species [11], casting doubt over the proposed neutral templating mechanism.

The final mechanism relevant to mesoporous silica synthesis, $S^{+}- I^{-}$, involves surfactants containing hydrolyzable silane groups which can directly react with silicate species, forming covalent bonds. The surfactants assemble into an ordered mesostructure without the need for an additional templating molecule.

2.4 Bio-Inspired Silica

In nature, many organisms, such as diatoms and sponges, have been observed to exhibit a wide variety of ordered silica structures [44]. This is achieved through the use of bio-molecules which are able to promote the growth of silica structures from low concentration silicic acid environments at ambient conditions. The structures formed exhibit order over even hundreds of micrometers, which is rarely achieved in synthetic systems, particularly under such mild conditions [45]. This implies that nature is capable of producing ordered silica structures using complex routes that have been found through evolution, an observation that has led to the development of bio-inspired silica (BIS). A better understanding of the mechanisms underpinning silica formation in nature may yield great insights into how the synthesis of ordered silica structures can be made more economical and sustainable.

Initially, investigations into silica synthesis following a bio-based pathway involved using bio-molecules thought to be responsible for silica formation in nature (such as in the cell walls of diatoms) outside of their natural environment (*in vitro*) in order to form porous structures. Two main classes of molecule were found to be tightly embedded within the cell walls of diatoms: proteins called silaffins, and long-chain polyamines [46]. These molecules were shown to promote the formation of silica nanostructures in the presence of silicic acid [47, 48]. In silaffins, key functional groups were identified, namely the presence of lysine amino acid residues and polyamine moieties [49]. In addition, long-chain polyamines were found to be present on lysine residues, and in certain silaffins, sulphate ions [50] and quaternary ammonium groups [51] have also been observed. Long-chain polyamines have been shown to catalyze the condensation of silicic acid in water, even becoming embedded within the silica structure after polymerisation [52]. Much like silaffins, polyamines can self-assemble *in vitro* to form silica nanospheres. In sponges, proteins called silicateins play a very similar role to the silaffins identified in diatoms, self-assembling into a larger template upon which silica precipitates [53]. These investigations clearly show that, similarly to fully synthetic ordered silica structures, the precipitation of silica into complex structures is largely dependent on complex electrostatic interactions, in particular the formation of a molecular template by amphiphilic molecules.

While gaining a better understanding of *in vitro* synthesis was a huge step toward producing porous silica structures under more environmentally friendly conditions than fully synthetic methods, the limited supply of these bio-molecules and costs associated with acquiring them prevent scale-up for industrial production. Nevertheless, the insights gained from these *in vitro* studies allow for consideration of which fully synthetic molecules have potential to control porous silica formation. These molecules, termed additives, have been identified as a result of having similar chemical and physical properties to bio-molecules that promote precipitation of silica [45]. These additives take on a variety of forms, from simple molecules to complex organic polymers. Additives can work in several ways, either by catalysing silica condensation, promoting the aggregation of silicates or by providing a template for silica to precipitate around. Some additives will fill more than one of these roles [54].

Patwardhan et al. used poly-L-lysine (PLL) and poly(allylamine hydrochloride) (PAH) to precipitate silica in just minutes at mild pH and temperature, forming polydisperse spherical particles with amorphous pores [55, 56]. Leading on from this, further studies using polymeric bio-inspired additives were carried out, including natural and synthetic polymers, block co-polymers, polypeptides and dendrimers [45]. The use of these additives allows the porosity of BIS to be controlled in a predictable manner, particularly in the case of multi-amine molecules [57]. However, synthesis of BIS with ordered pores is still not possible, with materials possessing amorphous pores, predominantly in the microporous range (less than 2 nm in diameter) [15].

Some examples exist of mesoporous silica that follow bio-inspired methods. Coradin et al. showed that porous silica with a high surface area (>500 m^2/g) could be synthesised at neutral pH and ambient temperatures using arginine-based surfactants. The material obtained from this method has a broad, bimodal distribution of pore sizes with micropores between 0.25-0.35 nm and meso-to-macropores between 10 and 100 nm [58]. Sun et al. used polyethylene glycol (PEG) to synthesise porous silica with high surface areas (1030 m^2/g) under acidic conditions. The pores in this material range from 2 to 20 nm in diameter depending on the silica to PEG ratio and possess a broad size distribution [59]. Li et al. synthesized chiral mesoporous silica (CMS) using the bio-inspired chiral surfactant N-palmityl-L-alanine (N-PLA) and 3-aminopropyltriethoxysilane (APTES) as a co-structure directing agent. This material exhibited a helical mesostructure with mesopore diameters ranging from 3.7 to 5.7 nm and surface areas up to 789 m^2/g, however the mesostructure was poorly ordered as evidenced by small-angle XRD patterns [60].

Another approach that has been taken is to create new, customised additives based on the chemical properties identified in bio-molecules that promote silicification. Investigations using such additives have the advantage of being able to test how each of these common properties affect silicification individually, enhancing our understanding of the interactions at play. For example, in order to better understand the role that polyamines play during silicification, Belton et al. investigated how the degree of polymerization, the level of amine methylation and the size of the amine chain spacers impacted the function of polyamines when forming silica structures. Their findings enabled the rapid synthesis of hollow silica particles under ambient conditions [57]. Another example is a study using an arginine-based surfactant, chosen due to the abundance of cationically charged groups. These surfactants simultaneously promoted silica formation and acted as templates, forming porous silica structures [58]. Specially designed polymers and block co-polymers containing amine groups have also been shown to promote the formation of a range of silica structures including hollow nanofibres [61] and monodispersed silica-polymer hybrid particles [62].

Some attempts have been made to better control bio-inspired mesoporous silica synthesis, which may provide insights into how order can be imparted to these materials. A recent study by Gorbunova et al. showed that the surface area, pore volume and pore size of PEG-mediated silica can be tuned by adjusting pH [63]. This pH dependence was explained by its effect on silica condensation rate. At lower pH values, there is an increase in the rate of condensation reactions resulting in the formation of larger particles, which in turn leads to the formation of larger pores as PEG works to bind these particles together. However, regardless of pH, a wide, bimodal pore size distribution is obtained. It was also demonstrated that the structure of bio-inspired CMS was dependent on the pH and stirring speed employed during synthesis. At higher pH values, a more well ordered structure is produced, while stirring at lower speeds allowed for the formation of longer particles [60]. Although the final material obtained is ultimately still poorly ordered, this provides promise that some level of structural order can be achieved in bio-inspired silicas by tuning synthesis conditions.

Studies into bio-inspired silica have allowed for the creation of a diverse array of new silica structures with different porosity, morphology and size. In addition, bio-inspired additives allow for control over the rate of condensation and growth of silica structures, most notably allowing for silica structures to form under ambient conditions in just seconds. This offers an advantage over traditional mesoporous silica materials that require much harsher synthesis conditions and significantly longer synthesis times. Despite this, bio-inspired synthesis suffers from a lack of control over the structure of the final product. Porous silica structures produced using bio-inspired additives typically possess a broad pore size distribution and are always disordered, hampering their performance versus OMS materials that possess well ordered, monodisperse pores (see Figure 2.7).

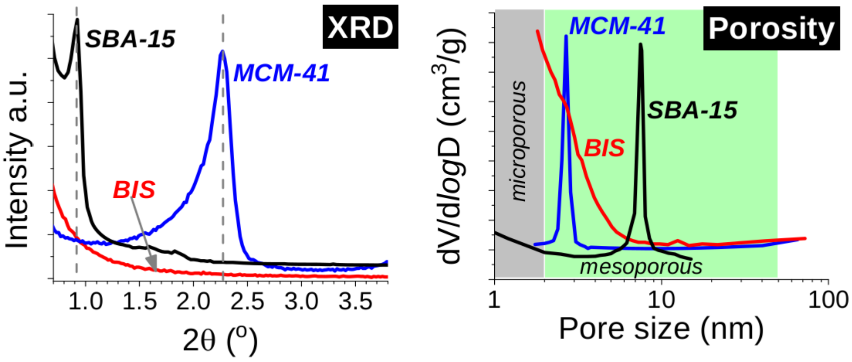

Figure 2.7: A comparison of the XRD and pore size distribution of bio-inspired silica with two archetypal ordered mesoporous silica materials, SBA-15 and MCM-41.

2.5 Computational Modelling of Porous Silica Synthesis

Computational modelling offers an invaluable tool in our attempts to better understand the mechanisms at play in complex chemical systems, particularly those in which experimental evidence proves inadequate in explaining the underlying interactions that govern the system. The synthesis mechanism of mesoporous silica materials such as MCM-41 is a prime example of this, where the synthesis mechanism was originally postulated by comparing various synthesis conditions and the properties of the final product. The challenge in this approach is the complex nature of the synthesis process, which includes self-assembly, condensation reactions and phase separation, all taking place simultaneously in solution [64]. Computational models provide a way of describing these complex systems, giving us a clearer picture of the interactions taking place. The first computational model of the synthesis of MCM-41 was developed in the early 2000s [65], and since then, significant advances have been made allowing for a near complete description of this synthesis process, as well as gaining key insights that can be extrapolated to similar systems.

The first computational model developed by Siperstein and Gubbins was used to investigate the ternary phase diagrams of the surfactant/solvent/silica systems present in the synthesis of MCM-41 [65, 66]. Due to the simplicity of the lattice Monte Carlo (MC) simulations used, only qualitative trends could be observed, however they were able to demonstrate the phase separation into a concentrated, hexagonally ordered silica/surfactant phase and a dilute aqueous phase. The model was later extended to describe the phase equilibrium of periodic organosilica precursors [67–70] and block copolymer-templated materials [71, 72]. A further extension to explicitly account for silica polymerisation reactions showed that allowing silica condensation to occur too early in the self-assembly process resulted in a disordered amorphous silica, rather than an ordered hexagonal liquid crystal (HLC) phase [73]. Despite these successes, the simplifications inherent in lattice-based models make it difficult to retain chemical specificity (e.g. a lattice model for a surfactant can represent a number of different chemical species) and hence to make direct connections with experimental systems.

The first molecular dynamics (MD) studies of MCM-41 synthesis were published in 2007 by Jorge et al. [74]. This fully atomistic model simulated the surfactant decyltrimethylammonium bromide (DeTAB) instead of the more commonly used CTAB to reduce the size and therefore computational expense of the simulation. This model showed that silicates interacted more strongly with small micelles than with free surfactant monomers, and also showed that silica promoted the formation of larger micelles than a reference simulation without silica. This provided strong evidence for the co-operative templating pathway. Due to the computational demand of the atomistic simulation, it was not possible to extend this investigation to study the aggregation of CTAB micelles, or to observe transitions in micelle shape. In an effort to bypass these limitations, the same group developed a coarse-grained (CG) model to describe the self-assembly of silica/surfactant mesostructures during periodic mesoporous silica synthesis [75]. Pérez-Sánchez et al. developed this model using the Martini CG potential developed by Marrink and co-workers [76]. The model was calibrated by comparing CG behaviour with atomistic data for a small system containing a single CTAB micelle. The model could then be used to investigate time and length scales that were previously out of reach of atomistic simulations. This was used to show that the presence of silica allowed for the formation of long wormlike micelles at concentrations that would form only spherical micelles without silica present, and it was proposed that this was due to charge screening by the silicate species. This model was later extended to include silicate oligomers [77]. The CG model showed that the formation of a hexagonal mesophase, reminiscent of OMS materials such as MCM-41, was only possible when the concentration of dimers (as a percentage of total silicate species) was over 33%, in agreement with experimental observations [43]. This suggests that some condensation of the silicate species is required before the formation of a hexagonal structure, because this allows silicates to bind to more than one micelle at a time. This study also found that a transition from a hexagonal to a lamellar mesophase could be induced either by increasing the charge density of silica oligomers (thereby decreasing the effective area per surfactant headgroup), or by the introduction of a benzene co-solvent (which increased the effective volume of the surfactant tail). These results were all in qualitative agreement with experimental observations.

Further investigations were carried out by the authors of this model to probe the phase diagram of the silica/surfactant/solvent system [78]. They found that the addition of monomers actually inhibited the formation of the hexagonal mesophase, favouring instead the formation of a bi-continuous or lamellar mesophase even when the starting configuration was a pre-equilibrated hexagonal arrangement. Similarly to the previous study, it was found that higher oligomers were required to allow for the transition to a hexagonal mesophase. These results provide strong evidence against the LCT templating mechanism for the synthesis of MCM-41. In fact, it was shown that the addition of silica to a concentrated CTAB system actually initially destroys the CTAB template, which is then reformed later after sufficient condensation of silica to higher oligomers. It does however provide some evidence that the LCT route may be adopted in the synthesis of MCM-50. At high concentrations of CTAB, a lamellar mesophase is formed both for systems without silica, and for systems containing either silica monomers and dimers. This suggests that the addition of silica to solutions containing high concentrations of surfactant could cause silica to condense around the preformed lamellar mesophase without destroying the template.

Despite the useful insights gained from this work, only one of the studies mentioned above (the lattice model of Jin et al.. [73]) has directly taken into account silica polymerisation, which is a key aspect of understanding OMS synthesis. Other researchers have developed models describing these reactions using a variety of methods such as reactive potentials, kinetic MC, Continuous Random Network and reactive MC [79–89]. The only example in which these methods were applied directly to OMS synthesis, however, was in the work of Schumacher and co-workers [90], which used a kinetic Monte Carlo reaction scheme based on the Continuous Random Network model of the silica network [88]. This attempted to simulate the entire MCM-41 process by splitting it into several stages which were modelled separately. Significant simplifications had to be made to the models used to ensure computational feasibility, which casts some doubt on the reliability of insights gained from this model. It is important to consider that the original aim of this work was to generate realistic models of MCM-41 for adsorption predictions, not to model the synthesis process accurately. This method was improved upon by Ferreiro and co-workers [91] to study other OMS materials (SBA-2 and STAC-1). They were able to explain experimental adsorption isotherms by the roughness of pores and provide a hypothesis that explains the connecting "windows" between pores. In addition, this study provided evidence that dimers and higher oligomers were required in high concentration before an ordered mesostructure could form, in agreement with the conclusions drawn from the CG model presented by Pérez-Sánchez et al.. [77].

Recently, a new coarse-grained reactive silica model has been developed [92] based on the Martini framework. This "Sticky Martini" model simulates the polycondensation of silicates by the association of "Virtual Sites" which are able to mimic the making and breaking of chemical bonds between silicates on-the-fly during MD simulations. As a proof-of-concept for the applicability of this new approach, the authors were able to simulate the self-assembly of a surfactant micelle in the presence of reacting silicates and the encapsulation of that micelle with a shell of condensed silica. This approach opens up huge opportunities to investigate systems relevant to porous silica synthesis at the mesoscale whilst explicitly taking into account the condensation reactions of silica species.

Computational modelling studies of bioinspired silica synthesis have so far been much more limited. Some studies have examined the self-assembly of silaffin molecules without including silica [93], while other studies that included silica have focused on relatively simple amine-based surfactants without including the reactive features of the system [10, 11, 94]. As discussed previously, these simulations have shown that the formation of mesostructures for both polyamine and alkylamine surfactants is driven by electrostatic interactions [10, 11], rather than by weaker hydrogen bonding as originally postulated [34]. This may explain why the degree of order of porous silica materials is lowered as we approach neutral pH, since the driving force for order decreases with the concentration of charged species in the system; however, more detailed studies are needed to verify this hypothesis.

Chapter 3

Methodology

3.1 Principles of Molecular Simulation

Computer simulations of molecular systems are an invaluable tool to investigate many phenomena, particularly those which are expensive, dangerous or challenging to probe experimentally. Simulations allow unprecedented insight into the microscopic behaviour of chemical systems (i.e. the movement of atoms and molecules), allowing behaviour to be observed that is difficult or impossible to study with experimental methods. Molecular dynamics (MD) simulations study the evolution of the positions and velocities of atoms and molecules in time by numerically solving Newton's equations of motion by computing the forces acting between particles. MD simulations have been extensively applied in theoretical physics, biochemistry and materials science. Applications include studies of protein folding [95], surfactant properties including micelle self-assembly and phase behaviour [96], and even uncovering the origins of life [97]. As available computational power increases and improved algorithms are developed, molecular simulations are more often being used as a tool to study complex phenomena in an efficient and cost-effective way. In this section, the basic principles underpinning MD simulations are summarised. Attention is then given to coarse-grained MD, which is used extensively in this work, and in particular the Martini force field.

3.1.1 Statistical Mechanics

A given system can be described on various scales. However, these detailed descriptions do not necessarily tell us how the system will behave on a scale relevant to humans. In this case we make use of macroscopic quantities, for example temperature and pressure, which arise as a result of these microscopic interactions. Since computer simulation is carried out at the microscopic level, it is necessary to be able to convert this detailed information into macroscopic properties of the system. Statistical mechanics makes this possible, allowing us to take insights gained from computer simulation and apply these to real systems. The most detailed, microscopic level description of a given system may involve atoms and molecules, and in the case of quantum mechanics, even subatomic particles such as electrons. It is possible to express the Hamiltonian $\mathcal{H}$ as a function of the coordinates r_i and momenta p_i of each particle, i, by making the Born-Oppenheimer approximation which averages out the motion of electrons.

$$\mathbf{r} = (\mathbf{r}_1, \mathbf{r}_2, ..., \mathbf{r}_N) \tag{3.1}$$

$$\mathbf{p} = (\mathbf{p}_1, \mathbf{p}_2, ..., \mathbf{p}_N) \tag{3.2}$$

If this classical description is sufficient, the Hamiltonian $\mathcal{H}$ can be written as a sum of the kinetic and potential energy functions.

$$\mathcal{H}(\boldsymbol{p}, \boldsymbol{r}) = \mathcal{K}(\boldsymbol{p}) + \mathcal{V}(\boldsymbol{r}) \tag{3.3}$$

For simple systems consisting of discrete atoms, the kinetic energy $\mathcal{K}$ takes the form:

$$\mathcal{K} = \sum_{i=1}^{N} \sum_{\alpha} p_{i\alpha}^2 / 2m_i \tag{3.4}$$

where m_i is the molecular mass, and α is an index running over different directional components of the momentum of any given atom i.

A particular microscopic system containing N particles in 3-dimensional space can be completely described by specifying the positions $\boldsymbol{r}^N(t)$ and momenta $\boldsymbol{p}^N(t)$, giving the system $6N$ dimensions, which change with time (t). The positions and momenta taken together are described as the 'phase space' (Γ) of the system. The instantaneous value of a macroscopic property $\mathcal{A}$ must be a function of the phase space. Since these positions and velocities change with time, the experimentally observed value of this macroscopic quantity can be calculated by averaging this value over a very long time:

$$\mathcal{A}_{\mathrm{obs}} = \lim_{t \to \infty} \frac{1}{t} \int_0^{t_{\mathrm{obs}}} \mathcal{A}(\Gamma)\, \mathrm{d}t \tag{3.5}$$

Since the particles move according to Newton's equations of motion in a simple classical system, in theory this equation can be solved. However, the number of particles that represent a macroscopic quantity is on the scale of 10^{23} and therefore solving this system of equations for this number of particles up to an infinite time is not possible even on modern computers. Instead, it may be sufficient to average this macroscopic quantity over a large but finite number of timesteps τ_{obs}. We rewrite eqn (3.5) as:

$$\langle \mathcal{A} \rangle_{\mathrm{time}} = \frac{1}{\tau_{\mathrm{obs}}} \sum_{\tau=1}^{\tau_{\mathrm{obs}}} \mathcal{A}(\Gamma) \tag{3.6}$$

The time evolution of the phase space is incredibly complex for systems with many particles. For this reason, the time average is instead replaced by the ensemble average. An ensemble considers all possible microstates that a system may be in, which are independent, but macroscopically identical. These microstates are distributed according to a probability density function $\rho(\Gamma)$ which is determined by fixing macroscopic parameters. If we are able to sample the entire phase space, the ensemble average could be given by the sum over the entire phase space, weighted by the probability density function ρ_{ens} for the ensemble of interest.

$$\langle \mathcal{A} \rangle_{\mathrm{ens}} = \sum_{\Gamma} \mathcal{A}(\Gamma) \rho_{\mathrm{ens}}(\Gamma) \tag{3.7}$$

By way of example, if we choose to fix the total number of particles, the volume and the energy of the system, the possible microstates are distributed according to the various configurations of phase space Γ that result in the same number of particles in the system, and the same system volume and energy, i.e. we sample the microcanonical (NVE) ensemble. Each of these microstates has an equal probability, given by $\rho_{\mathrm{NVE}}(\Gamma)$. We can define a "partition function" for this ensemble (Q_{NVE}) which is a sum over all the possible states our system can be in, and can be evaluated to obtain other thermodynamic variables of the system.

$$Q_{\mathrm{NVE}} = \sum_{\Gamma} \delta\left[\mathcal{H}(\Gamma) - E\right] \tag{3.8}$$

where δ is the Kronecker delta if the set of states is discrete, either 0 or 1, or the Dirac delta function if the states are continuous. For an atomic system, this can be written as a classical expression for Q_{NVE} where the phase space (Γ) is given by the positions ($\boldsymbol{r}$) and momenta ($\boldsymbol{p}$) of the particles.

$$Q_{\mathrm{NVE}} = \frac{1}{N!}\frac{1}{h^{3N}} \int \delta\left[\mathcal{H}(\boldsymbol{r},\boldsymbol{p}) - E\right] \mathrm{d}\boldsymbol{r}\mathrm{d}\boldsymbol{p} \tag{3.9}$$

where the factor $1/N$ accounts for the indistinguishability of particles and h is Planck's constant. The fundamental thermodynamic potential of the microcanonical ensemble is entropy, which can be calculated from the partition function.

$$S = k_B \ln Q_{\mathrm{NVE}} \tag{3.10}$$

While it is possible to sample the microcanonical ensemble by solving Newton's equations of motion (since energy is conserved), and this ensemble is the default for MD, practically we are often more interested in systems at fixed temperatures and/or pressures, which can be more easily compared with laboratory experiments. To fix the temperature of a system, energy fluctuations must be allowed, while to fix pressure, the system volume must be allowed to change. The canonical (NVT) and isothermal-isobaric (NPT) ensembles are by far the most commonly used in MD simulations, with temperature and pressure control achieved through the use of thermostats and barostats, which are discussed further in Section 3.1.5. The ensembles commonly employed in molecular simulations are summarised in Table 3.1 with the respective classical partition function and relevant thermodynamic potential.

Table 3.1: Ensembles commonly employed in molecular simulations.

Name	Fixed Variables	Classical Partition Function (Q_{ens})	Thermodynamic Potential
Microcanonical	N, V, E	$\frac{1}{N!}\frac{1}{h^{3N}}\int \delta\left[\mathcal{H}-E\right] \mathrm{d}\boldsymbol{r}\mathrm{d}\boldsymbol{p}$	$S = k_B \ln Q_{\text{NVE}}$
Canonical	N, V, T	$\frac{1}{N!}\frac{1}{h^{3N}}\int \exp\left[-\mathcal{H}/k_BT\right]\mathrm{d}\boldsymbol{r}\mathrm{d}\boldsymbol{p}$	$A = -k_BT \ln Q_{NVT}$
Isothermal-Isobaric	N, P, T	$\frac{1}{N!}\frac{1}{h^{3N}}\frac{1}{V_0}\int \mathrm{d}V \int \exp\left[-(\mathcal{H}+PV)/k_BT\right]\mathrm{d}\boldsymbol{r}\mathrm{d}\boldsymbol{p}$	$G = -k_BT \ln Q_{NPT}$
Grand Canonical	μ, V, T	$\sum_N \frac{1}{N!}\frac{1}{h^{3N}} \exp\left(\mu N/k_BT\right) \int \exp\left[-\mathcal{H}/k_BT\right]\mathrm{d}\boldsymbol{r}\mathrm{d}\boldsymbol{p}$	$\Xi = -k_BT \ln Q_{\mu VT}$

According to Liouville's theorem, the probability density function ρ_{ens} for an equilibrium ensemble does not change with time, $\mathrm{d}\rho_{\text{ens}}/\mathrm{d}t = 0$. This means that as we move on from one time to another, when considering our full ensemble of possible microstates, no state can be created or destroyed. Instead, each state must be replaced by an identical state, creating a chain that necessarily must repeat itself. If during the course of this time evolution, the system is able to explore all possible microstates, it is considered 'ergodic'. However, the time taken to explore every single microstate for systems with many particles is always incredibly long. This makes the ergodicity of such a system impossible to prove, however it is an assumption that is frequently made in molecular simulation.

In MD, we take our system of interest at some initial state and allow the system to evolve in time, from one timestep to the next. So long as the initial starting distribution $\rho(\Gamma)$ tends towards the probability density $\rho_{ens}(\Gamma)$ of the ensemble of interest, which does not change with the evolution of the system, the ensemble average will be equal to a time average, provided that the system is ergodic.

$$\langle \mathcal{A} \rangle_{ens} = \langle \mathcal{A} \rangle_{\text{time}} = \frac{1}{\tau_{obs}} \sum_{\tau=1}^{\tau_{obs}} \mathcal{A}(\Gamma(\tau)) \tag{3.11}$$

The implementation of MD requires algorithms that are discussed further in Section 3.1.4. An alternative approach to MD which is used to sample statistical ensembles is the Monte Carlo (MC) method. Unlike MD, MC does not involve the evolution of a system in time. Instead, random sampling is used to generate a representative ensemble of system configurations. In an MC molecular simulation, each move made by an atom is either accepted or rejected based on a probability that depends on the potential energy change of the system, allowing the system to reach equilibrium. Since there is no time evolution in MC simulations, it can only be used to study equilibrium properties, however since the moves that are made can be tailored, the method is very flexible and can be useful in certain contexts.

3.1.2 Interaction Potentials in Molecular Systems

The potential energy $\mathcal{V}$ contains information on intermolecular interactions, which are frequently separated into terms that depend on individual atoms, pairs, triplets, etc.:

$$\mathcal{V} = \sum_i v_i(\mathbf{r}_i) + \sum_i \sum_{j>i} v_2(\mathbf{r}_i, \mathbf{r}_j) + \sum_i \sum_{j>i} \sum_{k>j} v_3(\mathbf{r}_i, \mathbf{r}_j, \mathbf{r}_k) + ... \tag{3.12}$$

The first term represents the effect of external fields on the system, while the second term, v_2, represents the pair potential, and is generally the only multi-body term that is calculated in molecular simulations due to the additional computational expense of calculating the additional terms (which involve triplets, quadruplets etc.). This pairwise potential is typically adequate to give a good description of liquid properties, and additional terms are often accounted for by defining an “effective” pair potential which accounts in part for the effect of three-body terms. The effective pair potential is always strongly positive at very short distances (i.e. repulsive) which reduces to reach a negative (i.e. attractive) well. This well is responsible for cohesion in condensed phases [98]. At distances beyond the well, the potential increases asymptotically towards zero, giving an attractive tail at large separations. There are many ways in which potentials can be treated in molecular simulations to reproduce the effective pair potential. This may involve splitting the repulsive and attractive regions of the potential and treating each with different functions, or using a single function to reproduce the desired behaviour of the pair potential, which is often derived empirically. Most frequently, the Lennard-Jones (LJ) 12-6 potential is used.

$$v^{LJ}(r_{ij}) = 4\varepsilon \left[(\sigma/r_{ij})^{12} - (\sigma/r_{ij})^{6} \right] \tag{3.13}$$

where r_{ij} is the distance between pairs of atoms. The parameters ϵ and σ are chosen to accurately represent the pair interactions of particles in the system of interest. This function approximates the effective pair potential well, representing the repulsive core, attractive well and attractive tail (see Figure 3.1). The value of ϵ gives the depth of the potential well while the value of σ gives the distance at which the potential energy between particles is zero. ϵ and σ are defined for identical pairs of atoms, while for non-identical pairs, the Lorentz-Berthelot combining rules are typically used.

$$\sigma_{ij} = \frac{1}{2}(\sigma_{ii} + \sigma_{jj}) \tag{3.14}$$

$$\varepsilon_{ij} = (\varepsilon_{ii} \cdot \varepsilon_{jj})^{\frac{1}{2}} \tag{3.15}$$

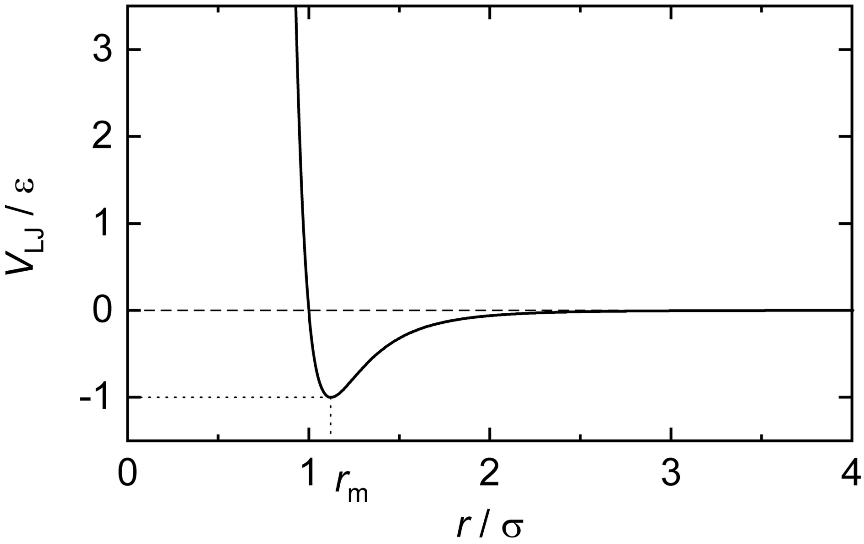

Figure 3.1: Graph of the standard Lennard-Jones potential function.

The Buckingham potential (Eq. 3.16) is an alternative potential function that is frequently used, which allows for increased flexibility and a more realistic repulsive term [99], however, it is more expensive to compute. Therefore, only the Lennard-Jones potential is used in this work.

$$v^{bh}(r_{ij}) = A_{ij} \exp\left(-B_{ij} r_{ij}\right) - \frac{C_{ij}}{r_{ij}^6} \tag{3.16}$$

For ions and polar molecules, additional consideration is needed to represent electrostatic interactions. Most simply, an additional Coulomb charge-charge interaction can be used to supplement the pair potential.

$$v^{qq}(r_{ij}) = \frac{q_i q_j}{4\pi\epsilon_0 r_{ij}} \tag{3.17}$$

where q_i and q_j are the charges on the ions i and j and ϵ_0 is the permittivity of free space. The charges on atoms and molecules may be placed at the same point as the Lennard-Jones interaction site, or partial charges may be distributed around the molecule in order to reproduce known multipole moments [100]. This is often sufficient for the representation of molecular systems. However, electronic polarization that results from the distortion of the electronic charge cloud of a molecule by the electronic field of other molecules is more challenging to represent, as it cannot be broken down into a sum over pairwise interactions [98]. In situations where electronic polarizability is important, several methods have been employed such as the induced point multipole model, the fluctuating charge model and the drude oscillating model [101, 102], however these models are not applied in this work.

While, ideally, chemical bonds in molecules could be treated with interatomic potential energy terms, this approach is rarely taken. Instead, chemical bonds within molecules are typically treated separately from effective pair potentials defined previously, either through the use of a harmonic potential (Eq. 3.18) or rigid fixed bond lengths which are handled by constraint algorithms in MD, such as LINCS [103], SHAKE [104] or SETTLE [105].

$$\mathcal{V}_b(r_{ij}) = \frac{1}{2}k^b_{ij}(r_{ij} - b_{ij})^2 \tag{3.18}$$

Angles and proper dihedrals are handled similarly between triplets or quadruplets of atoms, respectively.

$$\mathcal{V}_a(\theta_{ijk}) = \frac{1}{2}k_\theta(\theta_{ijk} - \theta_0)^2 \tag{3.19}$$

$$\mathcal{V}_d(\phi_{ijkl}) = k_\phi(1 + \cos{(n\phi_{ijkl} - \phi_s)}) \tag{3.20}$$

Taken together, the set of equations and parameters used to describe the interactions (both bonded and non-bonded) between atoms or particles in a particular system is called a force field. Many generic force fields are available (e.g. OPLS [106], AMBER [107], CHARMM [108]), and the choice of which force field to use is critical to ensuring correct representation of the system at hand. Force fields are typically developed semi-empirically using both experimental data and quantum calculations to derive potential terms. Coarse-grained force fields are of particular interest for this work, and are discussed further in Section 3.1.6.

3.1.3 Initiation Configuration and Boundaries

A given system is initially defined by two components. The first is the topology, which describes the force field, supplemented by information about which chemical bonds exist between atoms. The second is the initial configuration of atoms, which contains their initial positions and velocities, providing a starting point for simulations. Since calculations can only be carried out on a finite number of atoms, the simulation "box" in which calculations are carried out is a representative sample of a larger system. In order to avoid the complication and physical effects of implementing interfaces at the boundaries of the simulation box, periodic boundary conditions are typically employed. As an atom travels across the boundary of the simulation box, it re-enters through the opposite side of the box (see Figure 3.2). Bonded and non-bonded interactions also take place across periodic boundaries, allowing representation of an effectively infinite system in every direction as atoms interact with periodic replicas. When using periodic boundaries, care must be taken that the size of the box is large enough so that atoms do not interact with their own periodic replicas.

3.1.4 Molecular Dynamics Algorithms

In molecular dynamics simulations, the classical equations of motions for a system of N particles interacting with a potential $\mathcal{V}$ are solved. From this potential, the force, $\mathbf{F}$, acting on each particle can be resolved considering that the force is simply the negative gradient of the potential energy function.

$$\mathbf{F}(\mathbf{r}) = -\nabla\mathcal{V}(\mathbf{r}) \tag{3.21}$$

Since the potential acting on each atom in the system can be calculated at any particlar point in time, t, the new positions and velocities of atoms after a time step, δt, are straightforward to calculate. When choosing an appropriate time step, the most important factor is ensuring energy conservation which is degraded as the time step is

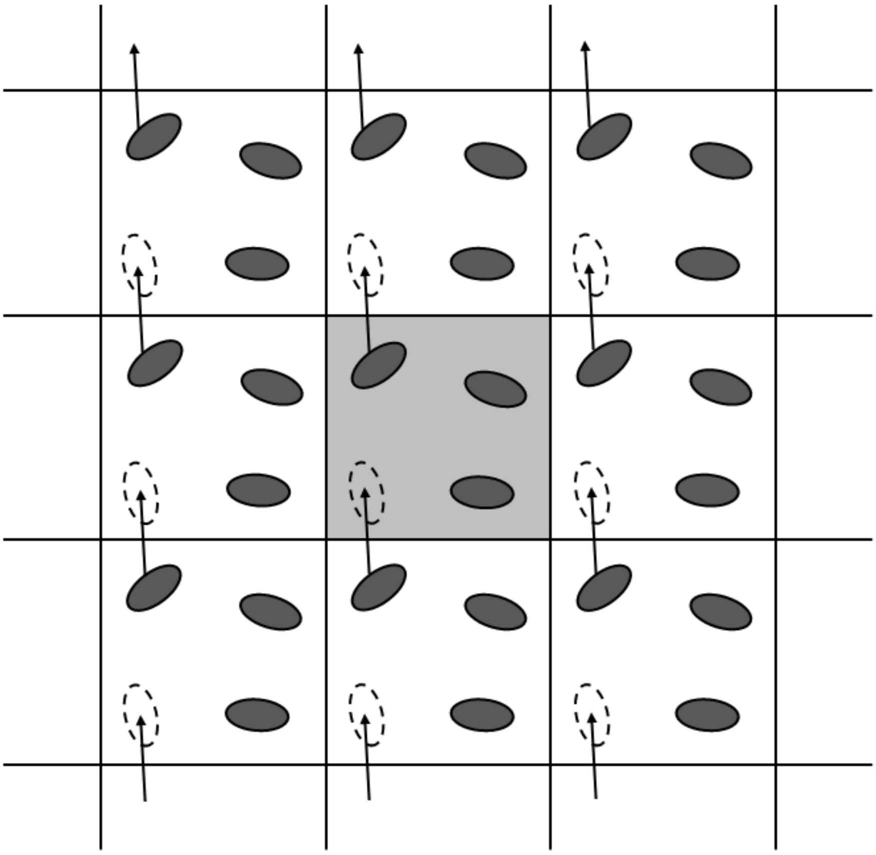

Figure 3.2: Diagram demonstrating a two-dimensional system with periodic boundaries.

increased. Since the computational cost of simulations is increased as the time step is reduced, the time step should be maximized whilst still conserving energy. The most common algorithm used in molecular dynamics codes to solve for the positions and velocities of atoms at each time step is the velocity Verlet algorithm [109], based upon the Verlet alogrithm [110].

$$\mathbf{v}(t+\tfrac{1}{2}\delta t) = \mathbf{v}(t) + \tfrac{1}{2}\delta t\,\mathbf{a}(t) \tag{3.22}$$

$$\mathbf{r}(t+\delta t) = \mathbf{r}(t) + \delta t\,\mathbf{v}(t+\tfrac{1}{2}\delta t) \tag{3.23}$$

$$\mathbf{v}(t+\delta t) = \mathbf{v}(t+\tfrac{1}{2}\delta t) + \tfrac{1}{2}\delta t\,\mathbf{a}(t+\delta t) \tag{3.24}$$

In the first step of this algorithm, the velocities at an intermediate “half time step” ($\mathbf{v}(t+\frac{1}{2}\delta t)$) are calculated from the velocities and accelerations of the atoms at the current timestep t. This velocity is then used to compute the new positions of the atoms after a time step δt. The velocities of the atoms at this new position are then calculated from the half step velocities and the acceleration of the atoms at their final position. This loop is repeated at every step, and since the velocitiy of the atoms at each step is explicitly calculated, quantities such as the kinetic energy of the system can easily be calculated.

Another alogirthm that is frequently employed for molecular dynamics simulatons is the “leapfrog” algorithm [111].

$$\mathbf{v}(t+\tfrac{1}{2}\delta t) = \mathbf{v}(t-\tfrac{1}{2}\delta t) + \delta t\,\mathbf{a}(t) \tag{3.25}$$

$$\mathbf{r}(t+\delta t) = \mathbf{r}(t) + \delta t\mathbf{v}(t+\tfrac{1}{2}\delta t) \tag{3.26}$$

In this algorithm, the mid-step velocities are calculated from the previous mid-step velocities using the acceleration of atoms at the current time step. These mid-step velocities are then used to calculate the new atomic positions. When using this algorithm, a further calculation is required to obtain the current velocities, which are needed to calculate energies.

$$\mathbf{v}(t) = \tfrac{1}{2}\left(\mathbf{v}(t + \tfrac{1}{2}\delta t) + \mathbf{v}(t - \tfrac{1}{2}\delta t)\right) \tag{3.27}$$

These algorithms rely on the calculations of intermolecular potentials, which were described previously in Section 3.1.2. Often, the Lennard-Jones potential is used to represent repulsion and dispersion interactions at short distances while Coloumbic charge-charge interactions describe electrostatic interactions. This approach is used in this work, with additional electrostatic interactions such as polarizability and multipole moments being neglected. Since the largest contribution to the potential acting on any particular atom comes from nearby particles, a spherical cutoff is frequently applied to both LJ and electrostatic potentials so that the pair potential between atoms at this cut-off distance is zero. To ensure that thermodynamic properties of the system are still maintained, long-range corrections are then applied to compensate for this truncation. For LJ interactions, it is generally assumed that the cut-off is sufficiently large that the repulsion term can be neglected and only the dispersion term is taken into account. This is particularly important for free energy calculations and ensuring correct pressure in the NPT ensemble, in which the correction can be large. The correction terms for energy and pressure are calculated by assuming that the radial distribution function $g(r) \approx 1$ beyond the cut-off distance. The relations between the radial distribution function and energy and pressure are then used to apply long-range corrections. For long-range electrostatic interactions, the Ewald summation was first introduced [112] which converts a single slowly-converging sum into two quicky-converging terms and a constant term. However, the particle mesh Ewald (PME) method [113], which assigns charges to a grid using interpolation, is more frequently used due to its much improved computational efficiency.

3.1.5 Thermostats and Barostats

Control of temperature and pressure in MD simulations is achieved through the use of thermostats and barostats, respectively. This is usually necessary to allow for comparison with experimental data, which is often obtained at a specific temperature and pressure. Many thermostats and barostats are available, so the discussion here is limited to a description of those used in this work.

Thermostats

Consider that the equipartition theorem relates the kinetic energy of a system ($\mathcal{K}$) to the veloctities of the atoms.

$$\mathcal{K} = \left\langle \sum_{i=1}^{N} \frac{1}{2} m_i v_i^2 \right\rangle = \frac{3}{2} N k_B T \tag{3.28}$$

where m is the mass of the atoms, v is the velocity of the atoms, N is the number of particles, k_B is the Boltzmann constant and T is the system temperature. Therefore, the most straightforward way of implementing temperature control is to scale the velocity of all atoms by some factor, λ at every time step.

$$\lambda = \sqrt{T_{\text{required}}/T_{\text{current}}} \tag{3.29}$$

However, this type of thermostat (known as a velocity-scaling thermostat) does not correctly reproduce the canonical ensemble because it does not allow for thermally realistic fluctuations. It is therefore not appropriate for most MD simulations, however it can be useful for quickly equilibrating systems at a particular temperature. A similar, approach, Berendsen temperature coupling [114], couples the system with an imaginary heat bath which is at a constant temperature, T_0, via coupling parameter τ.

$$\frac{\mathrm{d}T(t)}{\mathrm{d}t} = \frac{1}{\tau}(T_0 - T(t)) \tag{3.30}$$

While this allows for the strength of the temperature coupling to be controlled, the Berendsen thermostat still does not reproduce the canonical ensemble and so should only be used for equilibration purposes. A velocity rescaling thermostat with a stochastic component was proposed by Bussi et al. [115]. This thermostat is similar to the Berendsen thermostat, but adds a stochastic noise term to velocity rescaling. This allows temperature fluctuations that are consistent with the canonical ensemble, as velocities are sampled following the Maxwell-Boltzmann distribution.

$$\mathrm{d}\mathcal{K} = (\mathcal{K}_0 - \mathcal{K})\frac{\mathrm{d}t}{\tau_T} + 2\sqrt{\frac{\mathcal{K}\mathcal{K}_0}{N_f}}\frac{\mathrm{d}W}{\sqrt{\tau_T}} \tag{3.31}$$

where $\mathcal{K}$ is the kinetic energy, N_f is the number of degrees of freedom and $\mathrm{d}W$ is a Wiener process. This velocity rescaling thermostat is used in all production simulations in this work.

An alternative approach to controlling temperature of a system is the "extended-ensemble" approach, upon which the Nosé-Hoover thermostat is based [116, 117]. In the extended-ensemble approach, the system is extended to introduce a thermal reservoir and a friction force on each particle, which is a product of its velocity. This modifies the equations of motion for particles.

$$\frac{\mathrm{d}^2\mathbf{r}_i}{\mathrm{d}t^2} = \frac{\mathbf{F}_i}{m_i} - \frac{p_\xi}{Q}\frac{\mathrm{d}\mathbf{r}_i}{\mathrm{d}t} \tag{3.32}$$

where the equation of motion for the heat bath parameter ξ is:

$$\frac{\mathrm{d}p_\xi}{\mathrm{d}t} = (T - T_0)N_f k \tag{3.33}$$

where N_f is the number of degrees of freedom and k is Boltzmann's constant. The constant Q, called the mass parameter, determines the strength of the coupling. In some systems, the Nosé-Hoover dynamics can be nonergodic, so chains of Nosé-Hoover thermostats are often used to improve ergodicity [118]. However, this method still does not guarentee ergodicity [119]. The Hamiltonian for the extended system can be expressed as:

$$\mathcal{H} = \sum_{i=1}^{N}\frac{\mathbf{p}_i^2}{2m_i} + U(\mathbf{r}_1, \mathbf{r}_2, ..., \mathbf{r}_N) + \frac{p_\xi^2}{2Q} + N_f kT\xi \tag{3.34}$$

Barostats

The pressure of a system must be controlled by modifying the system volume. The Berendsen algorithm [114] for pressure coupling rescales all atom coordinates and box vectors at every time step (or at a set interval of time steps) with a matrix, μ. This relaxes the actual pressure of the system (P) towards the desired pressure (P_0) with a coupling parameter, τ_p, similar to Berendsen temperature coupling.

$$\frac{\mathrm{d}\mathbf{P}(t)}{\mathrm{d}t} = \frac{1}{\tau_p}(\mathbf{P}_0 - \mathbf{P}(t)) \tag{3.35}$$

The scaling matrix, μ, is related to the isothermal compressibility, β, of the system. The value of β must be estimated, but critically its value will only affect the time constant of pressure relaxation and will not affect the average pressure. This value is $\beta = 4.6 \times 10^{-5}$ bar^{-1} for water at 1 atm, 300 K, and is suitable for most liquids. While the Berendsen barostat is effective in achieving the correct average pressure, it does not reproduce the NPT ensemble accurately as, similarly to the Berendsen thermostat, it does not allow for realistic fluctuations in pressure or volume.

For production simulations, the Parrinello-Rahman [120, 121] barostat is used as it reproduces the correct NPT ensemble. For this barostat, the box vectors obey the matrix equation of motion, **b**.

$$\frac{\mathrm{d}\mathbf{b}^2}{\mathrm{d}t^2} = V\mathbf{W}^{-1}\mathbf{b}'^{-1}(\mathbf{P} - \mathbf{P}_{ref}) \tag{3.36}$$

where V is the box volume, and **W** is a matrix parameter that determines the strength of coupling, which is related to the estimated isothermal compressibility of the system at hand. Similarly to the Nosé-Hoover thermostat, the equations of motion of particles in the system are changed.

$$\frac{\mathrm{d}^2\mathbf{r}_i}{\mathrm{d}t^2} = \frac{\mathbf{F}_i}{m_i} - \mathbf{M}\frac{\mathrm{d}\mathbf{r}_i}{\mathrm{d}t} \tag{3.37}$$

$$\mathbf{M} = \mathbf{b}^{-1}\left[\mathbf{b}\frac{\mathrm{d}\mathbf{b}'}{\mathrm{d}t} + \frac{\mathrm{d}\mathbf{b}}{\mathrm{d}t}\mathbf{b}'\right]\mathbf{b}'^{-1} \tag{3.38}$$

Giving the modified Hamiltonian:

$$\mathcal{H} = \mathcal{V} + \mathcal{K} + \sum_{i} P_{ii} V + \sum_{ij} \frac{1}{2} W_{ij} \left(\frac{\mathrm{d}b_{ij}}{\mathrm{d}t} \right)^2 \tag{3.39}$$

3.1.6 Multi-Scale Modelling & Coarse-Graining

Since calculations for interactions between particles in a molecular simulation must be carried out between each pair of particles at every timestep, the number of calculations which must be carried out increases dramatically as the system size increases. Despite significant advances in the computational resources available in recent years, the time and length scales which are realistically accessible to traditional atomistic models (i.e. where each atom in the system is explicitly represented) remain limited. Therefore, molecular simulation studies of large systems or of phenomena that take place over relatively long time scales must employ special techniques to reduce the computational burden of these calculations. Coarse-graining is a technique that simplifies the representation of a molecular system whilst still capturing its essential behaviour, reducing the number of calculations that must be carried out to achieve a result. In coarse-grained (CG) modelling, atoms are grouped into “beads”. These beads interact via a potential which aims to accurately reproduce the key properties of the system without the need to explicitly simulate individual atoms. The increase in the characteristic length scale resulting from coarse-graining also usually allows for larger simulation timesteps to be used [98]. Multi-scale modelling is a technique which uses models at different scales (e.g. quantum, atomistic, coarse-grained) in conjunction to investigate a system of interest. Frequently, more detailed models from higher levels of theory are used to calibrate simplified models in a “bottom-up” approach, for example using quantum models to calibrate atomistic models, or atomistic models to parameterize coarse-grained models. Alternatively, CG models may be parameterized to reproduce experimental properties of the system, such as bulk density or liquid-vapor surface tension, in a “top-down” approach [122]. Often, a mixture of both bottom-up and top-down approaches are utilized, in a hybrid approach.

3.1.6.1 Approaches to Coarse-Graining

The first major consideration that must be made when developing a coarse-grained model is what atoms or parts of each molecule are represented by each bead, referred to as the “mapping” scheme. Here, a clear trade-off is made between improved speed of calculations and the accuracy of the model. If a mapping scheme is used in which beads represent only a small number of atoms, then it can reasonably be expected that a high degree of accuracy can be acheived due to the increased degrees of freedom. Although not commonly referred to as coarse-grained models, united atom models could be considered to have the highest level of detail when coarse-graining. In these models, only the hydrogen atoms bonded to organic chemical groups are not explictly represented and the interaction potential of “heavy” atoms bonded to hydrogen is modified to account for this. More commonly, larger groups of atoms containing both heavy (i.e. non-hydrogen) atoms and adjoined hydrogen atoms are respresented by beads, allowing for a far greater reduction in the number of calculations that must take place at each simulation step. For example, the popular Martini force-field maps, on average, four heavy atoms to each CG bead [76]. A higher resolution mapping typically allows for more chemical specificity to be maintained, since multiple chemical groups do not need to be represented by a single bead. Conversely, some generic, or “toy”, models forgo chemical specificity in favour of simplicity, aiming only to reproduce the general behaviour of the molecules represented [123].

Calculations involving solvent molecules, most often water, constitute a large proportion of the computational expense for simulations but are crucial as the solvent typically screens electrostatic interactions. Therefore, the coarse-graining approach to represent solvent molecules is particularly important. One possible approach is to forgo explicit representation of the solvent entirely, instead treating the solvent as a continuous medium with its properties reproducing the average behaviour of the real fluid and utilizing a modified dielectric constant to screen electrostatic interactions. While implicit solvent models can be effective, the dielectric potential used is often concentration dependent, which presents challenges in high concentration and heterogeneous systems [124]. Alternatively, the solvent may be represented explicitly. For larger solvents, the approach is the same as any other coarse-grained representation, and solvent molecules may be represented by a single or multiple coarse-grained beads, depending on the resolution of the model. The case for water, which is the most common solvent used in MD simulations, is more complicated as representing each molecule with a single CG bead affords little benefit in terms of computational efficiency over atomistic representation. Therefore, CG representations of water often aim to represent multiple molecules in a single bead, for example the Martini model maps four water molecules to each CG water bead, allowing for more significant computational savings [76]. A consequence of mapping multiple water molecules to a single bead is a loss of electrostatic charges, necessitating the use of a modified dielectric constant to account for screening of electrostatic interactions. To provide a more rigorous representation of electrostatic interactions, CG models have been developed that account for the polarizability of water. A noteworthy example is the polarizable water model for the Martini force-field, which introduces additional point charges connected to the LJ bead of each water molecule [125]. However, this approach comes with significantly increased computational cost.

After the mapping scheme is determined, the next crucial consideration is the intermolecular forces acting between beads. As previously mentioned, this may follow a top-down or bottom-up approach. In the bottom-up approach, the intermolecular potentials are calibrated to match a higher resolution model, most frequently at the atomistic scale. In practice, several approaches have been taken for this, including minimisation of relative entropy, force matching and machine learning [122]. Top-down approaches instead aim to choose intermolecular potentials for each bead that reproduce experimental data. While development of intermolecular potentials following a bottom-up approach can produce very accurate potentials for a particular system of interest, they are usually limited in their transferability, for example when the molecules being investigated are changed or when simulation conditions, such as component concentrations or system temperature, are altered.

3.1.6.2 The Martini Force Field

The Martini family of CG force fields takes a different approach to many coarse-graining methods that are developed and parametrised to study a particular system of interest. The first version of Martini was developed to study lipid and surfactant systems [126], but was later expanded to study a variety of biomolecular systems [76] including proteins [127] and DNA [128]. In Martini, beads are mapped based on underlying chemical specificity and parameterized based on a range of experimental data including free energies of vaporisation, free energies of hydration and water/oil partition coefficients. This creates a model which does not rely on rigorous fitting to particular systems and should therefore, in theory, permit a greater degree of transferability between different systems. The beads which are parametrised under the Martini scheme represent common chemical groups, allowing mappings for new molecules to be easily generated following a “building blocks” approach. While originally developed for studying biomolecular systems, the Martini model has been applied to a broad variety of contexts, including in nanotechnology [129] and material design [77, 130].

The Martini 3 force field [13] is a new version of Martini that looks to improve upon many issues that were inherent to the previous model [76], such as systematic deviations in packing and intermolecular interactions [131]. This new version is similar in many ways, employing the same “building block” approach which allows this model to be applied to a broad range of systems, but offers several improvements over the previous version. Like the previous version of Martini, the new version, on average, represents every 4 heavy atoms as a single “bead”. In total there are 29 different bead types, an improvement over the 18 available in Martini 2. The type of bead specifies the nonbonded interactions with other beads in the system, which are described by Lennard-Jones potentials. Charged beads (e.g. ions) also interact with Coulombic interactions. The bead type for any particular group of atoms is chosen based on the chemical structure of atoms represented by that bead. The bead types are grouped into the following categories; polar (P), intermediate/non-polar (N), apolar (C), halo-compounds (X), monovalent ions (Q), divalent ions (D), water (W). For example, a highly polar chemical group will be represented by a polar (P) bead and will interact more strongly with other polar beads than it does with apolar (C) beads. The authors of Martini 3 also provide suggested bead types for common chemical groups, for example the C1 bead type is suggested for linear alkanes while the P5 bead type is suggested for primary amides. An interaction matrix determines the strength of interaction between each pair of beads, depending on bead type, with 21 possible interaction levels ranging from “hyper attractive” to “super repulsive”, a vast improvement over the 10 interaction levels available in Martini 2 [76]. In addition, new to this version of Martini, several “labels” are available that modify this potential representing properties like hydrogen bonding capabilities and partial charges. The beads also come in three different “sizes”, tiny, small and regular. Small and tiny beads allow for higher resolution mapping, representing fewer heavy atoms per bead. Small beads, on average, represent 3 heavy atoms in a single bead while tiny beads represent 2. These smaller beads can also be used to provide improved mapping for fully branched or cyclic structures. While small beads were available in the previous version of Martini, tiny beads are new, allowing for higher resolution mapping than was previously possible. In addition, cross-interactions between beads of different sizes are modified, allowing for improved intermolecular interactions and packing [13].

Once a sensible bead type is selected, bond lengths, angles, dihedrals and their corresponding force constants need to be determined. Typically, harmonic potentials are used, or constraints in the case of very rigid bonds. The parameters of bonded potentials are determined from an atomistic reference simulation, following a bottom-up approach. The center-of-geometry of the group of atoms described by each bead is calculated from the atomistic trajectory at each timestep, and the harmonic potential parameters are fitted to this reference data for angles and dihedrals between beads.

3.2 Experimental Methods

3.2.1 Design of Experiments

Design of Experiments is a structured statistical method which allows the relationships between “factors” (inputs) and “responses” (outputs) to be determined. Factorial two-level experimentation is a particularly efficient technique to study the effect that combinations of changes in input factors have (i.e. identifying where changing two factors at once changes a response), which would otherwise be missed in simpler approaches that vary only one factor at a time. In factorial two-level studies, each factor is assigned two levels, typically a “low” and “high” value. An experiment is carried out for each combination of low and high factors, meaning that the total number of runs is equal to 2^k, where k is the total number of factors chosen [132]. This means that the number of experiments that must be carried out increases exponentially with the number of factors investigated, meaning it is important to limit the number of factors to a reasonable number (as every additional factor investigated will double the number of experiments that must be carried out). After the factorial two-level study, any interesting findings can then be investigated further through targeted experiments, making this method effective for screening potential factors at an early stage of investigation.

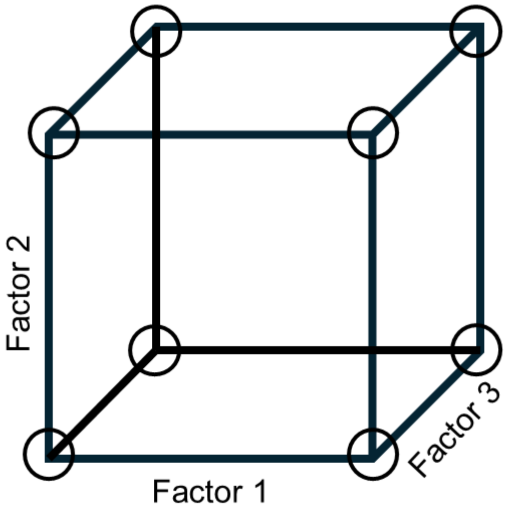

Figure 3.3: An example of a factorial two-level experimental design with 3 factors. The circled points are the conditions under which experiments would be carried out.

3.2.2 Gas Adsorption

Gas adsorption analysis is a widely used method in material science for characterizing the surface properties and porous structure of materials. It involves measuring the quantity of gas adsorbed onto a material's surface under controlled temperature and pressure. Nitrogen adsorption at 77 K is the most common technique, due to nitrogen's inert nature and well-characterized adsorption behaviour. In nitrogen adsorption, the same is cooled to 77 K under vacuum. Starting at low relative pressure, nitrogen is introduced to the sample at set points allowing the quantity of nitrogen adsorbed to be measured as a function of relative pressure, P/P_0.

The function of quantity of nitrogen adsorbed versus relative pressure is known as the nitrogen adsorption isotherm and can be analysed to obtain various properties of the material. The isotherm itself can be characterized according to the IUPAC classifications. There are 6 main classifications with two additional subtypes introduced in the 2015 reclassification [133]. These types are summarised in Table 3.2 and Figure 3.4.

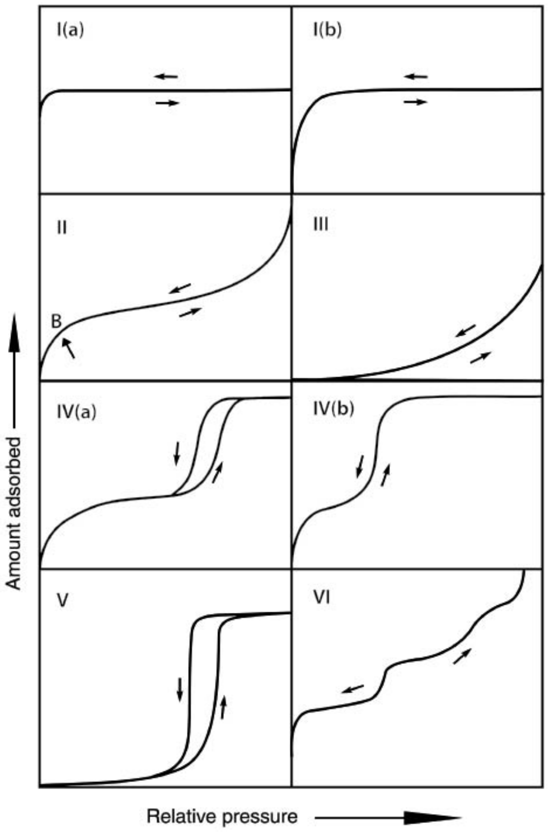

Figure 3.4: The IUPAC classifications of gas adsorption isotherms, taken from [133].

Table 3.2: Description of the IUPAC classifications of gas adsorption isotherms.

Type	Character	Description
I(a)	Narrow Microporous	Initial sharp increase corresponding to filling of small micropores followed by a plateau. Typical of microporous materials (pore width $<$ 1 nm)
I(b)	Wider Microporous	Gradual increase at low relative pressure corresponding to gradual filling of micropores followed by a plateau. Typical of microporous materials (pore width 1-2 nm)
II	Non-Porous or Macroporous	Continuous, convex upward adsorption curve with no plateau. Reflects adsorption on a relatively flat surface.
III	Weak Adsorbate-Adsorbent Interaction	Concave upward curve with no inflection point. Indicates weak interactions between the adsorbent and adsorbate with adsorption occuring primarily through adsorbate-adsorbate interactions. Typical of hydrophobic surfaces.
IV(a)	Mesoporous Adsorption with Capillary Condensation	Initially similar to Type II followed by sharp increase at intermediate pressures and a plateau. Hysteresis loop on desorption caused by capillary condensation in mesopores. Typical of mesoporous materials (2-50 nm).
IV(b)	Narrow Mesoporous Adsorption with Capillary Condensation	As Type IV(a) but with more pronounced hysteresis. Typical of materials with narrow mesopores (2-4 nm).
V	Weak Interaction with Capillary Condensation	Initially similar to Type III followed by steep rise at intermediate pressures. Occurs due to weak adsorbate-adsorbent interactions but capillary condensation occurs in mesopores. Typical of mesoporous materials with hydrophobic surfaces.
VI	Stepwise Multilayer Adsorption	Adsorption occurs in steps corresponding to successive molecular layers. Indicates a homogeneous, nonporous surface. Rarely observed except with highly ordered materials (e.g. graphite).

The adsorption isotherm can be used to determine the surface area of a material. The most common method is the Brunauer-Emmett-Teller (BET) method [134]. This method extends Langmuir's theory of adsorption to include multilayer adsorption. Langmuir's adsorption model makes the following assumptions:

- The surface is homogeneous.
- The energy of adsorption is equal for all sites.
- Each site can hold only one molecule.
- There are no interactions between adsorbed molecules.

Under BET theory, the above assumptions are applied to each adsorbed layer. In addition, the following assumptions are made:

- Gas molecules adsorb on solid layers infinitely.
- Each layer only interacts with adjacent layers.
- The enthalpy of adsorption of the first layer is greater than subsequent layers.
- The enthalpy of adsorption for the second layer and greater is equal to the enthalpy of liquefaction.

The BET equation is:

$$\frac{P}{V(P_0 - P)} = \frac{1}{V_m C} + \frac{C-1}{V_m C} \cdot \frac{P}{P_0} \tag{3.40}$$

where P is the equilibrium pressure of the adsorbate, P_0 is the saturation pressure of the adsorbate, V is the volume of gas adsorbed, V_m is the monolayer adsorbed gas volume and C is the BET constant which is related to the adsorption enthalpy. This equation is rearranged to plot $P/(V(P_0 - P)$ against P/P_0 at low relative pressures (typically $0.05 < P/P_0 < 0.3$), so that the slope and intercept of the linear region can be used to calculate V_m and C. The specific surface area can then be calculated from V_m:

$$S = \frac{V_m \cdot N_A \cdot \sigma}{M} \tag{3.41}$$

where S is the specific surface area, N_A is Avogadro's number, σ is the cross-sectional area of the adsorbate molecule and M is the molar volume of nitrogen.

While the BET method for determination of surface area is typically effective, there are limitations particularly when applied to microporous or mesoporous materials. Rouquerol et al. suggested modifications to the method which refine the analysis by improving the choice of pressure range for the BET region [135]. According to this, the following criteria must be met when selecting the pressure range for BET analysis:

- The fit against BET transformed data must be linear.
- The constant, "C", must be positive.
- A Rouquerol plot of $V(1 - P/P_0)$ against P/P_0 must be increasing in the range selected.
- V_m must be within the limits of the portion of the adsorption isotherm that was used for the BET fit.
- The value of $1/(\sqrt{C} + 1) \approx P/P_0$ at the monolayer capacity.

Applying these additional criteria ensures isotherm data represents physical monolayer adsorption and avoids errors due to capillary condensation or multilayer effects.

There are several methods available for determination of pore volume and pore size distributions from nitrogen adsorption isotherms, such as the Barrett-Joyner-Halenda (BJH) [136], Density Functional Theory (DFT) [137] and Horvath-Kawazoe (HK) [138] methods. Of these methods, only BJH and DFT are appropriate for determination of pore sizes in mesoporous materials. The DFT method is more flexible and allows for determination of properties in more complex pore systems with a broader range of pore size, however it requires careful model selection to ensure accurate results [139]. BJH is more straightforward to apply, but should only be applied to mesoporous materials (2-50 nm pores) and assumes that pores are cylindrical. Since the materials of interest in this work are expected to have cylindrical pores in the mesoporous range, this method is used for estimation of pore volume and pore size distribution.

The BJH method is an extension of BET theory that is typically applied to the desorption isotherm. When pressure is reduced during desorption, liquid in the pore evaporates from the "core" of the pore, leaving behind adsorbed molecules of a certain "thickness". The radius of the pore (r_p) simply results from the sum of the core radius (r_k) and adsorbate thickness (t):

$$r_p = r_k + t \tag{3.42}$$

The Kelvin equation can be used to calculate the core radius [140], and various methods, mostly empirical, are available to calculate adsorbate thickness as a function of the relative pressure. These include the Halsey [141], Harkins and Jura [142] and Broekhoff-de Boer [143] methods. The volume of gas desorbed at each pressure step during desorption is corrected by the volume of gas still adsorbed, and this is used to calculate the pore volume. As mentioned previously, the BJH method is only applicable to pores $>$ 2 nm, since below this diameter the adsorbate cannot be considered a real liquid with bulk properties and therefore the Kelvin equation does not apply. BJH also assumes cylindrical pores, and may be affected based on pore geometry (for example, if larger pores are only accessible through smaller pore windows).

3.2.3 X-Ray Diffraction

X-ray diffraction (XRD) is an analytical technique which is frequently used to characterize the crystalline structure and textural properties of porous materials. In XRD, the X-rays passing through a material are scattered by periodic atomistic planes, due to the material's structure, and their constructive interference is measured. The intensity of diffracted X-rays is measured against the angle of incidence of the X-rays giving a plot of intensity versus 2θ which is known as the diffraction pattern. Results can be interpreted by considering Bragg's law:

$$n\lambda = 2d\sin\theta \tag{3.43}$$

where n is the order of the diffraction, λ is the wavelength of the X-rays, d is the interplanar spacing and θ is the angle of incidence [144]. This creates a relationship between the angle at which peaks in the diffraction pattern are observed, and the size of related structural characteristics that cause these peaks. This has an inverse relationship, so peaks in the diffraction pattern at low angles indicate larger features, while peaks at high angles indicate smaller features. Often, XRD is carried out over a broad range of angles in order to record as many diffraction peaks as possible, corresponding to different crystal phases within the material, which can be referenced against known data from a database [145]. In addition, different 2θ values correspond to specific crystal planes. The orientation of a plane within a crystal lattice can be described by the Miller index, which is a set of three numbers, h, k and l (see Figure 3.5). For hexagonal lattices, the four-index Miller-Bravais notation is often used which introduces the redundant index i where $i = -(h + k)$.

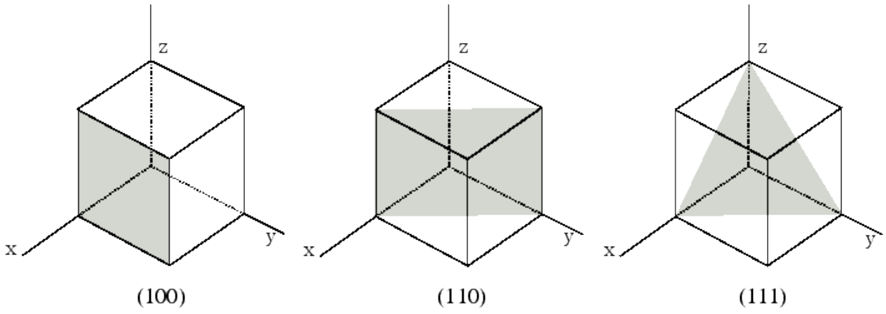

Figure 3.5: Miller notation for simple cubic planes.

Small angle XRD can be used to provide information on the long-range periodicity and pore arrangement in mesoporous materials, such as MCM-41 [5]. In this case, the XRD pattern does not come from atomic planes but instead from periodic mesoporous walls. The peaks in the diffraction pattern can be indexed assuming a hexagonal (p6mm) symmetery. The peaks which are typically indexed for MCM-41 are the (100), (110) and (200) peaks (see Figure 3.6). The (100) peak is the most intense and corresponds to the hexagonal periodicity of mesopores, while the (110) and (200) peaks correspond to higher order reflections which indicate further structural ordering.

As well as providing a qualitative analysis of whether certain phases exist within a material, the varying intensities of different diffraction peaks gives an indication of the amounts of each phase present [145]. In the case of MCM-41, this has been used to provide a measure of the long-range structural ordering in the material [146]. This is dicussed in further detail in Chapter 5.

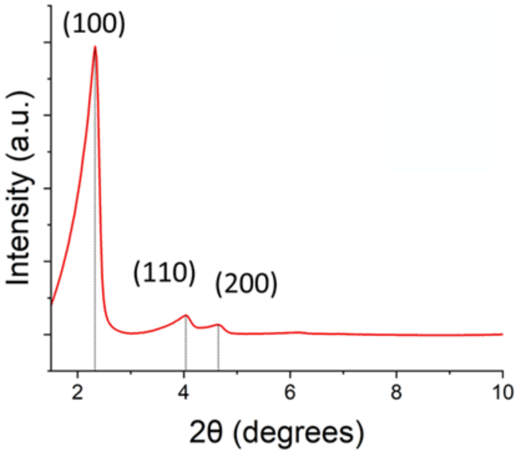

Figure 3.6: Example of a typical X-ray diffraction pattern for MCM-41 with the peaks corresponding to hexagonal lattice parameters labelled.

Chapter 4

Development and Validation of Coarse-Grained Model

4.1 Introduction

Since the morphology of OMS is determined by the silica-surfactant self-assembly process, understanding the formation of the liquid crystal phase allows for prediction of the structure of the resultant porous material, creating a crucial link between synthesis conditions and material properties. Many experimental studies have attempted to understand the mechanisms of self-assembly using a broad variety of techniques including in situ x-ray and neutron scattering [147]. However, due to the complexity of the synthesis process, which involves a range of phenomena including self-assembly, chemical reactions, nucleation and phase separation taking place simultaneously over a broad range of time and length scales, it is a challenging system to probe experimentally. Therefore, a variety of computational modelling techniques have been applied to study this system, which were extensively reviewed by Jorge et al. [9] and discussed in Section 2.5.

One fruitful approach followed a multi-scale strategy, using atomistic models of silica and surfactant species to tune coarse-grained molecular dynamics models using the Martini 2 framework [75, 77]. Later work using this model explored systems with higher surfactant concentrations to investigate the formation mechanism for OMS materials [78]. The system modelled by Pérez-Sánchez et al. involves silicate species, the cationic surfactant cetyltrimethylammonium bromide (CTAB) and water. First, the model for CTAB was validated with a binary CTAB and water system, comparing average micelle size and surfactant aggregation number to experimental data. Next, the model for anionic silica monomers was developed using a comparison between CG simulations and an atomistic reference [75]. The atomistic model used as a reference for anionic silicates was the model of Jorge et al. [74, 148] which was adapted from the neutral silicates model of Pereira et al. [149] with new charges and geometries obtained from DFT calculations [150]. This CG model was later extended to include higher oligomers of anionic silica, namely dimers, linear trimers and tetramers, cyclic trimers and tetramers, and cubic octamers [77]. In these higher oligomers, one CG bead is used per silicon atom and the same parameters are used for all beads in all oligomers with the exception of cyclic oligomers, which used the same bead type but with an “S” (meaning small) prefix, thus changing interactions with other small beads. However, in Martini 2, interactions between small beads and regular sized beads are unchanged when this prefix is applied. It should be noted, however, that the parameters used for higher oligomer beads are different from those used for monomers. This is because in atomistic simulations of a single CTAB micelle, the silica monomers were absorbed into the headgroup of the micelle whereas the dimers aggregated primarily outside the headgroup region. Therefore, the parameters of dimers were adjusted from the original monomer model to reproduce this behaviour.

The model of Pérez-Sánchez et al. was built using the Martini 2 force field [76]. This is a “building block” based force field where four heavy (non-hydrogen) atoms are mapped to each bead on average, based on their chemical specificity. Martini 2 is an incredibly popular force field with a broad range of applications. However, it has certain limitations. In particular, it lacks cross interactions between beads of different sizes and provides poor agreement with experimental data for both solutes and solvents where short bond lengths are used [131]. In recent years, the Martini 3 force field has been published which aims to fix some of the issues with the previous version whilst also expanding the range of bead types available [13]. The Martini 3 force field was discussed in more detail in Section 3.1.6.2.

The availability of the Martini 3 force field [13] and of a new force field for atomistic simulation of silicate species [12] presents an opportunity to improve upon the CG model for OMS formation of Pérez-Sánchez et al. [77]. The new atomistic model for silicates, recently developed by Jorge et al.[12], was parametrized according to the Polarisation Consistent Approach (PolCA) [151, 152] and validated against available experimental data for organosilicates. The availability of this improved model motivates the need to re-parametrize any CG model used in this work, to ensure that it is validated against the most up-to-date atomistic models for silicates. In addition, the increased degree of customisation built into the Martini 3 force field when compared to the previous iteration in terms of additional bead types, sizes and labels, allows for the CG model to be more finely tuned to match data from both experiment and more detailed (i.e. atomistic) simulations, permitting finer control over the interactions in the system that give rise to OMS formation. Furthermore, the use of the Martini 3 model provides an improved ability to incorporate additional species into the system. By creating a model using the Martini 3 force field, taking advantage of these improvements, compatibility with future models for species relevant to mesoporous silica formation (e.g. additives, surfactants, co-surfactants) is ensured. For these reasons, we adopt the Martini 3 framework in this work, which implies that the models for all molecules need to be re-developed and/or revalidated.

4.2 Defining the System

To allow for the investigation of the alternative bio-inspired mesoporous silica route, a model is required that accurately describes the self-assembly of the surfactant, CTAB, in the presence of orthosilicic acid residues (referred to as “silicates”) and the bio-inspired additives. From previous experimental work (see Section 1.1), the bio-inspired additive arginine was proposed to be effective at promoting the rapid precipitation of ordered mesoporous silica at ambient temperature. In experimental work carried out for this thesis (see Chapter 5), pentaethylenehexamine (PEHA) was also investigated as an alternative additive. Therefore, models for both of these additives are required. In a typical synthesis, the components are combined in solution forming a high pH mixture (pH > 13). Acid is then added, resulting in precipitation of ordered mesoporous silica. The addition of acid lowers the pH to a reaction pH which has been observed to yield ordered material, between pH 7 and 11. However, the self-assembly of the silica-surfactant HLC phase is expected to occur at the initial high pH, approximately 13.0-13.5, and therefore the CG model will focus primarily on species which are present at this pH.

Silicates are present in solution at varying degrees of oligomerisation (i.e. monomers, dimers, trimers etc.). Therefore, the model ideally needs to be able to represent these different oligomers. However, anionic silica dimers have been shown to be sufficient for representing the self-assembly of the HLC phase in prior work [77] and therefore the development of an accurate model for silica dimers is prioritised in this work. As in the work of Pérez-Sánchez et al., dimer parameters are thereafter assumed to be valid for higher oligomers; the validity of this assumption will be analysed later in the thesis. For dimers, the first two pKa values, which correspond to the deprotonation of a single silanol group bonded to each silicon atom, have been reported as 9.0 and 10.7, while the pKa value corresponding to the first deprotonation of a silanol group in silica monomers is 9.5 [17] (see Figure 4.2). The relative composition of the different degrees of protonation for dimers between pH 7 and 14 is given in Figure 4.1. Species with more than a single deprotonated silanol group per silicon atom are present only at extremely high pH values [17]. Thus, they are not present in significant quantities in the self-assembly of OMS materials, which typically occurs below pH 14, and are therefore not considered here.

As previously mentioned, in addition to being present as both neutral and anionic species in this system, silicates condense to form oligomers in solution, requiring the model to describe higher oligomers as well as monomers. Two approaches can be taken for this. The first is to develop a “non-reactive” model, in which silicates of multiple degrees of oligomerisation are parametrized separately. These pre-formed oligomers can then be inserted into CG simulations directly, either at the start of the simulation to

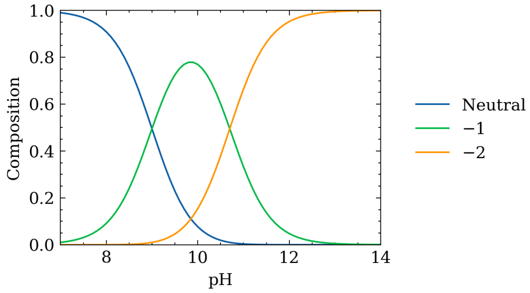

Figure 4.1: Distribution of charge states for siica dimers between pH 7 and 14. The total molecular charge for each degree of protonation is given in the legend.

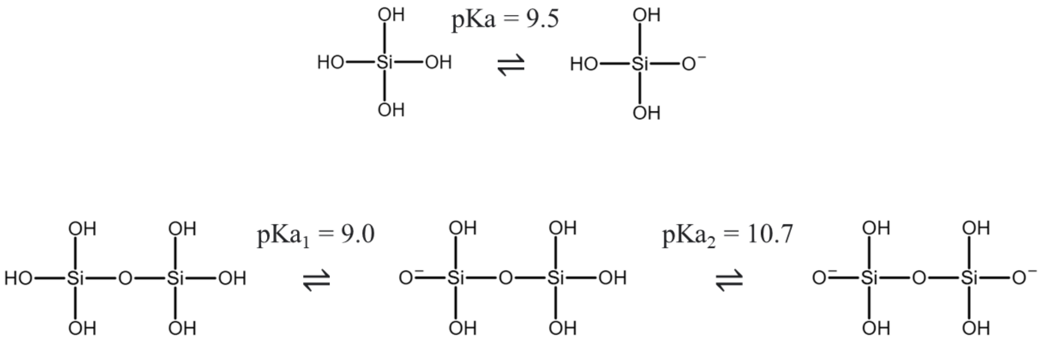

Figure 4.2: Diagram of pKa values corresponding to the ionisation of silanol groups in silica monomers and dimers.

represent a single stage in the condensation process, or added throughout the simulation manually to represent gradually increasing oligomerisation. With this approach, each oligomer should be validated separately, significantly increasing the number of molecules that must be validated. The second approach is to implement a reactive model, such as the model of Carvalho et al. [92], which explicitly includes silica polycondensation reactions. In this case, only monomers need to be parameterised as higher oligomers are simply represented by "reactive potentials" between monomers. The prior approach is taken in this work as the integration of the reactive model into self-assembly models is a significant challenge, and the representation of small oligomers (in particular, dimers and cubic octamers) is sufficient to study the self-assembly of OMS materials. However, to fully investigate the behaviour of the system during the reaction stage of synthesis (i.e. after acid is added to the mixture to trigger the precipitation of silica) the use of a reactive model would be required.

Arginine has three ionisation points, corresponding to pKa values of 2.17, 9.04 and 12.48 [153]. The most relevant protonation state in this work is shown as IV in Figure 4.3, which is present in high proportions (>75%) during HLC self-assembly in the early stages of OMS synthesis. This form has an overall negative charge situated on the carboxylate group of the amino acid backbone. The guanidinium group of the arginine sidechain, which is typically positively charged at physiological pH, becomes deprotonated at high pH.

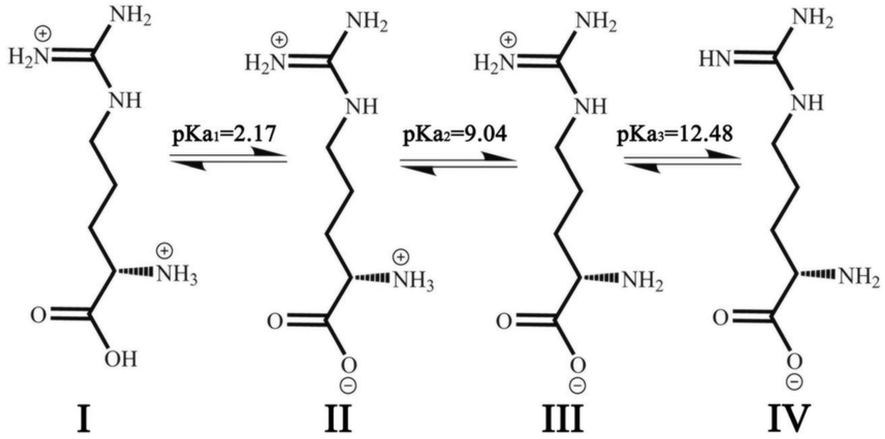

Figure 4.3: Diagram of pKa values corresponding to the ionisation of multiple chemical groups in an arginine molecule. Taken from Wang et al. [153].

PEHA has two ionisation points, corresponding to pKa values of 9.7 and 11.0 [154] (shown in Figure 4.4). The most relevant protonation state to this work is when the molecule bears an overall neutral charge with deprotonated amine groups, which occurs at high pH values. The relative composition of different degrees of protonation for both bio-inspired additives between pH 7 and 14 are given in Figure 4.5.

The pores formed are on the mesoscale, similar in size to that of MCM-41 (without the presence of an auxiliary organic), that is approximately 2-4 nm [5]. To observe self-assembly, large simulation box sizes are required; previous MD simulations have used cubic boxes with 36 nm side lengths [77]. Simulations of this size involve around 10^6 atoms, significantly out of reach of fully atomistic simulations. Therefore, as in previous work, a CG model must be employed [77].

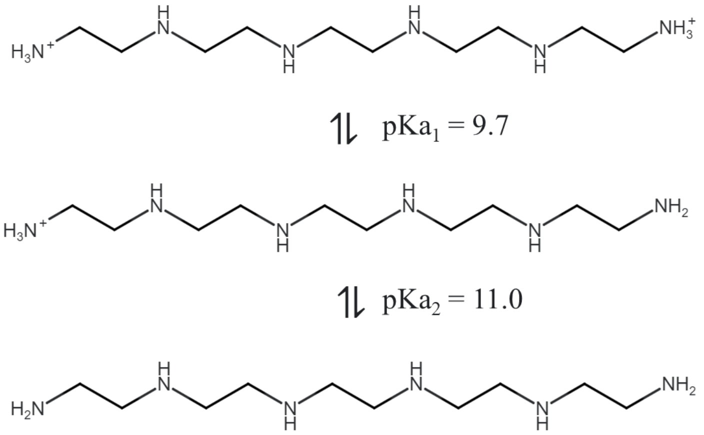

Figure 4.4: Diagram of pKa values corresponding to the ionisation of terminal amine groups in PEHA.

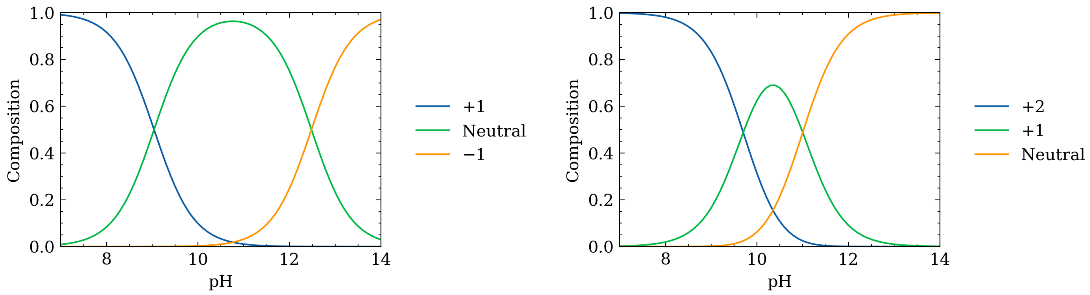

Figure 4.5: Distribution of charge states for bio-inspired additives arginine (left) and PEHA (right) between pH 7 and 14. The total molecular charge for each degree of protonation is given in the legend.

4.3 Model Development Methodology

A straightforward "building blocks" based approach is suggested by the authors of the Martini 3 force field, describing how new molecules should be parametrized under this framework [13]. The procedure follows these steps, which are described in more detail below:

1. Map CG beads to the atomistic model
2. Assign (first guess) bead types
3. Generate bonded parameters from atomistic reference data
4. Validate and refine bead type if required

As described previously, each Martini "bead" represents a number of atoms, with on average 4 heavy atoms being described by each bead ("4-1 mapping"). Atoms in the molecule must therefore be divided up into groups, taking care to avoid splitting chemical groups between beads. Where it is necessary to create a group of less than 4 heavy atoms, small or tiny beads can be used to represent 3 or 2 atoms, respectively. In addition, fully branched structures and aliphatic rings should typically use a smaller bead type than linear structures. For example, a fully branched structure representing 4 heavy atoms should use a small bead instead of a regular sized bead. Higher resolution (i.e. 3-1 or 2-1) should also be considered in cases where chemical groups with different behaviours would otherwise be mapped to the same bead, as this allows for better reproduction of site-specific molecular interactions.

When the molecule is fully mapped, each bead must be assigned a "type". In total there are 29 different bead types available in Martini 3, including a special bead type for water. The bead types are grouped into the following categories; polar (P), intermediate/non-polar (N), apolar (C), halo-compounds (X), monovalent ions (Q), divalent ions (D), water (W). The bead type chosen determines that bead's interactions with other beads in the system through a matrix using 21 discrete interaction levels from "hyper attractive" to "super repulsive". These interactions can be tweaked further with the use of "labels" as described previously. The selection of bead types is critical to the function of the CG model and will often need to be revised during the development and validation of the model.

Once a sensible bead type is selected, bond lengths, angles, dihedrals and their corresponding force constants need to be determined. This should be done according to the centre-of-geometry of each bead, and can be calculated from an atomistic reference simulation. This can be done easily by using PyCGTOOL [155] by supplying an atomistic simulation trajectory of a single molecule in water and the mapping scheme corresponding to the molecule to be mapped.

As described previously, Pérez-Sánchez et al. [75, 77] established a procedure for developing a CG model for silicates compatible with the Martini 2 CG force field in the context of OMS synthesis. In this work, a similar procedure to that presented by Pérez-Sánchez et al. [75] has been applied to develop the CG model under the Martini 3 framework. This involves first validating a model for CTAB, then extending this model to include silicates. The approach used for validation will depend upon the availability of either experimental data or atomistic level models for a particular chemical species. A summary of the species requiring validation and the data used for that validation is given in Table 4.1. For CTAB, the experimentally determined aggregation number and phase behaviour were used to validate the coarse-grained model, similar to the approach of Pérez-Sánchez et al. [75]. Silicates are only stable in aqueous solution at very low concentration and/or very high pH as silicic acid and its derivatives. At higher concentrations and closer to neutral pH, silicic acid precipitates as a gel [19] and therefore there are no pure-fluid experimental properties that can be used to directly validate the CG model. To circumvent this limitation, in our previous work, an atomistic model for silicates was validated against experimental data for organosilicates, such as density and enthalpy of vaporization, since organosilicates are stable as pure liquids [12]. In the present work, the CG model for silicates is validated against this atomistic model of Jorge et al., and therefore the CG model is also indirectly validated against experimental data. Therefore, for all new species modelled, a combination of "top-down" and "bottom-up" approaches is employed, increasing our confidence in the model

Table 4.1: Summary of experimental data and atomistic reference models that were used to validate the CG model. Species that are already present in the Martini 3 force field are excluded (e.g. water, ions).

Species	**Experimental Data**	**Atomistic Model**
Silicates (neutral and anionic)	None	Jorge et al. [12]
CTAB cation (CTA$^+$)	Aggregation number, mesophase diagram	OPLS-AA [106, 156–160]
Arginine (-1, neutral)	Transfer free energies	OPLS-AA [106, 156–160]
PEHA (neutral, +1, +2)	None	OPLS-AA with 1.14*CM1A-LBCC [106, 156–163]

to accurately predict real molecular level behaviour.

In this work, the following nomenclature for describing silica species is used: anionic silica is identified as “SI” while neutral silica is identified as “SN”. This is followed by a number indicating the degree of condensation of the silica molecule (i.e. the number of silicon atoms), for example “SI1” for anionic silica monomers and “SN2” for neutral silica dimers. For oligomers with three or more silicon atoms, a suffix label is used to indicate the structure: l for linear molecules, y for cyclic molecules (three silicon atoms with each bonded to the other two by the Si-O-Si bond) and c for cubic molecules (as in silica octamers). For example, anionic cyclic trimers are named “SI3y” while anionic silica octamers are labelled “SI8c”. Silica oligomers with both anionic and neutral groups are labelled with the number of anionic groups followed by the number of neutral groups, followed by a label indicating structure where applicable. For example, silica dimers with a single deprotonated silanol group (therefore bearing a -1 overall molecular charge) are identified as “SISN”, while cubic silica octamers with a -4 charge are identified as “SI4SN4c”.

4.4 General Simulation Methods

4.4.1 Software

All computational work was carried out using the GROMACS 2022.1 software package which allows molecular dynamics (MD) simulations to be carried out with high computational efficiency due to the use of state-of-the-art algorithmic optimizations and parallelization [164, 165]. Calculations for large simulations were carried out on a GPU.

The general purpose programming language Python 3 [166] was used to aid in setting up and running simulations. For analysis of simulation data the built-in GROMACS analysis tools were used as well as the MDAnalysis library for Python [167, 168]. Graphs were generated using the Matplotlib library for Python [169].

4.4.2 Atomistic Simulation Details

For atomistic simulations, the leapfrog algorithm [111] was used with a time step of 2 fs. All simulations took place at room temperature (298 K) and pressure (1 bar) using the velocity-rescaling thermostat [115] and the Parrinello-Rahman barostat [120, 121]. Cubic boxes with periodic boundary conditions were used. A 1.2 nm cut-off was used for Lennard-Jones (LJ) interactions with a switching function between 0.9 and 1.2 nm. Long range dispersion corrections for both energy and pressure were applied. Electrostatic interactions were accounted for using the particle-mesh Ewald method [113, 170]. Before MD for all atomistic simulations, energy minimisation was carried out using the steepest descent algorithm followed by equilibration in the NVT and NpT ensemble consecutively for 100 ps each.

The rigid single point charge (SPC/E) potential was chosen to represent water molecules [171]. CTAB molecules in this work are present as CTA^+ cations, and references to CTAB throughout this work refer to this cationic form. For the CTA^+ cations, parameters were taken from the OPLS potential [106, 156–160] using a fully atomistic model with explicit hydrogens. Silicates were modelled using the model of Jorge et al. [12] parametrized according to the Polarization-Consistent Approach (PolCA) [151, 152]. For arginine and PEHA, atomistic models were used only to determine bonded parameters for the CG model, so in both cases an atomistic model corresponding to an overall neutral molecular charge was used (removing the need to include counter-ions in these simulations). The parameters for arginine were taken from OPLS, with parameters initially generated using the `gmx pdb2gmx` tool in GROMACS. The charge of the alpha carbon was then reduced by 0.02 in order to achieve a neutral overall charge for the molecule, because the initial output of the `gmx pdb2gmx` did not achieve a overall neutral molecular charge for this form of arginine. However, this small change is not expected to affect the behaviour of the molecule. The atomistic model for PEHA was generated using the LigParGen OPLS/CM1A parameter generator utility with localised bond-charge corrected CM1A charges [161–163].

Atomistic simulations were used for two purposes. Firstly, simulations of single molecules solvated in water were used to generate atomistic reference data for bonded parameters based on centre of geometry mapping. In these atomistic simulations, a single molecule was placed in a cubic box with a side length of 3 nm. The box was then solvated with an appropriate number of water molecules to achieve a realistic density using the `gmx solvate` tool in GROMACS. A simulation time of 50 ns was used for calculation of these bonded parameters. Bonded parameters were generated from simulation trajectories using the PyCGTOOL utility [155]. Secondly, atomistic simulations of a single preformed CTAB micelle were used as a reference to assess how closely the CG model matched atomistic micelle morphology, and also to validate the interactions of other molecules in the system (i.e. silicates and bio-inspired additives) with the surfactant by examining their interaction with a single surfactant micelle in water. In order to evaluate this, radial density profiles for all species present in the simulations were calculated from the micelle centre-of-mass. Simulations involving a single micelle were set up starting from a pre-formed micelle used in previous work [77]. Any relevant solutes and bromide counter-ions were added randomly to the simulation box before solvation in water using the `gmx solvate` tool. For arginine, an additional simulation was carried out in the presence of anionic silica dimers in order to provide a reference for the interactions between arginine molecules and oligomeric silica species. A summary of all atomistic simulations carried out in this work is provided in Table 4.2.

Table 4.2: Details of single micelle atomistic simulations carried out. N is the number of molecules of each species (denoted by the subscript) present in the simulation. L is the box length in the x, y and z direction.

Simulation	N_{CTAB}	N_{SI}	N_{SI2}	N_{SI3l}	N_{SN}	N_{SN2}	N_{SN3l}	N_{SISN}	N_{Arg}	N_{Br}	N_{Water}	L (nm)
Preformed Micelle Simulations												
No solutes	100	0	0	0	0	0	0	0	0	100	49803	11.6
SI1	100	100	0	0	0	0	0	0	0	0	49470	11.6
SI2	100	0	50	0	0	0	0	0	0	0	49573	11.6
SI3l	100	0	0	33	0	0	0	0	0	1	49582	11.6
SN	100	0	0	0	100	0	0	0	0	100	49082	11.6
SN2	100	0	0	0	0	100	0	0	0	100	49057	11.6
SN3l	100	0	0	0	0	0	100	0	0	100	48721	11.6
SISN	100	0	0	0	0	0	0	50	0	50	49469	11.6
Arginine	100	0	0	0	0	0	0	0	25	100	49568	11.6
Arginine + SI2	100	0	50	0	0	0	0	0	25	0	49342	11.6

4.4.3 Coarse-Grained Simulation Details

Coarse-grained simulations were carried out using the suggested parameters proposed by the authors of the Martini 3 model [13]. After setting up the initial configuration, energy minimisation was carried out using the steepest-descent algorithm. NVT equilibration was carried out using a velocity-rescaling thermostat [115] with a 2 fs time step. NpT equilibration was carried out using the Berendsen barostat, also with a 2 fs time step. Full MD simulations used a timestep of 30 fs unless otherwise stated, using the leap-frog algorithm. For temperature control, a velocity-rescaling thermostat was used and the pressure was controlled with the Parrinello-Rahman barostat [120, 121]. For Lennard-Jones terms, the Verlet cutoff scheme [110] was used with a cutoff value of 1.1 nm. Electrostatics were accounted for using reaction field with a cutoff value of 1.1 nm and a relative permittivity of $\varepsilon_r = 15$. Full details of all simulations carried out in this chapter are provided in Table 4.3.

The thermodynamic integration free-energy technique was utilised in the development of the coarse-grained model for arginine. The free energy of solvation for a small molecule was calculated in each relevant solvent by first carrying out energy minimisation of a simulation box containing a single molecule surrounded by solvent molecules. A series of simulations were carried out in which the non-bonded interactions between solute and solvent were scaled from full to none according to a coupling parameter, λ, and the free energy difference was estimated through Bennett's acceptance ratio (BAR) [172] using the `gmx bar` command in Gromacs. 11 evenly spaced λ values between 0 and 1 were used. Soft-core potentials [173] were applied with an alpha parameter of 0.5 and linear change in coupling with λ.

Table 4.3: Details of coarse-grained simulations carried out for model validation. N is the number of molecules of each species (denoted by the subscript) present in the simulation. Note that each water bead represents 4 water molecules. L is the box length in the x, y and z direction. t is the total simulation time.

Simulation	Box Type	N_{CTAB}	N_{SI}	N_{SI2}	N_{SI3l}	$N_{SI8c(4-)}$	N_{SN}	N_{SN2}	N_{SN3l}	N_{SISN}	N_{Arg}	N_{PEHA}	N_{Br}	N_{Water}	L_x (nm)	L_y (nm)	L_z (nm)	t (µs)
Preformed Micelle Simulations																		
CTAB	Cubic	100	0	0	0	0	0	0	0	0	0	0	100	12500	11.6	11.6	11.6	0.15
SI1	Cubic	100	100	0	0	0	0	0	0	0	0	0	0	12500	11.6	11.6	11.6	0.5
SI2	Cubic	100	0	50	0	0	0	0	0	0	0	0	0	12500	11.6	11.6	11.6	0.5
SI3l	Cubic	100	0	0	33	0	0	0	0	0	0	0	1	12500	11.6	11.6	11.6	0.5
SN1	Cubic	100	0	0	0	0	100	0	0	0	0	0	0	12500	11.6	11.6	11.6	0.5
SN2	Cubic	100	0	0	0	0	0	100	0	0	0	0	100	12500	11.6	11.6	11.6	0.5
SN3l	Cubic	100	0	0	0	0	0	0	100	0	0	0	100	12500	11.6	11.6	11.6	0.5
SISN	Cubic	100	0	0	0	0	0	0	0	100	0	0	0	12500	11.6	11.6	11.6	0.5
Arg	Cubic	100	0	0	0	0	0	0	0	0	0	25	100	12500	11.6	11.6	11.6	0.5
Arg + SI2	Cubic	100	0	100	0	0	0	0	0	0	0	25	0	12500	11.6	11.6	11.6	0.5
CTAB Solutions																		
3 wt%	Cubic	500	0	0	0	0	0	0	0	0	0	0	500	82000	21.7	21.7	21.7	9.0
6 wt%	Cubic	2000	0	0	0	0	0	0	0	0	0	0	2000	160000	27.4	27.4	27.4	9.0
15 wt%	Cubic	840	0	0	0	0	0	0	0	0	0	0	840	24000	15.5	15.5	15.5	1.0
50 wt%	Cubic	2800	0	0	0	0	0	0	0	0	0	0	2800	14250	15.5	15.5	15.5	1.0
65 wt%	Cubic	3600	0	0	0	0	0	0	0	0	0	0	3600	9750	15.4	15.4	15.4	1.0
75 wt%	Cubic	4200	0	0	0	0	0	0	0	0	0	0	4200	7000	15.6	15.6	15.6	1.0
CTAB/Silica Solutions																		
SI1	Cubic	4000	4000	0	0	0	0	0	0	0	0	0	0	240000	31.6	31.6	31.6	3.0
SI2 #1	Elongated	1000	0	500	0	0	0	0	0	0	0	0	0	10000	8.2	8.2	27.3	6.0
SI2 #2	Half-Cubic	2000	0	1000	0	0	0	0	0	0	0	0	0	120000	31.6	31.6	15.8	12.0
SI4SN4c	Elongated	1000	0	0	0	250	0	0	0	0	0	0	0	13000	8.7	8.7	29.9	3.0
SN1	Cubic	2000	0	0	0	0	2000	0	0	0	0	0	2000	120000	25.0	25.0	25.0	6.0
SN2	Cubic	2000	0	0	0	0	0	1000	0	0	0	0	2000	120000	25.0	25.0	25.0	6.0
Additive Solutions																		
Arg	Half-Cubic	2000	0	0	0	0	0	0	0	0	250	0	2000	120000	31.6	31.6	15.8	6.0
PEHA	Cubic	500	0	0	0	0	0	0	0	0	0	250	500	160000	21.7	21.7	21.7	3.0

4.5 Model Development

4.5.1 CTAB

4.5.1.1 Atomistic Simulations

Atomistic single micelle simulations for CTAB with no solutes behaved as expected and in agreement with previous simulation work [75], with the micelle remaining stable over 5 ns of simulation time. The radial density profile is shown in Figure 4.6. The micelle size can be approximated by the modal value of the surfactant headgroup radial density profile, giving an approximate size of 2.4 nm, which is in agreement with experimental estimates [174, 175]. Bromide counter-ions are present at the surface of the micelle, as expected.

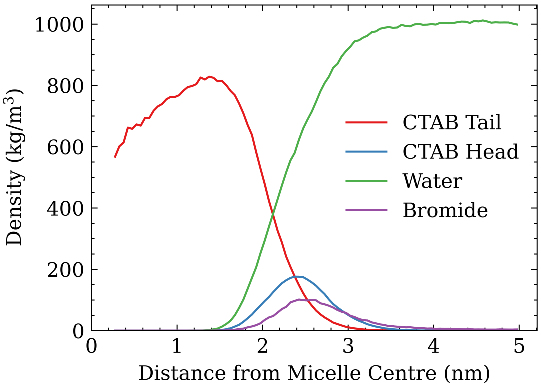

Figure 4.6: Radial density profile of single CTAB micelle taken from centre of mass.

4.5.1.2 Model Mapping and Bonded Parameters

CTA$^+$ is made up of 20 heavy (non-hydrogen) atoms in a linear arrangement, therefore the most straightforward mapping scheme is 5 regular size Martini beads (i.e. 4-to-1 mapping) as shown in Figure 4.7. The same mapping scheme was used in the model of Pérez-Sánchez et al. [75]. Linear alkanes are readily described by the C1 bead, so this bead type was used for the four beads representing the alkane tail of the molecule. The charged head group is similar in nature to a tetramethylammonium cation which is represented well in Martini 3 by a Q2 bead [13] (see Figure 4.7). Bonded parameters were generated from the reference atomistic model as described in 4.4.2 and are shown in Tables 4.4 and 4.5. The parameters generated indicate that the bond between the surfactant headgroup and first tail bead (H_1-T_2) is shorter and more rigid than bonds between surfactant tail group beads, which are slightly longer and more flexible.

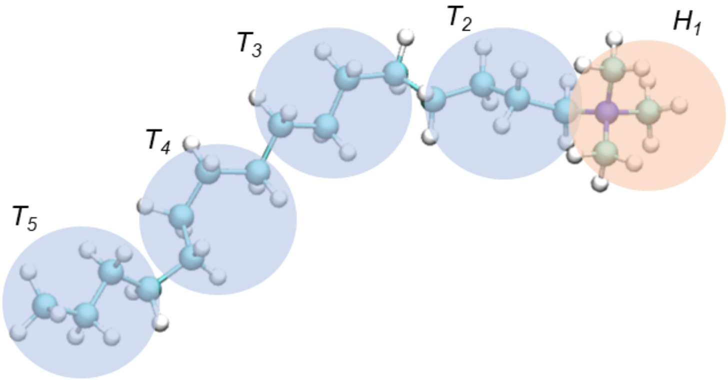

Figure 4.7: The Martini 3 mapping scheme for CTA$^+$ cations. The beads representing the alkane tail of the surfactant are shown in blue (T$_2$-T$_5$), while the bead representing the cationic head is shown in orange (H$_1$).

Table 4.4: Bonded parameters for CTA$^+$ Martini 3 model. Bead names refer to labels in Figure 4.7. b_{ij} is the bond length and k_{ij} is the bond force constant.

Bond	b_{ij} (nm)	k_{ij} (kJ mol^{-1} nm^{-2})
H_1-T_2	0.375	39,000
T_2-T_3	0.478	3,450
T_3-T_4	0.478	3,450
T_3-T_5	0.483	3,450

Table 4.5: Angle type parameters for CTA$^+$ Martini 3 model. Bead names refer to labels in Figure 4.7. θ_{ijk} is the angle between beads and k_{ijk} is the angle force constant.

Beads	θ_{ijk} (degrees)	Calculated k_{ijk} (kJ mol^{-1} deg^{-2})
H_1-T_2-T_3	156	180
T_2-T_3-T_4	150	100
T_3-T_4-T_5	150	100

4.5.1.3 Validation

For the single micelle simulation, the CG model reproduces the density profile of the atomistic simulation well (Figure 4.8). The micelle was stable over the simulation time, which confirms that this CG model produces stable micelles at an aggregation number of 100 surfactant molecules, in agreement with the atomistic model. In addition, bromide counter-ions are present on the surface of the micelle in CG simulations, as was observed in atomistic simulations. The density of the surfactant head and tail are similar in both the atomistic and CG model, implying that the CG model reproduces the morphology of a single micelle accurately. However, it should be noted that the surfactant headgroup, in particular, has a slightly broader and shorter peak in the radial density profile, which may indicate that the micelle is on average less symmetrical and adopts a more elliptical morphology. Taking block averages of the surfactant headgroup density for CG simulations (Figure 4.9) shows that the peak is broader and shorter in the final time interval (120-150 ns), indicating that over longer time periods the (average) micelle morphology shifts. This behaviour is not observed in similar block averages for the shorter atomistic simulations, where instead the micelle profile remains quite stable after a short initial equilibration period (within the first ns of simulation time). This might suggest that the distortion of the micelle that occurs in CG simulations is a slower process which will not be easily captured by atomistic simulations. However, it may also be the case that the CG model results in a more “flexible” micelle morphology. In any case, the modal density of the surfactant headgroup occurs at approximately 2.4 nm, which can be approximated as the size of a single micelle. This is in good agreement with experimental data [174, 175] and atomistic results.

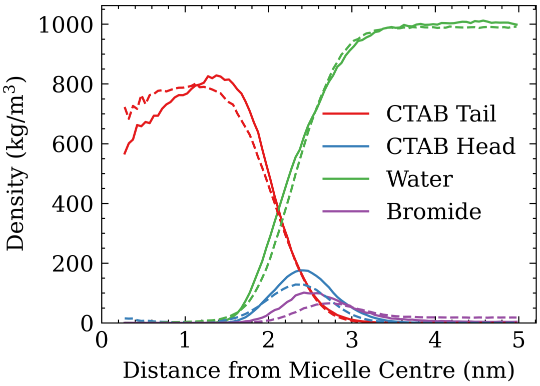

Figure 4.8: Comparison of single micelle density profiles for atomistic (filled line) and CG simulations (dashed line), calculated from the micelle centre of mass.

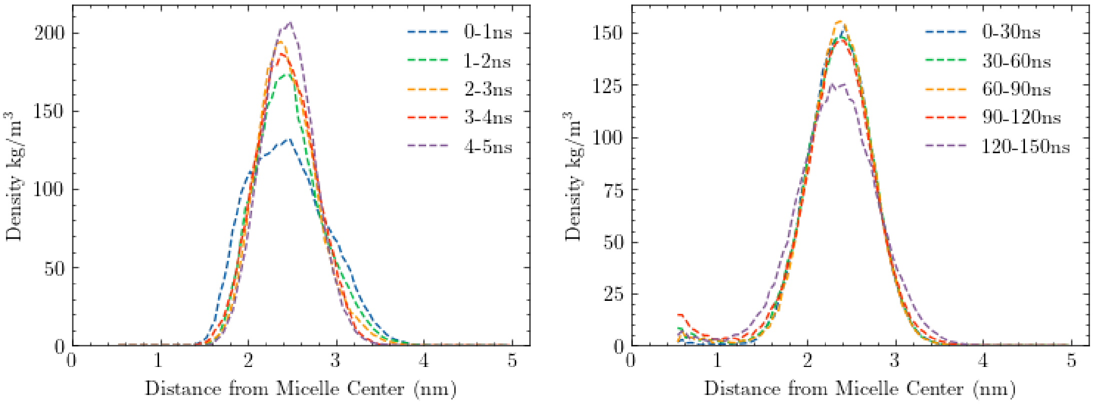

Figure 4.9: Average density of CTAB headgroup measured from the micelle centre of mass in atomistic (left) and CG (right) simulations taken over block averaged time intervals.

4.5.2 Silicates

4.5.2.1 Atomistic Simulations

Atomistic results obtained in this work for micelle radial density profiles in the presence of anionic silica monomers and dimers, and neutral silica monomers, are shown in Figure 4.10. Anionic silicates are shown to aggregate just outside of the micelle surface for all oligomers simulated. This is due to strong electrostatic interactions between the negatively charged silicate anions and the positively charged cationic surfactant headgroup. This result is in agreement with atomistic simulations carried out in previous work for anionic dimers [77] (shown by the dotted line in Figure 4.10c). However, the result for monomers differs from previous work. In the atomistic simulations used for model validation by Pérez-Sánchez et al. (shown by the dotted line in Figure 4.10a), anionic silicate monomers were absorbed within the headgroup of the micelle, whereas in this work, anionic monomers are located outside of the headgroup. This is likely to be due to the difference in the atomistic model used in this work, which results in slightly more hydrophilic silicate species.

The work of Pérez-Sánchez et al. used a silica model based on the work of Pereira et al.[149] modified according to DFT calculations [148] whereas this work employs the recently developed model of Jorge et al. which, as previously described, is validated against experimental data [12]. Thus, the atomistic results obtained in this work should be considered as a more accurate description of the behaviour of silicates. It was previously suggested that silica oligomers were required in order to bridge adjacent CTAB micelles to form the mesophase structure of MCM-41. However, this conclusion was drawn from a CG model in which monomers absorbed into the micelle surface whereas dimers aggregate on the surface outside the micelle, and therefore this behaviour will be re-examined later in this chapter.

Neutral silicates are much more soluble in water than their anionic counterparts, remaining largely in the bulk solution, as shown in Figure 4.10a. This trend decreases slightly as the degree of oligomerisation increases, however. There is a small peak in the radial density profile for neutral silica monomers which sits just inside the surfactant headgroup, suggesting that a small amount of neutral silicates is absorbed within the micelle surface. A peak is also present for neutral dimers, however it sits outside the headgroup (Figure 4.10d). This may be because the higher oligomers are larger and therefore too bulky to penetrate into the micelle surface. The new atomistic model for neutral silica is clearly more hydrophilic than the atomistic model employed by Pérez-Sánchez et al. [75] (shown by the dotted line in Figure 4.10b and d), with a much larger amount of silicates present in the bulk water and only a small amount of silicates aggregating near the micelle surface.

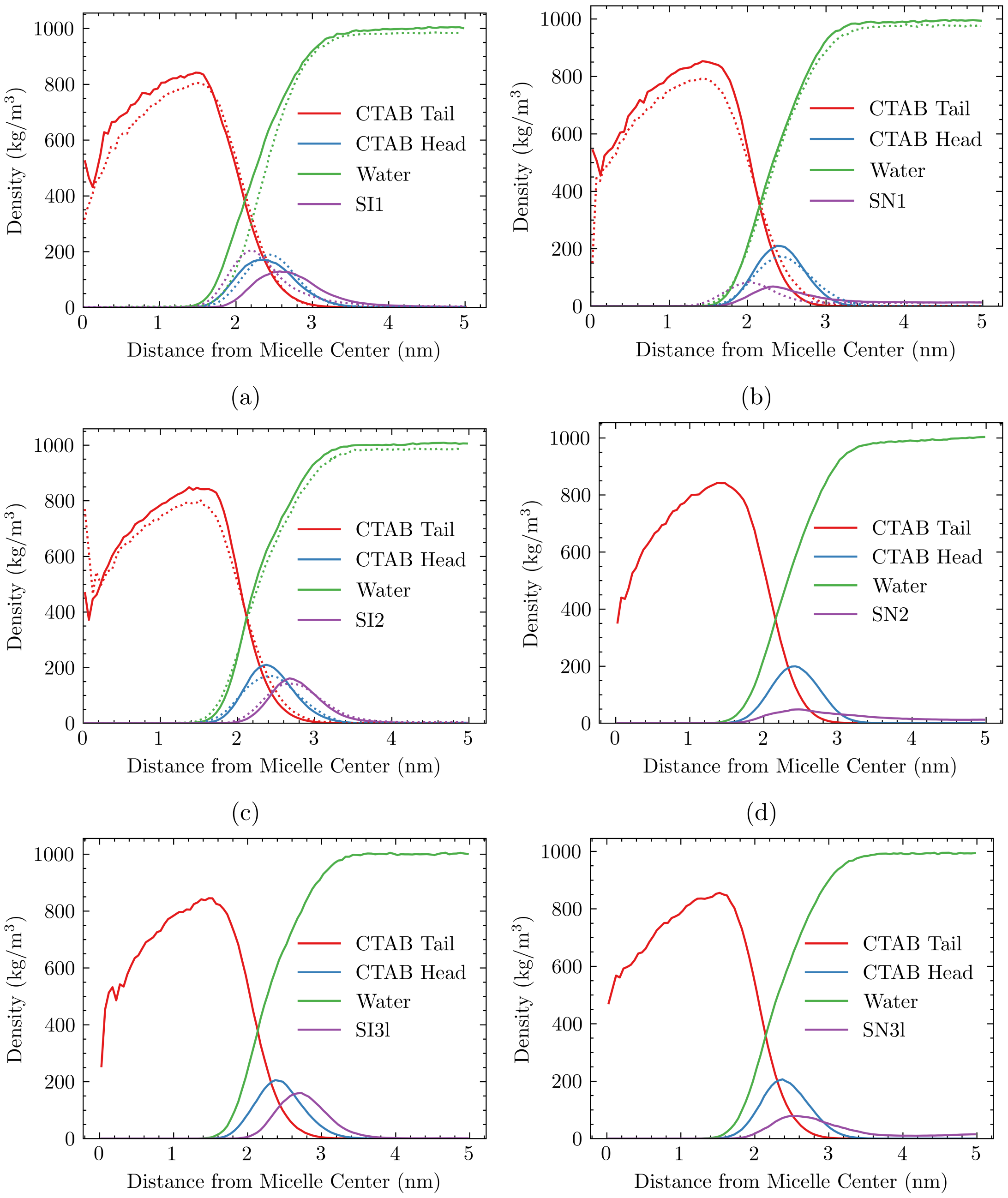

(a) (b)

(c) (d)

(e) (f)

Figure 4.10: Time averaged radial density profile of single micelles in the presence of anionic silicate monomers (a), dimers (c) and trimers (e) and neutral silicate monomers (b), dimers (d) and trimers (f). For SI1, SI2 and SN1 the results obtained from the atomistic model used in the work of Pérez-Sánchez et al. [75] are also shown by a dotted line (while the results obtained using the new atomistic model of Jorge et al. [12] are shown by the solid line).

4.5.2.2 Model Mapping and Bonded Parameters

Silicate monomers (both neutral and ionic) contain five heavy atoms in a branched arrangement and therefore were mapped to a single regular size Martini bead. Dimers and trimers were modelled with two and three regular beads, respectively, splitting bridging oxygen atoms between beads in order to maintain the symmetry of the molecule (see Figure 4.11). A similar procedure was carried out for cyclic and cubic fragments, with beads centred on the silicon atom and bridging oxygens split between beads where necessary (see Figure 4.12). For beads in cyclic and cubic molecules, the small bead size should be used as per the recommendation of the Martini 3 authors [13].

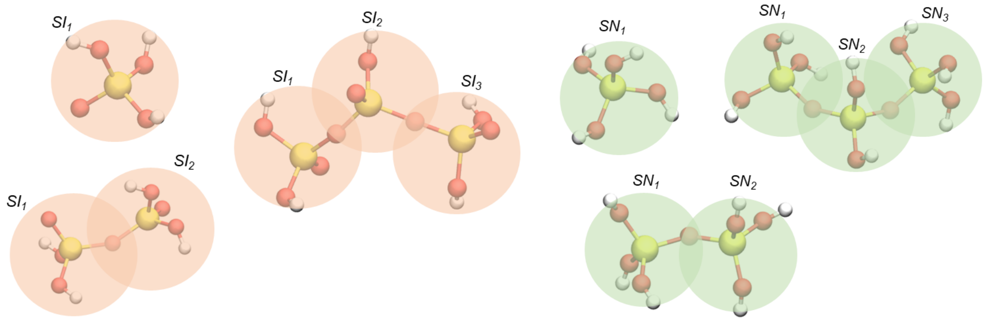

Figure 4.11: Martini 3 mapping scheme for neutral (green) and anionic (red) silicates showing monomers, dimers and linear trimers. Anionic and neutral silicates are given the label SI and SN, respectively.

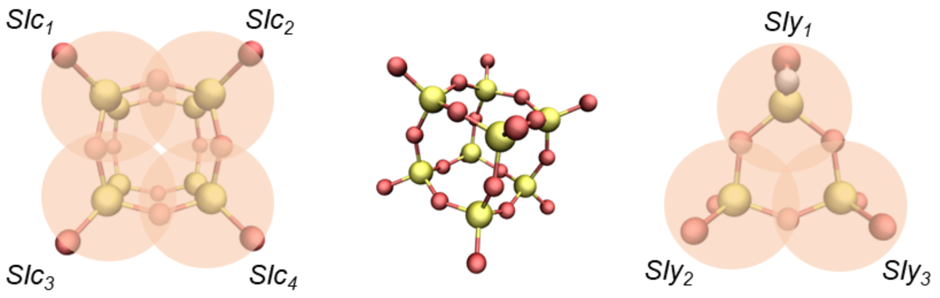

Figure 4.12: Martini 3 mapping scheme for cyclic silica oligomers. For cubic oligomers, the mapping scheme is displayed for the front face (leftmost image), for which there is a symmetrical arrangement on the back face (up to SIc$_8$.)

To allow the CG model for silicates to represent linear oligomers of any degree of condensation and at any ionisation state, it was necessary to generate bonded parameters for each possible combination of anionic and neutral silicates. Since the CG model only requires bond and angle parameters, it is straightforward to achieve this for linear fragments with a series of simulations of trimers of differing ionisation states. From these simulations, the average bond length was calculated for each bond type and these parameters were used for all CG simulations involving linear silicates. For cyclic fragments, reference atomistic simulations were carried out for fully deprotonated cyclic trimers and cubic octamers. These bonded parameters are given in Tables 4.6 and 4.7.

When using the larger timesteps of circa 30 fs, which are frequently employed using the Martini model, high bond force constants ($>$30,000 kJ mol^{-1} nm^{-2}), representing very stiff bonds, can cause the oscillation of the bond to be much faster than the simulation timestep. This can cause issues with energy conservation and the numerical stability of simulations. There are two approaches that could ideally be applied to handle this situation. The first is to reduce the simulation timestep to improve stability, however this has obvious and unacceptable impacts on the computational cost of simulations. The second is to instead treat these bonds as rigid by using a constraint algorithm, such as the LINear Constraint Solver [103]. This is practical in some circumstances, however large numbers of constraints, particularly when they are interconnected (as would be the case in cyclic fragments) can cause instabilities as identified by the authors of the Martini 3 force field [13]. Some unique approaches have been demonstrated to reduce the number of constraints required for describing stiff cyclic molecules, such as the hinge model of Melo and co-workers used for sterols and hopanoids [176]. However, this approach adds additional complexity to model development and is not compatible with the objective of creating a general model capable of representing larger silica oligomers whilst retaining numerical stability. Therefore, the approach taken in this work is to compromise strict agreement with atomistic reference data in favour of numerical stability. For all silicates, force constants greater than 30,000 kJ mol^{-1} nm^{-2} were reduced to 30,000 kJ mol^{-1} nm^{-2}. While the equilibrium bond length remains unchanged, this significantly improves numerical stability at larger timesteps (30 fs) whilst still retaining an element of bond rigidity.

Cubic octamers present an additional difficulty, as the large number of bonds in an interconnected network make achieving numerical stability difficult, even with a reduction in the bond force constant to 30,000 kJ mol^{-1} nm^{-2}. Therefore, the force constant of this bond was significantly reduced to 1250 kJ mol^{-1} nm^{-2} and in addition the angle force constant was relaxed to 25 kJ mol^{-1} deg^{-2} to further improve numerical stability. For simplicity, protonation states were not considered for cyclic oligomers, assuming the bonded parameters between neutral silicate beads in a cubic or cyclic arrangement are the same as the bonded parameters for anionic silicate beads. The bond lengths and angles in these oligomers were averaged to give a single bond length and angle for cyclic and cubic segments.

Table 4.6: Bond type parameters for silica Martini 3 model. b_{ij} is the bond length and k_{ij} is the bond force constant. The calculated k_{ij} values were produced from atomistic reference simulations while the model k_{ij} values are the values actually used for the CG model.

Bond	b_{ij} (nm)	Calculated k_{ij} (kJ mol^{-1} nm^{-2})	Model k_{ij} (kJ mol^{-1} nm^{-2})
SI - *SI*	0.3500	50,000	30,000
SI - *SN*	0.3570	67,000	30,000
SN - *SN*	0.3640	75,000	30,000
SIc - *SIc*	0.3135	>100,000	1250
SIy - *SIy*	0.3330	33,000	30,000

Table 4.7: Angle type parameters for silica Martini 3 model. θ_{ijk} is the angle between beads and k_{ijk} is the angle force constant. The calculated k_{ij} values were produced from atomistic reference simulations while the model k_{ijk} values are the values used for the CG model.

Silica Beads	θ_{ijk} (degrees)	Calculated k_{ijk} (kJ mol^{-1} deg^{-2})	Model k_{ijk} (kJ mol^{-1} deg^{-2})
SI - SI - SI	102	270	270
SI - SI - SN	103	440	440
SI - SN - SI	105	400	400
SI - SN - SN	104	530	530
SN - SN - SN	102	740	740
SN - SI - SN	101	640	640
SIc - SIc - SIc	90	8874	25

4.5.2.3 Bead Type Selection

Initially, an attempt was made to select a bead type to represent silicates from the standard bead types available in Martini 3. For anionic silicates, all available charged (Q) bead types were tested and for neutral silicates, various N (neutral) bead types were tested. Ideally, the same bead type should be used for segments of silica oligomers as is used for silica monomers, as this permits the simulation of oligomers of any length without the need to parametrize the model again for each different oligomer. The initial goal is therefore to choose a bead for each ionisation state of silica (neutral and anionic) that is capable of representing multiple oligomerisation states of silica with reasonable accuracy.

First, simulations involving monomers and dimers were compared against atomistic data, generated as described in Sections 4.5.2.1 and 4.5.2.2. There are several approaches that can be taken to assess the comparison between CG and atomistic data. Perhaps the most straightforward method is to directly compare the silica radial density profile generated from CG simulations with the silica radial density profile generated from atomistic simulations. This comparison is displayed in Figure 4.13. For anionic silicates, all bead types produced qualitatively similar radial density profiles for silica, with a region of high silicate concentration close to the micelle surface. To quantitatively describe the peaks, the peak density value and corresponding radial distance from the micelle centre were determined (see Table 4.8). From these results, it is clear that there is a balance to be struck when deciding on a bead type to match both the peak height and location of the atomistic reference data.

While the behaviour of silica monomers and dimers is quite similar in atomistic models, there is a large difference in behaviour between equivalent bead types in the CG model. In general, CG simulations of silica monomers result in silica density profiles that indicate more hydrophilic character than is present in the atomistic model, with a higher concentration of silicates present in the bulk solution (> 4 nm from micelle centre). In contrast, CG simulations of silica dimers result in silica density profiles that more closely match atomistic data, with a larger quantity of silicates aggregating close

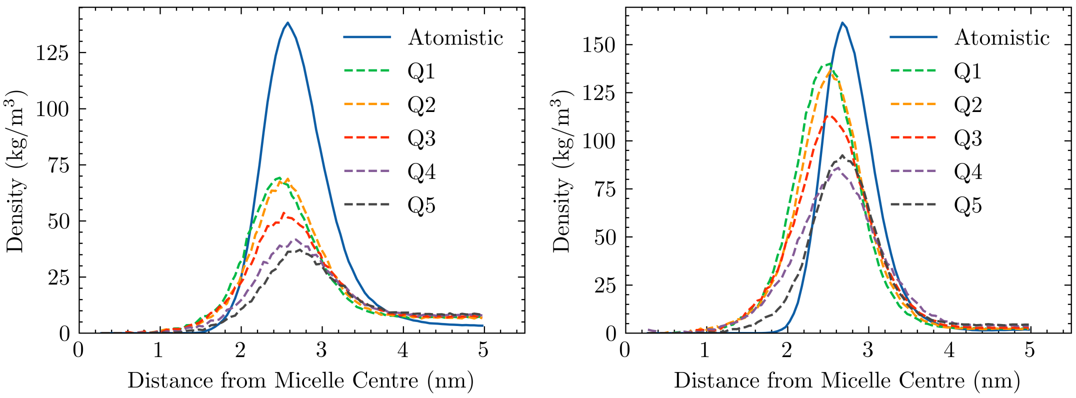

Figure 4.13: Radial density profiles for anionic silica monomers (left) and dimers (right) comparing atomistic results with various Martini 3 standard bead types.

Table 4.8: Comparison of silica peak density and location simulations for different Martini 3 bead types.

Species	Bead	Peak Density (kg m^{-3})	Peak Location (nm)
SI1	**Atomistic**	**138**	**2.575**
	Q1	69	2.475
	Q2	69	2.575
	Q3	54	2.525
	Q4	42	2.675
	Q5	37	2.725
SI2	**Atomistic**	**161**	**2.675**
	Q1	140	2.525
	Q2	136	2.525
	Q3	113	2.525
	Q4	86	2.625
	Q5	92	2.675

to the micelle surface. This suggests, firstly, that the standard Martini 3 bead types are not ideal for representing anionic silica monomers, and secondly that the best bead type used for representing monomers may not scale well to higher oligomers of silica using the Martini 3 model. Therefore, it was decided to select different bead types for silica monomers and dimers, with the choice for dimers being more likely to scale well to higher oligomers of silica.

However, direct comparison of the silica density in isolation does not give a complete picture of the quality of the fit between atomistic and CG simulation data. This is illustrated in Figures 4.14 and 4.15, which show the complete density profile of all species present in simulations involving silica monomers and dimers for all Martini 3 charged bead types (Q1 to Q5). Comparing the relative heights of the peaks for the CTAB headgroup and silicates throughout all bead types, one can see that all surfactant headgroup peaks are shorter and wider in CG simulations than in the atomistic reference. This will have an effect on the silica peak, which appears to follow a similar behaviour. Thus, it can be argued that consideration of the full profile of all species (in particular the surfactant headgroup and silica densities) is important to determining the best fit. However, from simply examining the profiles visually (as was done in previous work [75, 77]) it is difficult to draw distinctions between bead types, leading to a subjective choice of which bead type is most suitable.

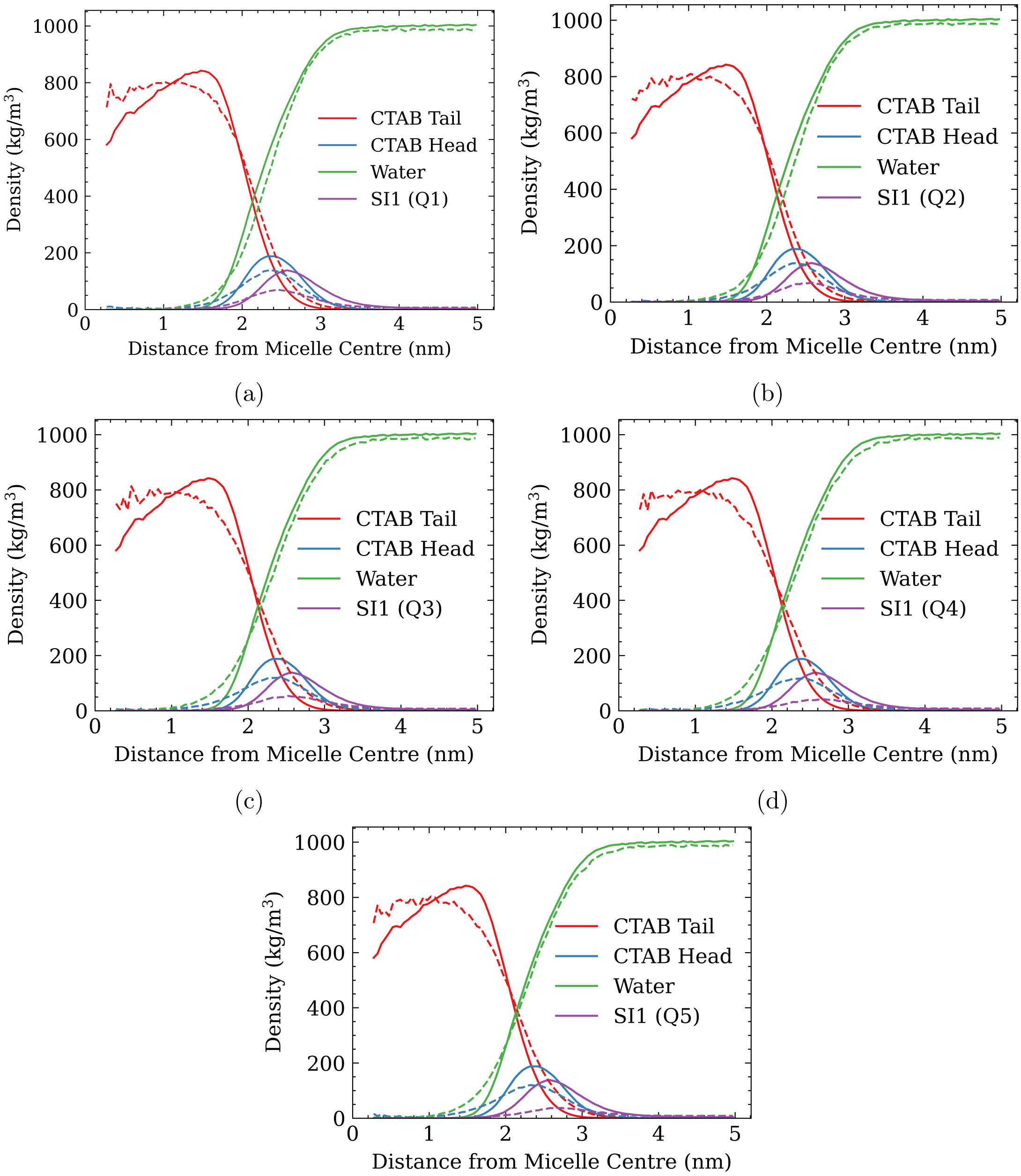

(a)

(b)

(c)

(d)

(e)

Figure 4.14: Comparison of the time averaged radial density profile around a single CTAB micelle in the presence of anionic silica monomers for the atomistic model (filled line) and CG model (dashed line). Silica monomers are represented using the Martini beads labelled in the legend.

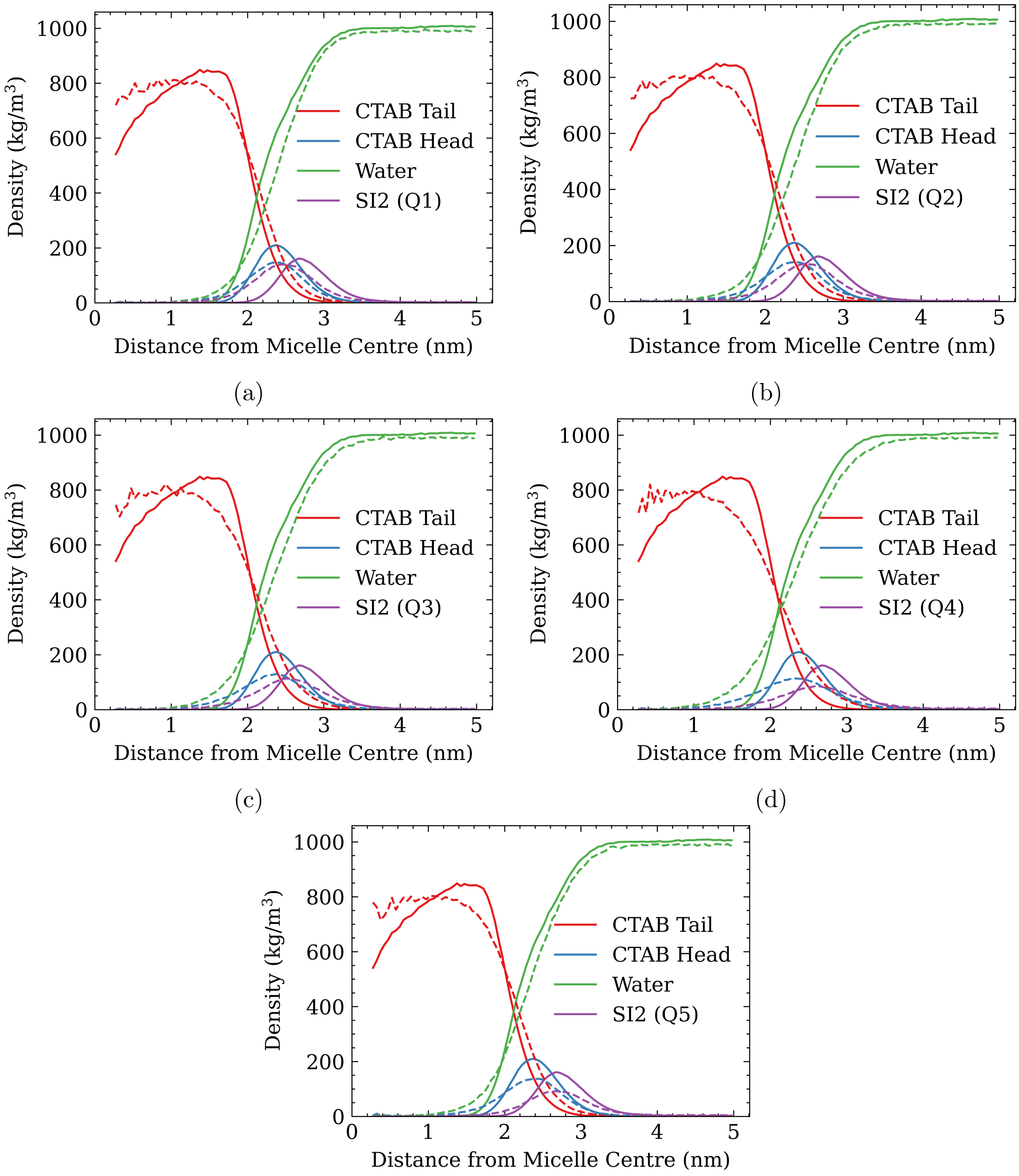

(a) (b) (c) (d) (e)

Figure 4.15: Comparison of the time averaged radial density profile around a single CTAB micelle in the presence of anionic silica dimers for the atomistic model (filled line) and CG model (dashed line). Silica dimers are represented using the Martini beads labelled in the legend.

Since a subjective assessment of the quality of fit between CG and atomistic data is not a robust method for model development, it is desirable to develop a more thorough procedure for comparing silica and surfactant interactions for simulations involving a single micelle, in order to provide an objective measure for bead type selection, which can also be more generally applied to other systems, particularly those which involve co-operative self-assembly. As such, the following fitting parameters were devised based on the results of single micelle systems (see Figures 4.14 and 4.15).

The first fitting parameter, H, is based on the relative peak heights of the surfactant headgroup and silicate species in the single micelle radial density profile:

$$H = \frac{\left(\frac{h_{SI,CG}}{h_{H,CG}}\right)}{\left(\frac{h_{SI,A}}{h_{H,A}}\right)} \tag{4.1}$$

where h represents the peak height in the radial density profile, with the subscript representing the species and type of simulation (atomistic or CG), respectively. A perfect fit gives an H value of 1 indicating that the relative heights of the surfactant headgroup and silica peaks are the same as atomistic simulations. To assess the fit for peak location, the fitting parameter R is used, which takes into account the relative locations (radial distance from micelle centre) where the peaks occur:

$$R = \frac{\left(\frac{r_{SI,CG}}{r_{H,A}}\right)}{\left(\frac{r_{SI,A}}{r_{H,A}}\right)} \tag{4.2}$$

where r is the radial distance from the micelle centre of mass where the peak occurs. A final fitting parameter, N_{ads}, is proposed, which is simply based on the quantity of silica molecules that are adsorbed onto the micelle surface in CG simulations versus the atomistic reference.

$$N_{ads} = \frac{N_{ads,CG}}{N_{ads,A}} \tag{4.3}$$

This figure is a simplistic measure of the relative balance between micelle surface adsorption and bulk water solubility. To determine N_{ads}, the average number of silica molecules adsorbed on the micelle surface is calculated over the simulation trajectory after equilibrium has been reached for both atomistic and CG simulations. For CG simulations, a silica molecule is considered adsorbed if any bead of it is within 0.73 nm of the CTAB headgroup bead, which is approximately the distance at which the first minimum in the radial density function between silicate species and surfactant headgroup is observed. For the atomistic reference simulation, the distance is calculated between each silicon atom in silicate species and the nitrogen atom in the surfactant headgroup.

The values of fitting parameters H, R and N_{ads} for the bead types tested are presented in Table 4.9 and plotted in Figure 4.16. Firstly, considering parameter H, which indicates how proportional the surfactant headgroup and silica peaks are to atomistic data, different optimum values are observed for monomers and dimers. The value of H for monomers is significantly lower than that of dimers for the same bead type. Examining the trends in the relative heights of the silica peaks for different bead types (shown in Table 4.8 and Figure 4.13) it can be seen that for all bead types, the silica peak height is much lower than the atomistic reference, with all bead types producing peak densities less than half the height of the atomistic reference. This indicates that all standard Martini bead types tested are too hydrophilic to represent silica monomers optimally, with a large proportion of silicates remaining in bulk water. This stands in contrast to simulations with dimers, where most bead types have a value of $H > 1$, indicating that dimer species for these bead types are too hydrophobic, with a disproportionate quantity of silica molecules being adsorbed onto the micelle surface. Overall, both the Q1 and Q2 bead types provide approximately equivalent fits for parameter H for monomers, while the Q4 bead provides a very good fit for dimers.

Now considering parameter R, which indicates the location at which silicate species adsorb on the micelle surface in CG simulations versus reference atomistic simulations. For monomers, the Q3 bead achieves the best fit, while for the dimers, the Q4 and Q5 beads both achieve perfect agreement with atomistic data. Finally, we consider parameter N_{ads} which indicates the quantity of silica bound to the micelle in CG simulations versus the atomistic reference. For monomers, the value of N_{ads} was significantly below

Table 4.9: Comparison of fitting parameters against atomistic data for different Martini 3 bead types.

Species	Bead	H	R	N_{ads}
SI1	Q1	**0.68**	0.94	**0.63**
	Q2	**0.68**	0.98	**0.63**
	Q3	0.61	**1.00**	0.51
	Q4	0.49	1.06	0.42
	Q5	0.42	1.06	0.36
SI2	Q1	1.24	0.94	1.10
	Q2	1.27	0.94	1.11
	Q3	1.14	0.94	**1.03**
	Q4	**0.98**	**1.00**	0.89
	Q5	0.88	**1.00**	0.83

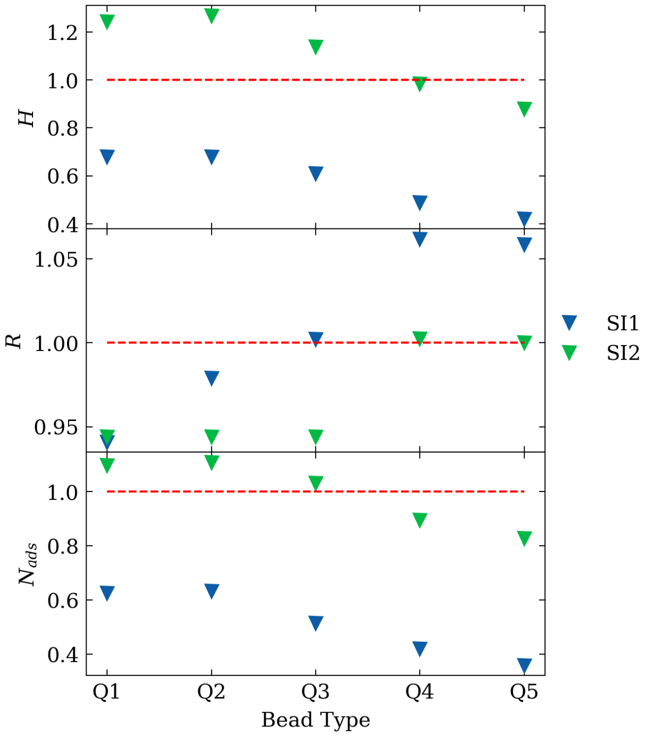

Figure 4.16: Comparison of fitting parameters for different Martini 3 bead types representing anionic silica monomers (SI1) and dimers (SI2) versus atomistic reference data. The red dashed line is a guide for the eye that indicates a perfect fit with atomistic data for each parameter.

1, once again indicating the standard Martini 3 bead types are too hydrophilic to represent silica monomers optimally. The closest agreement is once again achieved by both the Q1 and Q2 bead types, however it is worth noting that this value is still relatively low at 0.63. The standard Martini 3 bead types provide much better agreement for dimers, however, with the Q3 bead achieving the best fit with atomistic data in this case.

Overall, from examination of these parameters it can be concluded that the ideal bead type for representing anionic silica dimers lies between Q3-Q5, with Q4 providing overall the best balance between all fitting parameters. While the fit against atomistic data is generally poorer for monomers for all bead types (in particular for parameters H and N_{ads}), the Q1 and Q2 bead types provide the best fits out of the standard Martini 3 bead types, with either being likely to provide reasonable representation of anionic silica monomers. The Q2 bead type was favoured due to a slightly improved fit for parameter R. In either case, the bead type choice indicated by these parameters is different from the range identified for modelling silica dimers, which suggests that increasing the degree of condensation may alter the silica-surfactant interactions sufficiently to warrant the use of different charged bead types for oligomers. Indeed, the model of Pérez-Sánchez et al. employed different intermolecular interactions for silica oligomers than were used for monomers [77], setting a precedent for this approach.

The increased hydrophobicity of the Martini 3 monomer model versus the atomistic reference may be of some concern where this factor is critical to the result of future simulations. However, given that silica monomers are expected to play only a minor role in the formation of HLC phases versus multiply charged oligomers due to their inability to facilitate multidentate binding of micelles, this is less of a concern in this work. Improving the agreement of the CG model with atomistic data may be possible by scaling the hydrophobic/hydrophilic interactions of silicate species, a method adopted by Thomasen et al. to improve agreement with experimental data when using the Martini 3 force field to model flexible proteins [177]. Alternatively, the individual intermolecular parameters of the beads used for silicates could be manipulated (effectively creating a new "Q" bead type) to develop a bespoke model. However, both of these approaches are not straightforward and are likely to hinder compatibility with other species modelled using the Martini 3 force field.

Finally, a CG single micelle simulation was carried out using trimers, represented using Q4 beads. This allows us to assess the applicability of using the same bead choice for higher oligomers as is used for dimers by seeing how the atomistic agreement scales with increasing degree of condensation. Note that each silica bead in these trimers carries a negative charge (giving the molecule an overall -3 charge). As shown in Figure 4.17, the agreement when using the Q4 bead is reasonable, maintaining good agreement for both silica peak density location and height. However, when comparing the relative heights of the surfactant headgroup and silica peaks, the Q4 CG model appears to be slightly more hydrophobic than the atomistic model. This may suggest that as the degree of condensation for linear silicates increases, the hydrophobicity of the individual beads required to represent each segment should be reduced, as was the case when moving from silica monomers (Q2) to silica dimers (Q4). On balance, it was decided to sacrifice accuracy in favour of simplicity and transferability, and therefore Q4 beads were used to represent silicates in all anionic oligomers.

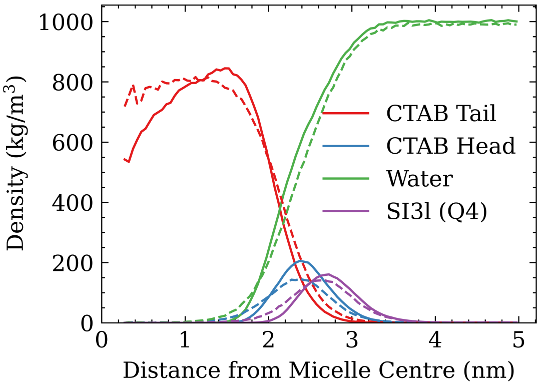

Figure 4.17: Comparison of the time averaged radial density profile around a single CTAB micelle in the presence of linear anionic silica trimers for the atomistic model (filled line) and CG model (dashed line). Silica trimers are represented using the Martini Q4 bead.

The radial density profiles generated using several different N (neutral) bead types to represent neutral silica species are shown in Figure 4.18, where the silica density is compared to the atomistic reference simulation. Since there is a peak in silica density near the micelle surface, the same procedure employing fitting parameters H, R and N_{ads} was used to select an appropriate bead type for both monomers and dimers. These values are tabulated in Table 4.10 and displayed graphically in Figure 4.19.

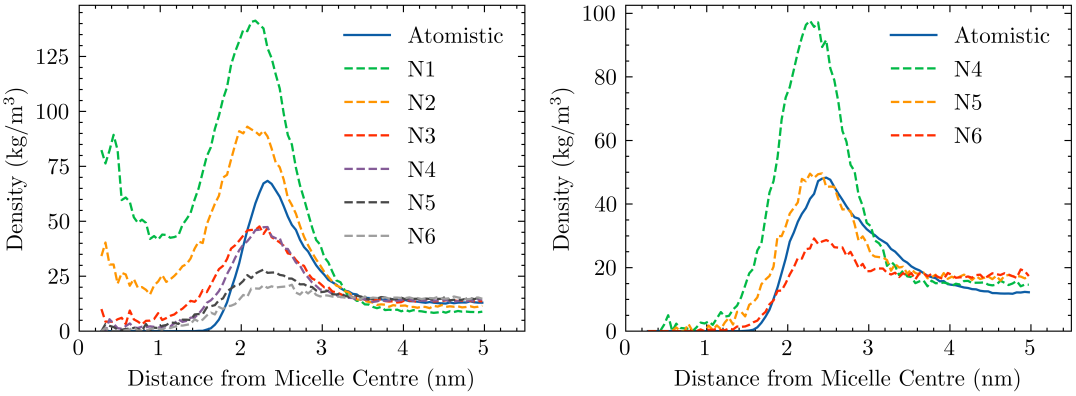

Figure 4.18: Radial density profiles for neutral silica monomers (left) and dimers (right) comparing atomistic results with various Martini 3 standard bead types.

Table 4.10: Comparison of fitting parameters against atomistic data for different Martini 3 bead types.

Species	Bead	H	R	N_{ads}
SN1	N1	3.85	0.94	**1.00**
	N2	2.56	0.91	0.68
	N3	1.29	0.98	0.37
	N4	**1.08**	**1.00**	0.34
	N5	0.75	**1.00**	0.24
SN2	N4	3.02	0.92	**0.90**
	N5	1.53	**1.00**	0.53
	N6	**0.86**	0.96	0.34

For neutral silica monomers, the N4 bead provides the best agreement with atomistic data for parameters H and R. Conversely, the N1 bead provides the best agreement for N_{ads}. However, examination of the radial density profile of silica indicates that the use of this bead type results in significant quantities of silica being absorbed within the micelle, a behaviour which is not present in the atomistic model. Therefore, the fitting of parameters H and R is prioritised, as this appears to give the most reasonable agreement with atomistic behaviour, and the N4 bead type was chosen for monomers.

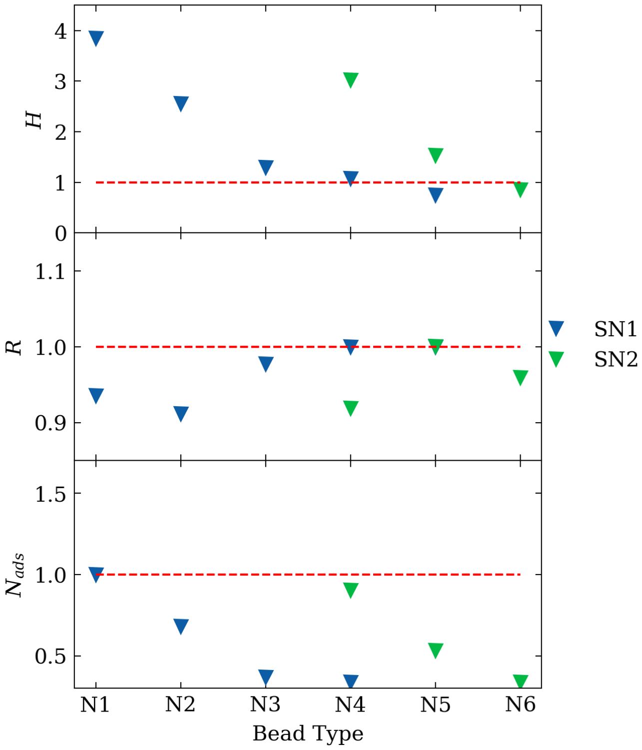

Figure 4.19: Comparison of fitting parameters for different Martini 3 bead types representing neutral silica monomers (SN1) and dimers (SN2) versus atomistic reference data. The red dashed line is a guide for the eye that indicates a perfect fit with atomistic data for each parameter.

For dimers and neutral silica fragments in higher oligomers of silica, the N5 bead was chosen as it achieves a good balance between the three fitting parameters.

The full radial density profiles for neutral silica monomers and dimers are shown in Figure 4.20. Both monomers and dimers show relatively good agreement with atomistic reference data, though in a similar manner to previous cases there is a broadening and shortening of the CTAB headgroup peak. Finally, the full radial density profile for linear neutral silica trimers is shown in Figure 4.20c. Here there is relatively good agreement against atomistic data, indicating that this bead type produces interactions that scale relatively well to higher oligomers of neutral silica species.

An important aspect of the CG model is the ability to represent silica oligomers with both anionic and neutral silica units. This allows larger oligomers with a variety of charge states to be investigated, which is particularly important when considering

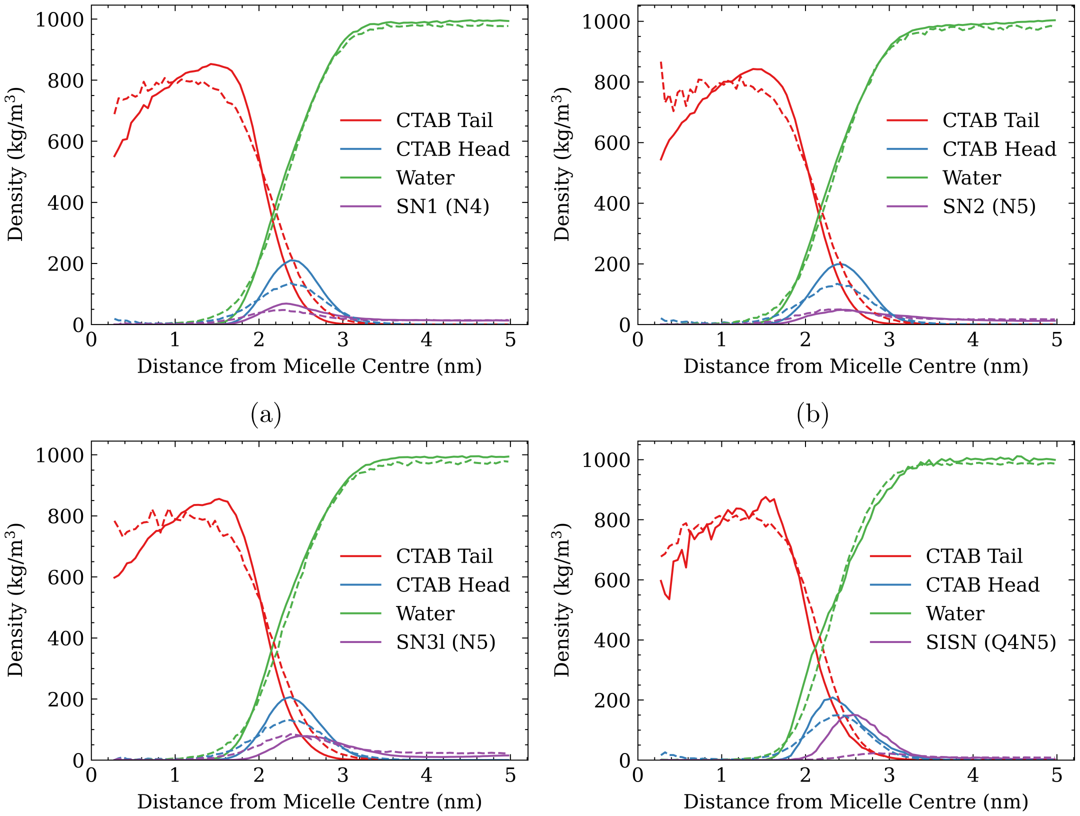

(a) (b)

(c) (d)

Figure 4.20: Comparison of the time averaged radial density profile around a single CTAB micelle in the presence of neutral silica monomers (a), dimers (b) and linear trimers (c) as well as singly charged dimers (d) for the atomistic model (filled line) and CG model (dashed line). Neutral monomers are represented using the N4 bead, while neutral beads in higher oligomers are represented using the N5 bead and charged beads are represented using the Q4 bead type.

systems at different pH values. Therefore, the model is tested by taking the simple case of a silica dimer with a single deprotonated hydroxyl group, giving the molecule an overall charge of -1. Under this model, this would be represented using one Q4 bead and one N5 bead. The bonded parameters for these mixed oligomers were also generated from atomistic data and can be found in Tables 4.6 and 4.7.

The results of this simulation compared with an atomistic reference simulation are shown in Figure 4.20d. The agreement between the atomistic reference and CG is relatively poor, with the silica peak of the CG model far less pronounced than in the atomistic model, even when accounting for the broadening and shortening of the surfactant headgroup peak. This might indicate that simply mixing charged and neutral CG beads is not particularly effective at estimating the atomistic behaviour for oligomers with mixed charge states. A possible reason for this are so called “proximity effects” which are discussed by the Martini 3 authors (supporting information of reference [13]). The interactions of a bead may be affected by their proximity to other beads, and this effect is especially pronounced for neutral beads which are connected to charged beads.

One way to account for the proximity effect of deprotonated silanol groups is to alter the bead type of beads adjacent to charged beads in oligomers. This is observed in some of the “built-in” models present in Martini 3, such as the model for arginine which uses the SC3 bead to represent the aliphatic carbons adjacent to the charged guanidinium chemical group, which is represented by a charged bead type. The bead type typically suggested for linear alkanes is the C1 bead type (or the SC1 bead type in the case of 3 carbon atoms) and therefore the SC3 bead type is slightly more polar than the bead type that would typically be employed if following the Martini “building blocks” approach, due to the adjacency to the very polar guanidinium group. Since the case with mixed silica oligomers is similar (i.e. a neutral bead adjacent to a polar charged group), the same technique of modifying the usual bead type to a more polar bead type could be applied, however this was not carried out in this work due to the additional complexity of the parameterization process.

4.5.2.4 Effect of Interactions on Fitting Parameters

While the model presented in this work, which was validated extensively against atomistic data, is deemed accurate for representing HLC phase formation for this system of interest, gaining a deeper understanding of how the model parameters affect HLC phase formation is useful to understand whether the model can be improved and to aid the development of future models of this system, as well as other systems with cooperative templating effects. It has previously been established that the use of different charged ("Q") bead types to represent silica dimers significantly alters self-assembly behaviour (see Figure 4.41). Since the previous model of Pérez-Sánchez et al. [77] using the Martini 2 force field also demonstrated hexagonal phase formation, it is useful to compare the preliminary models investigated in this work with the model developed in prior work. Electrostatic interactions in both models are identical, but Lennard-Jones parameters vary between the two models. Interaction strengths (dispersion energy) and distance (particle "size") are displayed in Tables 4.11 and 4.12 respectively.

Table 4.11: Comparison of the interaction strength between silica and other CG beads used in this work with those used in the work of Pérez-Sánchez et al. [77].

Interaction	**Interaction Strength (kJ mol^{-1})**			
	Martini 2	Q3	Q4	Q5
SI-SI	5.6	5.45	5.95	6.45
SI-W	5.6	5.69	5.96	6.34
SI-CTAB Head	4.5	4.7	4.45	4.45
SI-CTAB Tail	2	2.315	2.143	2.046

The difference in these interactions may explain the different behaviour exhibited in single micelle simulations, which are summarised in Table 4.8. Two interactions, in particular, strongly govern the affinity of silicate species to surfactant micelles. The first is the interaction of silica beads with surfactant tail groups. This interaction is likely to be important to determining the distance at which silicate groups aggregate at the micelle surface. As this value is reduced, silica species, which interact strongly with the surfactant head group, are able to move closer to the micelle centre, which is reflected in the trend observed in peak distance (Table 4.8). The second important interaction is between silicate species and water. The relative hydrophobicity of bead types is very important as it governs the quantity of silicates that aggregate at the micelle surface versus the quantity that are present in bulk water, reflected by the trend observed in peak height between different bead types (Table 4.8).

Other interactions in the system will also be critical to self-assembly behaviour, in particular surfactant-surfactant, surfactant-water and water-water interactions. This is further complicated by the addition of species such as co-surfactants and the bio-inspired additives which are investigated in this work. However, since the models for these species are validated independently of silica, it is not desirable to alter these interactions in this context as it will affect the compatibility of the model with new species and may have unintended consequences. In addition, tuning parameters for a specific system (i.e. particular components, component concentrations and component ratios) may lead to "overtuning" the model to achieve specific results. Thus, a basis in bottom-up calibration (i.e. against atomistic data) where possible should be maintained. Nevertheless, the improvement of existing models for species other than silica may yield more realistic results (though it may require a modified silica model to be retuned).

To create a completely new Martini 3 bead type, it would be necessary to specifiy the interaction parameters between that bead type, and every other bead type in the Martini 3 force field. To avoid this, an existing bead type can be used instead of creating a completely new bead type, only modifying specific interactions to achieve the desired behaviour. In this case, the Q5 bead is used as a basis, and only the silicate to water

Table 4.12: Comparison of the interaction distances between silica and other CG beads used in this work with those used in the work of Pérez-Sánchez et al. [77].

Interaction	**Interaction Distance (nm)**			
	Martini 2	Q3	Q4	Q5
SI-SI	0.47	0.47	0.47	0.47
SI-W	0.47	0.465	0.465	0.465
SI-CTAB Head	0.47	0.47	0.47	0.47
SI-CTAB Tail	0.62	0.52	0.57	0.62

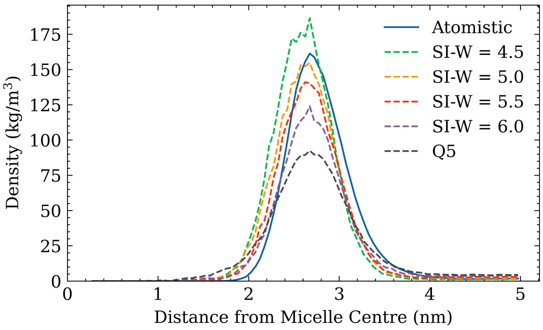

Figure 4.21: A comparison of the silica radial density profile in several simulations using a Q5 bead with modified silica to water interaction strengths, compared with the atomistic result and the result for a regular, unmodified Q5 bead. The silica to water interaction strengths for simulations using a modified Q5 bead are given in the legend in units of kJ mol^{-1}.

interaction strength is modified with the goal of achieving the correct hydrophobicity, creating a modified “Q5M” bead type. All other interactions remain identical to a standard Martini 3 Q5 bead.

Several values for silica to water interaction strength were tested in a single micelle simulation using the same procedure as in Section 4.5.2.3. A comparison of the silica radial density profile generated from these simulations is shown in Figure 4.21. The expected trend of higher peak density as the silica to water interaction strength is reduced can be observed. A slight shift in the peak location towards the micelle centre can also be seen. From a straightforward comparison of the silica peak height and location against atomistic data, it appears as if reducing the silica to water interaction strength of the Q5 bead from its standard value of 6.34 to 5.0 kJ mol^{-1} improves the fit with atomistic data.

While considering only the silica radial density may suggest that reducing the silica to water interaction strength is effective in improving the fit against atomistic data, it has previously been demonstrated that a more thorough fitting procedure which takes into account the relative densities of surfactant and silica species as well as amount of adsorbed silica may be more appropriate. The fitting parameters H, R and N_{ads} which are described in Section 4.5.2.3 are applied to the simulations using the modified Q5 bead. A summary of the results for these fitting parameters is given in Table 4.13

and parameters H, R and N_{ads} are plotted in Figure 4.22. In these results, it can be observed that reducing the silica to water interaction from 6.34 to 6.0 kJ mol^{-1} slightly improves the fit of the Q5 bead against atomistic data when considering these fitting parameters. Since it has previously been established that using a bead type that optimizes these fitting parameters allows for the expected liquid crystal phase behaviour of the CTAB/silica solution to be reproduced, it is possible that further optimising the interactions of the standard Martini 3 beads to match these parameters may yield a more accurate coarse-grained representation of silica species. Such an optimisation may also include simultaneously tweaking silica to water interactions and silica to silica interactions in order to achieve a perfect fit based on all three established fitting parameters. However, since the Q4 bead was previously demonstrated to be suitable for representing both anionic silica dimers and higher oligomers, this was not explored further in this work. It is also worth considering that this fitting procedure would be specific to the oligomer of silica that was being fitted, and other oligomers (e.g. monomers, cubic octamers) would have to be fitted individually, reducing the transferability of the model and negating the benefits of the Martini “building block” approach versus using the Martini 3 standard bead types.

Table 4.13: Comparison of fitting parameters against atomistic data for modified Martini 3 beads based on the standard Q5 bead type. SI-W refers to the interaction strength between silica and water beads in units of kJ mol^{-1}. For the Q5M bead types, all other interactions are the same as a regular Martini 3 Q5 bead.

Species	Bead	SI-W	H	R	N_{ads}
SI2	Q5M	4.50	1.34	0.93	1.25
	Q5M	5.00	1.28	0.95	1.16
	Q5M	5.50	1.22	0.97	1.05
	Q5M	6.00	0.91	1.00	0.94
	Q5	6.34	0.88	1.00	0.83

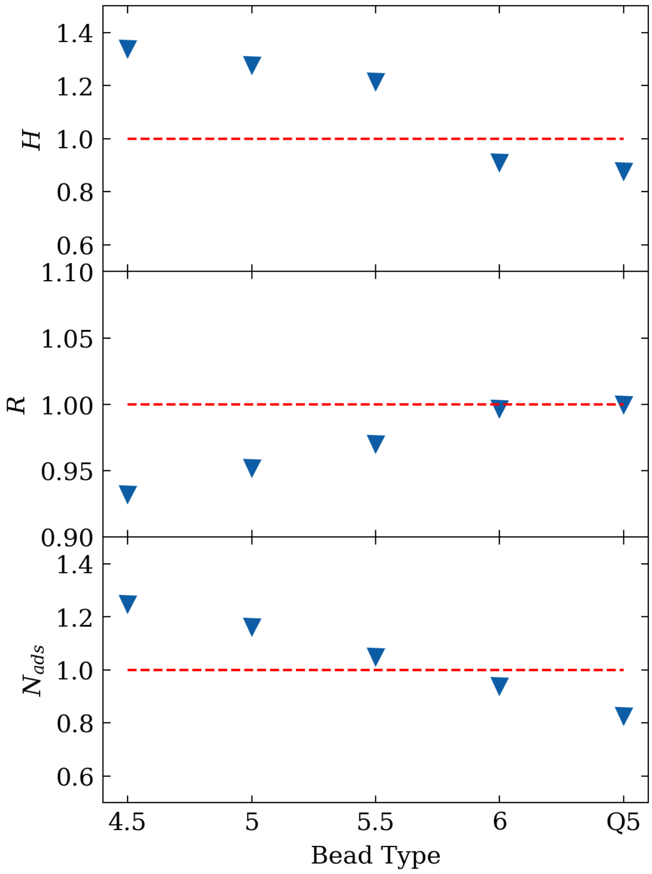

Figure 4.22: Comparison of fitting parameters H, R and N_{ads} for Martini 3 beads with different silica to water interaction strengths versus atomistic reference data. The red dashed line is a guide for the eye that indicates a perfect fit with atomistic data. Labels on the x axis indicate the silica to water interaction strength in units of kJ mol^{-1} for simulations using a modified Q5 bead, or the Martini 3 bead type.

4.5.2.5 Silica Bead Types Summary

The Martini 3 bead types used in the model developed in this work for a selection of silica oligomers are displayed in Table 4.14. For bonded parameters, refer to Tables 4.6 and 4.7.

Table 4.14: Examples of the bead types used in the Martini 3 model for silicates developed in this work. The bead type listed is used in each unit of the oligomer or in the case of mixed oligomers in each anionic/neutral unit respectively.

Species	Charge	Nomenclature	Bead Type(s)
Anionic Silica Monomer	-1	SI1	Q2
Anionic Silica Dimer	-2	SI2	Q4
Linear Anionic Silica Trimer	-3	SI3l	Q4
Cyclic Anionic Silica Trimer	-3	SI3y	SQ4
Cubic Anionic Silica Octamer	-8	SI8c	SQ4
Neutral Silica Monomer	0	SN1	N4
Neutral Silica Dimer	0	SN2	N5
Linear Neutral Silica Trimer	0	SN3l	N5
Cyclic Neutral Silica Trimer	0	SN3y	SN5
Cubic Neutral Silica Octamer	0	SN8c	SN5
Mixed Silica Dimer	-1	SISN	Q4/N5
Mixed Silica Octamer	-4	SI4SN4c	SQ4/SN5

4.5.3 Arginine

4.5.3.1 Atomistic Simulations

The single micelle density profile for arginine in the presence of a single CTAB surfactant micelle in atomistic simulations is shown in Figure 4.23. Arginine was present in its form with an overall neutral molecular charge (form III in 4.3). The results show that arginine does not interact strongly with the micelle surface, with no adsorption on the micelle surface and a high concentration of arginine remaining in the bulk water. However, the results of atomistic simulations where bromide counter-ions are replaced by anionic silica dimers (Figure 4.24) appear to show that the presence of these oligomeric silica species facilitates stronger interactions between arginine and the micelle surface, perhaps due to a double layer of charge-charge interactions between the positively charged surfactant headgroups, negatively charged silica species and positively charged side-chain of the arginine molecules. This results in a small amount of aggregation of arginine molecules close to the micelle surface, however this effect is small with a relatively high concentration of arginine remaining in the bulk water.

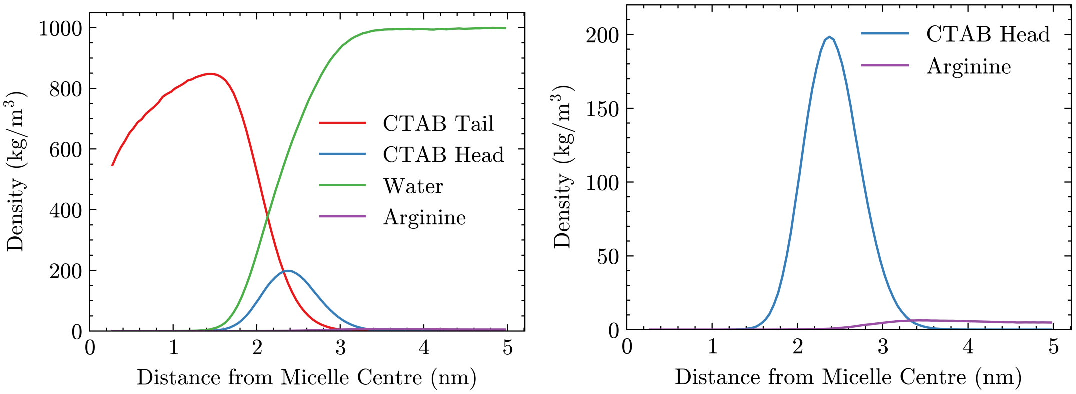

Figure 4.23: Time averaged radial density profile of single micelles in the presence of arginine in atomistic simulations. The full profile with all species (except for bromide counter-ions, which are hidden) is shown on the left, while only the surfactant headgroup and arginine densities are shown on the right.

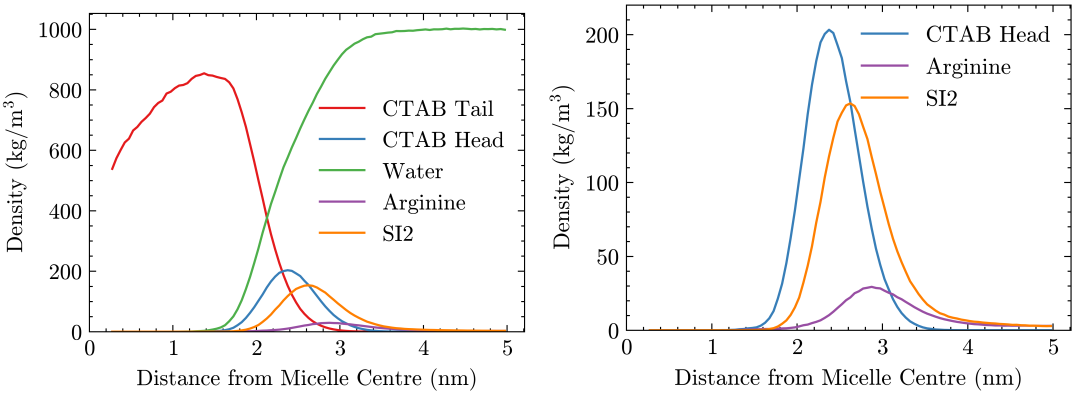

Figure 4.24: Time averaged radial density profile of single micelles in the presence of arginine and anionic silica dimers in atomistic simulations. The full profile with all species is shown on the left, while only the surfactant headgroup, arginine and silica densities are shown on the right.

4.5.3.2 Model Mapping and Bonded Parameters

Two potential mapping schemes were tested for arginine. The first, which follows the typical mapping used for arginine residues in proteins and is suggested by the authors of the Martini 3 model [13], is comprised of 3 beads with the amino acid backbone represented by a single bead (see Figure 4.25, left). While this is practical for models of proteins which contain many connected backbone beads, for forms of arginine that do not have a zwitterionic backbone, (instead having only either a positively charged amine group or a negatively charged carboxylate group) combining the carboxylate group and the primary amine group into a single bead may not be sufficient to capture the full behaviour of the molecule. Therefore, to more accurately capture this behaviour and allow for the representation of different protonation states of arginine (and in particular the high pH form present during OMS self-assembly), an alternative mapping scheme based on 4 beads is proposed, in which the backbone is divided into two beads, one representing the primary amine group and adjoined carbon whilst the other represents the charged carboxylate group (see Figure 4.25, right). The side chain is mapped with the alkane group represented by one bead with a 3-1 mapping, while the guanidinium group is captured in another bead.

For the 3 bead model, the same parameters are used as in the arginine model

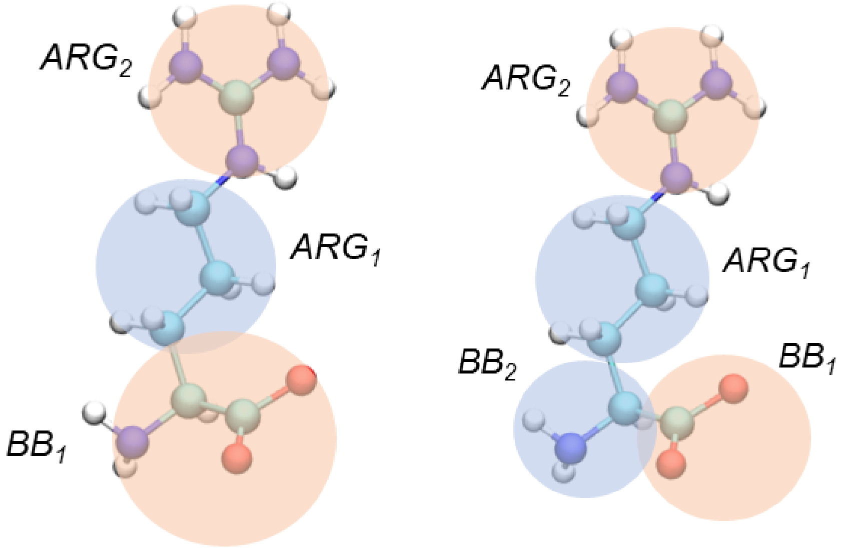

Figure 4.25: CG mapping schemes for arginine. The standard Martini 3 mapping scheme is shown on the left while the 4 bead model mapping used in this work is shown on the right.

for proteins developed by the Martini 3 authors [13]. For the 4 bead model bonded parameters are determined from a reference atomistic simulation as described in Section 4.4.2. Both sets of bonded parameters for bonds and angles are provided in Tables 4.15 and 4.16 respectively.

Table 4.15: Bonded parameters for arginine Martini 3 models. Bead names refer to labels in Figure 4.25. b_{ij} is the bond length and k_{ij} is the bond force constant.

Bond	b_{ij} (nm)	k_{ij} (kJ mol^{-1} nm^{-2})
3 Bead Model		
BB_1-ARG_1	0.330	5000
ARG_1-ARG_2	0.380	5000
4 Bead Model		
BB_1-BB_2	0.253	37000
BB_2-ARG_1	0.363	4500
ARG_1-ARG_2	0.387	9600

Table 4.16: Angle type parameters for arginine Martini 3 models. Bead names refer to labels in Figure 4.25. θ_{ijk} is the angle between beads and k_{ijk} is the angle force constant.

Beads	θ_{ijk} (degrees)	Calculated k_{ijk} (kJ mol^{-1} deg^{-2})
3 Bead Model		
BB_1-ARG_1-ARG_2	180	25
4 Bead Model		
BB_1-BB_2-ARG_1	84	60
BB_2-ARG_1-ARG_2	141	44

.

4.5.3.3 Bead Type Selection

The side chain beads for both the 3 and 4 bead models (ARG_1 and ARG_2) are identical and therefore can be considered separately from the backbone bead selection. The bead types for arginine side chain suggested by the Martini 3 authors are the SC3 bead for the alkane chain (ARG_1) and the SQ3p bead for the charged guanidinium group at the end of the side chain (ARG_2). However, to more finely tune the side chain interactions, an approach that can be taken is to calculate the free energy difference in different solvents of the side chain beads using different candidate bead types, and compare these to experimental values. This procedure was carried out for alternative charged bead types representing the guanidinium group (ARG_2). All small charged bead types were tested using the p label, which represents the hydrogen bonding potential of the group. The two solvents used were water and cyclohexane, for which there is experimental data for a neutral analogue of the arginine side chain, N-propylguanidine, [178, 179] which gives a free energy of partitioning value of -24.2 kJ mol^{-1}. The free energy of partitioning between water and cyclohexane for the arginine side chain was calculated by thermodynamic integration for each bead. The electrostatic charge of the ARG_2 bead was switched off and only Lennard-Jones contributions to the free energy were considered, as only these interactions are affected by the choice of bead type. The results are presented in Figure 4.26. These results show that the SQ4p bead provides the closest match to experimental data, with a calculated value of -22.95 kJ mol^{-1}, suggesting that this bead may be more appropriate to represent the guanidinium group

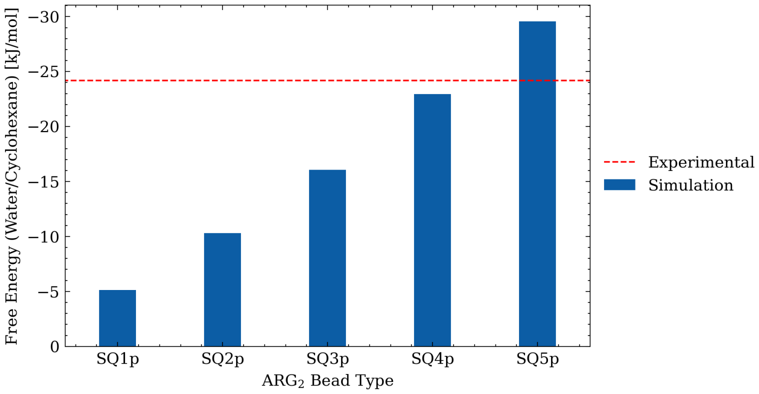

Figure 4.26: Partition free energy between water and cyclohexane for different Martini 3 bead types representing the guanidinium group in the arginine side chain analogue.

in arginine. Therefore, this bead type was considered for the CG model.

The mapping scheme used for the backbone of the 3 bead and 4 bead models is different, and therefore requires a different approach. For the 3 bead model a single bead is required to represent the negatively charged carboxylate group as well as the primary amine group of the backbone. The bead types suggested by the Martini 3 authors for a carboxylate group and primary amine group are Q5n and N6d, respectively, while the bead type used for amino acid backbone beads that are part of a protein (and therefore uncharged) is the P6 bead. This suggests that a highly hydrophilic bead type is likely to be required, and so the Q5 bead type is selected initially to represent the BB_1 bead for the 3 bead model.

For the 4 bead model, the carboxylate group and the primary amine group are split across two beads (BB_1 and BB_2). Therefore, the SQ5n bead type is used to represent the carboxylate group (a small bead size is used due to the 3-1 heavy atom to bead mapping) and the TN6d bead is used for the primary amine group (a tiny bead size is used due to the 2-1 heavy atom to bead mapping).

4.5.3.4 Coarse-Grained Model Validation

For validation simulations, three different candidate models were tested, one 3 bead model and two 4 bead models. The bead types assigned are summarised in Table 4.15. These three models were validated against atomistic single micelle radial density profiles. In these single micelle simulations, the form of arginine that was used was the one with an overall neutral molecular charge (form III in 4.3). The CG simulation results are compared for each model in Figure 4.27.

Table 4.17: Martini 3 bead type assignments for CG models tested. Bead names refer to labels in Figure 4.25.

Model	Backbone		Side Chain	
3 bead	BB_1		ARG_1	ARG_2
3	Q5		SC3	SQ3p
4 bead	BB_1	BB_2	ARG_1	ARG_2
4A	SQ5n	TN6d	SC3	SQ3p
4B	SQ5n	TN6d	SC3	SQ4p

All three candidate models showed qualitatively similar behaviour to the atomistic reference, with very little adsorption of arginine at the micelle surface and a large quantity of arginine molecules remaining in the bulk water. Looking more closely at the arginine radial density profile, the 4 bead models appear to better represent the behaviour of arginine in this system, as the 3 bead model shows slightly too much attraction towards the micelle surface compared with both 4 bead models. Comparing the two 4 bead models, model 4B, which uses the SQ4p bead to represent the guanidinium group of the arginine side chain, has a density profile that agrees slightly more closely with atomistic data. Given this result, and the closer agreement of this bead choice against experimental free energy determinations, the 4B model was chosen for subsequent use.

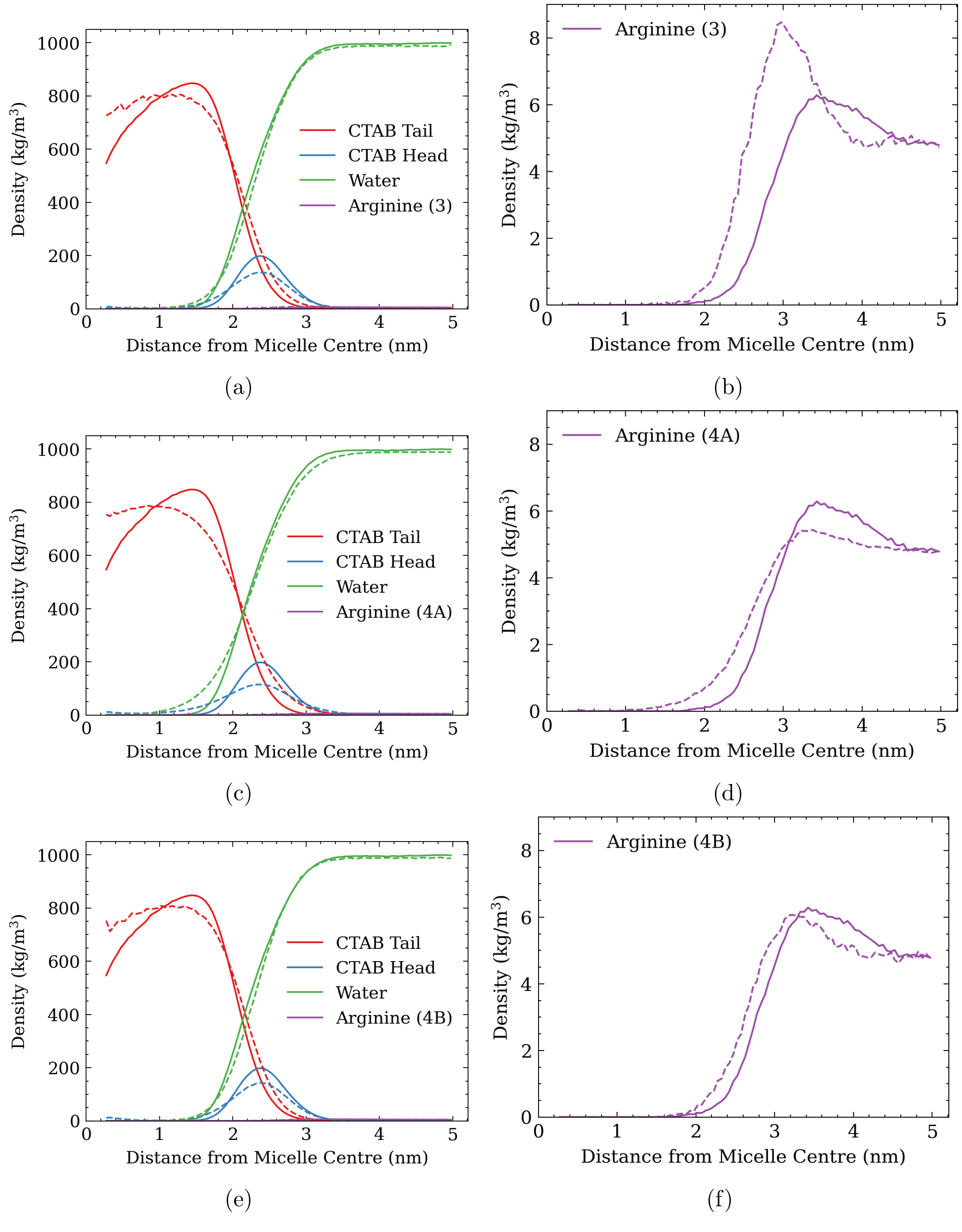

(a) (b)

(c) (d)

(e) (f)

Figure 4.27: Radial density profiles of a single CTAB surfactant micelle in the presence of arginine comparing atomistic (filled line) and CG (dashed line) simulations. Full density profiles including all species (except bromide counter-ions which are hidden) are shown on the left hand side while density profiles of only arginine are shown on the right. The model used to represent arginine is indicated in the legend in brackets and refers to the bead assignments given in Table 4.17.

Next, a CG simulation was carried out of a single CTAB micelle with arginine and anionic silica dimers. The micelle radial density profiles are shown in Figure 4.28. Much like in previous CG micelle simulations, the surfactant headgroup and silica peaks are shorter and broader than atomistic simulations, but accounting for this, the agreement with atomistic data for these species remains good. However, the CG model shows much weaker attraction of arginine molecules to the surface of the micelle than is present in the atomistic model. This may suggest that the Martini 3 model is not able to fully capture the double-layer charge interactions between surfactant, silica and arginine species, leading to a weaker attraction of arginine to the micelle surface and most arginine remaining in the bulk water. This may be explained by the relatively simple representation of electrostatic interactions in the Martini 3 model, where charged groups are represented by a single integer point charge, compared to the atomistic model which is able to more accurately describe the charge distribution within each molecule. In addition, water in the Martini 3 model is represented by neutral beads without electrostatic charge, with electrostatic screening provided by an effective relative permittivity value. Therefore, the models' ability to accurately describe more complex electrostatic interactions between multiple charged species is limited. Due to these factors, it is unlikely that the model can be further improved to display the full behaviour of arginine in this system without significant modification of the core Martini 3 framework.

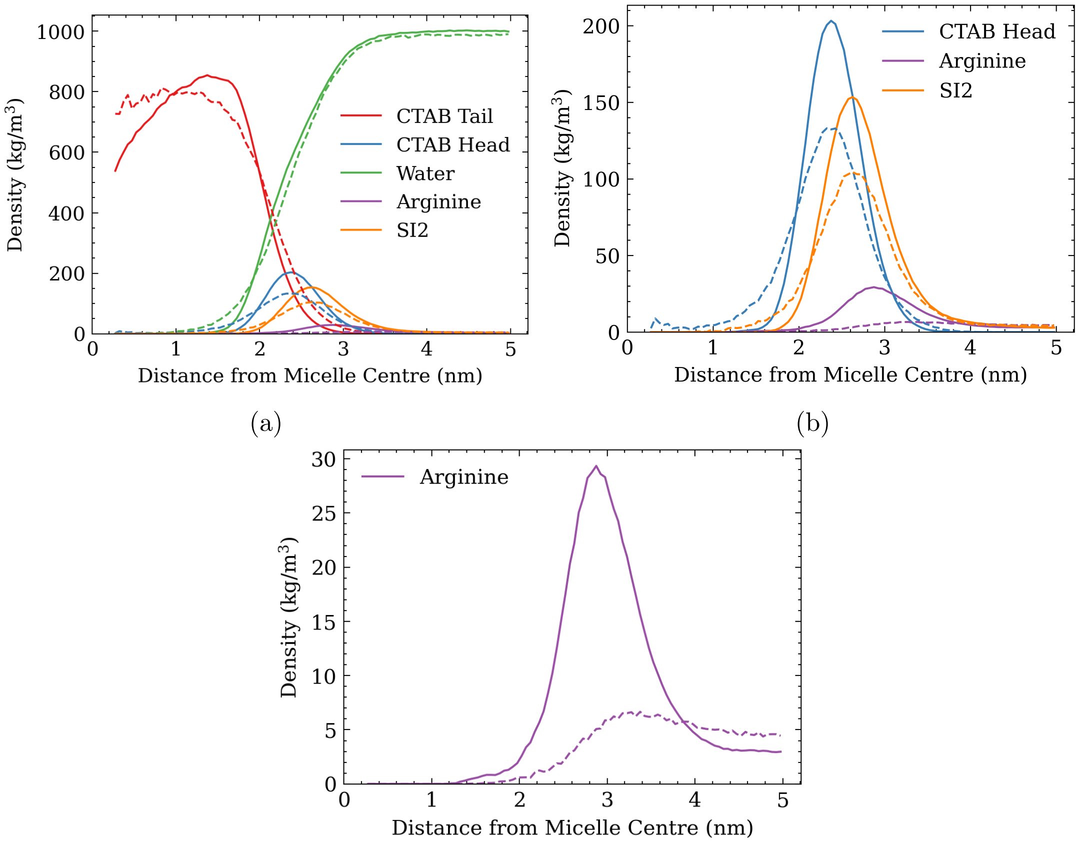

(a)

(b)

(c)

Figure 4.28: Time averaged radial density profile of a single CTAB micelle in the presence of arginine and anionic silica dimers comparing atomistic (filled line) and CG (dashed line) simulations. The full profile with all species is shown in (a), the surfactant headgroup, arginine and silica densities are shown in (b) and only arginine is shown in (c).

4.5.3.5 Arginine Bead Types Summary

The Martini 3 bead types used in the model selected in this work for arginine are summarised in Table 4.18. For bonded parameters, refer to Tables 4.15 and 4.16.

Table 4.18: Summary of bead type assignments for arginine.

Bead	Charge	Bead Type
BB_1	-1	SQ5n
BB_1	0	SP2
BB_2	0	TN6d
BB_2	+1	TQ4p
ARG_1	0	SC3
ARG_2	+1	SQ4p
ARG_2	0	SQ4p

4.5.4 PEHA

4.5.4.1 Model Mapping and Bonded Parameters

Pentaethylenehexamine is made up of 16 heavy atoms. Each end of the molecule terminates in a primary amine group which is connected by repeating secondary amine groups interspersed with two carbons. To maintain the symmetry of the molecule, each of these repeating units is represented by a single small Martini bead, while the end groups are represented by a tiny Martini bead representing the primary amine and nearest bonded carbon atom (as well as bonded hydrogen). The mapping scheme is presented in Figure 4.29.

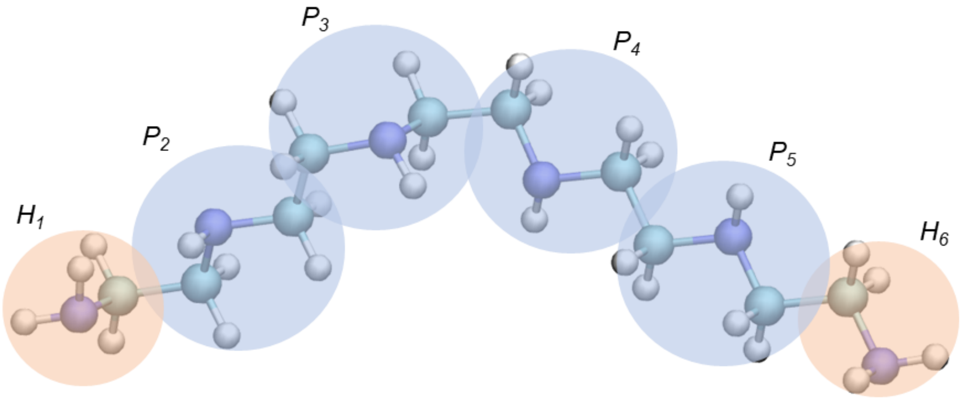

Figure 4.29: Martini 3 mapping scheme for PEHA molecule. Terminal primary amine groups with adjacent carbon are given the label H_1 and H_6 while secondary amine groups have labels P_{2-5}.

Bonded parameters generated for this mapping scheme are presented in Tables 4.19 and 4.20. Calculated bond lengths and force constants for *H*-*P* and *P*-*P* bonds and *H*-*P*-*P* and *P*-*P*-*P* angles are averaged to a single value. Bonded parameters were generated using a single PEHA molecule with an overall neutral charge, and the parameters are also used for CG models of charged PEHA molecules.

4.5.4.2 Bead Type Selection

The bead type assignment for the chosen mapping is straightforward, since both primary and secondary amines have bead types recommended by the authors of the Martini 3

Table 4.19: Bonded parameters for PEHA Martini 3 model. Bead names refer to labels in Figure 4.29. b_{ij} is the bond length and k_{ij} is the bond force constant.

Bond	b_{ij} (nm)	k_{ij} (kJ mol^{-1} nm^{-2})
H_1-P_2	0.308	6900
P_2-P_3	0.368	9400
P_3-P_4	0.368	9400
P_4-P_5	0.368	9400
P_5-H_6	0.308	6900

Table 4.20: Angle type parameters for PEHA Martini 3 model. Bead names refer to labels in Figure 4.29.θ_{ijk} is the angle between beads and k_{ijk} is the angle force constant.

Beads	θ_{ijk} (degrees)	Calculated k_{ijk} (kJ mol^{-1} deg^{-2})
H_1-P_2-P_3	144	238
P_2-P_3-P_4	146	384
P_3-P_4-P_5	146	384
P_4-P_5-H_6	144	238

force field [13]. The assignment is therefore only dependent on the charge state of the bead. For neutral primary amines and adjacent carbon (H_1 and H_6), with a 2-1 mapping, the TN6d bead type is recommended with the label representing the hydrogen bond donor characteristic of the amine group. When the terminal primary amine group is positively charged, the TQ5p bead is used instead. For the secondary amine groups and adjoining carbons (P_{2-5}), the SN4 bead type is recommended for neutral amine groups. While not explored in this work, the SQ2p bead could be used to represent positively charged secondary amine groups in PEHA, which occur at low pH. These bead type assignments are summarised in Table 4.21.

Table 4.21: Summary of bead type assignments for PEHA.

Bead	Charge	Bead Type
H	0	TN6d
H	+1	TQ5p
P	0	SN4
P	+1	SQ2p

In this work, three charge states are considered, which correspond to pKa values of 9.7 and 11 and an overall molecular charge of +2, +1 and 0. For the neutral molecule (i.e. net charge of 0), both terminal beads (H_1 and H_6) are uncharged and therefore represented by the TN6d bead type. For the +1 charge molecule, a single terminal bead (H_1) is represented by the TQ5p bead type, and for the +2 charge molecule, both terminal beads are represented by the TQ5p bead type.

4.5.4.3 Micelle Coarse-Grained Simulations

Simulations of PEHA at the three different charge states (0, +1 and +2) in the presence of a single CTAB micelle, both without silica present and in the presence of anionic silica dimers, were carried out. The radial density profiles generated from these simulations are shown in Figures 4.30 and 4.31.

In the simulations without silica present, generally there is weak interaction between PEHA species and the surfactant micelle, with a majority of PEHA therefore remaining in the bulk water. Out of the three charge states, the neutral molecules interacted most strongly with the micelle and a small peak in density can be observed close to the micelle surface. The charged PEHA species interacted less strongly with the micelle, which is to be expected given that both the charge of the micelle surface and the overall charge of PEHA molecules are positive.

In simulations with silica, as expected, the negatively charged silica molecules adsorb strongly onto the positively charged micelle surface. When PEHA molecules possess no overall charge, their behaviour is similar to simulations without anionic silica dimers present, with only a small peak in density close to the micelle surface. As the degree of positive charge possessed by PEHA molecules is increased, the interaction between PEHA and the surfactant micelle is reduced, however it is notably higher than in simulations that do not contain silica. This can be explained by attraction of positively charged PEHA molecules to negatively charged bound silica species. In addition, the peak in silica density is reduced, which suggests that the presence of charged PEHA species slightly reduces the interaction of silica with the surfactant micelle. This may be explained by the increased quantity of positively charged species in the bulk water, which in turn increases the propensity of silica to be solvated.

Overall, these results indicate that the interaction of PEHA with surfactant micelles is generally low, but strongest when PEHA molecules bear a neutral charge. The interaction strength between PEHA and silica, however, increases as the charge of PEHA molecules increases. At high pH, relevant to the self-assembly of OMS materials, PEHA species will predominantly be uncharged. However, as pH is lowered towards neutral, the proportion of charged PEHA species will increase. Therefore, the nature of the interaction between PEHA species and the silica-surfactant template may change as the pH is lowered during synthesis.

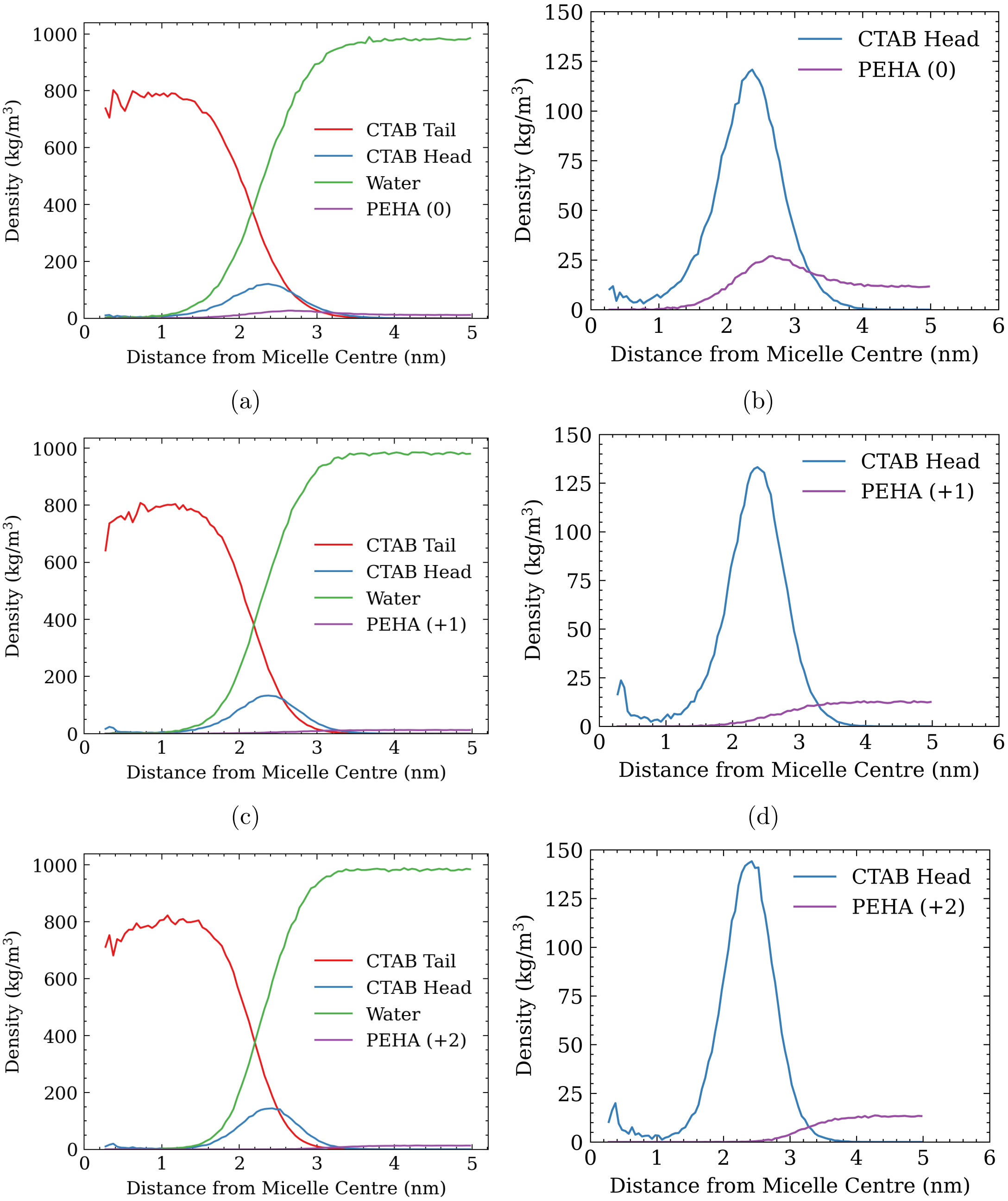

(a) (b)

(c) (d)

(e) (f)

Figure 4.30: Time averaged radial density profile of single micelles in the presence of PEHA. The overall molecular charge of PEHA is given in the legend of each figure. Left hand figures (a, c and e) show all species excluding bromide counter-ions while right hand figures (b, d and f) show only CTAB headgroup and PEHA densities.

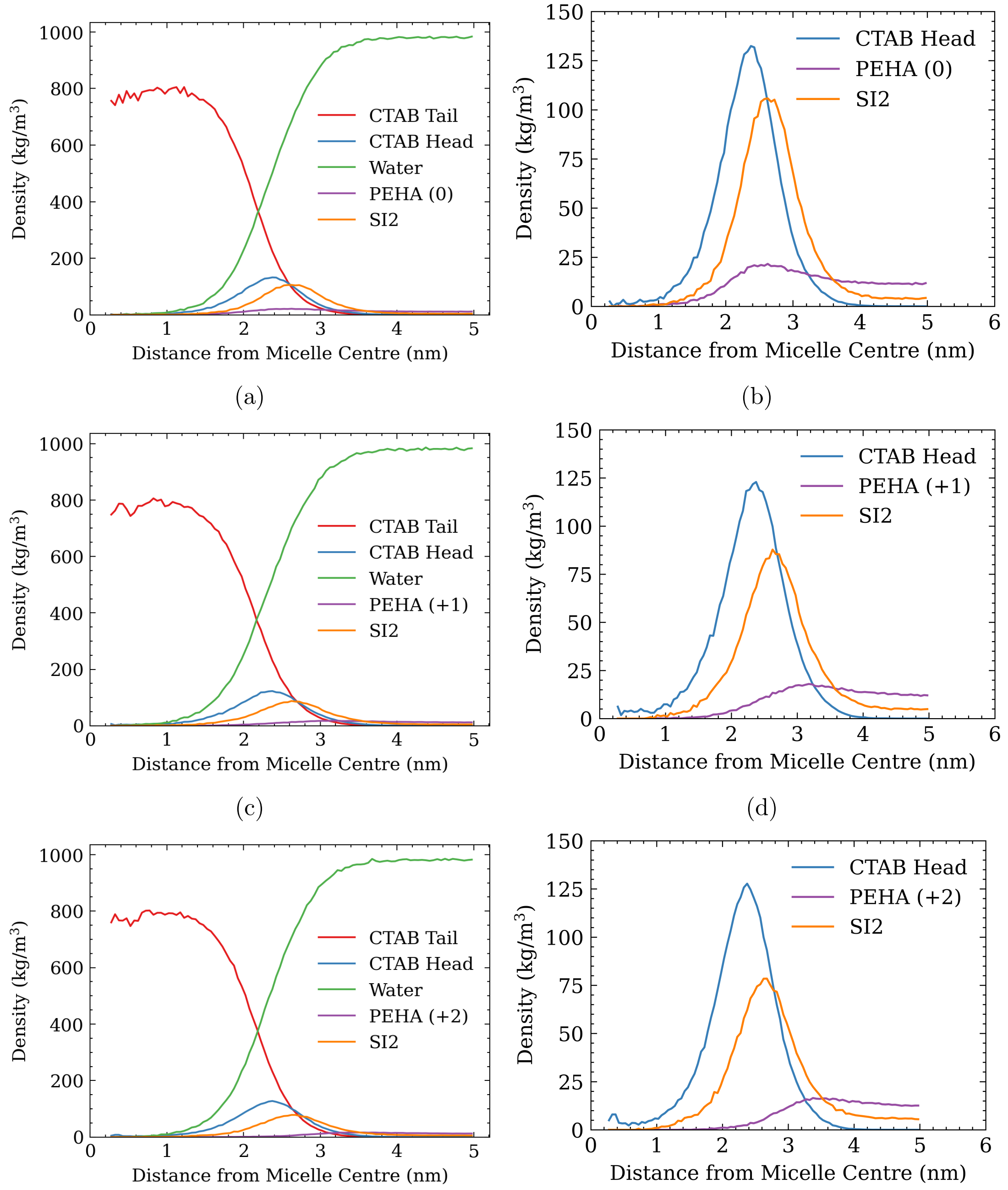

(a) (b)

(c) (d)

(e) (f)

Figure 4.31: Time averaged radial density profile of single micelles in the presence of PEHA and anionic silica dimers. The overall molecular charge of PEHA is given in the legend of each figure. Left hand figures (a, c and e) show all species excluding bromide counter-ions while right hand figures (b, d and f) show only CTAB headgroup, PEHA and silica densities.

4.6 Coarse-Grained Simulations of Self-Assembly

4.6.1 CTAB Solutions

CTAB self-assembly simulations at 3 wt% and 6 wt% resulted in an average aggregation number of 125 and 167 surfactant molecules, respectively (see Figure 4.33, left). Note that in Figure 4.33, left, a time of 0 µs corresponds to the start of production MD (i.e. after equilibration). The experimental aggregation number for CTAB in water has been shown to increase with concentration [180, 181], and experimental data from literature [174, 175, 180–186] is presented in Figure 4.33, right. The CMC of CTAB in water is approximately 0.03 wt% [187], and all literature values presented here are above this value. Only values for pure CTAB/water systems are taken. It can be seen that the aggregation numbers obtained in the 3 wt% and 6 wt% simulations agree well with the experimental trend. Snapshots of the initial and final configurations of the 6 wt% system are shown in Figure 4.32.

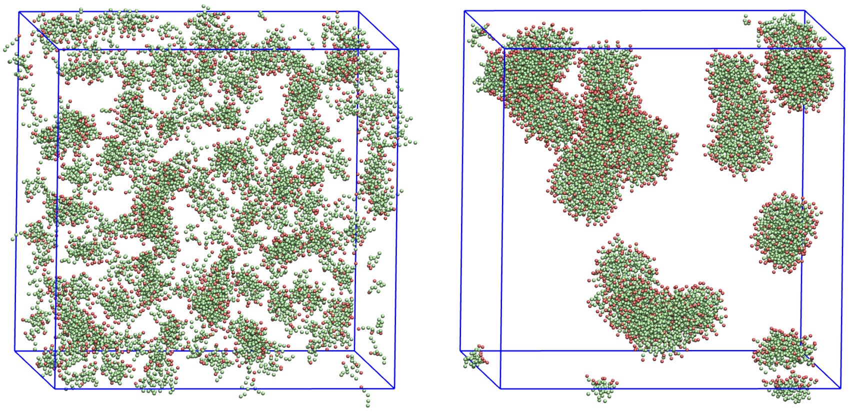

Figure 4.32: Simulation snapshots of the 6 wt% CTAB system, showing the initial configuration (left) and final configuration (right) after 9 µs of simulation time. CTAB head group beads are shown in red and tail group beads are shown in green. Bromide counter-ions and water are hidden for clarity.

Figure 4.34 shows visualisations of the mesophases formed after 1000 ns of simulation time for higher concentrations of CTAB. The CTAB model showed qualitative agreement with experimental observations for mesophases formed upon increasing the

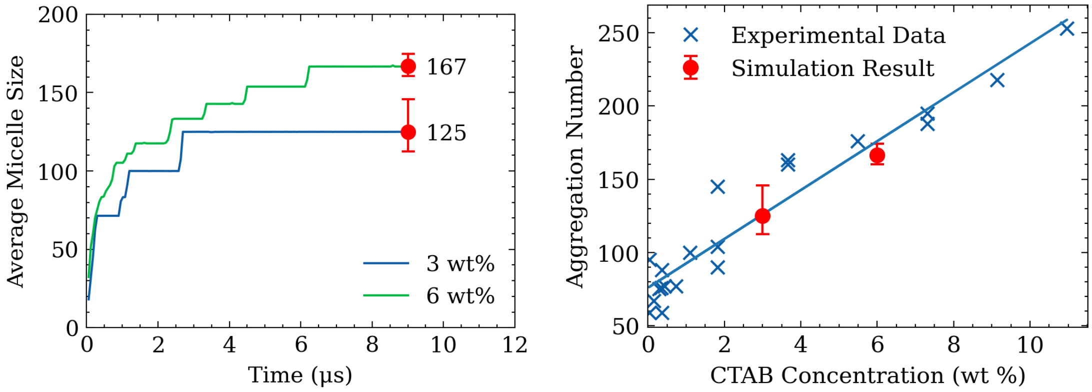

Figure 4.33: (Left) Aggregation number during self-assembly simulations using CG model for CTAB at 3 and 6 wt%. (Right) The experimental aggregation numbers for CTAB are plotted at various concentrations with data taken from [174, 175, 180–186]. The aggregation number obtained in the simulations is shown by red circles.

concentration of CTAB surfactant in an aqueous system [188]. At relatively low concentrations (15 wt%) micellar rods are formed, then upon increasing concentration first a hexagonal mesophase is formed (50 wt%), followed by a bicontinuous phase (65 wt%) and finally a lamellar phase (75 wt%). These points are plotted on the experimental phase diagram in Figure 4.35.

Overall, the results of all CG simulations agree with both atomistic simulation results and available experimental data, suggesting that the surfactant model is suitable for reproducing surfactant behaviour.

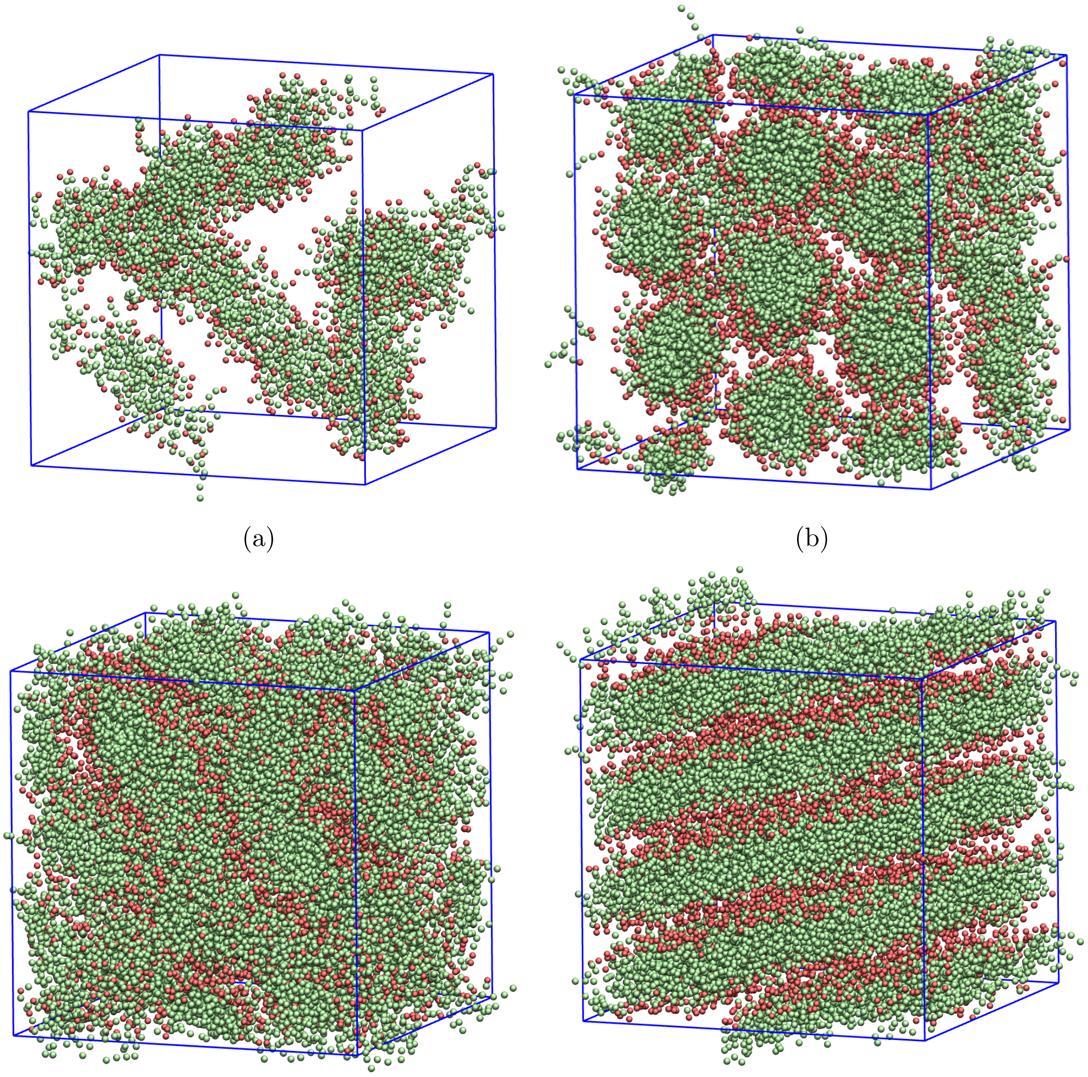

(a) (b) (c) (d)

Figure 4.34: Simulation snapshots obtained at CTAB concentrations of: 15 wt% showing micellar rods (a), 50 wt% showing hexagonal phase (b), 65 wt% showing bicontinuous phase (c) and 75 wt% showing lamellar phase (d). Surfactant heads are shown in red while surfactant tails are shown in green. Water and bromide counter-ions are hidden for clarity. All simulations were carried out at 390 K.

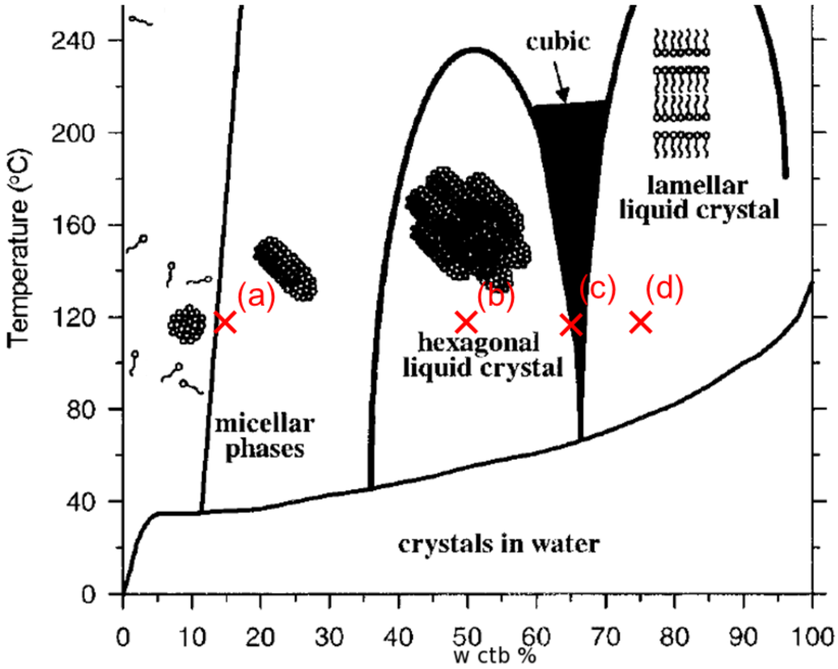

Figure 4.35: Phase diagram for CTAB in water showing the experimentally observed liquid crystal phases at a range of surfactant concentration and temperature values. The labels on the diagram refer to the visualisations shown in Figure 4.34. Adapted from [25].

4.6.2 CTAB/Silica Solutions

4.6.2.1 Effect of Surfactant Concentration and Box Dimensions on Self-Assembly

The choice of simulation box dimensions over which periodic boundaries are drawn is an important practical consideration for simulations studying self-assembly behaviour of the ternary surfactant/silica/water system. Employing appropriately sized boxes may allow systems to more easily phase separate and promote the formation of periodic phases across boundaries. This is particularly important for hexagonal liquid crystal (HLC) phase formation at relatively low concentrations of surfactant ($<$ 20 wt%), as equilibration of a well-ordered hexagonal phase requires the alignment of several rods. This is a slow process, and the system is prone to becoming kinetically arrested in metastable arrangements due to periodic boundary conditions.

This decision is also closely related to surfactant concentration, which determines the quantity of surfactant molecules in the system and therefore the "size" of the surfactant phase in relation to the box volume. Ideally, to demonstrate formation of the HLC phase there should be a sufficient quantity of surfactant to achieve a separated surfactant phase that bridges periodic boundaries, with a large enough size to demonstrate the periodicity of the phase. This must be carefully balanced with the increased computational demand incurred from increasing the total size of the system, which quickly becomes prohibitive for systems with a number of coarse-grained beads greater than 1×10^5. In this section, the self-assembly behaviour of a silica/surfactant/water system is studied using different box dimensions and surfactant concentrations. All simulations use the silica dimer model described previously using the Q5 bead to represent dimers (note that this is a different bead type than is used in the model validated elsewhere in this work, see Section 4.6.2.2), and start from a completely random initial configuration. In all cases, a 1:1 ratio of silicon atoms to surfactant molecules was adopted (giving a 2:1 ratio of surfactant molecules to silica dimers). Simulations are run for a maximum of 6 µs, and details are summarized in Table 4.22.

Table 4.22: Details of coarse-grained self-assembly simulations carried out to study the effect of box dimensions and surfactant concentration on self-assembly behaviour. N is the number of molecules of each species (denoted by the subscript) present in the simulation. Note that each water bead represents 4 water molecules. L is the box length in the x, y and z direction. t is total simulation time.

Simulation	C_{CTAB} (wt%)	N_{CTAB}	N_{SI2}	N_{Water}	L_x (nm)	L_y (nm)	L_z (nm)	t (µs)
Small Cubic	6	1000	500	60000	19.9	19.9	19.9	6.0
Small Cubic	12	2000	1000	60000	20.5	20.5	20.5	6.0
Large Cubic	6	4000	2000	240000	31.7	31.7	31.7	6.0
Elongated	20	1000	500	13000	8.7	8.7	28.9	6.0
Slab	6	1000	500	60000	7.9	31.7	31.7	6.0
Slab	12	2000	1000	60000	8.1	32.5	32.5	6.0
Slab	20	2000	1000	29000	6.7	26.7	26.7	6.0
Half-Cubic	6	2000	1000	120000	31.7	31.7	15.8	6.0
Half-Cubic	12	4000	1000	120000	32.4	32.4	16.2	6.0

Cubic Boxes

The most straightforward box shape is a cubic box where each dimension (x,y and z) is equal in length. Initially, small systems containing 60,000 water beads (representing 240,000 water molecules) were run at two concentrations of surfactant, 6 and 12 wt%. Simulation snapshots of the final configurations are shown in Figure 4.36a and 4.36b. At the lower concentration (Figure 4.36a) the separated silica/surfactant phase fails to bridge the periodic boundaries of the simulation box, which prevents the formation of rods. This is most likely due to there being an insufficient number of surfactant molecules to bridge the box length and form a continuous phase. For the higher concentration simulation (Figure 4.36b) the number of surfactant molecules was doubled, and as expected the surfactant phase is able to bridge the periodic boundaries of the simulation. However, rods do not have a particular preference to form across a particular box dimension, which leads to a surfactant phase bridging multiple boundaries (2 in this case). In the simulation time allowed, the configuration appears to be trapped in this arrangement where further organisation of the surfactant rods is impeded by the phase being “stretched” across multiple dimensions, preventing the rods from achieving a parallel and ordered arrangement as is expected for these systems. This behaviour was also demonstrated in a larger simulation at 6 wt%, which is shown in Figure 4.36c.

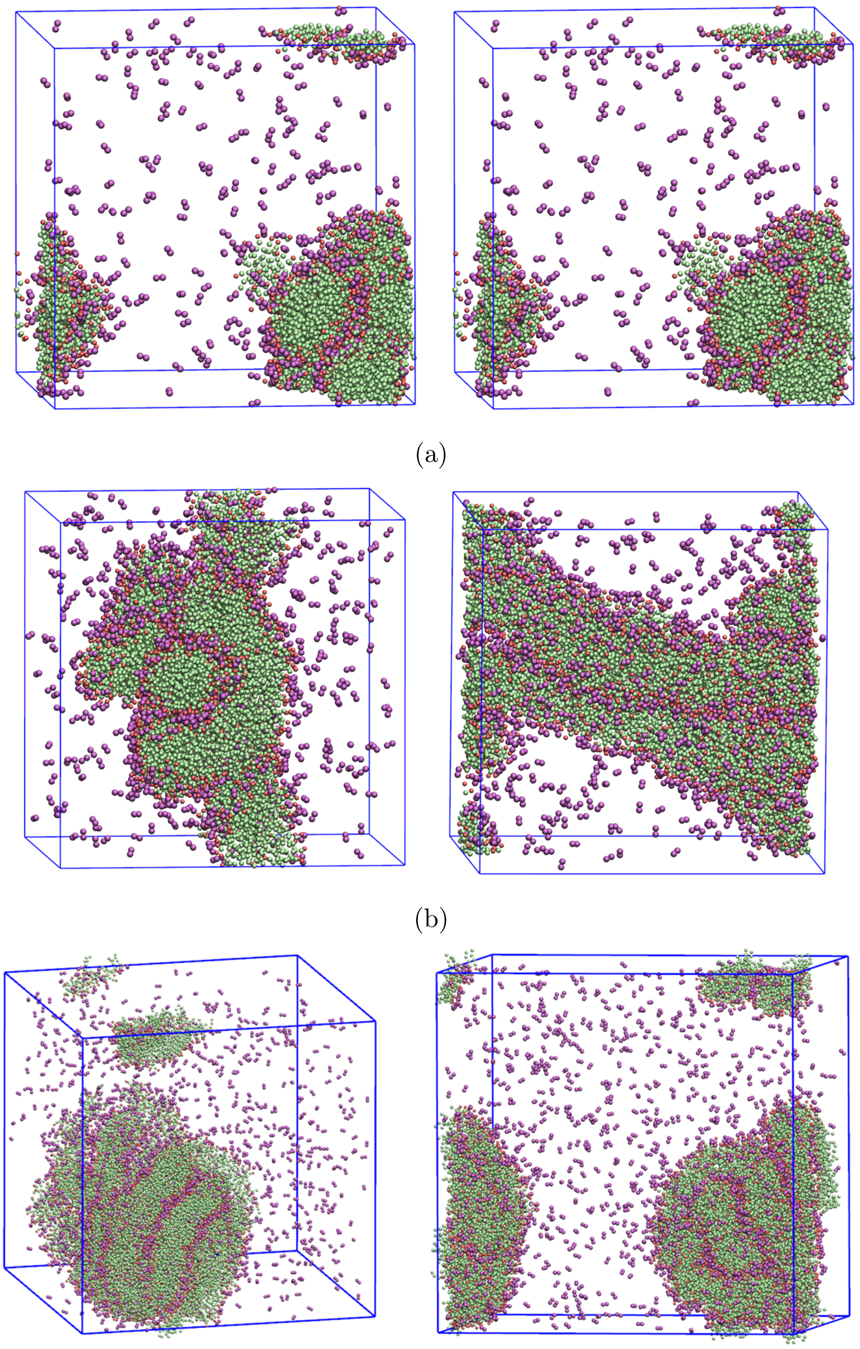

(a)

(b)

(c)

Figure 4.36: Final configuration after 6 µs of simulation time starting from a random configuration of surfactant, silica dimers and water using a cubic box type. (a) shows a small box at 6 wt % surfactant, (b) shows a small box at 12 wt % and (c) shows a large box at 6 wt%. Full details are provided in Table 4.22. CTA$^+$ head group beads are shown in red, tail group beads are shown in green and silica is shown in purple, and water beads hidden for clarity.

Elongated Boxes

One approach that has been used in previous work to promote faster phase separation is the use of "elongated" simulation boxes. These periodic boundary conditions are characterised as having a single dimension (in this case the z dimension) which is significantly longer than the two other dimensions, allowing periodic phases to form easily over the shorter box dimensions.

While the resultant phase appears to have rods ordered in a hexagonal arrangement, the limitations of this box type are also observed. While phase separation is rapid, rod-like micelles have a tendency to bridge across periodic boundaries in different orientations. Since these rods are effectively infinitely long due to the periodicity of the simulation box, reorganisation of the rods is not possible (within reasonable simulation time) and the system appears to become kinetically arrested. However, evidence of parallel ordering of rods in a hexagonal arrangement can still be observed. Due to the small size of this system (in terms of total number of coarse-grained beads) this makes elongated boxes a useful tool for the quick investigation of periodic phases.

Due to the small system size and therefore lower computational cost of running simulations using this elongated configuration, one strategy that could be employed is to run multiple replicas of these simulations in parallel, in order to assess the tendency of the simulation to achieve a well-ordered HLC phase. However, perhaps a more pragmatic approach is to use these simulations to assess whether the model is providing some evidence of HLC formation (for example during model development), followed by a larger simulation using a different configuration (e.g. cubic, slab or half-cubic) to further validate the model. The former method is employed in the development of the silica model described in this chapter.

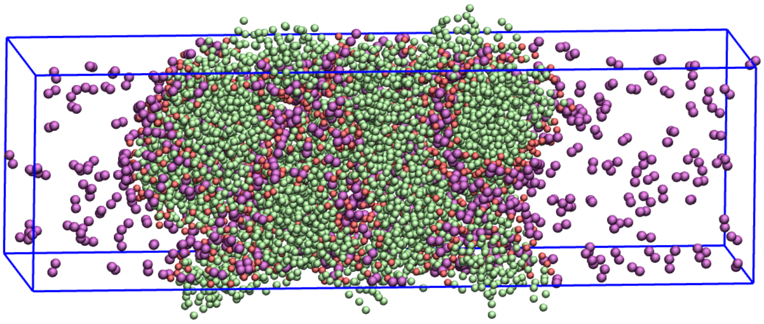

Figure 4.37: Simulation snapshot of the final configuration for a system containing CTA$^+$ and anionic silica dimers in water after 6 μs of simulation time at 20 wt% surfactant. The Colour code is the same as in Figure 4.36.

Slab Boxes

One possible solution to allow for periodic boundaries to be bridged more easily, whilst preventing rods from forming in multiple directions, is to use a simulation box with a single shorter dimension across which the HLC can easily form. This box configuration can be considered a “cross-section” of a cubic box, which reduces the total simulation size, thereby reducing computational demand. The ratio of box dimensions used for the “slab” configuration is 1:4:4 (x:y:z).

Simulations using this slab configuration were carried out at three concentrations of surfactant, 6, 12 and 20 wt%. At 6 wt%, some evidence of hexagonal phase formation is observed (see Figure 4.38a) with parallel ordered rods, however, due to the limited number of surfactant molecules, it is difficult to conclusively state that this is a true HLC phase. Increasing the concentration to 12 wt% allows for a more extensive surfactant phase which has the potential to better demonstrate the periodicity of the HLC phase, however as was observed in simulations using the cubic box type this causes the surfactant phase to bridge the longer box dimensions (see Figure 4.38b), causing the structure to become kinetically trapped. This effect is further pronounced at a surfactant concentration of 20 wt%, in which surfactant rods bridge all three box dimensions (see Figure 4.38c).

Aside from the obvious issues at higher concentrations, one potential cause of concern with using this box configuration is that the short dimension is not sufficiently long to distinguish whether the rods formed represent the long parallel rods we would expect to aggregate during HLC formation, or if the appearance of parallel rods is simply an artefact of the short periodic boundary dimension. In order to clearly show this, the short box dimension should be many times the width of a surfactant rod. An exact ratio of surfactant rod length to radius is not clear, but increasing this ratio should provide more confidence in the structure formed at the cost of increased computational expense.

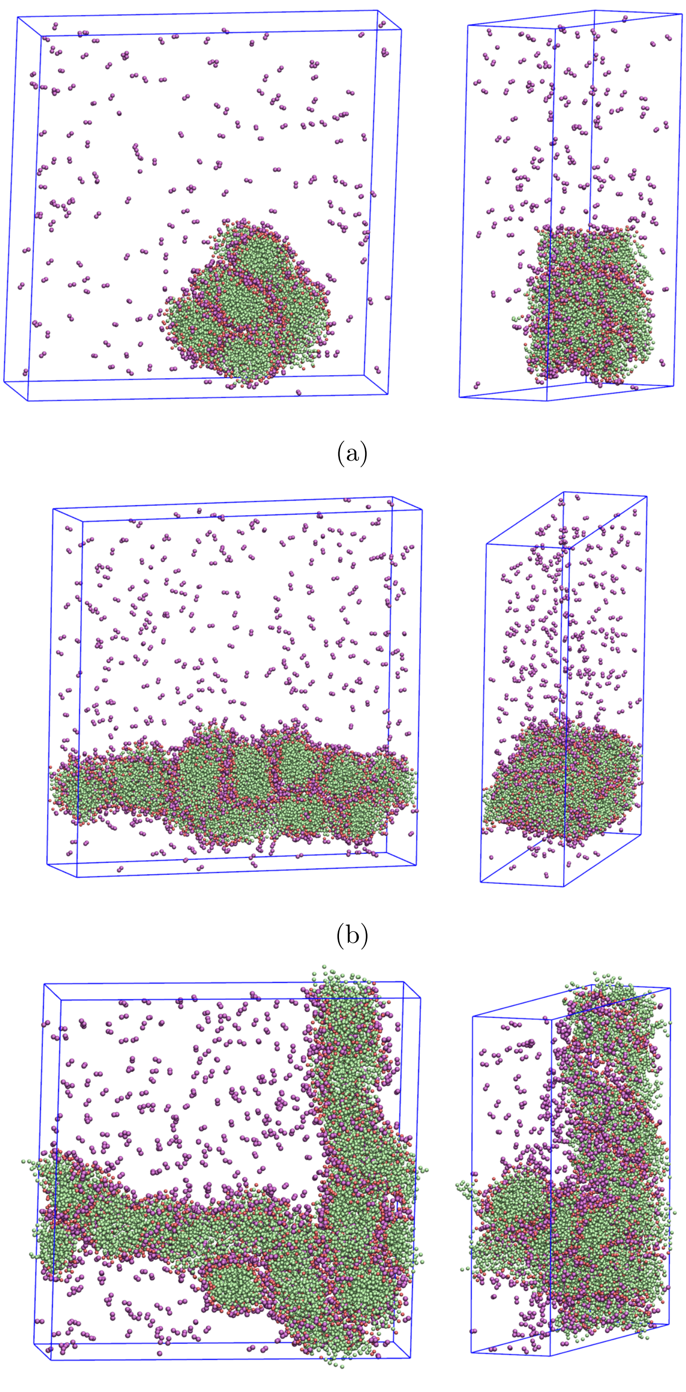

(a)

(b)

(c)

Figure 4.38: Final configuration after 6 µs of simulation time starting from a random configuration of surfactant, silica dimers and water using a slab box type. The surfactant concentration is 6 wt% in (a), 12 wt% in (b) and 20 wt % in (c). Full details are provided in Table 4.22. Colour code is the same as in Figure 4.36.

Half-Cubic Boxes

The use of a "half-cubic" box follows the same concept as the slab box type, but using a smaller ratio between the short and long box dimensions. As the name suggests, this box configuration uses a box dimension ratio of 2:1:1 (x:y:z), allowing for easy bridging of the short box dimension while maintaining a high ratio of surfactant rod length to radius across the shorter dimension.

Simulations using the half-cubic box type were run at a surfactant concentration of 6 wt% and 12 wt%. The final configuration at 6 wt% is shown in Figure 4.39a. Clear evidence of HLC phase formation can be observed, however, similarly to the simulations at low concentration using slab type boxes, there are not enough surfactant molecules to form a full HLC structure (i.e. at least 7 parallel rods in a hexagonal arrangement). In addition, the rods appear to be somewhat twisted and further organisation of the rods may not occur within reasonable simulation time. However, the final configuration provides sufficient evidence for hexagonal phase formation in this model, and therefore is useful as a final validation of the silica model.

The simulation at a higher surfactant concentration of 12 wt% results in a final configuration with a more extensive surfactant phase, consisting of many rods (see Figure 4.39b. However, there is significant twisting of rods, which may require significant time to resolve into a well-ordered structure. The time taken to reach a well-ordered arrangement may be further increased by the larger quantity of surfactant and therefore number of surfactant rods. However, some evidence of hexagonal ordering is still observable and is still likely to accurately represent the early stages of HLC formation.

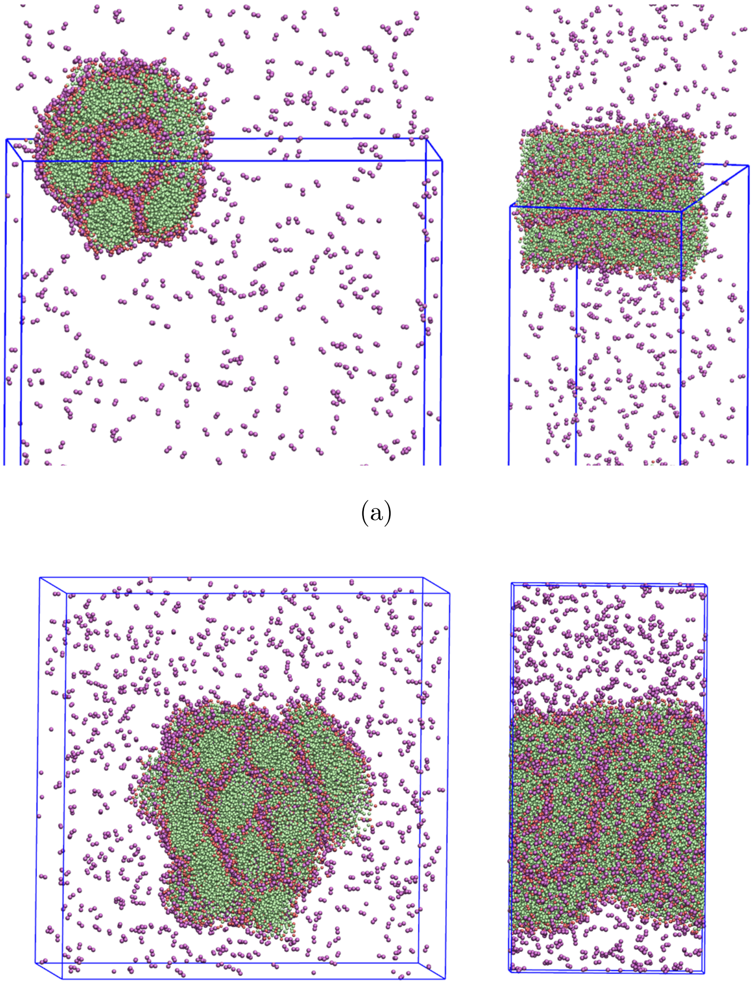

(a)

(b)

Figure 4.39: Final configuration after 6 µs of simulation time starting from a random configuration of surfactant, silica dimers and water using a half-cubic box type. The surfactant concentration is 6wt % in (a) and 12 wt% in (b). Full details are provided in Table 4.22. Colour code is the same as in Figure 4.36.

Conclusions on Box Types

Overall, out of the box types investigated in this section, the two box types and surfactant concentrations which appear useful for investigating HLC formation are the elongated boxes at 20 wt% and half-cubic box types at a lower concentration. The former may be used at an early stage (such as in model development or the assessment of a new system) to give an indication of whether HLC phase formation is likely to occur whilst keeping computational cost low, while the larger half-cubic simulations provide a more thorough assessment of the mesophase formed. There is a clear relationship between the quantity of surfactant, the short box dimension and the number of rods that form. This may be used to inform the appropriate system size for investigating HLC phase formation for a given system.

4.6.2.2 Validation of Coarse-Grained Model

After initial calibration against the atomistic model for silicates, validation of the bead type selection is carried out by studying the self-assembly behaviour of the ternary silica/surfactant/water system and comparing this with expected behaviour from experiments and previous simulation studies. Simulations are carried out with different speciation of silica (degree of condensation and ionisation states), with different expected behaviour in each case. For this initial validation, the number of silicate species was set so that the system contains an equal number of silicon atoms as surfactant molecules, which also results in a net zero charge without any counter-ions when fully deprotonated anionic silicates are used. For simulations with neutral silicates, bromide counter-ions are added. The concentration of surfactant used in all simulations for this section corresponds to the micellar region of the CTAB phase diagram (see Figure 4.35) and, without the presence of silica, should produce spherical and/or elongated micelles similar to those shown in Figure 4.32. All simulations started from a completely random arrangement of the molecules in the simulation box.

Firstly, neutral silicates were added to an initial random configuration of surfactant molecules. Snapshots of the final configurations achieved in self-assembly simulations involving neutral silicates (both monomers and dimers) are shown in Figure 4.40 (a and b). The configurations obtained in both cases are very similar to the control system without silicates present, suggesting that the presence of neutral silicates is not sufficient to promote aggregation of surfactant micelles, as expected.

Next, anionic silica monomers were added to an initial random configuration of surfactant molecules. The final configuration after 3 µs of simulation time is shown in Figure 4.40c. The presence of anionic silicate monomers promotes the fusion of spherical micelles to form long worm-like micelles. However, in agreement with previous simulation studies [75] and experimental observations [43], anionic silica monomers are not sufficient to promote phase separation and hexagonal phase formation at this concentration of surfactant. These observations support the choice of bead type (Q2) made for anionic silica monomers. This also indicates that despite the differences in the atomistic models used for parameterization in this work and in the previous work of Pérez-Sánchez et al. [75], resulting in monomers adsorbing outside the surfactant headgroup rather than being absorbed within the micelle surface, the self-assembly behaviour of CTAB in the presence of silica monomers remains qualitatively unchanged.

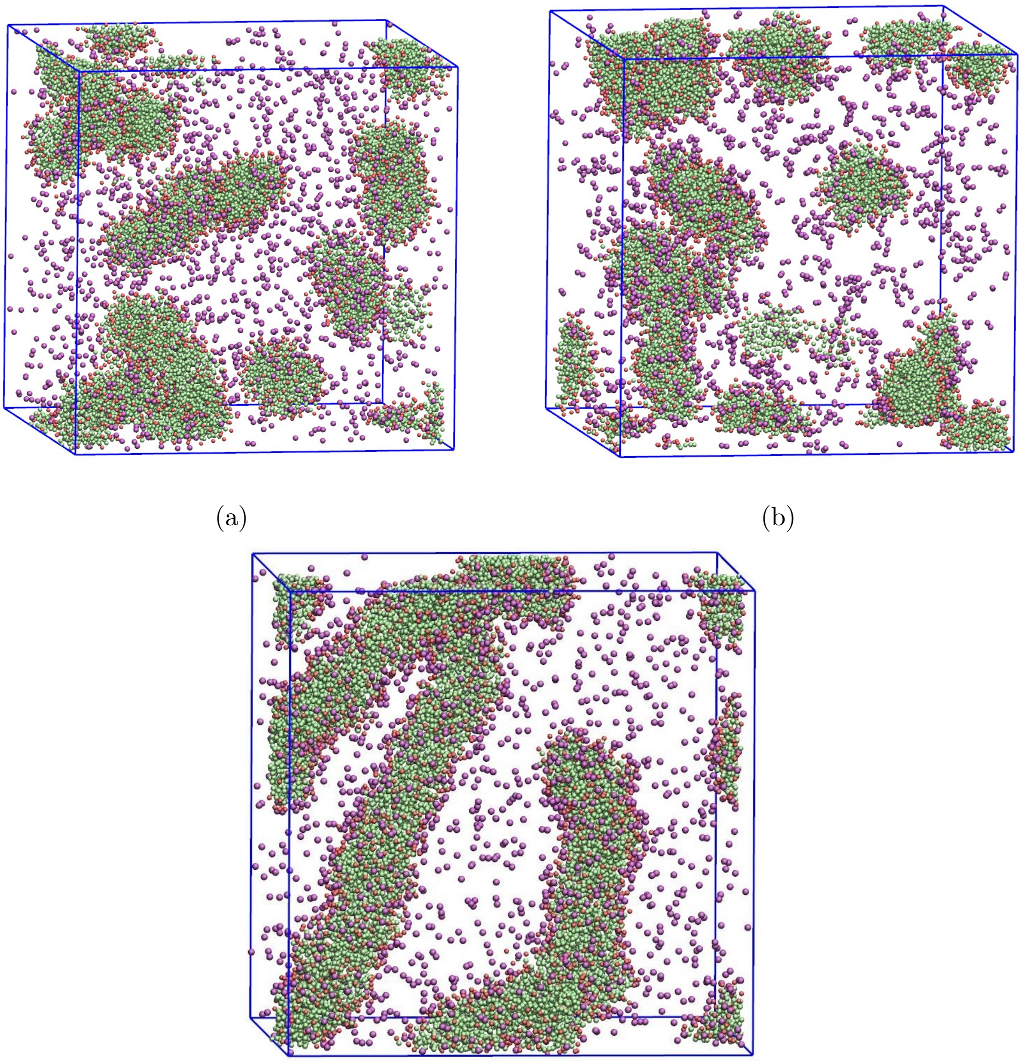

(a)

(b)

(c)

Figure 4.40: Simulation snapshots of the final configuration starting from a random configuration of surfactant, water and bromide counter-ions with neutral silica monomers (a), neutral silica dimers (b) and anionic silica monomers (c). CTA$^+$ head group beads are shown in red, tail group beads are shown in green and silica is shown in purple, with bromide counter-ions and water beads hidden for clarity.

Previously, comparison against atomistic data for a single micelle identified that the correct bead type for anionic silica dimers lies in the range of Q3-Q5, with Q4 being selected as a good compromise. Therefore, it is important to test the sensitivity of the self-assembly results to this choice of bead. Hexagonal phases were observed to be formed experimentally in the presence of a distribution of silicate oligomers [43], and in previous simulation studies, in the presence of both oligomers and dimers [77, 78]. Therefore, we tested the ability of our new model to reproduce these observations in a solution of CTAB and anionic silica dimers. This initial test makes use of elongated simulation boxes, which were used in previous work [77] in order to promote faster phase separation and organisation. A relatively high surfactant concentration (of 20 wt%) was used to ensure that the surfactant phase is large enough to show the periodicity of the HLC phase whilst keeping the total simulation time small enough to reduce computational demand (see Section 4.6.2.1). Note that this is still within the micellar region of the pure CTAB phase diagram (Figure 4.35). Each simulation was carried out for 6 µs.

Simulation snapshots of the final configurations obtained for these initial tests are shown in Figure 4.41. For the Q3 bead type, the presence of dimers promotes the aggregation of surfactant micelles into rods, full phase separation does not occur, and there is no evidence of HLC phase formation. This may be due to the Q3 bead resulting in a model for silica that is too hydrophobic, with excessive adsorption of silica dimers at the interface between surfactant headgroup and water, preventing adequate aggregation of the surfactant phase. For the Q4 bead type, clear evidence of phase separation and HLC phase formation can be observed, with several surfactant rods ordered in a “honeycomb” arrangement. This provides strong evidence that the Q4 bead is the right choice for modelling silica dimers. For the Q5 bead type, while phase separation does occur in this case and some evidence of parallel ordered rods can be observed, the arrangement of these rods appears to be somewhat disordered. Compared with the Q4 bead, the Q5 bead is more hydrophilic, which results in a higher proportion of silica dimers remaining in the bulk water rather than adsorbing at the interface between surfactant headgroup and water. This may result in there being too few silicate species to permit the assembly of an ordered HLC phase. These results indicate that the bead type selection for representing silicates is critical to reproducing the co-operative templating phenomena observed in silica/surfactant/water systems.

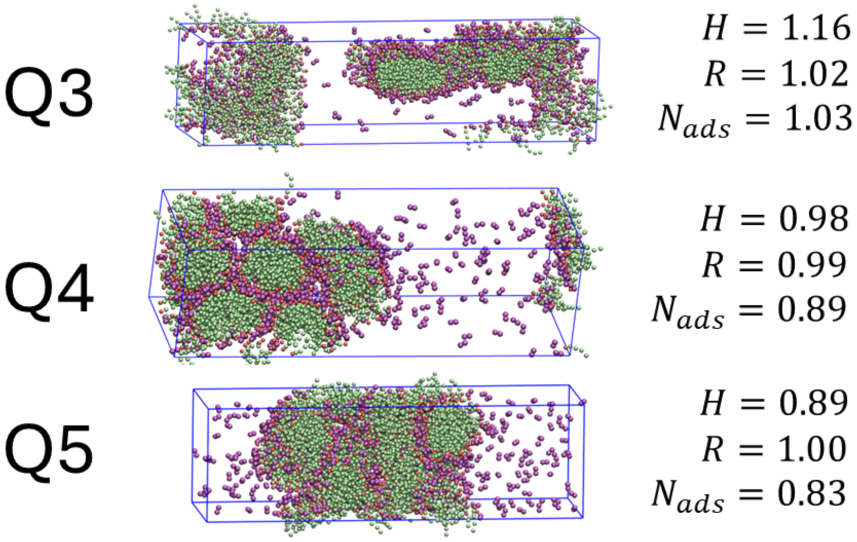

Figure 4.41: Simulation snapshots of the final configuration for a system containing CTA^+ and anionic silica dimers in water after 6 µs of simulation time using the Q3, Q4 and Q5 bead types to represent anionic silica beads. The colour code is the same as in Figure 4.40. The corresponding fitting parameters for these bead types are displayed alongside.

For a more thorough validation, larger simulations using a rectangular, "half cubic", box with dimensions of 31.6 x 31.6 x 15.8 nm were carried out (see Section 4.6.2.1). The shorter dimension in the z direction allows the surfactant phase to more easily bridge periodic boundaries and promotes rod formation in a single direction whilst ensuring that the small simulation box size does not artificially produce periodic phases. This z dimension is large enough (many times larger than a surfactant micelle) to ensure rods that form are sufficiently long compared to their width. The final configuration of this simulation after approximately 24 µs is shown in Figure 4.42. The formation of a hexagonal phase made up of multiple parallel rods spanning the shorter z dimension is clearly visible. The progression of the simulation with time is also shown in Figure 4.43. Starting from a random arrangement of surfactant and silicate species dispersed in water, surfactants very quickly form micelles, which occurs within 15 ns of simulation time. Silicates are attracted to the surface of micelles, screening the repulsive interactions between them and promoting the aggregation of micelles into several long worm-like micelles, which occurs approximately in the first 60 ns. The rod-like micelles then aggregate and phase separate, which is complete after approximately 600 ns. After this point, reorganisation of the surfactant phase into a more ordered HLC arrangement takes place, which is a much more lengthy process.

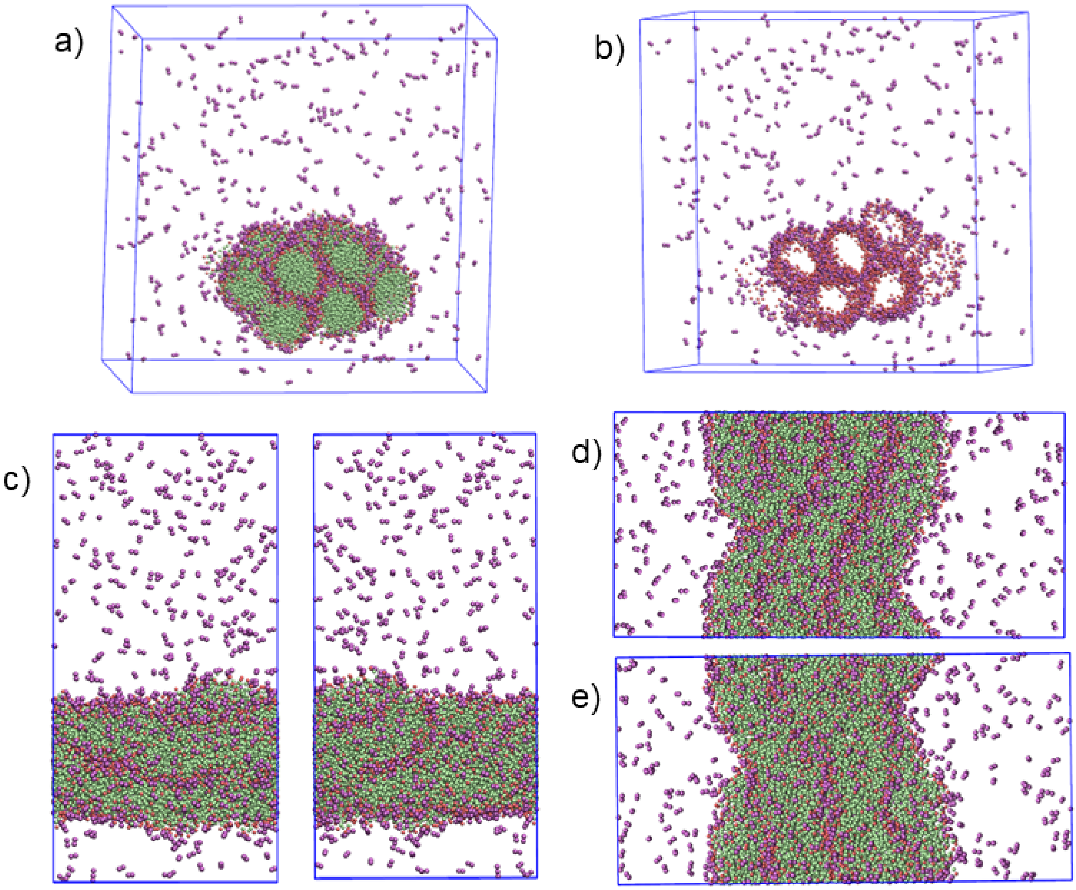

Figure 4.42: Simulation snapshots of the final configuration obtained using Q4 beads to represent silica dimers from different angles. Panel a) shows all species present, while in panel b) silica tail group beads are hidden to show the formation of rods across the short box dimension. Snapshots in panel c) are taken from a side-on perspective (y direction) while panels d) and e) are taken from top-down (positive z) and bottom-up (negative z) directions, respectively. Colour code is the same as in Figure 4.40.

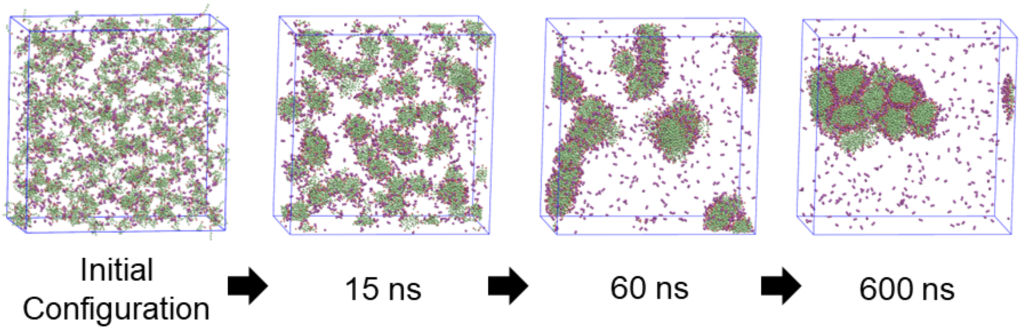

Figure 4.43: Simulation snapshots that show the progression of simulations for self-assembly of the surfactant HLC phase in the presence of silica dimers. Colour code is the same as in Figure 4.36.

While the presence of anionic silica dimers has been demonstrated to be sufficient to promote the formation of the HLC phase, higher oligomers such as cubic octamers and cyclic trimers have been shown to promote HLC formation in prior computational work [77]. These larger oligomers are often more directly relevant to experimental systems, for example under the synthesis conditions of MCM-41 approximately 70% of silicate species are present as cubic octamers. Therefore, a simulation was carried out to ensure that HLC formation is possible in the presence of these larger oligomers of silica. The final configuration after 3 µs is shown in Figure 4.44, revealing the formation of a very well-ordered phase-separated HLC.

While the presence of anionic silica dimers has been demonstrated to be sufficient to promote the formation of the HLC phase, higher oligomers such as cubic octamers and cyclic trimers have been shown to promote HLC formation in prior computational work [77]. These larger oligomers are often more directly relevant to experimental systems, for example under the synthesis conditions of MCM-41 approximately 70% of silicate species are present as cubic octamers [43]. Therefore, a simulation was carried out to ensure that HLC formation is possible in the presence of these larger oligomers of silica. The final configuration after 3 µs is shown in Figure 4.42d, revealing the formation of a very well-ordered phase-separated HLC.

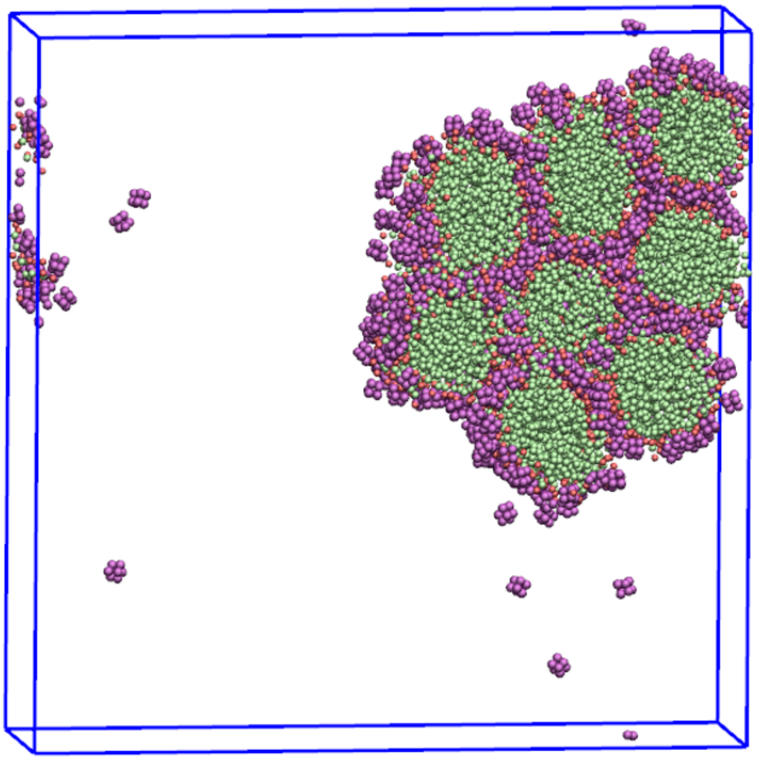

Figure 4.44: Simulation snapshot of the final configuration for a system containing CTA$^+$ and anionic silica octamers with a -4 charge in water after 3 µs of simulation time, using SQ4 beads to represent anionic segments and SN5 beads to represent neutral segments. Colour code is the same as in Figure 4.36.

4.6.3 CTAB/Arginine Solutions

To study the effect that arginine has on the self-assembly of CTAB surfactants, a simulation was carried out starting from a random configuration of CTAB and arginine dispersed in water with a surfactant concentration of 8 wt%. A half-cubic box type was used with full simulation details given in Table 4.3. The final configuration after 6 µs of simulation time is given in Figure 4.45. The behaviour of the surfactant is very similar to that of the system with no arginine present (see Figure 4.32) suggesting that the presence of arginine does not influence the self-assembly process when silicates are not present, which can be explained by the weak interaction between arginine and the surfactant identified in single micelle simulations.

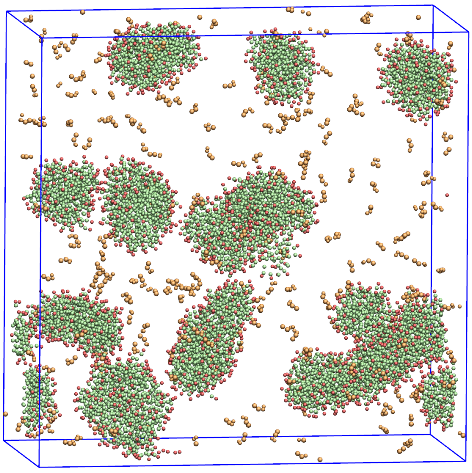

Figure 4.45: Simulation snapshots of the final configuration after 6 µs starting from a random configuration, for self-assembly simulations with CTAB surfactant and arginine using a half-cubic box. CTAB headgroups are shown in red, tails shown in green and arginine is shown in orange. Bromide counter-ions and water are hidden for clarity.

4.6.4 CTAB/PEHA Solutions

Initially, a self-assembly simulation was carried out for a system containing only CTAB and neutral PEHA molecules (with bromide counter-ions to balance charge), with a surfactant concentration of 1.5 wt%. A cubic box was used, full simulation details are given in Table 4.3. The final configuration after 3 µs of simulation time is shown in Figure 4.46. The surfactant behaviour does not seem to be affected by the presence of neutral PEHA and forms spherical micelles. This suggests that the self-assembly of the surfactant is not affected by PEHA at high pH when silica species are not present, which can be explained by weak interactions between PEHA species and surfactant that were identified in single micelle simulations.

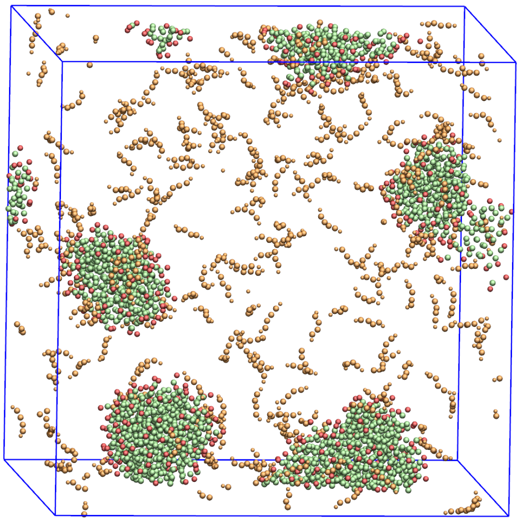

Figure 4.46: Simulation snapshots of the final configuration after 3 µs starting from a random configuration, for self-assembly simulations with CTAB surfactant and neutral PEHA molecules using a cubic box. CTAB headgroups are shown in red, tails shown in green and PEHA is shown in orange. Bromide counter-ions and water are hidden for clarity.

4.7 Conclusions

In this Chapter, a coarse-grained model that is able to describe the early stages of ordered mesoporous silica synthesis is presented, capable of accurately representing the interactions of silica precursor species (monomeric and oligomeric silicates with a variety of sizes and charge states) in the presence of templating surfactant species, and the bio-inspired additives arginine and PEHA. This coarse-grained model is the first to be calibrated against the atomistic model of Jorge et al. which provides improved interactions that are validated against experimental data [12]. It is based on the Martini 3 force-field [13], which offers several advantages over previous coarse-grained models. While this model is calibrated based on interactions with the popular cationic surfactant, CTAB, it can readily be extended to include other surfactant species that are compatible with the Martini 3 framework, or by following the procedure for surfactant model development described here. The development of this model is supported by a robust multi-scale modelling methodology based on fitting parameters which employs a rational approach to determining appropriate interaction parameters between inorganic precursor and templating species. This will aid future model development for similar systems as well as indicating how manipulation of these parameters affects self-assembly behaviour. The effect of using different simulation box dimensions was also studied, showing that elongated and half-cubic box shapes were most useful for studying the self-assembly of HLC phases. In addition, the effectiveness of carrying out simple modifications to standard Martini 3 bead types when parameterising silica models was discussed.

Self-assembly simulations of pure CTAB solutions as well as CTAB/silica solutions yielded results in excellent agreement with available experimental data. In particular, the experimental dependence of the CTAB aggregation number with concentration is captured accurately by our CG model, while the silica model can describe the formation of hexagonal mesophases under conditions observed experimentally. Neutral silicate species were observed to have very little influence on the surfactant self-assembly process, in agreement with previous observations that the degree of order of OMS-like materials decreases as the pH decreases due to the reduction in the ability of silicates to balance the charge around surfactant micelles [11]. The bio-inspired additives arginine and PEHA were shown to have no significant influence on surfactant self-assembly behaviour, which can be attributed to their weak interactions with the surfactant. Anionic silica monomers, on the contrary, rapidly induced a sphere-to-rod transition in dilute surfactant solutions, again in agreement with experimental observations. Despite the fact that our new CG model for silica monomers (and, by implication, the atomistic model it was based on) is substantially more hydrophilic than previous models [74, 75, 148], this does not seem to affect the morphology or self-assembly mechanism of the worm-like micelles obtained in those solutions. Simulations of CTAB solutions with silica dimers and cubic octamers, representative of the early stages of OMS synthesis, confirmed the crucial role played by silica oligomers in promoting micelle aggregation into an ordered hexagonal array by acting as "bridges" between different micelles.

Chapter 5

Experimental and Computational Study of Bio-Inspired Routes to OMS

5.1 Introduction

Bio-inspired silica (BIS) is characterised by extremely mild synthesis conditions, which make it appealing from both an economical and environmental standpoint [7, 189]. BIS makes use of simple organic amine-based "additives" to precipitate porous silica and has been discussed further in Section 2.4. In contrast, ordered mesoporous silica (OMS) materials (e.g. MCM-41 [5], SBA-15 [6]) have incredibly narrow pore size distributions. This is due to their well-ordered porous network, formed from a surfactant liquid crystal template that self-assembles in solution during synthesis. However, achieving this highly ordered porous structure currently involves the use of much harsher synthesis conditions than those employed for BIS synthesis. In particular, a typical synthesis of MCM-41 involves a lengthy hydrothermal treatment step to increase the mesoscopic regularity of pores, which takes place at high temperatures (between 80 and 150 °C) making the process both time and energy intensive [1]. Only a handful of previous studies reported the synthesis of ordered MCM-41 materials at room temperature, but the evidence is somewhat contradictory. Lin et al. [190] used a "delayed neutralization" method, whereby acid was added after the silica precursor (sodium silicate) and surfactant were allowed to self-assemble at high pH. They obtained MCM-41 materials at room temperature, but achieving a high degree of order required prolonged ageing of the synthesis solution over a period of several days. Cai et al. [146] reported the formation of highly ordered MCM-41 at room temperature from tetra-ethyl orthosilicate (TEOS), but only in a very narrow window of pH values. Results from a later study, however, suggest that hydrothermal treatment is necessary to produce MCM-41 materials with a high degree of order, such that they show well resolved XRD peaks at reflection lines (110) and (200) [191]. Moreover, even in the study of Cai et al., synthesis times of at least 2 hours were required [146]. As such, the exact mechanisms by which well-ordered structures can be obtained and controlled without hydrothermal treatment remain unclear, and, at best, reaction times on the scale of hours are required.

BIS synthesis is much faster than OMS synthesis and takes place under milder conditions. For this reason, it was hypothesised that bio-inspired additives can be used to promote the formation of OMS under milder conditions than those typically utilised for OMS synthesis [1]. Preliminary work indicated that hexagonally ordered mesoporous silica could be formed in minutes at room temperature in the presence of arginine (see Section 1.1). Arginine was initially chosen due to its known importance in biological silica formation and its reported ability to accelerate bio-inspired silica synthesis [14, 15, 192]. However, the behaviour of the bio-inspired additive in this system, and its interactions with both templating surfactants and silica precursors, are not well understood from a mechanistic perspective.

In this Chapter, we attempt to elucidate the role of arginine in this system and understand if and how bio-inspired additives may aid the formation of well-ordered mesoporous silica materials under ambient conditions, with the goal of enabling a more sustainable and scalable synthesis approach for OMS that does not rely on an energy-intensive hydrothermal treatment step or a lengthy ageing period. A design of experiments (DoE) approach is taken to identify which conditions impact the synthesis and resultant material properties, focusing on material porosity and morphology at the mesoscale (2-50 nm) as proxies for its performance in potential applications. Attention is also given to factors that influence the scalability and economics of the synthesis, for example the material yield and the quantity of reagents required for synthesis [189].

The experimental work is supported by coarse-grained molecular dynamics simulations of the co-operative self-assembly of the surfactant and silica precursor species, which gives rise to the resulting structure of these materials. The computational modelling work in this chapter uses a coarse-grained model based on the Martini 3 framework, the development of which has been presented in the previous chapter. In this chapter, new insight is provided into how bio-inspired additives interact with silica and surfactants, and how these interactions can influence the onset of order in mesporous silica materials.

5.2 Methods

5.2.1 Synthesis of Mesoporous Silica

Learning from the synthesis of BIS, we adopted a synthesis method that is similar in spirit to the "delayed neutralization" approach of Lin et al. [190]. In a typical synthesis procedure, sodium metasilicate pentahydrate, $Na_2SiO_3{\cdot}5\,H_2O$ (Sigma Aldrich $\geq$ 95.0%), cetyltrimethylammonium bromide (CTAB, Sigma Aldrich $\geq$ 98%) and L-arginine (Sigma Aldrich 99%) were dissolved in 100 mL of deionised water in a 150 mL plastic tub, under constant stirring with a magnetic stirring rod at 800 rpm, at room temperature. The initial pH was measured to ensure the resulting solution had a stable pH $>$ 13, which was the case for all experiments carried out here. A solution of 1.0 M hydrochloric acid was then added rapidly to the mixture under constant stirring at 800 rpm to achieve the final desired pH (typically between 7 and 10) - we henceforth refer to this as simply the "pH", since it is one of our control variables. The pH was monitored using a pH probe throughout the reaction and maintained to within ± 0.05 of the synthesis pH after the initial addition of acid by dropwise addition of additional hydrochloric acid. Rapid precipitation was observed within seconds of acid addition, indicated by a visible increase in turbidity. The rapid rate of reaction may indicate that precipitation reaction kinetics could be limited by mixing. The mixture was left under stirring for 5 minutes, at which point it was transferred to 50 mL conical centrifuge tubes. These were centrifuged for 7 minutes at 5000 rpm and the supernatant was discarded. The solid white precipitate was re-suspended in deionized water and shaken vigorously in order to wash the precipitate. The suspension was then centrifuged again. This washing procedure was repeated 3 times for each sample, and the conductivity of the supernatant for each wash was measured each time using a handheld conductivity probe to ensure a significant reduction of salts present in the supernatant by the final wash, below the detectability limit of the probe. The precipitate was then dried in an oven at 60 °C for 48 hours. The dried sample was weighed, and then placed in a furnace in a heat-proof crucible for 6 hours at 550 °C, obtaining the final mesoporous silica product which was then weighed. A diagram illustrating the synthesis procedure is shown in Figure 5.1.

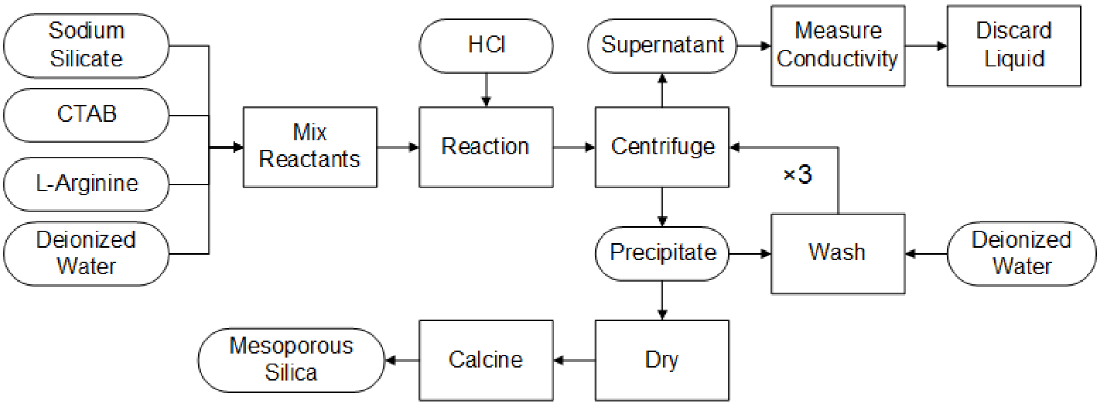

Figure 5.1: Flow diagram showing the typical procedure used for the synthesis of mesoporous silica with bio-inspired additives.

5.2.2 Design of Experiments

The design of experiments (DoE) involves systematically changing input parameters (factors) to study how this affects output variables (responses), allowing for an understanding of the relationship between these factors and responses to be obtained.

This procedure was applied to the synthesis of mesoporous silica following the method outlined in Section 5.2.1 to create a link between synthesis conditions and material properties. Initially, a two-level full factorial design was used, meaning that for each factor, two-levels are explored, and every combination of these factors is tested. Compared with an experimental design that modifies one factor at a time, this design has the advantage of being able to identify the effects of changing combinations of factors [132].

From prior work with bio-inspired silica [15] and surfactant-templated silica materials [22], four factors were initially identified as having potential importance in the synthesis system, giving 16 synthesis conditions in total for the initial two-level four-factor experimental design: concentration of the silica precursor ([Si]), silicon to amine molar ratio (Si:N), silicon to CTAB molar ratio (Si:CTAB), and final reaction pH. The silicon to amine ratio (Si:N) refers to the molar ratio of silicon atoms to amine groups in the bio-inspired additive, which has been shown to be important in directing bio-inspired silica synthesis [15, 57], and does not include the nitrogen in the ammonium group present in CTAB molecules. The final reaction pH refers to the pH following the addition of hydrochloric acid, which induces the precipitation of silica. The levels used in the two-level four-factor experiment design are given in Table 5.1 (Samples 1-1 through 1-16). These are compared with three samples from literature, the synthesis conditions of which are labelled A, B and C in Table 5.1. The first sample (A) chosen for comparison is the initial synthesis of MCM-41 by Beck et al. In this synthesis, a relatively high surfactant concentration was used (25 wt %) and hydrothermal treatment was carried out at 100 °C for 144 hours [5]. The second sample (B) is a synthesis of well-ordered MCM-41 at room temperature using a low surfactant concentration, presented by Cai et al.. This synthesis used TEOS as a silica precursor, and ammonia was used to control the synthesis pH. A minimum reaction time of 2 hours was used in this synthesis [146]. The third sample (C) is a synthesis of MCM-41 from sodium silicate. This synthesis used the same silica to surfactant ratio as Cai et al. but did not obtain very well ordered materials except after hydrothermal treatment was used, as indicated by reported XRD patterns. The sample chosen for comparison was the one synthesised at room temperature without hydrothermal treatment [191].

After the initial two-level four-factor study, further experiments were carried out to look in more detail at the responses of modifying particular factors on material properties. Full details of these experiments are also given in Table 5.1, including the effect of modifying the component ratios, Si:N and Si:CTAB (Samples 2-1 through 2-6); the effect of using alternative bio-inspired additives (Samples 3-1 through 3-5); the effect of modifying Si:N ratio and reaction time for a system with pentaethylenehexamine (PEHA, Sigma Aldrich technical grade) instead of arginine (Samples 4-1 through 4-7).

Table 5.1: Input parameters for synthesis of bio-inspired ordered mesoporous silica. The conditions of selected syntheses from literature (labelled A-C) are also included for comparison.

Sample No.	**[Si] (mM)**	**Additive**	**N per additive**	**Si:N**	**Si:CTAB**	**pH**	$t_{\mathbf{rxn}}$ **(min)**
A [5]	800	None	-	-	0.87	> 13	2880
B [146]	106	Ammonia	1	0.014	8	11.4	120
C [191]	106	None	-	-	8	11	120
Preliminary	100	Arginine	4	2	2	10	5
1-1	24	Arginine	4	0.10	0.40	7	5
1-2	112	Arginine	4	0.22	0.28	7	5
1-3	24	Arginine	4	0.10	4.00	7	5
1-4	112	Arginine	4	0.22	4.08	7	5
1-5	27	Arginine	4	5.00	0.45	7	5
1-6	128	Arginine	4	5.00	0.32	7	5
1-7	27	Arginine	4	5.00	4.50	7	5
1-8	126	Arginine	4	5.00	4.59	7	5
1-9	27	Arginine	4	0.10	0.45	10	5
1-10	100	Arginine	4	0.20	0.25	10	5
1-11	27	Arginine	4	0.10	4.50	10	5
1-12	112	Arginine	4	0.20	4.08	10	5
1-13	27	Arginine	4	5.00	0.45	10	5
1-14	120	Arginine	4	5.00	0.30	10	5
1-15	27	Arginine	4	5.00	4.50	10	5
1-16	126	Arginine	4	5.00	4.59	10	5
2-1	100	Arginine	4	2	2	10	5
2-2	100	Arginine	4	2	8	10	5
2-3	100	Arginine	4	2	16	10	5
2-4	100	Arginine	4	16	2	10	5
2-5	100	Arginine	4	16	8	10	5
2-6	100	Arginine	4	16	16	10	5
3-1	100	Arginine	4	2	2	10	5
3-2	100	Ammonia	1	2	2	10	5
3-3	100	PEHA	6	2	2	10	5
3-4	100	Propylamine	1	2	2	10	5
3-5	100	None	-	-	2	10	5
4-1	100	PEHA	6	0.333	8	10	5
4-2	100	PEHA	6	0.083	8	10	5
4-3	100	PEHA	6	0.056	8	10	5
4-4	100	None	-	-	8	10	5
4-5	100	PEHA	6	0.333	8	10	60
4-6	100	PEHA	6	0.083	8	10	60
4-7	100	None	-	-	8	10	60

5.2.3 Sample Analysis

After the synthesis was carried out following the procedure in Section 5.2.1, critical responses were measured. The critical responses identified and the analysis techniques used to identify them are summarised in Table 5.2. To identify whether any responses to changes in synthesis conditions were statistically significant, uncertainties were estimated based on repeat samples synthesised under the same conditions (described in Section 5.3.2).

Table 5.2: Measured responses to two-level four-factor experimental design and their respective analytical technique.

Response	**Variable**	**Unit**	**Uncertainty**	**Analysis Technique(s)**
Yield	Y	%	10	Weighing after calcination
Organic Content	-	%	5	Weight loss after calcination
BET Surface Area	S_{BET}	m^2g^{-1}	70	N_2 Adsorption (BET)
Pore Size Distribution	-	-	0.06	N_2 Adsorption (BJH Desorption)
Pore Volume	V_{pore}	cm^3g^{-1}	0.1	N_2 Adsorption (BJH Desorption)
Pore Size	d_{pore}	nm	0.1	N_2 Adsorption (BJH Desorption)
Diffraction Pattern	-	-	-	XRD
d_{100} spacing	d_{100}	nm	-	XRD
Pore Wall Thickness	t_{wall}	nm	0.1	XRD / N_2 Adsorption (BJH Desorption)
Order Parameter	I_{200}/I_{110}	-	0.1	XRD

The yield of silica is defined as the percentage of silica precursor that is converted into mesoporous silica product. Since the initial concentration of silicon is known, the yield can be calculated from the final mass of silica after calcination:

$$\text{Yield (\%)} = \frac{\left(\frac{m_{\text{SiO}_2}}{M_{\text{SiO}_2}}\right)}{C_{\text{Si}} \cdot V} \times 100 \tag{5.1}$$

where m_{SiO_2} is the mass of dried silica after calcination, M_{SiO_2} is the molecular weight of silica (60.02 g mol^{-1}), C_{Si} is the concentration of silicates in the reaction mixture and V is the reaction volume. It is assumed that dried samples contain no water after 48 hours of drying at 60°C, so the dried weight includes only precipitated silica, the bound surfactant template and any additive embedded within this structure. Since these species are completely removed by the calcination step, the organics content of the precipitate before calcination can be calculated.

$$\text{Organic Content (\%)} = \frac{m_{dry} - m_{\mathrm{SiO_2}}}{m_{dry}} \times 100 \tag{5.2}$$

where m_{dry} is the dry mass of silica before calcination.

N_2 adsorption measurements (at 77K) were taken using the Micromeritics Tristar II 3020. BET surface area was determined using the Brunauer-Emmett-Teller (BET) method [134] and following the procedure of Rouquerol et al. to improve consistency in surface area determination [135]. The pore size distribution was determined through the Barrett-Joyner-Halenda [136] method from desorption data, which can be used to determine total pore volume within a particular range of pore sizes in the mesoporous region. These methods are described in greater detail in Section 3.2.2. Pore volumes (V_{pore}) reported in this work were calculated by taking the cumulative pore volume between 1 and 10 nm as determined by BJH desorption. The average pore size (d_{pore}) was determined from the location of the primary peak of the pore size distribution.

Diffraction data was obtained using the Panalytical X'Pert^3 X-ray diffraction (XRD) system. The XRD method is described in further detail in Section 3.2.3. The d_{100} spacing, which relates to the inter-pore distance (a_0) for hexagonally ordered pores, can be determined from the location of the first XRD peak using Bragg's equation.

$$2d_{100}\sin(\theta) = n\lambda \tag{5.3}$$

a_0 can be determined from d_{100} for a hexagonal lattice:

$$a_0 = \frac{2d_{100}}{\sqrt{3}} \tag{5.4}$$

The inter-pore distance (a_0) can also be used in conjunction with the pore size (d_{pore}) to estimate the pore wall thickness (t_{wall}).

$$t_{wall} = a_0 - d_{pore} \tag{5.5}$$

A diagram showing the relevant dimensions reported in this work is shown in Figure 5.2.

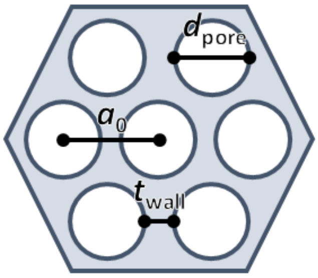

Figure 5.2: Diagram displaying the important dimensions describing a hexagonally ordered porous material.

In order to quantify the degree of structural ordering present in samples, an order parameter is devised, based on the relative XRD intensity of reflection lines (200) and (110). This procedure was previously used by Cai et al. in the characterisation of MCM-41 materials [146]. A ratio closer to 1 indicates a higher level of structural ordering as there is a proportional relationship between the two directions of the crystal structure. Where no peak at reflection line (200) is detectable by the software but a peak exists at reflection line (110), the order parameter I_{200}/I_{110} is considered to be 0, indicating a very low level of hexagonal ordering. To determine the order parameter I_{200}/I_{110} from literature data, the intensity of peaks I_{200} and I_{110} were measured graphically and the baseline reflection was subtracted (see Figures 5.3 and 5.4). For samples characterised in this work, the intensity of each peak, I_{200} and I_{110}, is taken as the net height of these peaks as reported by the Panalytical Data Viewer software version 1.9a. An example of a typical XRD reflection pattern for a hexagonally ordered MCM-41 type material can be found in Chapter 3, Figure 3.6, with the expected reflection lines labelled.

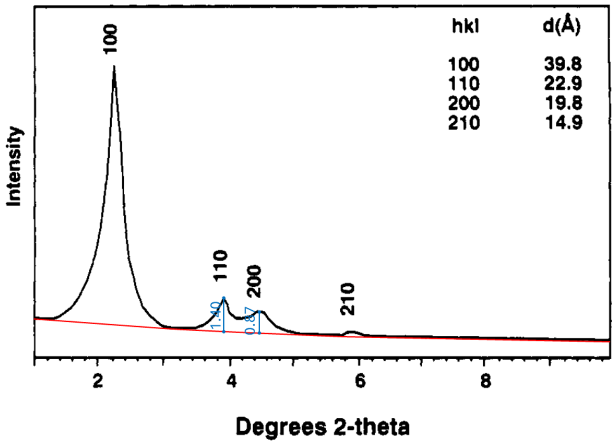

Figure 5.3: XRD pattern reported by Beck et al. in the original synthesis of MCM-41, taken from [5]. The red line indicates the baseline reflection from which the relative intensities of peaks (110) and (200) were measured (labelled in blue).

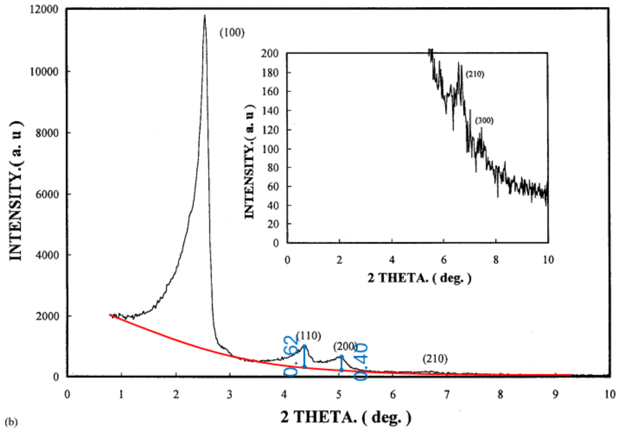

Figure 5.4: XRD pattern reported by Cai et al. in their synthesis of MCM-41, taken from [146] for the most well-ordered sample, produced at room temperature. The red line indicates the baseline reflection from which the relative intensities of peaks (110) and (200) were measured (labelled in blue).

5.2.4 Simulation Details

All computational work was carried out using the GROMACS software package, which allows molecular dynamics (MD) simulations to be carried out with high computational efficiency due to the use of state-of-the-art algorithmic optimizations and parallelization [164, 165]. The general purpose programming language Python 3 [166] was used to aid in setting up and running simulations. For analysis of simulation data, the built-in GROMACS analysis tools were used as well as the MDAnalysis library for Python [167, 168]. Graphs were generated using the Matplotlib library for Python [169].

To better understand the experimental findings, coarse-grained MD was used to study the formation of the silica/surfactant mesophase under different conditions. This self-assembly occurs in solution during the early stages of OMS synthesis (i.e. before addition of acid), at high pH (≥ 13). The CG models for silicates and CTAB and the bio-inspired additives arginine and PEHA under high pH conditions (at which self-assembly takes place) were developed and validated in the previous chapter, consistent with the Martini 3 framework [13]. After setting up the initial configuration, energy minimisation was carried out using the steepest-descent algorithm. NVT equilibration was carried out using a velocity-rescaling thermostat [115] with a 2 fs time step. NpT equilibration was carried out using the C-rescale barostat [115], also with a 2 fs time step. Production MD runs used a timestep of 30 fs unless otherwise stated, using the leap-frog algorithm. For temperature control, a velocity-rescaling thermostat was used and the pressure was controlled with the Parrinello-Rahman barostat [120, 121]. For Lennard-Jones terms, the Verlet cutoff scheme [110] was used with a cutoff value of 1.1 nm. Electrostatics were accounted for using reaction field with a cutoff value of 1.1 nm and a relative permittivity of $\varepsilon_r = 15$.

The effect of Si:CTAB ratio and pH on self-assembly was studied initially, as these factors were identified as having the greatest impact on the degree of order of the materials that were synthesised experimentally. For these simulations, arginine was neglected for simplicity. Self-assembly simulations were carried out at Si:CTAB ratios between 0.5 and 16, and pH values of 7, 10 and 13. A “slab” shaped rectangular box arrangement was adopted with a single short dimension (L_z) and two longer box dimensions (L_x and L_y). This short dimension allows for phase separation to occur while using fewer surfactant molecules and thus limiting the overall size of simulations, preventing them from becoming too computationally demanding. A fixed number of surfactant molecules are used for each simulation ($N_{CTAB} = 1000$) and the total number of silicon atoms are set to achieve the desired Si:CTAB ratio. The speciation of silica species represents an experimentally realistic population at pH 13, based on the work of Firouzi et al. [43], of 25% monomers and 75% cubic octamers.

To account for the deprotonation of hydroxyl groups of silica oligomers at varying pH, a series of pKa values for each subsequent deprotonation needs to be determined. Each pKa value corresponds to the deprotonation of an exposed hydroxyl group bonded to a different silicon atom. The number of pKa values required is therefore equal to the number of silicon atoms in the oligomer (or in the case of the coarse-grained model, the number of silica beads). Note that this ignores the possibility of multiple hydroxyl groups bonded to a single silicon atoms becoming deprotonated, which can occur in small oligomers. However, this only occurs at extremely high pH values [17], and therefore for simplicity this is neglected in this model.

Only very limited experimental data is available for the pKa values of silicate species. The most comprehensive review on the topic gives the required pKa values only for monomers and dimers [17]. However, the pKa value of a silica surface (that is, the surface of a significantly condensed silica network) is also known [18]. Therefore, an empirical relationship can be devised between the number of silicate units in an oligomer and the pKa value of the first deprotonation. A simple functional form is chosen which has a horizontal asymptote at 6.8, meaning that at large values of silica units (i.e. corresponding to a silica particle), the pKa is equal to the pKa of a silica surface. The equation takes the form:

$$pKa = \frac{a}{b \times N_{Si} + 1} + 1.7(i-1) + 6.8 \tag{5.6}$$

where N_{Si} is the number of silicon units in the oligomer, i corresponds to the degree of deprotonation (i.e. $i = 1$ gives the pKa of the first deprotonation, $i = 2$ gives the pKa of the second deprotonation and so on). The values of a and b are found by fitting to the known values for the first deprotonation of silica monomers and dimers, which are 9.5 and 9.0, respectively [17], and found to be $a = 3.49412$ and $b = 0.294118$ by non-linear least squares fitting. The prefactor before the term i is the difference in pKa between the first and second deprotonation in dimers, and it is assumed that this difference is maintained for subsequent deprotonations in higher oligomers. The pKa values determined by this method for silica oligomers containing up to 8 silicon atoms (i.e. octamers) are given in Table 5.3 and Figure 5.5.

It is important to note that this model only allows for a single negative charge per silicon atom, including the case of monomeric silicic acid. Based on pKa values reported in literature [17], a significant proportion of monomeric silicic acid will be present as doubly charged at pH 13, the initial pH of the system in this work, however, this is neglected for simplicity under the assumption that silicic acid is primarily present as higher oligomers [43].

Table 5.3: Table of pKa values for silica oligomers with up to 8 silicon units. N_{Si} gives the number of silicon units while i corresponds to the degree of deprotonation. pKa values are calculated from Eq. 5.6.

		i							
		1	2	3	4	5	6	7	8
N_{Si}	1	9.50	-	-	-	-	-	-	-
	2	9.00	10.70	-	-	-	-	-	-
	3	8.68	10.38	12.08	-	-	-	-	-
	4	8.47	10.17	11.87	13.57	-	-	-	-
	5	8.30	10.00	11.70	13.40	15.10	-	-	-
	6	8.16	9.86	11.56	13.26	14.96	16.66	-	-
	7	8.05	9.75	11.45	13.15	14.85	16.55	18.25	-
	8	7.95	9.65	11.35	13.05	14.75	16.45	18.15	19.85

This model can be applied to approximate the proportion of silicate species of each degree of deprotonation for a given system pH. This is shown in Figure 5.6 for silica octamers between pH 7 and 15.

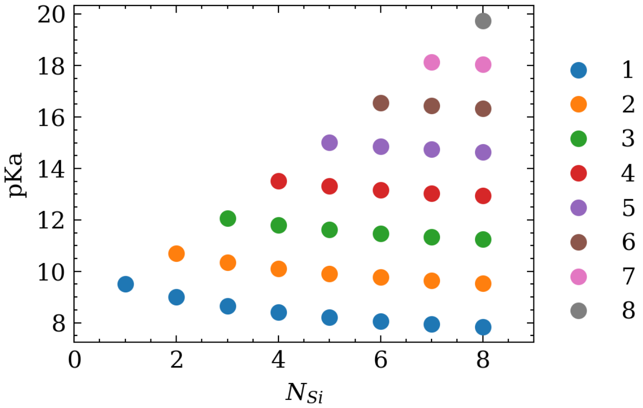

Figure 5.5: Estimated pKa values for silica oligomers with up to 8 silicon units. The legend labels refer to the value of i, which is described by Eq.5.6.

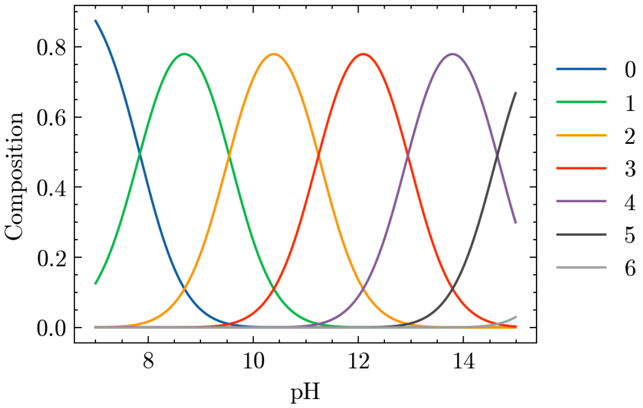

Figure 5.6: Charge composition for silica octamers between pH 7 and 15. The legend labels refer to the total (negative) molecular charge.

The charge of silica species is calculated based on system pH, following the method described above. Charged states with a low proportion of species (less than 5%) are disregarded and the total population is adjusted proportionally. The populations of charged silica species used in these simulations are summarised in Table 5.4. For Si:CTAB ratios between 2 and 16, the number of water molecules is adjusted to achieve a constant concentration of silica species. For Si:CTAB ratios of 0.5 to 1, a silica concentration 4 times lower is used in order to prevent the simulation volume from becoming too small, leading to low values of box dimensions x and y, which allows the concentrated surfactant phase to bridge across these dimensions (see Section 4.6.2.1 for further discussion of box dimensions). This lower silica concentration is not expected to affect self-assembly behaviour, as at low Si:CTAB ratios the silicate species become concentrated in the surfactant rich region of the simulation box, regardless of the bulk concentration of silica. In order to speed up phase separation and equilibration of the system, the initial configuration concentrates all surfactant species within one area of the simulation box, while other species are randomly distributed throughout the entire box. After initial equilibration, calculations are carried out for 3 µs of simulation time.

Table 5.4: Population of charge states for silica octamers and monomers used in simulations to represent different system pH.

pH	% Octamer Charge					% Monomer Charge	
	0	-1	-2	-3	-4	0	-1
13	0	0	0	50	50	0	100
10	0	26	74	0	0	76	24
7	87	13	0	0	0	100	0

Self-assembly simulations were also carried out in the presence of the bio-inspired additives. For these simulations, only anionic silica dimers were used, as these have been shown to be sufficient to permit the formation of the hexagonal liquid crystal phase [77], and the interactions of the additives with the silica/surfactant interface are not expected to be significantly different when a more realistic population of silica species (i.e. cubic octamers and monomers) is used. These simulations started from a random configuration of CTAB, arginine/PEHA and silica dimers in water, using an elongated simulation box to speed up phase separation and the formation of a HLC phase as in the work of Pérez-Sánchez et al. [77]. Full simulation details are given in Tables 5.5 and 5.6.

Table 5.5: Details of coarse-grained simulations carried out to investigate the effect of Si:CTAB ratio and pH on self-assembly. N is the number of molecules of each species (denoted by the subscript) present in the simulation. Note that each water bead represents 4 water molecules. L is the box length in the x, y and z direction. t is the total simulation time.

Si:CTAB	pH	Box Type	N_{CTAB}	N_{SN1}	N_{SI1}	N_{SN8c}	$N_{SI8c(1-)}$	$N_{SI8c(2-)}$	$N_{SI8c(3-)}$	$N_{SI8c(4-)}$	N_{Br}	N_{TMA}	N_{Water}	L_x (nm)	L_y (nm)	L_z (nm)	t (µs)
0.5	13	Slab	1000	0	20	0	0	0	30	30	770	0	26000	22.4	22.4	7.5	3.0
1	13	Slab	1000	0	40	0	0	0	60	60	540	0	52000	31.6	31.6	6.9	3.0
2	13	Slab	1000	0	80	0	0	0	120	120	80	0	26000	22.4	22.4	7.5	3.0
4	13	Slab	1000	0	160	0	0	0	240	240	0	840	52000	31.6	31.6	7.1	3.0
8	13	Slab	1000	0	320	0	0	0	480	480	0	2680	104000	44.7	44.7	6.8	3.0
16	13	Slab	1000	0	640	0	0	0	960	960	0	6360	208000	63.3	63.3	6.7	3.0
2	10	Slab	1000	61	19	0	62	178	0	0	563	0	26000	22.4	22.4	6.8	3.0
4	10	Slab	1000	122	38	0	125	355	0	0	127	0	52000	31.6	31.6	7.1	3.0
8	10	Slab	1000	243	77	0	250	710	0	0	0	747	104000	44.7	44.7	6.8	3.0
16	10	Slab	1000	486	154	0	499	1421	0	0	0	2495	208000	63.3	63.3	6.7	3.0
2	7	Slab	1000	80	0	209	31	0	0	0	969	0	26000	22.4	22.4	6.8	3.0
4	7	Slab	1000	160	0	418	62	0	0	0	938	0	52000	31.6	31.6	7.1	3.0
8	7	Slab	1000	320	0	835	125	0	0	0	875	0	104000	44.7	44.7	6.8	3.0
16	7	Slab	1000	640	0	1670	250	0	0	0	750	0	208000	63.3	63.3	6.6	3.0

Table 5.6: Details of coarse-grained simulations carried out with bio-inspired additives. N is the number of molecules of each species (denoted by the subscript) present in the simulation. Note that each water bead represents 4 water molecules. L is the box length in the x, y and z direction. t is the total simulation time.

Simulation	Box Type	N_{CTAB}	N_{SI2}	N_{Arg}	N_{PEHA}	N_{Water}	L_x (nm)	L_y (nm)	L_z (nm)	t (µs)
SI2	Elongated	1000	500	0	0	10000	8.2	8.2	27.3	6.0
Arg + SI2	Elongated	1000	500	250	0	10000	8.3	8.3	27.5	6.0
PEHA + SI2	Elongated	1000	500	0	250	13000	8.8	8.8	29.3	6.0

5.3 Results

Full tables of all results and plots of adsorption isotherms, XRD diffraction patterns and pore size distributions obtained in experimental work can be found in Appendix A. In this section, the key results are discussed alongside supporting simulation results.

5.3.1 Preliminary Sample

The characterisation results for a material synthesised following the method described in Section 5.2.1 using arginine as an additive are shown in Figure 5.7. The conditions for this synthesis were; [Si] = 100 mM, [Si:N] = 2, Si:CTAB = 2, pH = 10, t_{rxn} = 5 min. The TEM imaging shows that particles are hexagonally ordered, and this is supported by XRD, which shows three well-resolved peaks (100), (110) and (200) that indicate a hexagonal arrangement of pores. The sample possesses a high BET surface area of 1149 m^2 g^{-1} and pore volume of 0.789 cm^3 g^{-1}. The pore size distribution is relatively narrow with a mean pore diameter of 2.18 nm.

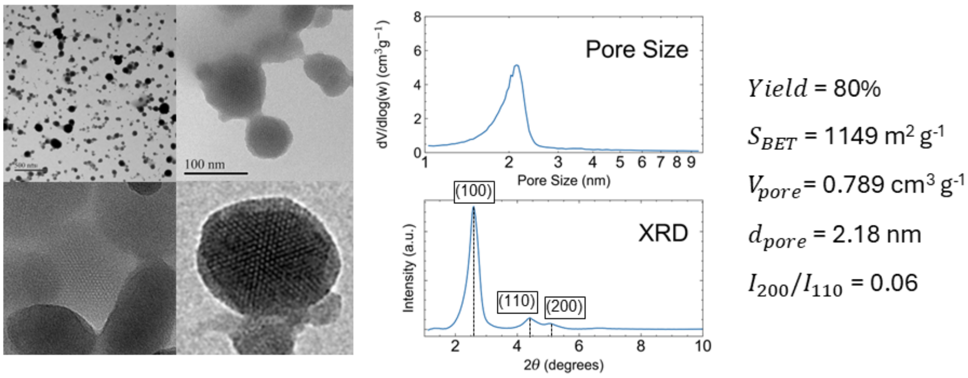

Figure 5.7: Characterization results for representative OMS samples produced using our synthesis method. TEM imaging is shown on the left, BJH pore size distribution (top) and XRD reflection patterns (bottom) are shown in the middle, and a summary of the yield, BET surface area, pore volume, mean pore diameter and order parameter I_{200}/I_{110} is shown on the right. On the XRD graph, the reflection lines (100), (110) and (200) are labelled. TEM images shown are for the preliminary sample while the remainder of the results are for Sample 3-1, which was synthesised under the same conditions.

To investigate the effect of the multiple synthesis parameters in more detail, we carried out an initial two-level four-factor experimental design, the conditions of which are shown in Table 5.1 (Samples 1-1 through 1-16). A plot showing the parameter space covered by this design is shown in Figure 5.8, together with the parameters of the preliminary experiment. Each factor has two-levels, one low and one high value, and expands the parameter space from the original sample in all directions. We now examine the effect of each synthesis parameter separately.

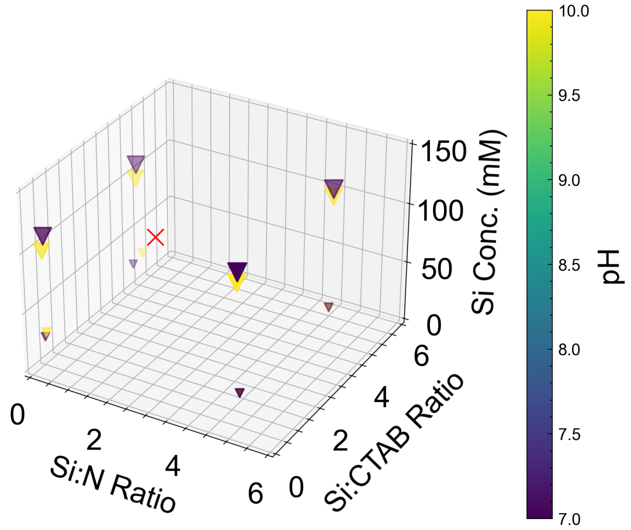

Figure 5.8: Parameter space covered by the two-level four-factor experimental design detailed in Table 5.1. The preliminary experiment is shown as a red cross. Symbol size is proportional to silicate concentration.

5.3.2 Uncertainty Analysis

To estimate the uncertainty in results for yield, organic content and material properties of samples in this work, the values obtained for two sets of two samples that were synthesised under the same conditions were compared to give an approximate expected range of results. The first set of samples are 2-1 and 3-1, which were synthesised under the same conditions (see Table 5.1 of the main paper). The second set of samples (R-1 and R-2) were synthesised under the following conditions: [Si] = 100 mM, Si:N = 2, Si:CTAB = 2, pH = 10.8. For this second set of results, only gas adsorption results were available. The estimated uncertainty for each property is given in the final column of Table 5.7, which is estimated based on the range of results for both sets of samples (where available). Although a more rigorous analysis, based on multiple repeat experiments would have been desirable, we believe the vaues in Table 5.7 provide a conservative estimate of the real experimental uncertainty. Results were considered statistically significant when the p-value was less than 0.05, and error bars on graphs represent the 95 % confidence interval.

Table 5.7: Summary of differences in yields, organic contents and material properties obtained for repeat samples synthesised under the same conditions.

Parameter	**R-1**	**R-2**	**Δ**	**2-1**	**3-1**	**Δ**	**Estimated Uncertainty (±)**
Yield (%)	-	-	-	87	80	7	10
Organic Content (%)	-	-	-	56	59	3	5
BET Surface Area (m^2 g^{-1})	1211	1277	66	1159	1149	10	70
Pore Volume (cm^3 g^{-1})	0.958	0.952	0.006	0.843	0.789	0.054	0.06
Pore Diameter (nm)	2.31	2.21	0.1	2.13	2.18	0.05	0.1
Wall Thickness (nm)	-	-	-	1.31	1.21	0.1	0.1
Order Parameter	-	-	-	0.12	0.06	0.06	0.1

5.3.3 Silica Precursor Concentration and Final Synthesis pH

Although not commonly reported in OMS synthesis studies, the yield is a crucial variable for scale-up, strongly influencing the economic viability of the material manufacturing process. Yield results for the screening experiments are summarized in Table 5.8, while Figure 5.9 shows the dependence of yield on both silica concentration and pH (notice that, as explained in section 5.2.1, this is the final synthesis pH). At low silica precursor concentration ($<$ 30 mM), the yield of all samples synthesised at pH 10 is consistently higher than samples synthesised at pH 7. At high silica precursor concentration ($>$ 100 mM) samples showed much higher yields than low concentration samples, and the dependence on pH was no longer observed. A majority of samples produced at the higher silica precursor concentrations showed high yields of over 75%, suggesting that a large amount of silica precursor present in the system is precipitated in the solid product. The Si:N ratio and Si:CTAB ratio did not appear to have any strong influence on yield.

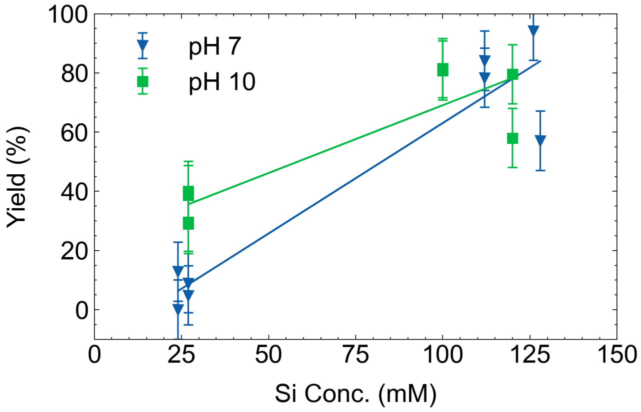

Figure 5.9: Dependence of yield on silica concentration and pH for all samples produced in the two-level four-factor factorial design.

These results clearly suggest that a higher silica concentration is favourable to improve the overall yield of the synthesis, which may be explained by faster reaction kinetics due to the increased concentration of silicate oligomers. The reduced yield at low silica concentration and pH 7 can be explained by the fact that the proportion of charged silicates will be much lower at pH 7 than pH 10, with a significant proportion of silicates being present as uncharged molecules [17]. These neutral silicate species will react to form small colloidal silica particles rather than being attracted to the surfactant mesophase [19]. These colloidal particles, which remain suspended, are then lost during centrifugation as they cannot be easily separated from water. At pH 10, a higher proportion of the silicate oligomers are charged and therefore are strongly attracted to the surfactant interface, which improves yield. This effect is reduced at higher silica concentrations, possibly due to the abundance of silicate species which could favour the Ostwald ripening process, causing small silica particles to dissolve and provide material for the growth of larger MCM-41 particles.

A summary of the porosity data is also shown in Table 5.8, while the corresponding adsorption isotherms, pore size distributions (PSD) and X-ray diffraction (XRD) spectra for each sample are provided in Appendix A (Figures A.1 and A.5). Note that samples synthesised at low concentration are not included because the sample mass obtained was too low for reliable characterisation by N_2 adsorption and XRD. Since the focus of this investigation was to identify possible "green" synthesis routes for OMS, the samples synthesised at low silica concentration are not of particular interest due to their low yield, and were disregarded from further discussion.

Table 5.8: Summary of yield and porosity data for two-level four-factor screening samples that were characterized by N_2 adsorption and XRD. The variables are fully described in Section 5.2.3. Comparison is made to available material properties for MCM-41 samples from literature (Samples A, B and C).

Sample No.	**Yield (%)**	$S_{\mathbf{BET}}$ **(m^2 g^{-1})**	$V_{\mathbf{pore}}$ **(cm^3 g^{-1})**	$d_{\mathbf{pore}}$ **(nm)**	$d_{\mathbf{100}}$ **(nm)**	$a_{\mathbf{0}}$ **(nm)**	$t_{\mathbf{wall}}$ **(nm)**	$I_{\mathbf{200}}$ **/$\mathbf{I_{110}}$**
A [5, 26]	-	1040	0.79	4.00	3.98	4.60	0.60	0.62
B [146]	-	-	-	-	3.48	4.02	-	0.65
C [191]	-	1312	0.86	3.14	3.05	3.52	0.38	0.00
1-2	78	1120	0.906	2.48	4.03	4.65	2.17	0.00
1-4	84	1005	0.828	2.45	3.88	4.48	2.03	0.28
1-6	57	970	0.721	2.51	3.98	4.60	2.09	0.00
1-8	94	1030	0.839	2.30	3.81	4.40	2.10	0.27
1-10	82	1181	0.966	2.63	3.80	4.39	1.76	0.00
1-12	81	1259	0.834	2.12	3.50	4.04	1.92	0.06
1-14	80	1217	1.003	2.55	3.82	4.41	1.86	0.04
1-16	58	1210	0.850	2.14	3.68	4.25	2.11	0.08

According to the extended IUPAC classifications [133], all samples with the exception of Samples 1-12 and 1-16 exhibit Type IV(a) behaviour (Figure A.1): mono and multilayer adsorption plus capillary condensation [193], which is typical of mesoporous materials [194], with a hysteresis loop indicating irreversible adsorption. However, the hysteresis effect is not strong, indicating small mesopores close to or below the critical width (< 4 nm). Samples 1-12 and 1-16 show Type IV(b) isotherms, indicating mesopores with dimensions much smaller than the critical width. The average pore sizes d_{pore}, which are also reported in Table 5.8, confirm these observations. Most PSDs (Figure A.5) show a relatively narrow peak centered around 2-2.5 nm, indicating that those samples contain mesopores with a regular size.

The BET surface area for all samples was high (> 970 m^2 g^{-1}) indicating a high level of porosity. This is comparable to the value of 1070 m^2 g^{-1} reported in the initial discovery of MCM-41, which was synthesised with a hydrothermal treatment step [5].

Surface area was most strongly dependent on synthesis pH, with samples synthesised at pH 10 having a surface area that was, on average, 186 m^2 g^{-1} greater than samples synthesised at pH 7 (see Figure 5.10), which is statistically significant. While the pore volume also seems to be slightly higher at pH 10, this is within the estimated statistical uncertainty (Figure 5.11).

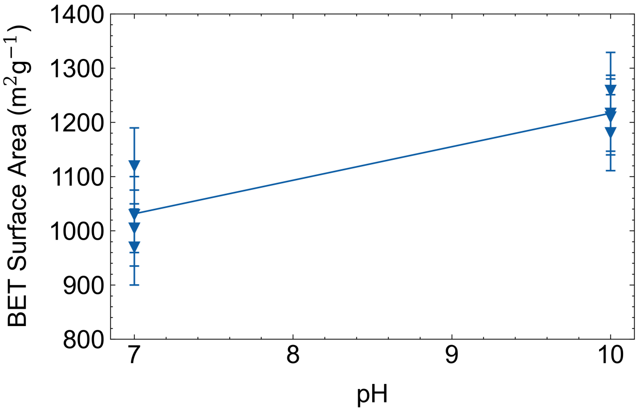

Figure 5.10: Dependence of BET surface area on pH. The line is a guide to the eye.

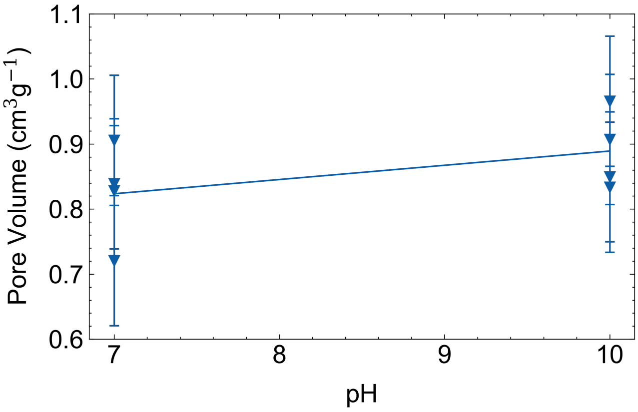

Figure 5.11: Dependence of pore volume on pH. The line is a guide to the eye.

All samples showed a well-resolved XRD peak at approximately $2\theta = 2°$(Figure A.5), corresponding to the reflection line (100) and indicating the presence of an ordered hexagonal structure. Two further peaks can be seen between $2\theta =$ 4-5°, which correspond to the reflection lines (110) and (200). The intensity of these lines indicates a well-ordered hexagonal pore geometry for these materials [195]. All samples possess a discernable peak at reflection line (110), however only five of the samples (Samples 1-4, 1-8, 1-12, 1-14 and 1-16) possess a clear peak corresponding to reflection line (200). This suggests that the degree of structural ordering of the remaining samples (Samples 1-2, 1-6 and 1-10) is poor. This finding is in agreement with the pore size distributions generated from N_2 adsorption isotherms (Figure A.5), suggesting that a high Si:CTAB ratio promotes the formation of a more well-ordered hexagonal structure than when a low Si:CTAB ratio is used. The samples synthesised using both a high Si:CTAB ratio and a pH of 7 had the highest order parameter by a significant margin. This may be attributed to the faster reaction rate of silica condensation at pH 7 versus pH 10, which allows the hexagonal mesophase formed at high pH to become "locked in" as suggested by computational studies of mesoporous silica synthesis [9], a point to which we will return later in this chapter. It also indicates that, while samples synthesised at both pH values have comparable pore size distributions, the samples synthesised at pH 7 possess a higher degree of order despite having lower surface area and pore volumes, suggesting that there is a trade-off between achieving high surface area and a high degree of order, and that the surface area of the material is not strongly dependent on the level of ordering of pores.

The material properties of samples obtained by this synthesis procedure are compared with selected MCM-41 samples from literature (Samples A, B and C in Table 5.8). Note that no gas adsorption data was provided by Cai et al. (Sample B) preventing comparison of some material properties. Materials synthesised in this work showed similar BET surface areas and pore volumes when compared to samples A and C. The pore diameters of samples synthesised in this work are smaller than reported in samples A and C, while the pore wall thickness is much larger. Thick pore walls were also observed in the work of Lin et al. [190], which was attributed to the "delayed neutralization" procedure, in which the self-assembly of the material takes place at high pH, prior to addition of an acid, which brings the pH to a value in which silica condensation takes place. However, Lin et al. did not observe ordered materials at reaction times of 30 minutes, with samples requiring several days of ageing in order to achieve well-resolved XRD peaks characteristic of hexagonal ordering. The reason that ordered materials were obtained without ageing in this work may be due to the rapid addition of acid, which is added in a single step rather than being added slowly. This rapid addition of acid may allow the highly ordered structure to be more effectively locked in before disorganisation of the mesophase can occur.

The largest difference from literature samples is observed in the order parameter I_{200}/I_{110}. All samples synthesised in this two-level four-factor screening possess a lower order parameter than sample A, which was synthesised using hydrothermal treatment. However, two of the samples synthesised by this method, samples 1-4 and 1-8, possess significantly higher order parameters than sample C, which was synthesised from sodium silicate without hydrothermal treatment. This demonstrates that a high level of structural ordering can be obtained without the need for hydrothermal treatment by modification of the synthesis method. The key difference is that the reaction pH is achieved by first obtaining a high pH mixture, and then rapidly adding acid to induce precipitation of the porous silica mixture. As discussed by Lin et al. [190], this pH control method helps to maintain the well-ordered structure that forms at high pH throughout the synthesis step. Sample B, which was synthesised at room temperature using a low surfactant concentration, has a higher degree of order than the samples obtained in our DoE study. However, this was achieved through manipulation of the Si:CTAB ratio, which is investigated further in Section 5.3.5. Sample B also had a significantly longer reaction time of 2 hours, while the samples presented here were precipitated in just 5 minutes. None of the literature synthesis studies compared here presented yield values, which are rarely reported in material synthesis despite being critical for scale-up.

5.3.4 Si to N Ratio

In the two-level four-factor screening investigation, changes in the Si:N ratio, at least within the examined range, did not produce any noticeable changes in the responses examined, either in structural properties or yield. This was somewhat surprising, and casts some doubt on the role of the chosen bio-inspired additive, arginine, for promoting the rapid formation of ordered silica materials under ambient conditions. To investigate this further, additional experiments were carried out with different Si:N ratios at the high end of the range, as well as a "control" experiment without any additive - i.e. with a Si:N ratio of infinity. The Si:CTAB ratio was also varied in this new set of experiments, in order to study the effect of that parameter in more detail (see Section 5.3.5). The synthesis procedure is the same as was laid out in Section 5.2.1, and the silica concentration and synthesis pH were kept fixed at 100 mM and 10, respectively. The synthesis conditions used in this investigation are shown in Table 5.1 (Samples 2-1 through 2-6).

The yield results and porosity data are summarised in Table 5.9 (see also Appendix A, Figure A.2 for the nitrogen adsorption isotherms). The yield seems to be virtually independent of the Si:N ratio, and no strong correlations were found between that factor and BET surface area, pore volume, pore size, d_{100} spacing or wall thickness. This confirms the conclusion of the screening study, and suggests that the presence of arginine does not play a major role in controlling the structural properties of the material. More importantly, it also seems to have no effect on the promotion of order within the pore network, as observed by comparing the pore size distributions and XRD spectra (see Figure 5.12) for these samples. In fact, it is quite remarkable that the sample synthesised without any bio-inspired additive also produces mesoporous silica with a high degree of order.

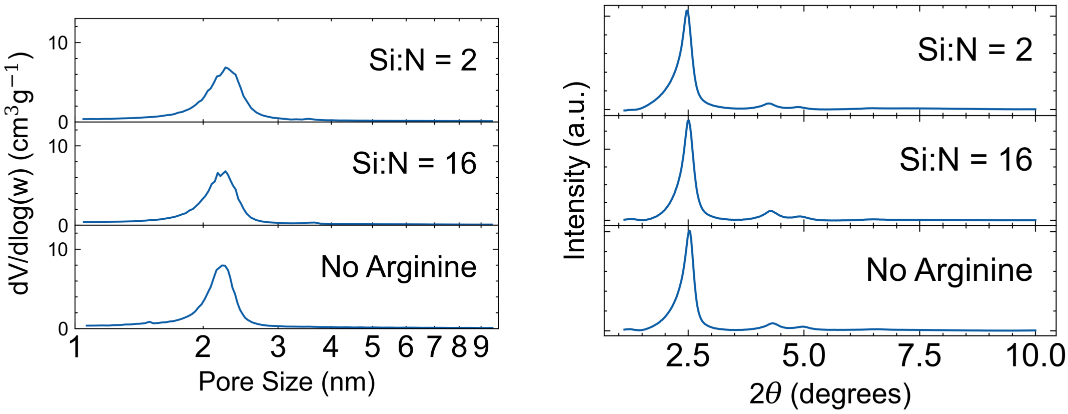

Figure 5.12: Pore size distributions (left) and XRD data (right) for selected samples with varying quantities of arginine. For XRD data, baseline intensity was removed manually to allow for easier comparison between peaks.

Table 5.9: Summary of yield and porosity data for component ratio investigation samples that were characterized by N_2 adsorption and XRD. The variables are fully described in Section 5.2.3.

Sample No.	**Yield (%)**	$\mathbf{S_{BET}}$ $\mathbf{(m^2\ g^{-1})}$	$\mathbf{V_{pore}}$ $\mathbf{(cm^3\ g^{-1})}$	$\mathbf{d_{pore}}$ **(nm)**	$\mathbf{t_{wall}}$ **(nm)**	$\mathbf{I_{200}/I_{110}}$
2-1	87	1259	0.971	2.31	1.80	0.12
2-2	47	1165	0.841	2.15	1.78	0.46
2-3	16	1159	0.843	2.13	1.84	0.00
2-4	91	1193	0.857	2.22	1.84	0.11
2-5	39	1144	0.824	2.14	1.82	0.50
2-6	17	1194	0.898	2.25	1.76	0.07

In order to understand why arginine does not impact the structure of materials formed in this synthesis, a coarse-grained MD simulation of the self-assembly of the silica/surfactant mesophase was carried out with arginine present. The final configuration after 6 µs of simulation time is shown in Figure 5.13b. The surfactant can clearly be seen to adopt a HLC arrangement, identical to the behaviour exhibited in a system containing CTAB and silica dimers where arginine is not present [77]. This suggests that the presence of arginine does not affect the silica-surfactant mesophase formation.

A snapshot of a cross section of the simulation box showing only arginine and surfactant headgroup beads is shown in Figure 5.13c. From this snapshot, it is clear that arginine primarily inhabits the bulk water region, with only a small number of arginine molecules being present within the surfactant-rich region. This can be attributed to weak interaction of arginine with the silica-surfactant interface. This is further evidenced in Figure 5.13d, where the relative density of arginine approximately follows the relative density of water, with high relative density in the bulk water and very low relative density in the surfactant rich region. This may explain why incorporating arginine into OMS synthesis does not affect the properties of the material produced. Since the arginine primarily inhabits the bulk water, it is likely to be excluded from the self-assembled surfactant template. However, given the previous reports on the interfacial interactions and catalytic effects of arginine in silica formation [14, 15, 192], results reported herein on the self-assembly do not rule out arginine's potential role in catalysing the early stages of silicic acid condensation. We aim to address this in future work using *in situ* measurements of chemical kinetics coupled with simulations of the reactions using reactive models for silica condensation [92].

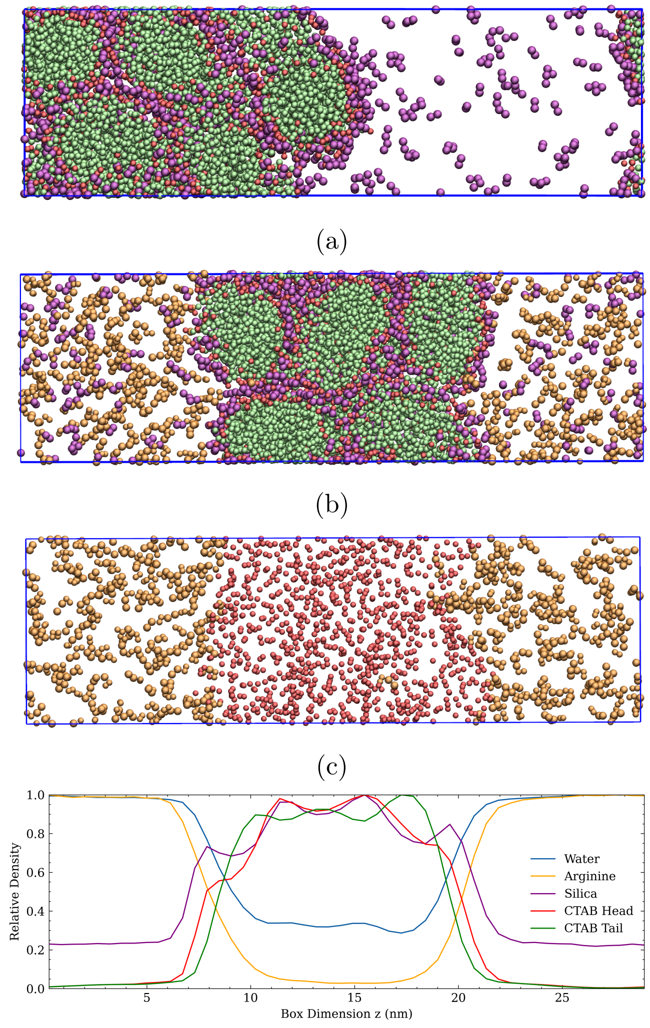

(d)

Figure 5.13: Snapshots of the final configuration after 6 µs are shown for self-assembly simulations without additive (a) and with arginine ((b) and (c)) starting from a random configuration. CTAB headgroups are shown in red, tails in green, silica dimers in purple and arginine in orange. Water is hidden in all snapshots for clarity. In (d), the time averaged relative densities (calculated as ρ/ρ_{max}) across the z axis for all species are shown.

5.3.5 Silica to Surfactant Ratio

Contrary to the Si:N ratio, our experiments revealed that the Si:CTAB ratio can have a pronounced effect on at least some material properties. First of all, there is a clear correlation between Si:CTAB ratio and yield, as shown in Figure 5.14. While data for low Si:CTAB ratios is rather noisy, it is clear that when Si:CTAB is increased above approximately 4, the yield decreases dramatically, reaching below 20% at a Si:CTAB ratio of 16. As the quantity of surfactant is reduced (increasing Si:CTAB), the amount of surfactant likely becomes insufficient to form large quantities of the product. These observations can be explained by the limited quantity of surfactant compared to silicon being ineffective in adequately concentrating silicate species within the surfactant mesophase. Therefore, when the pH is lowered to promote the reaction, silica predominantly forms as colloidal silica particles, as fewer silicate species are bound to the surfactant species, and these colloidal particles are lost during post-synthesis separation (washing and centrifuging).

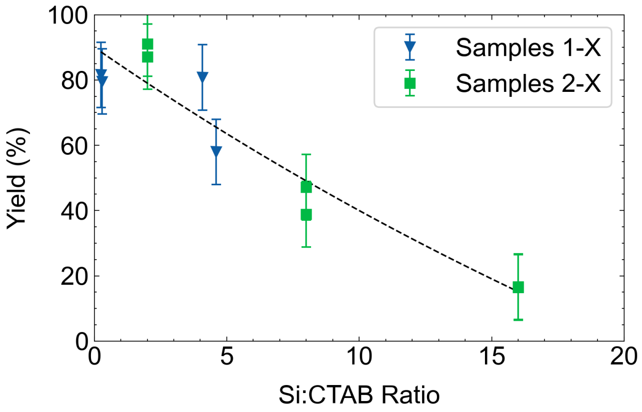

Figure 5.14: Dependence of yield on Si:CTAB ratio for samples synthesised at pH 10 with a high silica concentration (>100 mM). Data points for series Samples 1-X correspond to samples 1-10, 1-12, 1-14, and 1-16. The dashed line provides a guide for the eye.

The organics content of the precipitate is also strongly dependent on the Si:CTAB ratio, as shown in Figure 5.15. Synthesis carried out at a low Si:CTAB ratio, i.e. with a high concentration of surfactant species compared with the silica concentration, produced a precipitate with a high content of organic species, suggesting that additional surfactant molecules are bound to condensed silica when compared with syntheses where less surfactant is present. Sample 1-3 appears to be an outlier with a high organic content despite the high Si:CTAB ratio; however this can be explained by the extremely low quantity of material that was obtained under these synthesis conditions, which resulted in no measurable quantity of silica being present after calcination. Therefore, this sample is not shown in the plot of Figure 5.15.

A significantly higher organics content present in samples at a low Si:CTAB ratio (prior to calcination) indicates a greater surfactant uptake in the precipitated solid phase when the concentration of surfactant is increased. However, since this is not accompanied by an increase in yield of silica, this is more likely to be the result of surfactant rich assemblies that are bound to silica particles but do not possess sufficient silica to result in a porous solid being obtained after calcination. This is generally unfavourable, as the quantity of surfactant needed for these syntheses is much higher, without resulting in an increase in the quantity of mesoporous silica obtained. This is particularly pertinent when using calcination to remove the surfactant template from silica, as this bound surfactant is destroyed. Thus, a high ratio of Si:CTAB (and therefore a low concentration of CTAB) is desirable, particularly in terms of process scalability and economics.

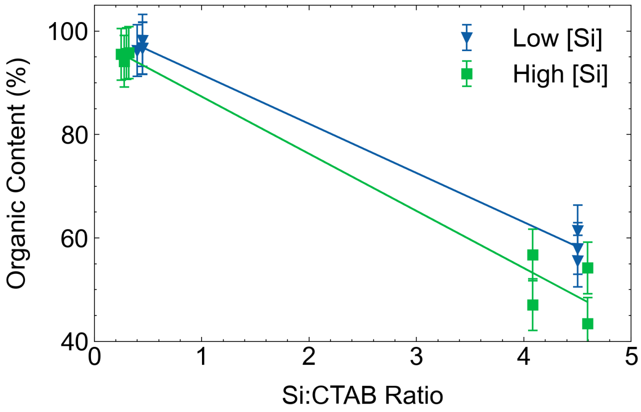

Figure 5.15: Dependence of organic content on Si:CTAB ratio for all samples produced in the two-level four-factor factorial design. The line is a guide to the eye.

While there are no strong correlations between Si:CTAB and BET surface area, pore volume, pore size, d_{100} spacing or wall thickness (Table A.2), this factor does seem to affect the degree of order of the pores. For instance, samples synthesised using a Si:CTAB ratio of 8 appear to possess a narrower pore size distribution and more clearly defined XRD peaks (Figure 5.16), and a higher I_{200}/I_{110} order parameter (Table A.2). This suggests improved regularity of pores in these samples and a higher degree of structural ordering. However, this does not result in improved bulk characteristics, such as increased surface area or total pore volume. In contrast, the resolution of the XRD peaks in samples obtained with a Si:CTAB ratio of 16 is extremely poor and their order parameter is close to zero (Figure 5.16). This suggests that these samples possess a very low degree of hexagonal ordering. Examining the order parameter more closely over the whole range of samples synthesised (see Figure 5.17), it appears to be highest in samples synthesised with a Si:CTAB ratio of 8. The degree of order obtained for these samples is similar to the highly ordered MCM-41 samples synthesised by Cai et al., but with a much shorter reaction time [146]. This indicates that the degree of structural ordering of hexagonally arranged pores is improved as the Si:CTAB ratio is increased from 2 to 8, but that this effect is diminished as the ratio is increased further from 8 to 16.

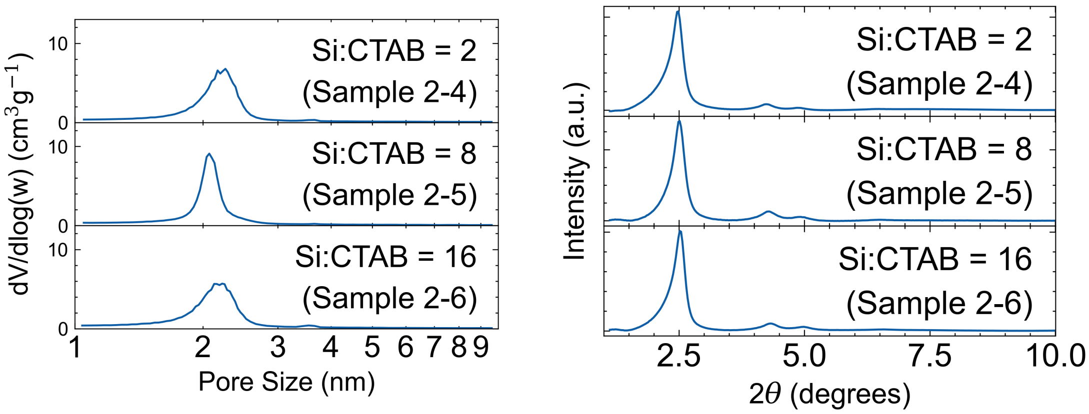

Figure 5.16: Pore size distributions (left) and XRD data (right) for selected samples synthesised with different Si:CTAB ratios. For XRD data, baseline intensity was removed manually to allow for easier comparison between peaks.

This demonstration of the dependence of both yield and degree of order on Si:CTAB ratio is particularly important, as although previous studies have highlighted the importance of silica to surfactant ratio on material properties [146, 191], most studies do not

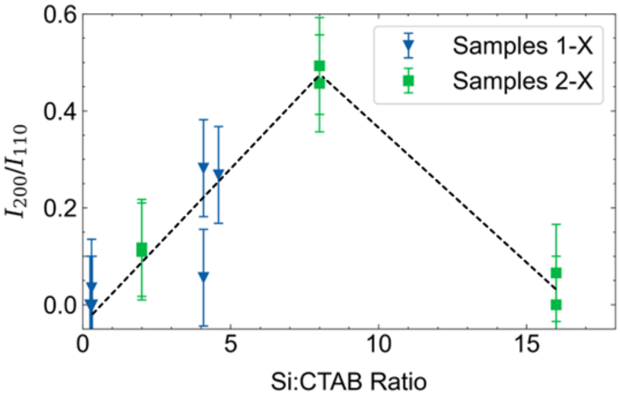

Figure 5.17: Dependence of order parameter I_{200}/I_{110} on Si:CTAB ratio for all samples synthesised at a high silica concentration. The blue line is a guide for the eye.

consider yield. As demonstrated, the optimal conditions for achieving a well-ordered porous structure do not achieve the greatest yield, indicating that a trade-off exists that must be considered when attempting to scale-up these synthesis processes.

To understand the effect of the Si:CTAB ratio and pH on the degree of order, coarse-grained MD simulations of self-assembly were carried out under different conditions. Snapshots of the final configurations obtained at varying Si:CTAB ratios are shown in Figure 5.18. At pH 13, which represents the system during the early stages of synthesis before the addition of acid, at all Si:CTAB ratios, the presence of silicates is effective in promoting aggregation and phase separation of the surfactant phase. However, the degree of order of this surfactant phase varies with the Si:CTAB ratio. At low Si:CTAB ratios, 0.5-2 (Figure 5.18 a, b, c), the degree of order is low and (at best) only an incipient HLC phase is observed. However, at a Si:CTAB ratio of 4 (Figure 5.18d), a much more well ordered HLC phase is formed. This well-ordered arrangement is preserved at a ratio of 8 (Figure 5.18e). At a ratio of 16 (Figure 5.18f), the curvature of the surfactant phase appears to increase, resulting in a less well-ordered arrangement.

In Figure 5.19, the relative amount of silica that is bound to the surfactant phase is compared with the overall Si:CTAB ratio (i.e. in the entire simulation box). The former is calculated by taking an average of the number of silicates that are within 0.73 nm of a surfactant headgroup bead, which corresponds to the first minimum of the

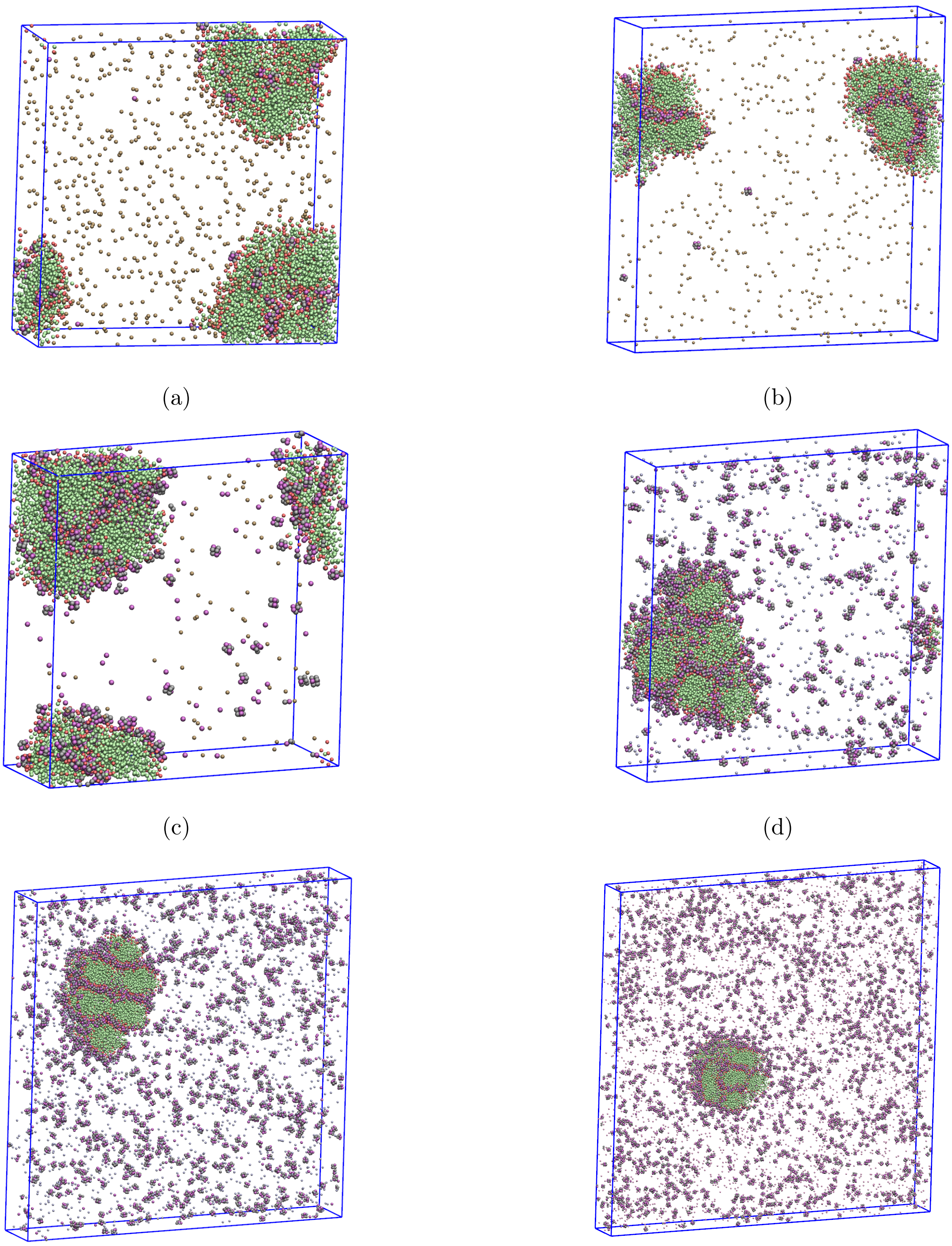

(a)

(b)

(c)

(d)

(e)

(f)

Figure 5.18: Snapshots of the final configurations obtained from self-assembly simulations at pH 13 with varying Si:CTAB ratios: (a) = 0.5, (b) = 1, (c) = 2, (d) = 4, (e) = 8, (f) = 16. Full simulation details are given in Table 5.5.

surfactant to silica radial distribution function, after the initial equilibration period. The red dashed line indicates where these quantities are equal, i.e. all silicon atoms are bound to the surfactant phase. At low Si:CTAB ratios, the data (orange circles in Figure 5.19) closely follow this line, indicating that all silica species are bound to the surfactant phase. As the Si:CTAB ratio is increased, the divergence from the ideal line increases, which indicates that as more silicates are added to the system, more remain in solution while the interface becomes saturated. This divergence increases dramatically at a Si:CTAB ratio between 2 and 4, which corresponds to the formation of the HLC phase observed in simulation snapshots (Figure 5.18). The bound Si:CTAB ratio then reaches a maximum, at which point further increases in the overall Si:CTAB ratio do not increase the bound Si:CTAB ratio, suggesting that the surfactant interface is fully saturated with silicates. This can be explained by considering the overall charge at the surfactant interface, shown in Figure 5.19, which takes into account all charged species that are bound to the surfactant interface, including bromide counter-ions. As the Si:CTAB ratio is increased, the interface charge, which is initially positive due to excess of cationic surfactant heads, decreases until it becomes approximately neutral. At this point, there is no strong driving force for further attraction of silicates to the surfactant interface, as this process is primarily driven by electrostatic interactions between the positively charged surfactant headgroups and the negatively charged anionic silica species. Hence, further addition of silicates past this point does not result in an increase in silica species at the surfactant interface.

Figure 5.19 also shows data for bound Si and charge obtained at lower pH values, while Figure 5.20 shows snapshots of the final simulation configurations at a Si:CTAB ratio of 8. A hexagonal arrangement is observed at pH 13 (Figure 5.20a) as previously discussed. However, at pH 10 (Figure 5.20b), while the presence of silica is effective in promoting phase separation, this phase is less well-ordered and appears to have reduced curvature of the silica/surfactant interface, forming wider, less cylindrical “pores”. As the pH is reduced further to 7 (Figure 5.20c), the silicates are less effective at promoting phase separation, with the surfactant instead forming worm-like and spherical micelles. This can be attributed to the much lower proportion of charged silica species present at this pH, which appears to be insufficient to screen the repulsive charge between surfactant micelles, preventing further aggregation of the surfactant phase. This interpretation is confirmed by the data in Figure 5.19. At pH 13, the charge at the interface is approximately neutralised at a Si:CTAB ratio of 4, however at pH 10 it is still strongly positive, which may explain the disorder of the phase. While further increases in Si:CTAB ratio appear to reduce the interface charge, the effect is diminished as Si:CTAB ratio is increased, and it is possible that the charge may not be fully neutralised at this pH even at very high Si:CTAB ratios. The positive charge of this interface allows for more silicates to be attracted to the surfactant phase as the Si:CTAB ratio is increased, as shown in Figure 5.19.

The snapshot at pH 7 (Figure 5.20c) shows that silicates appear to aggregate into solid clusters due to the lack of charged groups, which would otherwise prevent clustering. This behaviour is not likely to be realistic, as in reality these silica species would undergo condensation reactions to form a more extensive silica network. During the experimental synthesis, these condensation reactions may occur before such extensive rearrangements of the silica/surfactant phase take place, effectively locking in the more well-ordered structure that forms at higher pH. However, since the model used in this work does not allow for silica polymerisation reactions to take place, this process cannot be accurately observed. Since in the experimental synthesis it was observed that

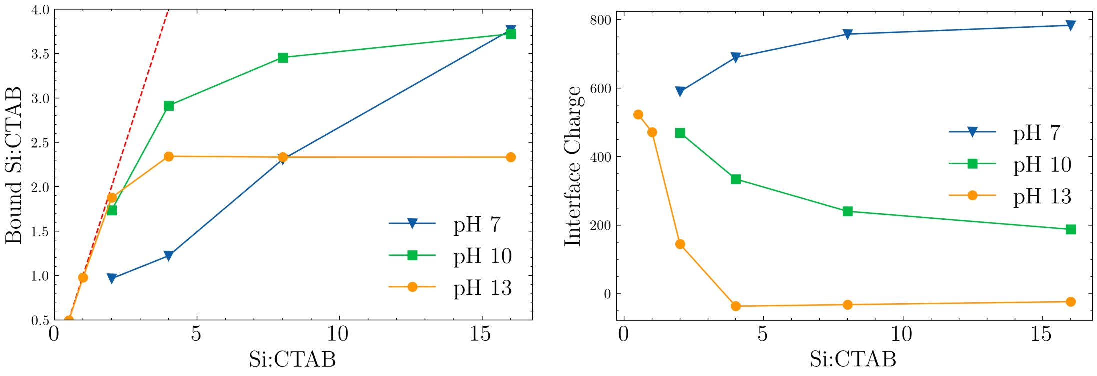

Figure 5.19: Effect of varying the Si:CTAB ratio on the quantity of silicon atoms bound to the surfactant phase (left) and the overall charge at the surfactant interface (right) at different pH values, determined from MD simulations. The dashed red line represents an ideal case where all silicon atoms are bound to the surfactant phase.

hexagonally ordered structures were obtained at both pH 7 and 10, we can conclude that extensive rearrangement of the silica/surfactant phase does not take place upon the reduction in pH, which facilitates silica precipitation. Furthermore, the fact that experimental materials synthesised at pH 7 possess a higher degree of order than the materials synthesised at pH 10 suggests that the faster reaction kinetics of silica condensation reactions at pH 7 allows for the highly ordered structure that forms at high pH ($>$13) to become locked in more rapidly before rearrangement of the silica/surfactant phase can occur.

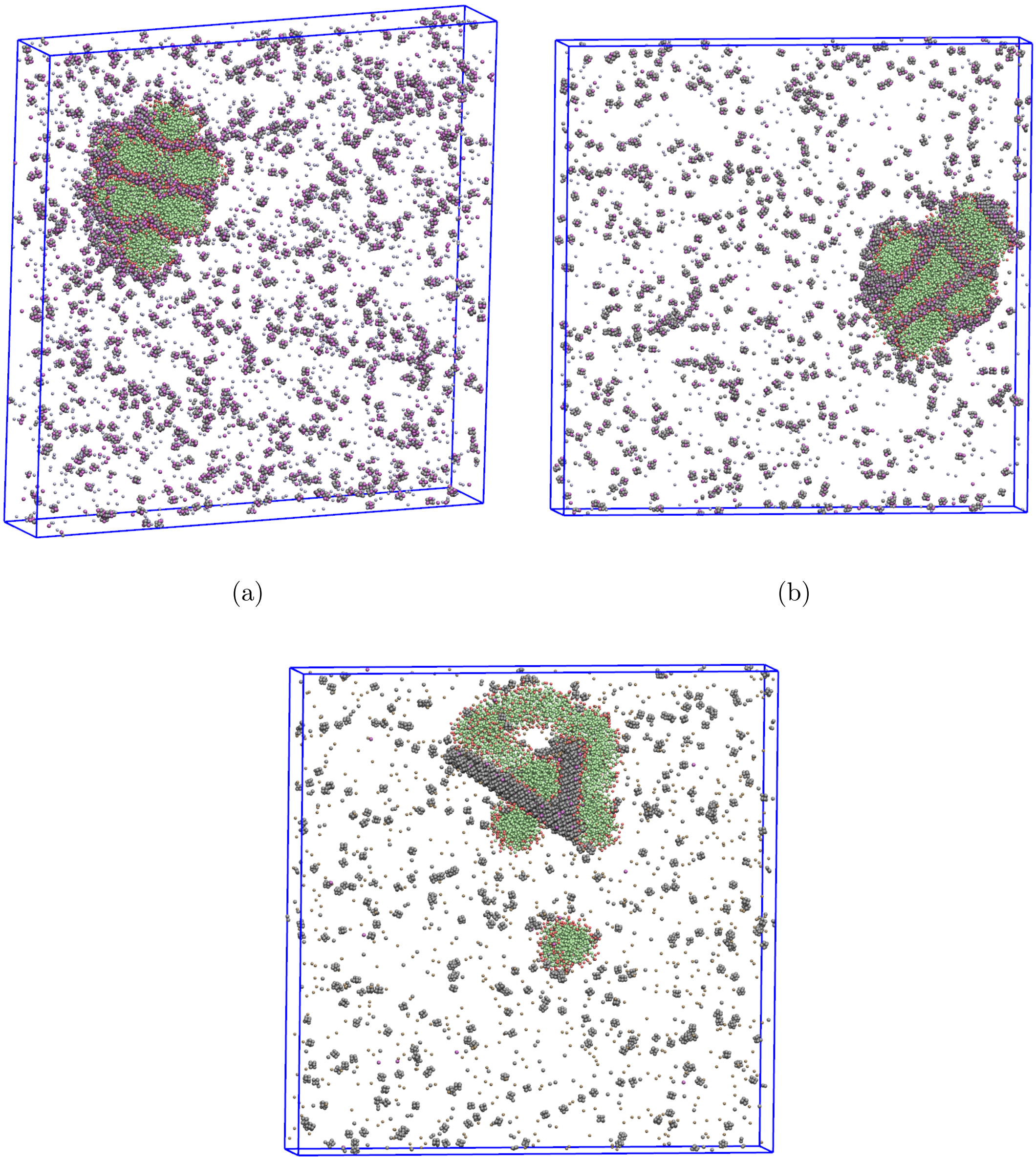

(a)

(b)

(c)

Figure 5.20: Snapshots of the final configurations obtained from self-assembly simulations at a Si:CTAB ratio of 8 and at varying system pH: (a) = 13, (b) = 10, (c) = 7. Full simulation details are given in Table 5.5.

5.3.6 Alternative Bio-Inspired Additives

Since the presence of arginine did not appear to affect the assembly of OMS by this method, it was decided to carry out the same synthesis procedure (Section 5.2.1) using alternative bio-inspired additives. Aside from the additive used, all synthesis conditions were kept the same between samples and are displayed in Table 5.1 (Samples 3-1 through 3-4). The common feature of all additives in this investigation is the presence of primary or secondary amine groups. The number of these groups present in each additive is also listed in Table 5.1.

Yield results are shown in Table 5.10. The yield did not change significantly with the use of different additives, although there was a small decrease in yield when using propylamine. Bulk porosity data is also similar, with all samples exhibiting mesopores of similar size (see Figure 5.21) and similar BET surface areas and pore volumes (Table 5.10). Furthermore, these values are comparable to the sample synthesised without an additive, confirming that the presence of an additive is not essential to obtaining high surface area silica following this synthesis method.

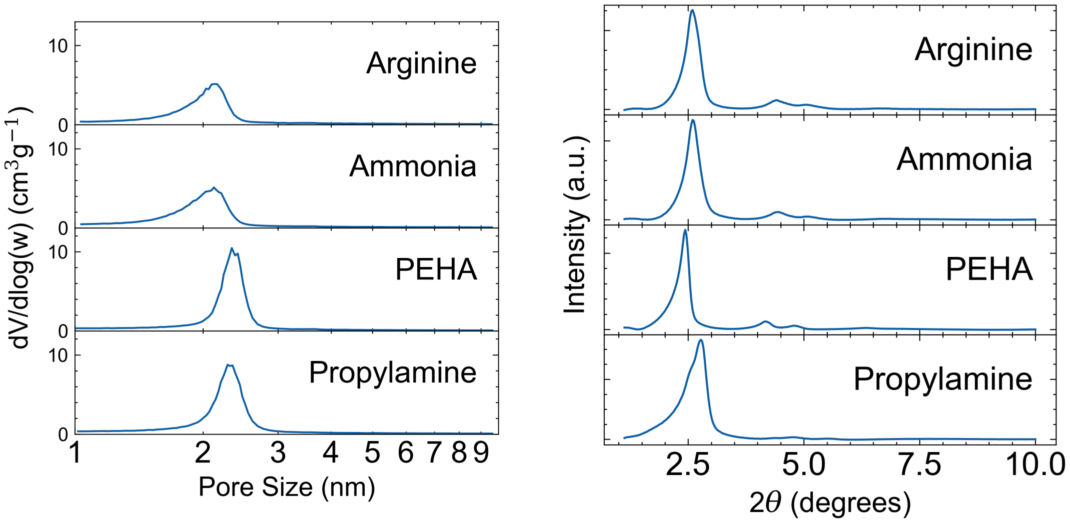

Figure 5.21: Pore size distributions (left) and XRD data (right) for selected samples synthesised with different additives. For XRD data, baseline intensity was removed manually to allow for easier comparison between peaks.

A closer look at the pore size distributions (see Figure 5.21), however, shows that

Table 5.10: Summary of yield and porosity data for additive investigation samples that were characterized by N_2 adsorption and XRD. The variables are fully described in Section 5.2.3.

Additive	**Yield (%)**	$S_{\mathbf{BET}}$ **($\mathbf{m^2\ g^{-1}}$)**	$V_{\mathbf{pore}}$ **($\mathbf{cm^3\ g^{-1}}$)**	$d_{\mathbf{pore}}$ **(nm)**	$t_{\mathbf{wall}}$ **(nm)**	$I_{\mathbf{200}}$ **/$\mathbf{I_{110}}$**
Arginine	80	1149	0.789	2.18	1.21	0.06
Ammonia	78	1203	0.835	2.17	1.21	0.00
PEHA	74	1218	0.938	2.40	1.23	0.28
Propylamine	65	1273	0.969	2.35	-	0.00
None	81	1218	0.911	2.24	1.26	0.20

samples synthesised with arginine and ammonia have slightly broader pore size distributions that extend below 2 nm, towards the microporous region, whereas the presence of PEHA appears to result in a narrower pore size distribution, suggesting improved structural ordering compared to the other samples. This is confirmed by the XRD results shown in Figure 5.21. The sample that was synthesised with PEHA has exceptionally well-resolved reflection lines (100), (110) and (200), and the highest order parameter I_{200}/I_{110} of all samples (Table 5.10).

To understand why the presence of PEHA was effective in increasing the degree of order of OMS synthesised following this method, a self-assembly simulation was carried out for silica and CTAB in the presence of neutral PEHA molecules, which resembles the system at high pH (pH $>$ 13). The final configuration after 6 µs of simulation time is shown in Figure 5.22. The formation of a HLC phase can be observed, indicating that PEHA does not significantly alter mesophase formation at the beginning of the synthesis, while the pH is still high. However, unlike what was previously observed with arginine (see Figure 5.13), PEHA molecules are present in significant quantities at the silica-surfactant interface, interspersed throughout the HLC phase. This is illustrated in Figure 5.22c, which shows that the relative density of PEHA peaks at the same positions as the CTAB headgroup and silica densities. This indicates that at high pH, where the formation of the OMS template takes place, PEHA is incorporated into the framework that will become the porous silica network. Since amine groups (which are numerous in PEHA) are known to catalyse the condensation of silica [15], this behaviour may provide insight into how the presence of PEHA during synthesis is able to improve the degree of structural ordering in OMS. Incorporation of PEHA species into the HLC may allow it to catalyse the condensation of silica, "locking in" the structure more quickly before it can become disordered due to the drop in quantity of anionic silicates after acid addition.

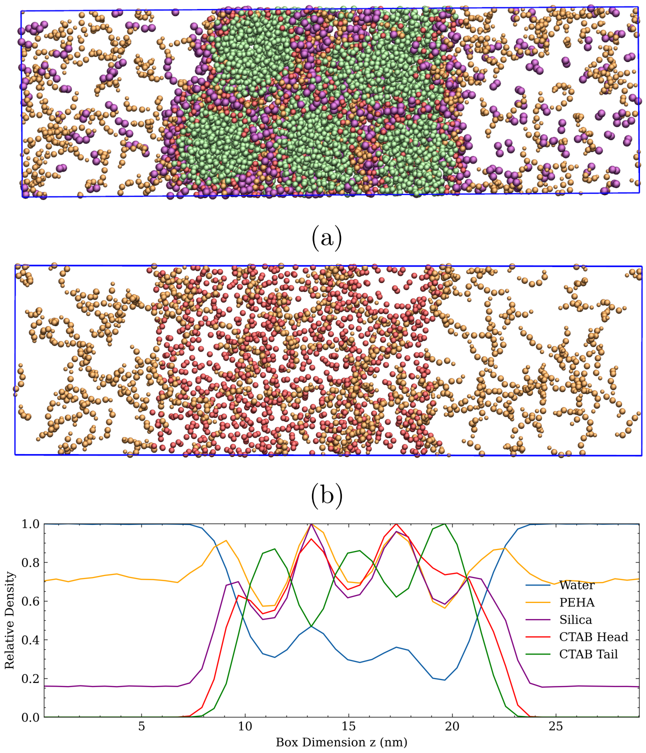

(a)

(b)

(c)

Figure 5.22: Simulation snapshots of the final configuration after 6 µs are shown for self-assembly simulations with PEHA ((a) and (b)) starting from a random configuration. CTAB headgroups are shown in red, tails in green, silica dimers in purple and PEHA in orange. Water is hidden in all snapshots for clarity. In (c), the time averaged relative densities (calculated as ρ/ρ_{max}) across the z axis for all species is shown.

Given the promising results obtained in the sample with PEHA, we have carried out additional experiments using several ratios of silica to PEHA, with Si:N between 0.333 and 0.056. The Si:CTAB ratio was kept fixed at a value of 8, which was previously identified to produce the most well-ordered materials (see Section 5.3.5). To test if the degree of structural ordering is also affected by reaction time, some of the syntheses were also carried out with two different reaction times, 5 and 60 minutes. A summary of the synthesis conditions is given in Table 5.1 (Samples 4-1 through 4-7).

The results (Table 5.11) show that the presence of PEHA leads to a significant increase in yield for reaction times of both 5 and 60 minutes, compared to the case where no additive is present (samples 4-4 and 4-7) as well as samples with arginine under equivalent conditions (samples 2-2 and 2-5, cf Table A.1). For both reaction times, the highest yield is achieved with PEHA at a Si:N ratio of 0.083. This suggests that PEHA addition may be an effective way to increase the yield of silica at higher ratios of Si:CTAB, where previously yields decreased but product quality improved (see Section 5.3.5).

Table 5.11: Summary of yield and porosity data for PEHA investigation samples that were characterized by N_2 adsorption and XRD. The variables are fully described in Section 5.2.3. Additional data is provided in Section A (Tables A.2 and A.1).

Sample No.	**Yield (%)**	$S_{\mathbf{BET}}$ **($\mathbf{m^2\ g^{-1}}$)**	$V_{\mathbf{pore}}$ **($\mathbf{cm^3\ g^{-1}}$)**	$d_{\mathbf{pore}}$ **(nm)**	$t_{\mathbf{wall}}$ **(nm)**	$I_{\mathbf{200}}$ **/$\mathbf{I_{110}}$**
4-1	65	983	0.706	2.20	1.35	0.52
4-2	80	961	0.736	2.27	1.41	0.49
4-3	69	926	0.679	2.24	1.37	0.00
4-4	41	1186	0.830	2.09	1.35	0.18
4-5	78	783	0.608	2.80	-	0.00
4-6	86	878	0.686	2.74	-	0.00
4-7	57	1142	0.841	2.10	1.30	0.29

Looking at the results for porosity (Table 5.11), the samples synthesised with PEHA generally possess somewhat lower BET surface areas and pore volumes than samples synthesised without PEHA, and this effect is enhanced at long reaction times. However, examination of the XRD data and pore size distributions (Figure A.8) shows that, with the exception of the sample synthesised with the lowest Si:N ratio (4-3), samples synthesised with PEHA and a reaction time of 5 minutes have a markedly improved degree of order when compared with the control samples (4-4 and 4-7). Specifically, if we take porosity, yield and degree of order into consideration, a PEHA concentration of 0.083 appears to strike a good balance, yielding materials with well-resolved reflection lines at (100), (110) and (200) that indicate hexagonally ordered mesopores with a narrow size distribution.

An increase in the reaction time had the inverse effect on samples synthesised with and without PEHA. Without any additive present, a longer reaction time seems to slightly increase the degree of order (although the difference is only marginally above statistical uncertainty), in line with previous observations [190]. In contrast, the XRD patterns for samples 4-5 and 4-6, which were synthesised with PEHA present and a reaction time of 60 minutes, are significantly different from other samples. There are no discernible peaks corresponding to reflection lines at (100), (110) and (200) indicating materials with no hexagonal ordering. The shift and broadening of the peaks towards values below 2° 2θ suggests that these samples possess larger, amorphous pores, which is well supported by the broader pore size distributions presented in Figure A.8. This is accompanied by a reduction in BET surface area of about 200 $\mathrm{m}^2\ \mathrm{g}^{-1}$. No such large mesopores are present in the corresponding sample without PEHA (4-7). This suggests that PEHA interacts with the system through a relatively slow mechanism that results in a broader pore size distribution. This may be explained by the formation of a secondary disordered porous silica phase, promoted by the presence of PEHA, which reduces the porosity of the bulk material, but occurs at a slower rate than the formation of the primary mesoporous silica phase, and therefore is not present in significant quantities at low reaction times.

Although high yields of OMS were achieved previously without the use of an additive, this necessitated the use of larger quantities of surfactant, with Si:CTAB ratios of 2 being required to achieve yields $>80\%$ when either no additive or arginine was used in synthesis. The use of PEHA allows for high yields to be achieved with a relatively low quantity of surfactant, e.g. a Si:CTAB ratio of 8. This ratio also has benefits in terms of material structure, as identified in Section 5.3.4. However, when reaction time is increased, there is a reduction in surface area, pore volume and degree of structural ordering. Since these phenomena happen at different time scales, it may be favorable to carry out synthesis with a low reaction time to maximize the quantity of well-ordered porous silica, whilst minimizing the secondary process that reduces the degree of order in the resultant material.

5.4 Conclusions

In this work, a detailed investigation was carried out to study the effects that bio-inspired additives have on ordered mesoporous silica synthesis under mild conditions with short reaction times. Initially, a two-level four-factor design of experiments approach that utilised arginine as an additive was adopted. This identified that both pH and Si:CTAB ratio have a pronounced effect on the structural properties of the mesoporous silica obtained. A high Si:CTAB ratio appeared to be essential for well-ordered materials to be obtained, and the degree of order was significantly higher for samples synthesised at pH 7. A further investigation into the effect of component ratios identified that the most well-ordered materials were obtained with a Si:CTAB ratio of 8, while the degree of order was actually reduced as this ratio was increased to 16. Coarse-grained molecular dynamics simulations showed that the Si:CTAB ratio is critical to achieving a balance of charge at the silica/surfactant interface, which appears to be the key for achieving a well-ordered hexagonal mesophase. This structure was also shown to be significantly disrupted by changes in pH, suggesting that for well-ordered materials to be obtained as pH is lowered during synthesis, the structure formed at high pH must become "locked in" by silica condensation reactions, which proceed most rapidly at pH close to 7. While this method of "delayed neutralization" was explored by Lin et al. [190], rapid addition of the acid appears to facilitate the formation of well-ordered materials with significantly shorter synthesis times than previously reported.

Throughout these investigations, the quantity of arginine used did not appear to have any effect on yield or material properties, even when more extreme ratios of Si:N were used. In response to this, several different additives were trialled and compared to a control system in which no additive was used. Surprisingly, the control system resulted in a very well-ordered mesoporous material with a reaction time of just 5 minutes and without hydrothermal treatment. This confirmed that hydrothermal treatment is not required in order to obtain well-ordered mesoporous silica from a sodium silicate precursor, and rapid precipitation is possible simply by modifying the system pH.

The tests with alternative bio-inspired additives showed that the sample synthesised using PEHA had a higher degree of order compared with the sample synthesised with both alternative additives and no additive present. Coarse-grained molecular dynamics studies of self-assembly at high pH were carried out with both PEHA and arginine, which showed that while the self-assembly of the HLC phase is not directly affected, PEHA is readily absorbed within the silica/surfactant interface, while arginine remains largely in the bulk water phase. This suggests that the role played by additives is most likely catalytic, aiding in locking in the well-ordered structure that forms during the early stages of OMS synthesis by increasing the rate of silica condensation reactions whilst the structure is well-ordered, preserving the well-ordered structure by creating an extensive network of silica before it is rearranged by the change in system pH. The influence of PEHA was investigated further, where it was shown that at low reaction times the presence of smaller quantities of PEHA significantly improved both the degree of structural ordering and the synthesis yield. However, the presence of PEHA resulted in pores becoming broader and less well ordered as the reaction time or concentration of PEHA was increased. This suggests that PEHA may be used to promote the formation of well-ordered mesoporous silica particles, but reaction times must be kept low to avoid changes in the material's morphology. Both high Si:N and Si:CTAB ratios are desirable from a process economics point of view, as higher ratios of silica to other components lowers the quantity of reactants required. It is also desirable from a green chemistry perspective due to improved atom economy.

Chapter 6

pH-Responsive Phase Behaviour of Amine Surfactants

6.1 Introduction

The structure of surfactants, consisting of a polar or hydrophilic head and a nonpolar or hydrophobic tail, gives surfactants interesting properties, as discussed in Section 2.1.2. A particularly interesting class of surfactants are those that exhibit a dynamic response to their environment, e.g. changing their self-assembly behaviour in response to changes in pH [196], light [197], CO_2 concentration [198], magnetism [199], etc. These "switchable" surfactants most often have amine-containing headgroups, as their responsive behaviour depends on switching of this headgroup between neutral and cationic forms. Injection of CO_2 can be used to trigger this behaviour, as it reacts with pure water to form carbonic acid, making the solution more acidic. The reaction can be reversed by bubbling nitrogen, air or argon through the solution [198]. This switchable behaviour can be exploited to aid separation processes in emulsion polymerization [200] and demulsification in enhanced oil recovery [201], and the separation and transport of crude oil [202].

In solution, long-chain alkylamines behave as surfactants, as they consist of a hydrophobic alkyl tail and a hydrophilic amine headgroup. While similar in nature to cationic surfactants such as cetyltrimethylammonium bromide (CTAB), a unique feature of alkylamine surfactants is their ability to donate a proton of their headgroup (at high pH) to become uncharged, a process that does not occur when this amine group is fully methylated. Amine surfactants have been studied for use in flotation [203–205], the synthesis of carbon nanotubes and nanowires [206, 207], and as a templating agent in the synthesis of hexagonal mesoporous silica (HMS) [34]. In these applications, their effectiveness is often highly dependent on the pH of the environment. For example, Yuhua et al. found that dodecylamine (DDA) was most effective at recovering iron-bearing minerals at increased pH [203], which is likely related to deprotonation of the amine group with a pKa value of 10.63 [208].

Given that the surfactant-templated synthesis of mesoporous silica materials is primarily driven by charge matching between cationic surfactant and anionic silicate precursor species [9, 209], permanently charged surfactants have been generally used. However, this imposes limits on the economic viability and environmental impact of those processes, since ammonium surfactants are toxic and hard to remove and recover. Amine-based species, which are at the heart of recent bio-inspired silica synthesis processes [8, 15, 37, 189], offer an interesting alternative because they are more environmentally friendly and potentially easier to remove [7, 37]. However, when amine surfactants were used previously for this purpose, a much lower degree of order was present in the materials produced, resulting in disordered worm-like mesoporous silicates [210–212]. A deeper understanding of the self-assembly of amine surfactants as a function of solution pH is therefore needed in order to promote the formation of ordered mesoporous silica materials under “green” conditions [1].

Alkylamine surfactants show interesting properties in mixtures with acids due to proton transfer between the acid and the alkylamine. The phase behaviour that results from this proton transfer depends strongly on the nature of the acid present. For mixtures of alkanoic acids and alkylamines in solution, this proton transfer results in the formation of amphiphilic species, and the relative lengths of the alkyl chains in these species strongly dictate the phases that form. When the length of the alkyl chains of both species is similar, a catanionic surfactant complex is formed. The morphology of this complex tends towards a lamellar liquid crystalline phase in equilibrium with nearly pure water close to an equimolar ratio of acid and amine, dominating a large region of ternary amine/acid/water phase diagrams [213, 214]. Mixtures of alkylamine and alkanoic acids where the alkyl chain of the acid is much shorter than that of the alkylamine, produce a larger variety of phases including isotropic (micellar), as well as cubic, lamellar and hexagonal liquid crystalline phases, more similar to the phase diagrams of cationic surfactants such as CTAB [215]. Ternary phase diagrams have been created for systems containing dodecylamine (DDA), water and acids including acetic acid [216], acrylic acid and methacrylic acid [217].

Since the phase diagrams are different when different acids are used, this implies that phase transitions are driven by both proton transfer between the acid and amine species, and interactions between the resulting salts and surfactant species. Experimental studies that examine the phase behaviour of alkylamine surfactants provide limited information, and isolating the dependence on surfactant charge is not possible due to the presence of salts that form by proton transfer between acid and surfactant species [216, 217]. Computational approaches offer the ability to isolate this phenomenon, permitting greater understanding of the fundamental mechanisms underpinning liquid crystal phase formation of pH-responsive surfactants.

Due to advances in computational modelling algorithms and increased availability of computing resources, various modelling approaches have been successfully applied to study surfactant self-assembly, as reviewed recently by Taddese et al. [96]. Atomistic molecular dynamics (MD) models are of limited effectiveness for studying surfactant phase behaviour due to the relatively small time and length scales that are accessible, and therefore are typically limited to studying properties of preformed micelles. Although a few studies have been able to simulate micelle self-assembly with fully atomistic models [218–220], they are limited to surfactants that self-assemble quickly and form relatively small aggregates. Furthermore, even very lengthy atomistic simulations often fail to reproduce experimental aggregation numbers [221].

Given the difficulty in simulating important surfactant phenomena using atomistic simulations, coarse-grained (CG) methods are frequently applied, as discussed in Section 3.1.6. Different "flavours" of CG approaches have been used in the past to study surfactant phase diagrams, including dissipative particle dynamics (DPD) [222–225], the 'SDK' model [226–228], implicit-solvent models [229, 230], and even lattice-based models [231–234]. The 'SDK' model, was presented by Shinoda et al. [226, 227] based on the behaviour of surfactants in atomistic simulations. The SDK model has been used to study surfactant micellization [228], lipid bilayer loading [235] and adsorption in the lamellar phase of nonionic surfactants [236]. However, the SDK model has not been applied to study phase behaviour at higher surfactant concentrations. Dissipative particle dynamics (DPD) [222] has been applied extensively to study surfactant systems. The soft repulsions used in DPD allow systems to behave as a mean-field fluid, meaning they can be mapped to polymeric Flory-Huggins χ-parameters, which is useful for parameterisation of DPD models [222, 237, 238]. DPD models have been used to study micelle formation for nonionic [239] and ionic surfactants, [223] and to construct phase diagrams for sodium laurylethoxysulfate [224] and alkyl ethoxylate surfactants [225]. More recently, machine learning approaches have been applied to produce phase diagrams for nonionic surfactants and were found to be particularly effective in filling missing data from incomplete data sets [240].

In this context, the MARTINI CG force field [76] offers a good balance between computational efficiency and realism, and has been widely used to study the self-assembly of micelles [229, 241, 242] and the phase behaviour of anionic and cationic surfactants [243], as well as nonionic surfactants [244–246], providing good agreement with experimental phase diagrams. The MARTINI model has also been successfully applied to reproduce the self-assembly of the cationic surfactant CTAB in the context of periodic mesoporous silica synthesis [75], generating phase diagrams for both binary surfactant/water and ternary silica/surfactant/water systems [77, 78]. A similar approach was applied to study the self-assembly behaviour of the alkylamine DDA in the presence of silica precursor species, which occurs in the early stages of the synthesis of HMS. Centi et al. [11] found that the formation of the mesophase must be driven by charge matching between surfactant and silica precursor species, in marked contrast with the neutral templating mechanism that was originally proposed for the synthesis of these materials [34] . They identified that the synthesis was heavily dependent on solution pH due to its effect on the relative quantities of charged species present [11].

In this chapter, a coarse-grained molecular dynamics approach is applied using the most recent version of the Martini force field [13], which has previously been used to accurately model the self-assembly behaviour of silica/CTAB/water systems [247]. The modelling approaches that were previously applied to study permanently charged binary CTAB systems [78] are applied to study the phase behaviour of DDA with varying degrees of charge, allowing the phase transitions that occur by protonation of the primary amine group to be studied directly, a property which can be controlled experimentally by modification of system pH. This is the first computational study that focuses on isolating this pH-responsive behaviour of alkylamine surfactants in the context of liquid crystal phase behaviour. The same modelling approach is then applied to study the phase behaviour of ternary DDA/water/silica systems at relatively low surfactant concentrations, which is particularly relvant to the synthesis of HMS [34].

6.2 Methods

6.2.1 Simulation Details

The GROMACS 2022.1 software package was used to carry out simulations [164, 248]. Simulations were set up and analysed using built-in GROMACS tools and visualisations were created using the Visual Molecular Dynamics software package [249]. The size and density profiles of micelles were measured using an in-house cluster counting script based on the Hoshen-Kopelman counting algorithm [250]. Graphs were created using the Matplotlib library [169] for Python [166].

Atomistic simulations were used to generate bonded parameters for the CG DDA model. For bonded parameter generation, a single neutral DDA molecule was placed in a cubic periodic simulation box with a side length of 3 nm and solvated with an appropriate number of water molecules to achieve a realistic density using the `gmx solvate` tool in GROMACS. The rigid single point charge (SPC/E) potential was chosen to represent water molecules [171]. The atomistic models for both positively charged DDA and neutral DDA were generated using the LigParGen OPLS/CM1A parameter generator utility [161–163]. The leapfrog algorithm [111] was used for all atomistic simulations with a time step of 2 fs. Atomistic simulations were at room temperature (298 K) and pressure (1 bar). The velocity-rescaling [115] thermostat and Parrinello-Rahman barostat [120, 121] were used to control temperature and pressure, respectively. The Lennard-Jones (LJ) cut-off was set at 1.2 nm, with a switching function between 0.9 and 1.2 nm. Long range dispersion corrections were used for both energy and pressure. The particle-mesh Ewald method [113, 170] was used to account for electrostatic interactions. Energy minimisation was carried out using the steepest descent algorithm, and equilibration was carried out for 100 ps, first in the NVT ensemble, followed by NpT. A simulation time of 50 ns was used for calculations of bonded parameters. The PyCG-TOOL utility was used to generate bonded parameters from the atomistic trajectories [155].

The Martini 3 force field was used for all coarse-grained simulations [13]. Before production MD runs, energy minimisation, NVT equilibration and NpT equilibration were carried out. The steepest descent algorithm was used for energy minimisation. During equilibration, the velocity-rescaling thermostat [115] and the Berendsen barostat [114] were used with a 2 fs time step. A 20 fs time step using the leap-frog algorithm was used for production MD. Temperature and pressure were controlled with the velocity-rescaling thermostat and Parrinello-Rahman barostat [120, 121], respectively. The Verlet cutoff scheme [110] was used with a cutoff value of 1.1 nm. The reaction field scheme was used to account for electrostatic interactions with a cutoff value of 1.1 nm and relativity permittivity set to $\varepsilon_r = 15$. The thermostat for CG simulations of surfactant self-assembly was set to 348 K to allow phase formation to occur within a reasonable simulation time.

Self-assembly simulations of binary DDA/water systems were carried out starting from a random configuration of DDA molecules in a cubic simulation box. Simulations with a low concentration of DDA (i.e. 5 wt%) used 200 molecules, while higher concentration simulations used 1000 DDA molecules. Chloride counter-ions were used to neutralize the total charge of the system. Chloride counter-ions were used as they have weak nucleophilic behaviour, and are therefore relatively inert compared with other anions. Therefore, they are least likely to modify surfactant phase behaviour allowing the phase behaviour of DDA to be studied in isolation. It should be noted that the degree of charge of DDA molecules in these simulations is at a fixed value, and therefore assumes that the surfactant charge is independent of aggregation state. However, in experimental systems the degree of charge of some surfactants has been observed to be strongly dependent on aggregation state [251]. Water molecules were then added to achieve the desired concentration of DDA. Calculations were carried out to achieve a total simulation time of 1 µs initially, and in some cases these calculations were extended until an equilibrium configuration was obtained. In cases where the nature of the phase that formed was not clear, simulations of larger systems (i.e. increased number of DDA molecules) were carried out. Full simulation details for binary DDA/water simulations are given in Table 6.1.

Self-assembly simulations of ternary DDA/water/silica systems were carried out at DDA concentrations that correspond to the micellar region of the binary surfactant/water phase diagram. The model for silicates which was developed in Chapter 4 was used. For these simulations, the total number of charged DDA species was kept constant at 1000 DDA molecules, with additional neutral DDA species added to achieve the correct proportion of charged DDA species. The total number of silicon atoms (i.e. CG beads of silica) was set to achieve a Si:DDA ratio of 4, which is close to the Si:DDA ratio of 3.7 used in the synthesis of HMS reported by Tanev and Pinnavaia [34]. The first set of simulations was carried out using only silica dimers. The ionisation state for the population of dimers in each simulation was determined from the proportion of charged DDA species by calculating the pH at which that proportion of charged surfactant species would be found, using the pKa value corresponding to the deprotonation of the amine group which is 10.63.

$$\mathrm{pH} = \mathrm{pKa} + \log\left(\frac{DDA^{+}}{DDA}\right) \tag{6.1}$$

This pH was then used to calculate the proportion of silica dimers that are present as doubly charged (SI2), singly charged (SISN) and uncharged (SN2), using the experimentally determined pKa values corresponding to the first and second deprotonation of silica dimers (9.0 and 10.7, respectively). The second set of simulations used only silica cubic octamers, using the same Si:DDA ratio of 4. For these simulations, only fully charged (SI8c), half charged (SI4SN4c) and neutral (SN8c) species were used. The proportions of each of these species were taken from the equivalent proportion of dimers (i.e. the proportion of fully charged, half charged and neutral dimers) for that proportion of charged DDA. It should be noted that this is a different procedure than was used in Chapter 5, and the drawbacks of this approach are discussed in more detail later in this chapter. TMA counter-ions were then added to the system to achieve a neutral overall system charge. Finally, the required number of water molecules was then calculated to achieve the correct overall concentration of DDA, and the initial system volume was then determined to achieve the correct density for the system. Box dimensions x and y were set to 8 nm initially, while the z dimension was set to achieve the desired system volume. For the initial configuration of these simulations, the surfactant molecules were all inserted close together in the centre of the simulation box to reduce the simulation time needed for aggregation to occur.

Table 6.1: Details of coarse-grained simulations of DDA phase formation. N is the number of molecules of each species (denoted by the subscript) present in the simulation. Note that each water bead represents 4 water molecules. L is the box length in the x, y, and z direction. t is the total simulation time.

No.	C_{DDA} (wt%)	Charge %	T (K)	N_{DDA^+}	N_{DDA^n}	N_{Cl}	N_{Water}	L_x (nm)	L_y (nm)	L_z (nm)	t (µs)
1	1.86	100	348	210	0	210	28550	15.34	15.34	15.34	1.2
2	5	100	348	200	0	200	10000	11.00	11.00	11.00	1
3	5	90	348	180	20	180	10000	11.00	11.00	11.00	1
4	5	80	348	160	40	160	10000	11.00	11.00	11.00	1
5	5	70	348	140	60	140	10000	11.01	11.01	11.01	1
6	5	60	348	120	80	120	10000	11.03	11.03	11.03	1
7	5	50	348	100	100	100	10000	11.03	11.03	11.03	1
8	5	40	348	80	120	80	10000	11.02	11.02	11.02	1
9	5	30	348	60	140	60	10000	11.03	11.03	11.03	1
10	5	20	348	40	160	40	10000	11.04	11.04	11.04	1
11	5	10	348	20	180	20	10000	11.06	11.06	11.06	1
12	5	0	348	0	200	0	10000	11.06	11.06	11.06	1
13	13	80	348	800	200	0	17200	13.55	13.55	13.55	2
14	20	100	348	1000	0	1000	10000	11.64	11.64	11.64	1
15	20	90	348	900	100	900	10000	11.64	11.64	11.64	1
16	20	80	348	800	200	800	10000	11.65	11.65	11.65	1
17	20	70	348	700	300	700	10000	11.65	11.65	11.65	1
18	20	60	348	600	400	600	10000	11.68	11.68	11.68	1
19	20	50	348	500	500	500	10000	11.69	11.69	11.69	1
20	20	40	348	400	600	400	10000	11.68	11.68	11.68	1
21	20	30	348	300	700	300	10000	11.72	11.72	11.72	1
22	20	20	348	200	800	200	10000	11.76	11.76	11.76	1
23	20	10	348	100	900	100	10000	11.81	11.81	11.81	1
24	20	0	348	0	1000	0	10000	11.84	11.84	11.84	1
25	26	100	348	1000	0	1000	7500	10.82	10.82	10.82	3
26	35	100	348	1000	0	1000	4780	9.77	9.77	9.77	5
27	35	100	348	4000	0	4000	22885	16.11	16.11	16.11	12
28	35	90	348	900	0	900	4780	9.76	9.76	9.76	3
29	35	80	348	800	0	800	4780	9.76	9.76	9.76	3
30	35	80	348	3200	800	3200	22885	16.11	16.11	16.11	12
31	35	70	348	700	0	700	4780	9.76	9.76	9.76	3
32	35	70	348	2800	1200	2800	22885	16.11	16.11	16.11	6
33	35	60	348	600	0	600	4780	9.78	9.78	9.78	3
34	35	60	348	2400	1600	2400	22885	16.14	16.14	16.14	6
35	35	50	348	500	0	500	4780	9.79	9.79	9.79	3
36	35	40	348	400	0	400	4780	9.79	9.79	9.79	3
37	35	30	348	300	0	300	4780	9.84	9.84	9.84	3
38	35	20	348	200	0	200	4780	9.85	9.85	9.85	1
39	35	10	348	100	0	100	4780	9.91	9.91	9.91	1
40	35	0	348	0	0	0	4780	9.98	9.98	9.98	1
41	35	100	348	4000	0	4000	22885	16.12	16.12	16.12	6
42	54	100	348	1000	0	1000	2191	8.52	8.52	8.52	1
43	60	100	348	1000	0	1000	2054	8.44	8.44	8.44	1
44	60	90	348	900	100	900	2054	8.39	8.39	8.39	1
45	60	80	348	800	200	800	2054	8.46	8.46	8.46	1
46	60	70	348	700	300	700	2054	8.47	8.47	8.47	1
47	60	60	348	600	400	600	2054	8.42	8.42	8.42	1
48	60	50	348	500	500	500	2054	8.41	8.41	8.41	1
49	60	40	348	400	600	400	2054	8.43	8.43	8.43	1
50	60	30	348	300	700	300	2054	8.46	8.46	8.46	1
51	60	20	348	200	800	200	2054	8.52	8.52	8.52	1
52	60	10	348	100	900	100	2054	8.57	8.57	8.57	1
53	60	0	348	0	1000	0	2054	8.64	8.64	8.64	1
54	75	5	348	50	950	5	857	7.82	7.82	7.82	1

Table 6.2: Details of coarse-grained simulations of DDA/silica phase formation. N is the number of molecules of each species (denoted by the subscript) present in the simulation. Note that each water bead represents 4 water molecules. L is the box length in the x, y, and z direction. t is the total simulation time.

No.	C_{DDA} (wt%)	Charge %	T (K)	N_{DDA^+}	N_{DDA^n}	N_{SI2}	N_{SISN}	N_{SN2}	N_{SI8c}	$N_{SI4SN4c}$	N_{SN8c}	N_{TMA}	N_{Water}	L_x (nm)	L_y (nm)	L_z (nm)	t (µs)
Silica Dimers																	
1	13	95	348	1000	52	63	1413	628	0	0	0	539	18108	8.26	8.26	45.60	2
2	13	90	348	1000	111	160	1703	359	0	0	0	1023	19124	8.28	8.28	48.32	2
3	13	80	348	1000	250	407	1914	179	0	0	0	1728	21517	8.28	8.28	48.32	2
4	13	70	348	1000	428	733	2013	110	0	0	0	2479	24581	8.35	8.35	62.58	2
5	13	65	348	1000	538	938	2049	89	0	0	0	2925	26474	8.36	8.36	67.49	2
6	13	60	348	1000	666	1179	2080	73	0	0	0	3438	28678	8.37	8.37	73.24	2
7	11	70	348	1000	428	733	2013	110	0	0	0	2479	29718	8.32	8.32	72.47	3
8	9	80	348	1000	250	407	1914	179	0	0	0	1728	32509	8.26	8.26	75.70	1
9	7	90	348	1000	111	160	1703	359	0	0	0	1023	37966	8.22	8.22	84.56	1
Silica Octamers																	
10	13	95	348	1000	52	0	0	0	15	354	157	536	18108	8.06	8.06	44.49	4
11	13	80	348	1000	250	0	0	0	101	480	44	1728	21517	8.10	8.10	53.13	6
12	13	60	348	1000	666	0	0	0	294	521	18	3436	28678	8.16	8.16	71.36	4

6.2.2 DDA Model

For the Martini 3 DDA model, one bead is used to represent the headgroup which contains the charged amine group, while the alkane tail is described by three beads, representing four carbon atoms (and adjoining hydrogens) each (see Figure 6.1). The bond and angle parameters generated for this mapping scheme are presented in Tables 6.3 and 6.4 respectively. The same mapping scheme is used for both neutral and charged DDA species. Martini 3 bead types were selected following the suggestions of the authors of the Martini 3 forcefield [13]. The alkane tail beads (T_2-T_4) are assigned the C1 (strongly apolar) bead type in both neutral and charged models. For neutral DDA, the headgroup bead (H_1) is assigned the TN6d bead type (N6 describes a neutral and mildly polar group), while for the charged model, the TQ5p bead type is used (Q5 describes a charged polar bead). These headgroup beads use the tiny bead size (since they represent only one heavy atom), and the 'd' and 'q' labels represent hydrogen bond donor behaviour.

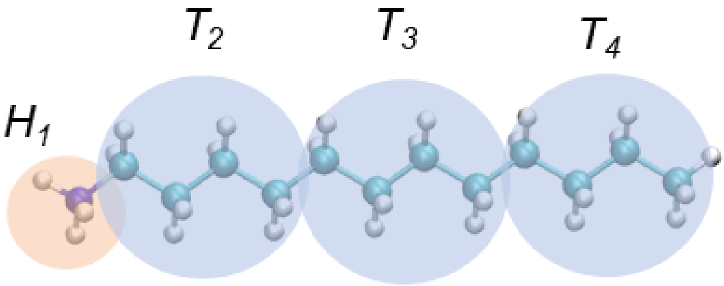

Figure 6.1: The Martini 3 mapping scheme for DDA cations. Alkane tail beads are shown in blue (T_2-T_4), while the charged head bead is shown in orange (H_1).

Table 6.3: Bonded parameters for DDA Martini 3 model. Bead names refer to labels in Figure 6.1. b_{ij} is the bond length and k_{ij} is the bond force constant.

Bond	b_{ij} (nm)	k_{ij} (kJ mol^{-1} nm^{-2})
H_1-T_2	0.420	4,070
T_2-T_3	0.379	4,600
T_3-T_4	0.369	5,690

Table 6.4: Angle type parameters for DDA Martini 3 model. Bead names refer to labels in Figure 6.1. θ_{ijk} is the angle between beads and k_{ijk} is the angle force constant.

Beads	θ_{ijk} (degrees)	Calculated k_{ijk} (kJ mol^{-1} deg^{-2})
H_1-T_2-T_3	141	62
T_2-T_3-T_4	144	72

6.2.3 Phase Diagrams of DDA

The closest description of experimental phase behaviour for the amine surfactant, DDA, to protonation/deprotonation of the primary amine group is given in the work of Karlsson et al., who studied the phase behaviour of a ternary system of water, DDA and acetic acid [216]. In that study, acetic acid was added to systems to induce phase transition of the DDA/water phase, driven by proton transfer between the acid and DDA species. Since the acid used by Karlsson et al. is much smaller than DDA, the salt produced by this proton transfer is less likely to influence phase behaviour, acting as an organic counter-ion rather than forming a catanionic surfactant complex, which occurs when the length of the alkyl chain in acid and amine is similar [213, 214]. In order to isolate the effect of changing the protonation state of the amine group, the salt of acetic acid is not simulated explicitly here; instead, only the proportion of charged DDA species is varied. As previously discussed, chloride counter-ions are added to achieve a neutral overall charge for the system due to their relatively inert nature, allowing the effect of modifying the proportion of charged DDA species to be isolated.

To compare with phase behaviour in this experimental system, it is necessary to transform the experimental phase diagram produced in that study (shown in Figure 6.2a) to a plot of the proportion of charged DDA species (which results from the addition of acid) against the surfactant concentration, as this phase diagram can be directly explored through simulation by varying the proportion of charged DDA molecules in the system. In Figure 6.2a, the black line indicates an equimolar ratio of acetic acid to DDA, at which point it is assumed that all DDA species become charged due to proton transfer between acid and DDA. Below this line (the shaded region in Figure 6.2a) only a proportion of DDA species are charged. The proportion of charged DDA species at any point in this region is simply calculated from the ratio of acid to DDA:

$$x_{DDA^+} = \frac{C_{acid}}{C_{amine}} \tag{6.2}$$

where x_{DDA^+} is the proportion of charged DDA species, and C_{acid} and C_{amine} are the molar concentrations of the acid and amine, respectively. Through this method, the ternary phase diagram in Figure 6.2a is transformed into a phase diagram for a binary DDA/water system dependent on the DDA concentration and the proportion of charged DDA species, presented in Figure 6.2b.

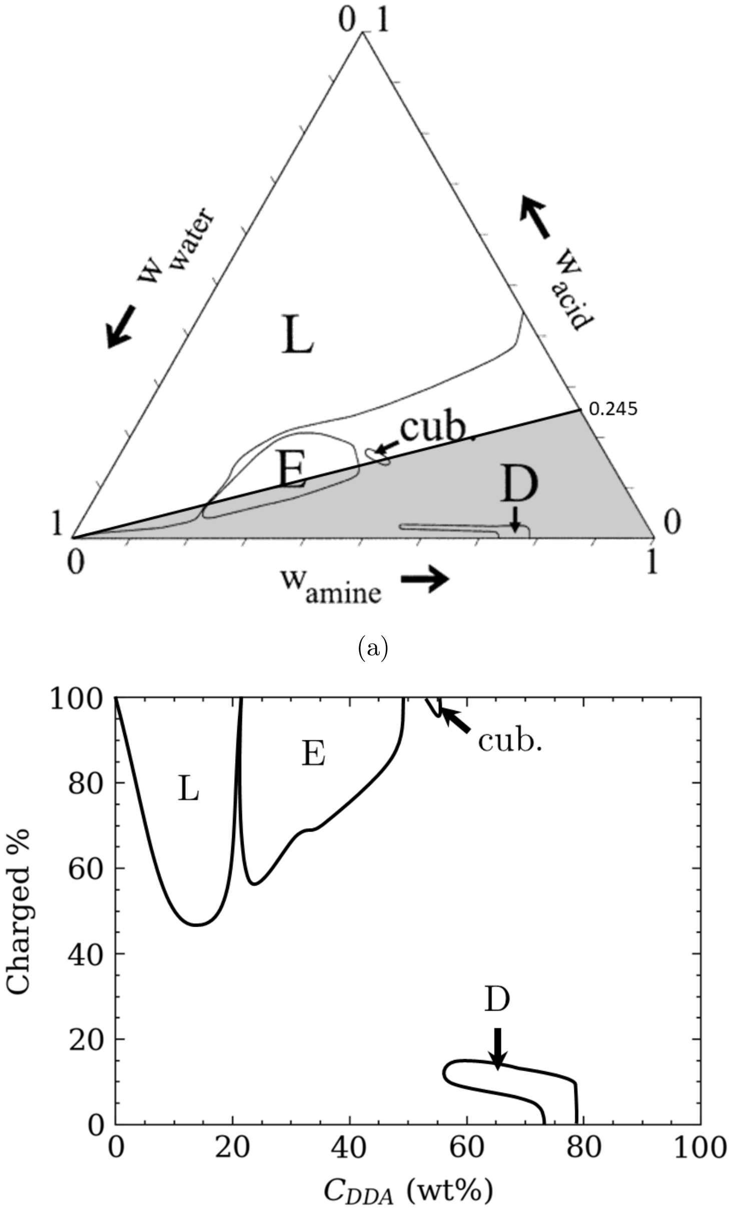

(a)

(b)

Figure 6.2: In (a), a ternary phase diagram of the water/DDA/acetic acid system is shown, adapted from [216]. The black line represents an equimolar ratio of acetic acid and DDA and the shaded region under this line represents the region in which a proportion of DDA species are uncharged. The figure labels correspond to the experimentally observed phases: liquid/micellar (L), hexagonal (E), cubic (cub.) and lamellar (D), while the unlabelled region indicates insolubility of DDA in water. In (b), the shaded region of the phase diagram in (a) is transformed to an experimental phase diagram for a binary DDA/water system dependent on DDA concentration and proportion of charged DDA species.

6.3 DDA Simulation Results

6.3.1 Cationic DDA System

Initially, a set of simulations was carried out with all DDA molecules fully protonated to assess the validity of the model against the experimental phase diagram for a binary DDA/water system (see Figure 6.3). One simulation was carried out at very low surfactant concentration (0.1 M or 1.86 wt%) in the liquid region of the phase diagram, one near the interface between liquid and hexagonal regions (26 wt%), one in the hexagonal region (35 wt%) and one in the lamellar region (60 wt%). Snapshots of the final configurations obtained in these simulations are shown in Figure 6.4. At 0.1 M, a small number of approximately spherical micelles are formed. At 26 wt%, worm-like micelles are formed, indicating that this concentration lies above the sphere-to-rod transition. At 35 wt%, a well-ordered hexagonal phase is observed, and at 60 wt%, a lamellar phase forms. All phases observed in simulations agree well with the experimental phase diagram for DDA, indicating that the model reproduces the experimentally observed phase behaviour well.

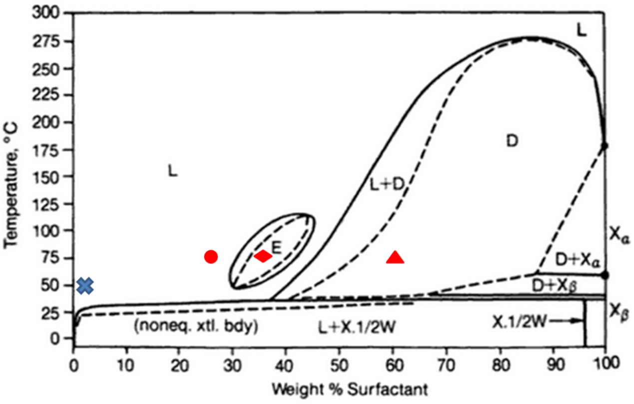

Figure 6.3: Experimental phase diagram for a binary DDA/water system dependent on DDA concentration and temperature, adapted from [252] with experimental data taken from [253]. Letters indicate the following phases: L, liquid; E, hexagonal liquid crystal; D, lamellar liquid crystal; X_α and X_β, dry crystal; X.nW, crystal hydrate with n water molecules. The dashed lines indicate boundaries for metastable regions. The symbols indicate points at which simulations were carried out: 0.1 M at 50 °C (blue cross) and 26 wt% (red circle), 35 wt% (red diamond) and 60 wt% (red triangle) at 75 °C.

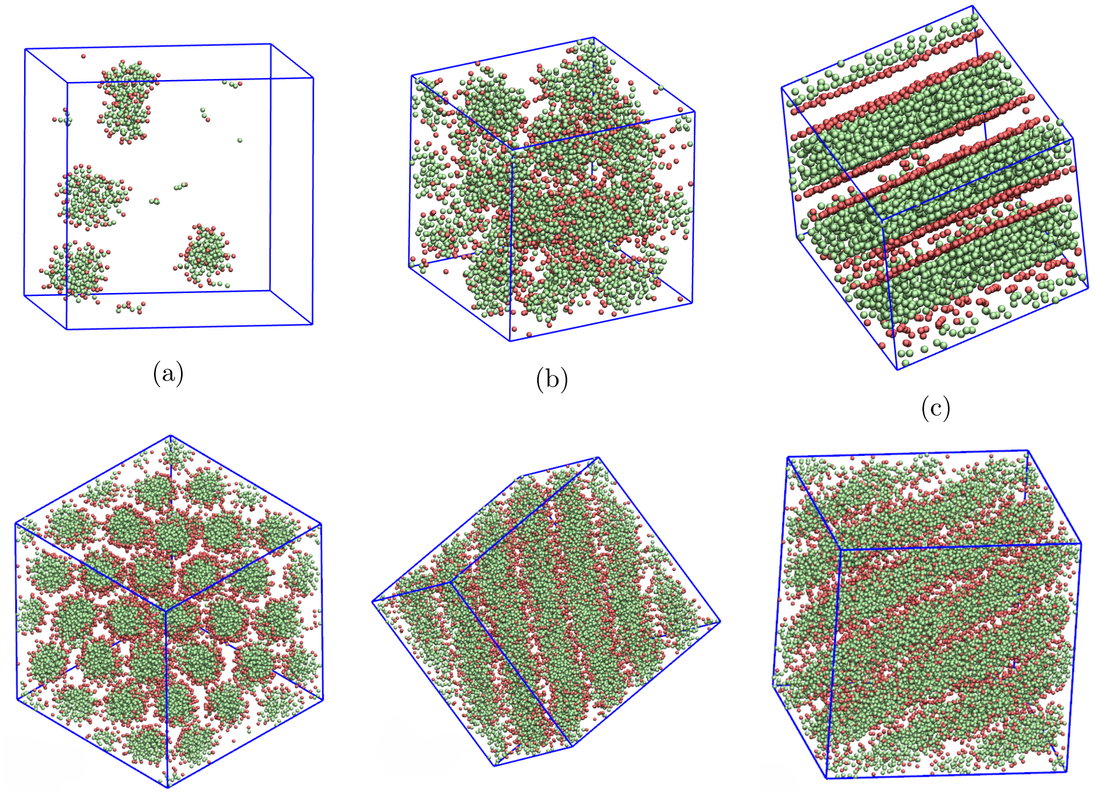
(a) (b) (c) (d) (e) (f)

Figure 6.4: Simulation snapshots of the final configurations for DDA self-assembly at 1.86 wt% (a), 26 wt% (b), 60 wt% (c) and 35 wt% (d-f), corresponding to points marked on the experimental phase diagram (Figure 6.3). Red beads represent charged DDA headgroups, while green beads represent DDA tail groups. Water and chloride counterions are hidden for clarity.

6.3.2 Effect of Proportion of Charged DDA

To understand the influence of charge on the phase behaviour of DDA, the phase diagram of DDA concentration against proportion of charged species (presented in Figure 6.2b) was explored computationally by selecting points to probe the regions at which phase transitions are expected to occur, as summarized in Table 6.1. The phases observed in simulations were superimposed on the experimental phase diagram [216], in Figure 6.5. At points on the phase diagram that lie between distinct phases, phase determination is more difficult. These points are labelled as “transition” points on the phase diagram in Figure 6.5. Under these conditions, the arrangement of surfactant molecules may exhibit characteristics of multiple phases, which can be attributed to overlapping free energy minima that trap the surfactant phase in a metastable arrangement in which one particular phase is not dominant.

At lower DDA concentrations ($C_{DDA} \leq 35$ wt%) agreement with the experimental phase diagram is excellent. In particular, the phase transition from a liquid (micellar) to an insoluble phase is very well predicted by the computational model. The hexagonal region of the phase diagram predicted by the computational model appears to be somewhat contracted when compared with experimental data, and a disordered region is observed in the transition between the hexagonal and insoluble regions (i.e., as the proportion of charged DDA species is reduced). At high surfactant concentrations, the phases observed differ significantly from those reported experimentally by Karlsson et al. [216]. Namely, the cubic and lamellar phases reported experimentally are not reproduced by the computational model. Instead, a large lamellar region is observed at higher proportions of charged DDA, while an insoluble region is observed when only very few charged DDA molecules are present. This large lamellar region is, however, observed in other experimental studies of ternary DDA/water/acid systems at high surfactant concentrations, close to the equimolar ratio of amine and acid. Harmann et al. observed large lamellar regions under these conditions with both acrylic acid and methacrylic acid [217], while studies of binary amine surfactant/water systems consistently observe lamellar phases at high amine surfactant concentrations [213, 253, 254].

The differences between the phases observed in this work and in the experimental study of Karlsson et al. can be explained by three main factors. Firstly, as previously discussed, acetic acid, which is present in the experimental study of Karlsson et al., is not explicitly present in our simulations. Acetate ions, the conjugate base of acetic acid, may well play a role in phase behaviour and its effect is likely to be more pronounced at high surfactant concentrations, i.e. close to the equimolar ratio of surfactant and acid, due to the larger proportion of acid and conjugate base present compared with water. Secondly, the simulations in this work take place at a higher temperature (348 K) than that of the experimental system (298 K), which was necessary to promote phase formation within achievable computational time. Thirdly, simulations are limited in terms of both system size and simulation time. Therefore, it cannot be guaranteed that systems reach a true equilibrium state within the permitted simulation time, or that the relatively small simulation box sizes do not inhibit the formation of certain phases, particularly those that are periodic. In particular, the disordered phases observed in the region that is predicted to form hexagonal phases may actually represent a metastable state that occurs before a true stable equilibrium is reached. However, it is not clear how long would be required for these simulations to reach a true equilibrium state. It is also possible that the experimental data presented by Karlsson et al. is not entirely accurate. This is particularly true of the lamellar and cubic regions of the phase diagram (labelled D and cub. in Figure 6.5, respectively). As mentioned previously, an extensive lamellar region is typically observed for binary water/alkylamine surfactant systems at high surfactant concentrations, however, this region is surprisingly absent from the phase diagram produced by Karlsson et al., and instead there is a small cubic region that is not observed in other work [213, 253, 254]. In addition, since DDA has poor solubility in water at low proportions of charged DDA, as shown by both simulations in this work and the large insoluble region in the phase diagram produced by Karlsson et al., the observation of a lamellar region where no acid is added is surprising. Since the experimental observations of Karlsson et al. have not been verified by further studies, it is possible that these unusual observations do not represent the real behaviour of these systems.

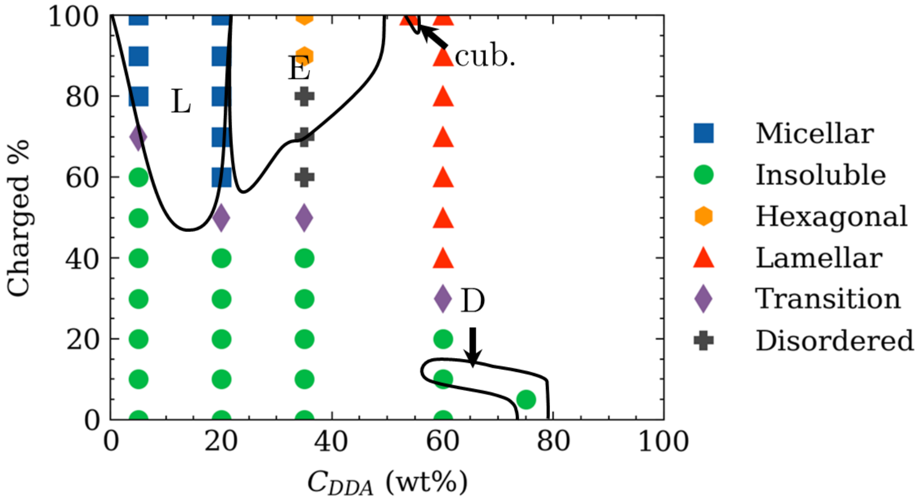

Figure 6.5: Experimental phase diagram for a binary DDA/water system dependent on DDA concentration and proportion of charged DDA species with simulation observations plotted. Data is derived from [216]. Labels on the diagram which correspond to experimental observations are the same as in Figure 6.2a while observations at points where simulations were carried out are given in the legend.

Simulation snapshots of the final configurations obtained at 5 wt % DDA for selected values of x_{DDA^+} are shown in Figure 6.6. At 5 wt % DDA and high proportion of charged surfactant ($x_{DDA^+} > 0.7$), DDA molecules arrange into spherical micelles that are stabilised by repulsive electrostatic interactions between surfactant headgroups, similarly to what takes place in solutions of permanently charged alkylammonium surfactants [220]. As small proportions of neutral DDA species are added, these are incorporated into the micelles. Although the neutral amine head group is not nearly as polar as when it is charged, it still shows some degree of amphiphilic behaviour, and so it adopts a similar position as charged DDA at the micelle surface - i.e., with alkyl tails in the micelle core and amine head groups at the surface. However, because they are not charged, the more neutral DDA molecules are present, the lower the repulsion between head groups. This decrease in electrostatic repulsion causes a decrease in the overall curvature of the aggregates, and therefore the average micelle size increases (see Figure 6.7). At x_{DDA^+} $= 0.7$, this curvature decrease drives a sphere-to-rod transition wherein much larger, elongated micelles are formed, incorporating both charged and neutral DDA. At x_{DDA^+} < 0.6 the DDA species become insoluble in water and separate out into a single cluster, with a small number of charged DDA molecules remaining present in water as isolated monomers.

It is important to note that the insoluble cluster formed at a low proportion of charged DDA species is different in nature to the micelles formed when there is a higher proportion of charged DDA species present. This is demonstrated in Figure 6.8, where the average radial density profiles of the cluster(s) are compared. At $x_{DDA^+} = 1.0$ (Figure 6.6a), the headgroup is concentrated in a single region at the surface of the clusters, indicating a well-defined micellar structure. This structure is initially retained as the proportion of neutral DDA increases (Figure 6.6b). However, at $x_{DDA^+} = 0.0$ (Figure 6.6d) a significant proportion of the headgroups of DDA molecules is contained within the cluster and its distribution is nearly flat, indicating that the aggregate is amorphous in nature.

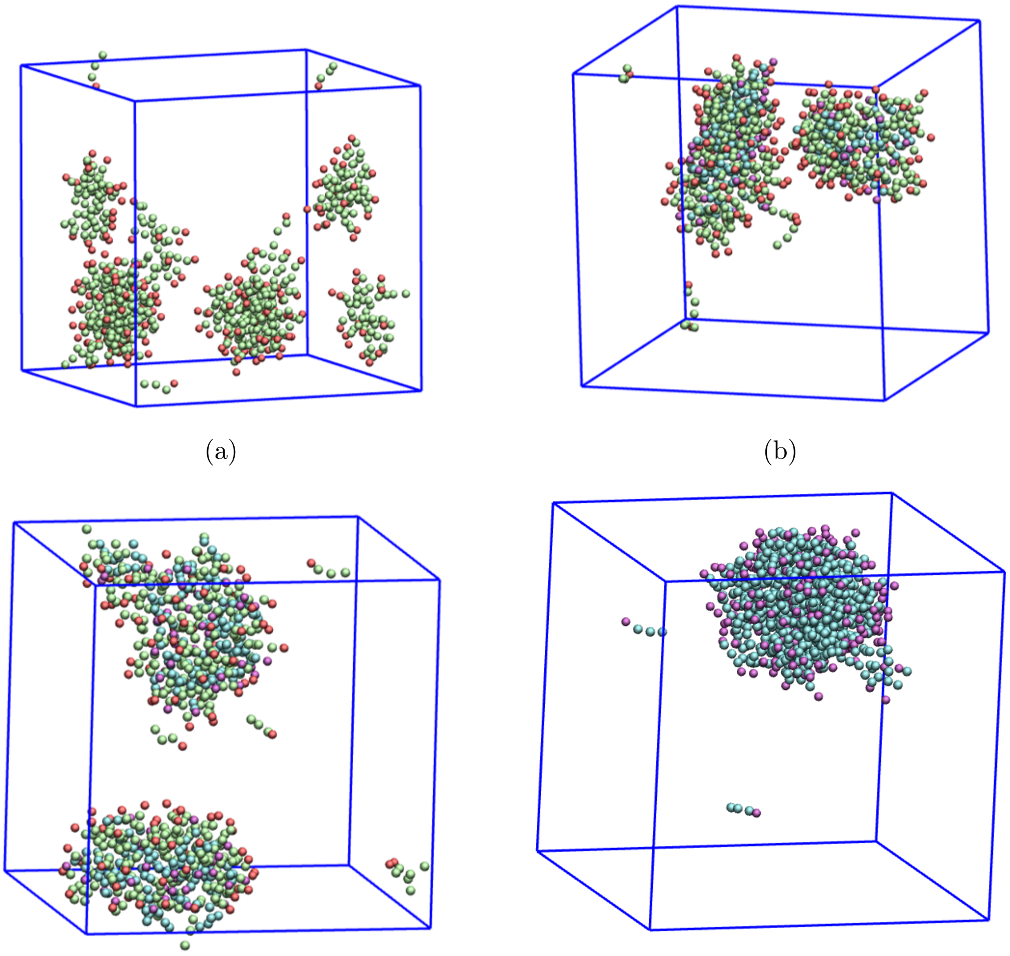

(a)

(b)

(c)

(d)

Figure 6.6: Simulation snapshots of the final configurations for DDA self-assembly simulations at 5 wt % of DDA at varying x_{DDA^+}, (a) = 1.0, (b) = 0.7, (c) = 0.6, (d) = 0.0. Red and purple beads represent charged and neutral DDA headgroups respectively, while green and blue beads represent neutral DDA tail groups respectively. Water and chloride counter-ions are hidden for clarity.

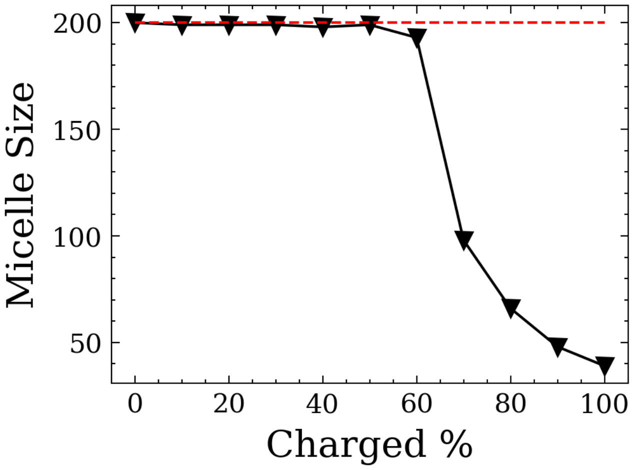

Figure 6.7: DDA micelle size (average number of DDA molecules) for different degrees of charge at 5 wt% DDA as determined by simulation. The dashed red line indicates the maximum possible micelle size, which is equal to the total number of surfactant molecules in the simulation box.

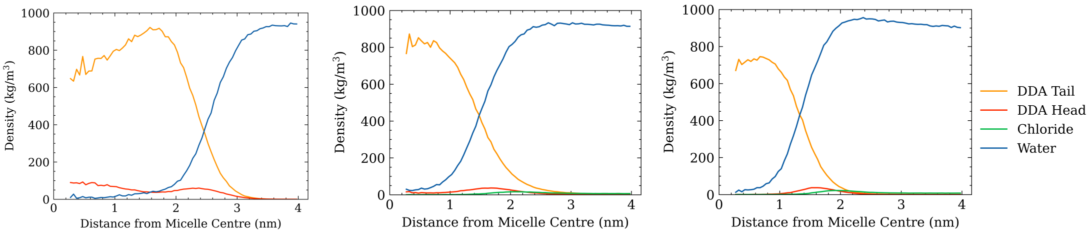

(a) (b) (c)

Figure 6.8: Radial density profiles taken from the centre of mass of aggregates for systems at 5 wt % DDA for $x_{DDA^+} = 0.0$ (a), $x_{DDA^+} = 0.8$ (b) and $x_{DDA^+} = 1.0$ (c).

When the total concentration of DDA is increased to 20 wt % (see snapshots in Figure 6.9) the behaviour is analogous. Spherical micelles are still observed at high proportions of charged DDA ($x_{DDA^+} > 0.6$) and a similar transition to an insoluble phase is observed at $x_{DDA^+} = 0.5$, below which DDA appears to be insoluble in water.

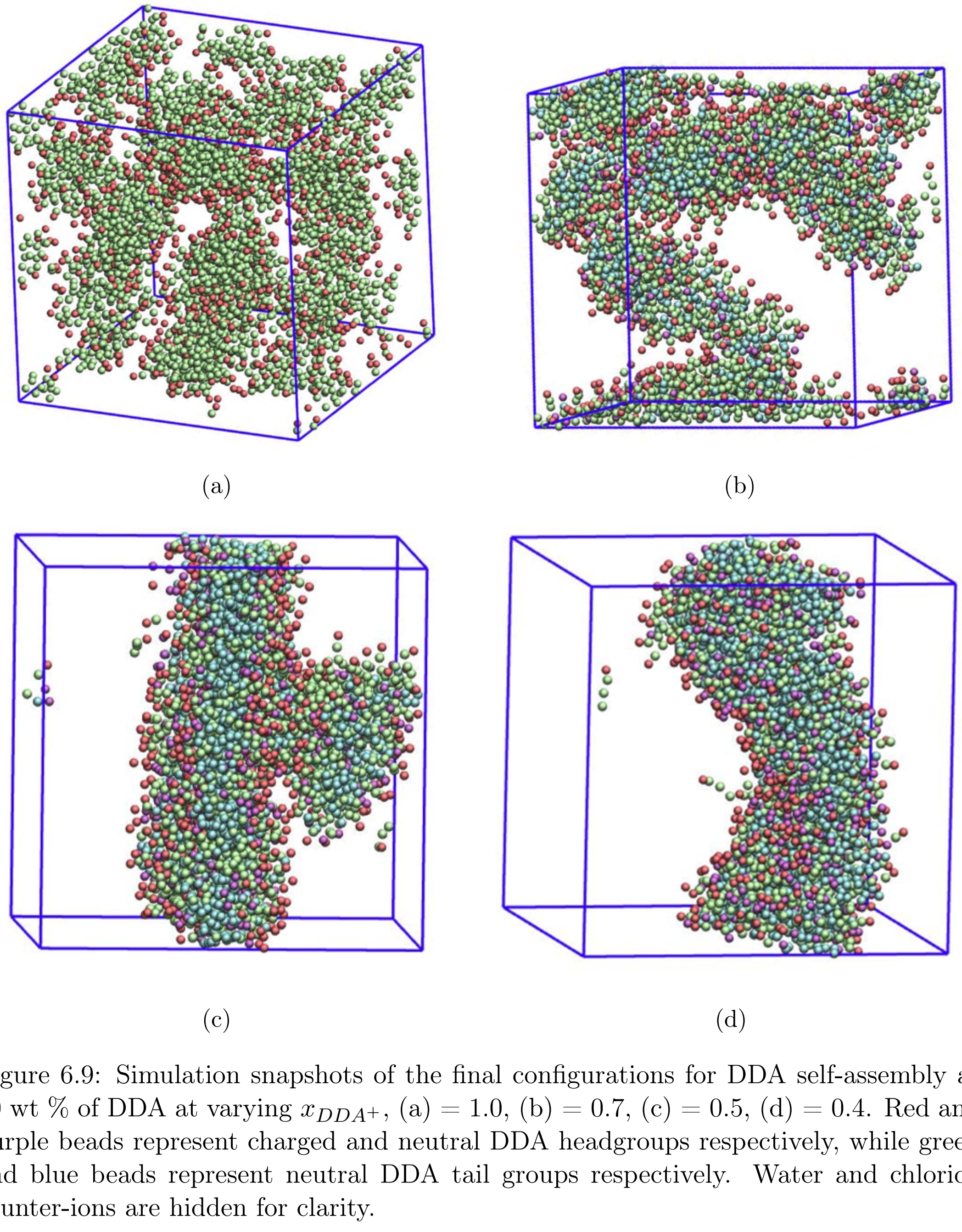

(a) (b) (c) (d)

Figure 6.9: Simulation snapshots of the final configurations for DDA self-assembly at 20 wt % of DDA at varying x_{DDA^+}, (a) = 1.0, (b) = 0.7, (c) = 0.5, (d) = 0.4. Red and purple beads represent charged and neutral DDA headgroups respectively, while green and blue beads represent neutral DDA tail groups respectively. Water and chloride counter-ions are hidden for clarity.

Upon increasing DDA concentration to 35 wt % (see snapshots for selected values of x_{DDA^+} in Figure 6.10), a well ordered hexagonal liquid crystal (HLC) phase is observed at high proportions of charged DDA ($x_{DDA^+} \geq 0.9$). As the proportion of charged DDA is reduced to $x_{DDA^+} = 0.8$, while the system still consists of long wormlike micelles, these become disordered because the proportion of charged species is not sufficient to promote the formation of a stable ordered phase. At $x_{DDA^+} = 0.5$, a transition is observed, with this system showing a lamellar character, with several bilayer sheets being stabilised by charged DDA species at the surface. Once again, this transition from a hexagonal to a (potentially) lamellar phase can be traced back to the decrease in curvature caused by decreasing electrostatic repulsion between head groups as the percentage of neutral DDA increases. As the proportion of charged species is lowered even further ($x_{DDA^+} \leq 0.4$), the DDA phase fully separates into an insoluble region.

At a DDA concentration of 60 wt % (see snapshots in Figure 6.11), a well ordered lamellar phase is observed for a broad range of proportions of charged DDA ($x_{DDA^+} \geq 0.4$). At $x_{DDA^+}= 0.3$, a transition is observed towards an insoluble phase, as there are too few charged species to stabilise the bilayers of the lamellar phase. Notably, this transition phase is similar to that observed at 35 wt % DDA at $x_{DDA^+} = 0.5$ (Figure 6.10c), suggesting that the lamellar phase may extend to even lower DDA concentrations than 60 wt %. At $x_{DDA^+} \leq 0.3$, the DDA phase fully separates from water, becoming insoluble.

Two further regions of the experimental phase diagram in Figure 6.2b were explored in simulations. The first is at a DDA concentration of 54 wt % and $x_{DDA^+}= 1.0$, which is predicted to assemble into a cubic phase. However, in this simulation a well-ordered lamellar phase is observed (Figure 6.12a). The second region explored lies in the lamellar region of the experimental phase diagram at a DDA concentration of 75 wt % and $x_{DDA^+}= 0.05$. In this simulation the DDA species remain insoluble in water with no lamellar phase observed.

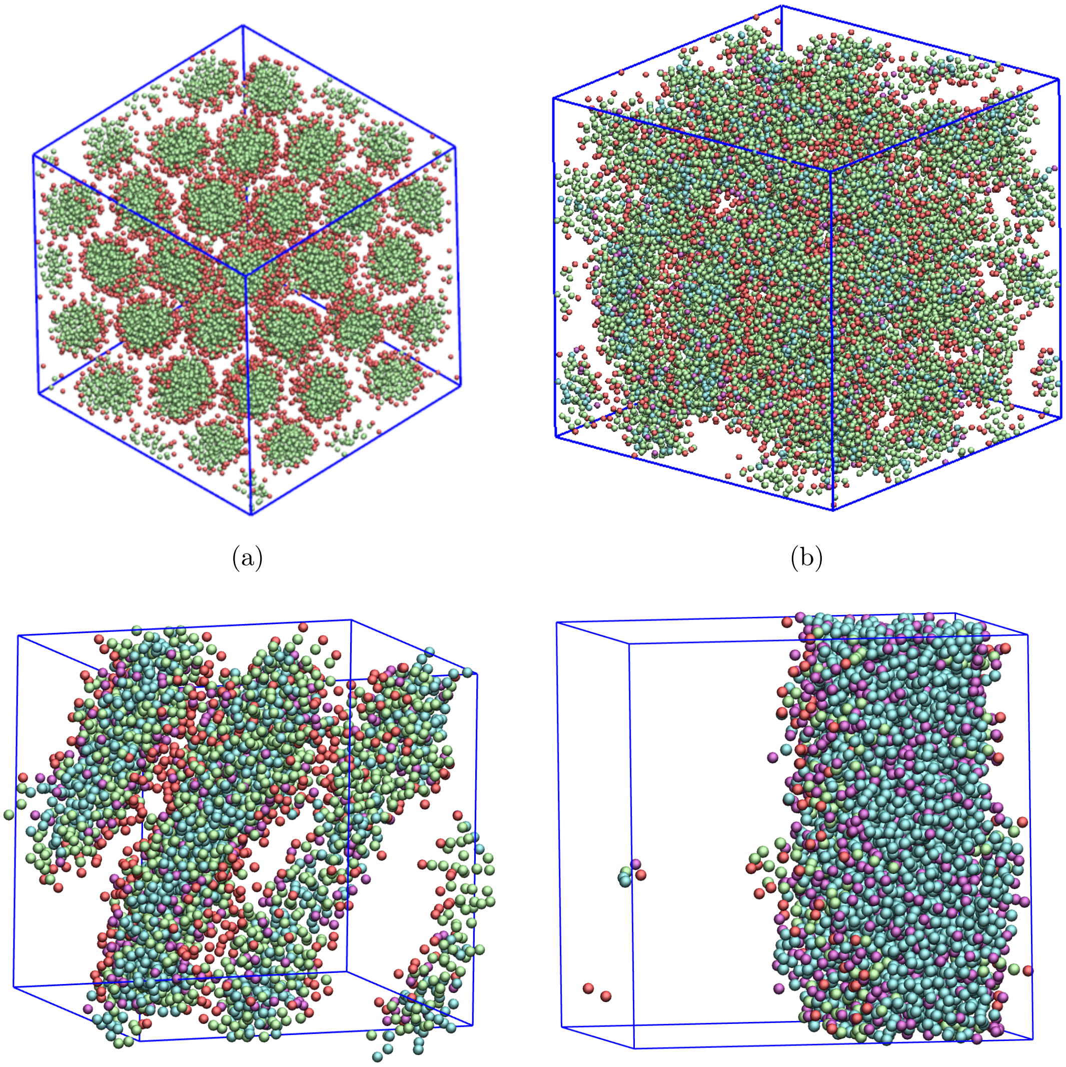

(a) (b)

(c) (d)

Figure 6.10: Simulation snapshots of the final configurations for DDA self-assembly simulations at 35 wt % of DDA at varying x_{DDA^+}, (a) = 1.0, (b) = 0.8, (c) = 0.5, (d) = 0.1. The colour code is the same as in Figure 6.6 with water and chloride ions hidden for clarity.

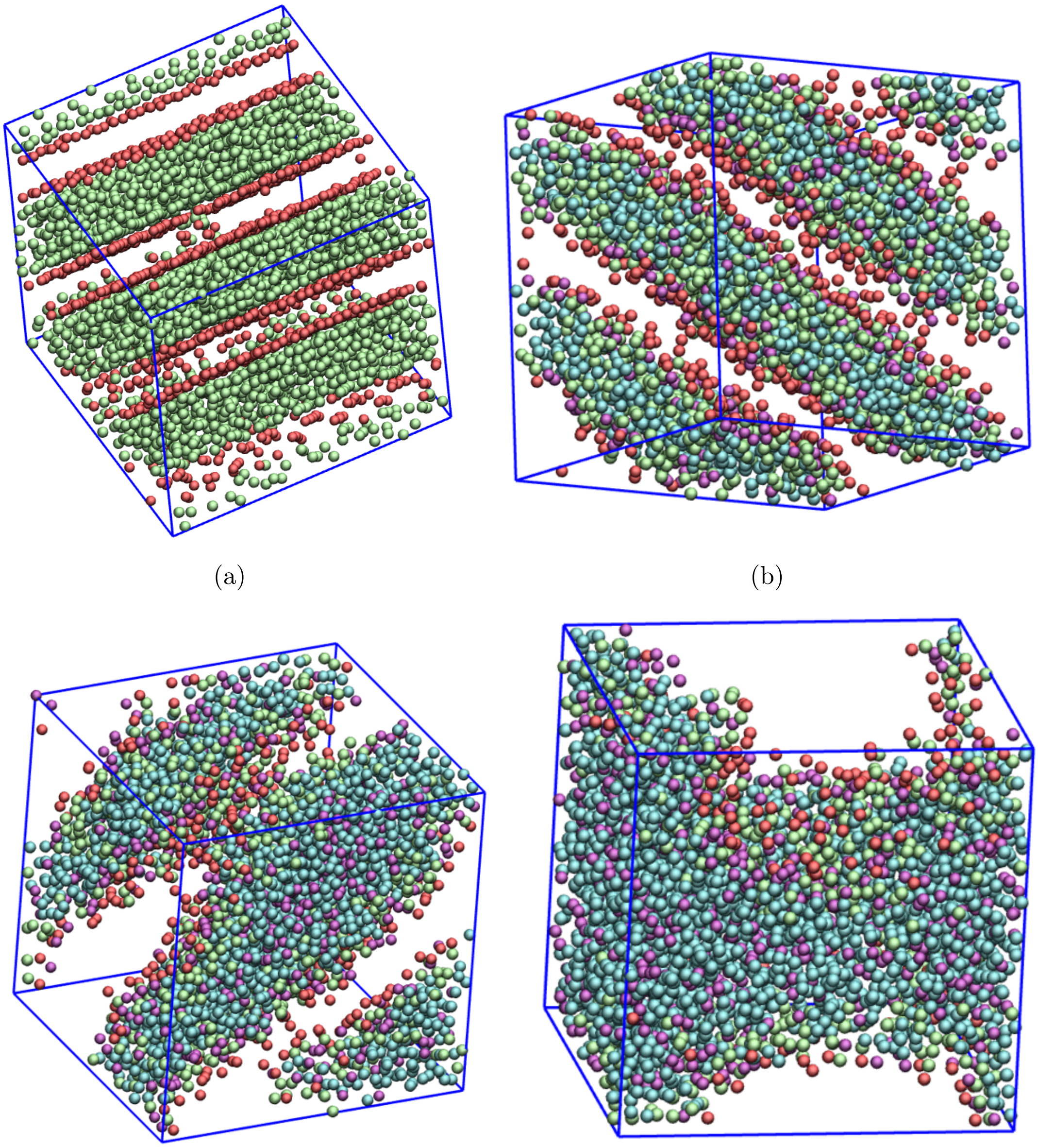

(a)

(b)

(c)

(d)

Figure 6.11: Simulation snapshots of the final configurations for DDA self-assembly simulations at 60 wt % of DDA at varying x_{DDA^+}, (a) = 1.0, (b) = 0.5, (c) = 0.3, (d) = 0.2. The colour code is the same as in Figure 6.6 with water and chloride ions hidden for clarity.

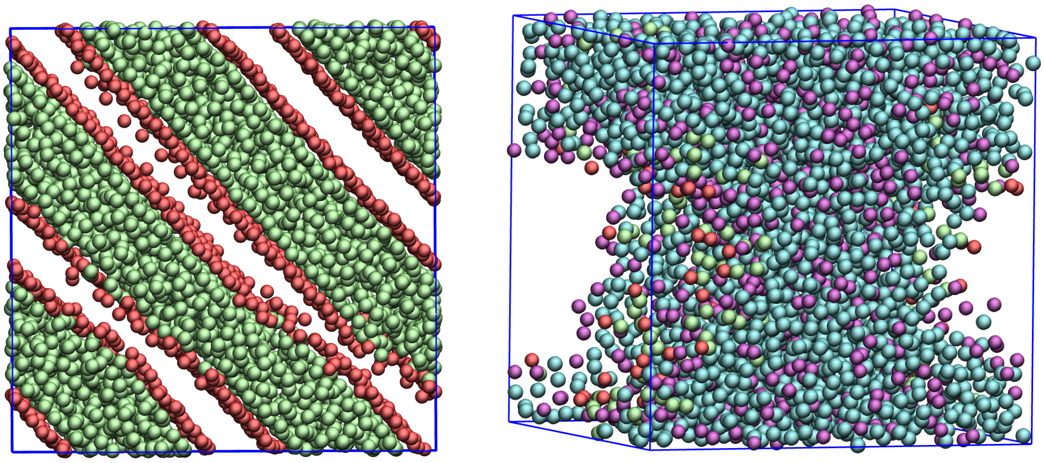

(a) (b)

Figure 6.12: Simulation snapshots of the final configurations for DDA self-assembly simulations at 54 wt % of DDA, $x_{DDA^+} = 1.0$ (a) and 75 wt %, $x_{DDA^+} = 0.05$ (b). The colour code is the same as in Figure 6.6 with water and chloride ions hidden for clarity.

6.3.3 DDA/Water/Silica Systems

In Figure 6.13, the phases observed in simulations of ternary DDA/water/silica dimer systems are superimposed on the experimental binary DDA/water phase diagram. The points where simulations were carried out correspond to the micellar region of the experimental phase diagram, for which good agreement was observed with previous simulations of binary DDA/water systems. With the addition of silica dimers at higher proportions of charged DDA ($x_{DDA^+} \geq 0.7$), DDA molecules arrange into micelles that are smaller at higher proportions of charged DDA, and grow in size to form long, worm-like micelles as the proportion of DDA is reduced (see Figures 6.14 and 6.15b and c), similarly to the behaviour of the binary DDA/water system. To assess whether the aggregation into longer, worm-like micelles is promoted by the inclusion of silicates, an additional simulation at 13 wt% DDA without silica was carried out (for full details, see Table 6.1, simulation number 13). The surfactant aggregation number for the simulation with silica was 215, versus an aggregation number of 105 for the simulation without silica. This indicates that the presence of silicate species promotes the aggregation of spherical micelles into longer, worm-like micelles, similarly to the behaviour observed with the CTAB surfactant in this work (see Chapter 4), and in literature [75, 220]. At lower proportions of charged DDA ($x_{DDA^+} \leq 0.6$), the DDA phase becomes completely separated from water. However, instead of an insoluble phase, which was observed in binary DDA/water simulations, an ordered lamellar phase is observed, as shown in Figure 6.15a.

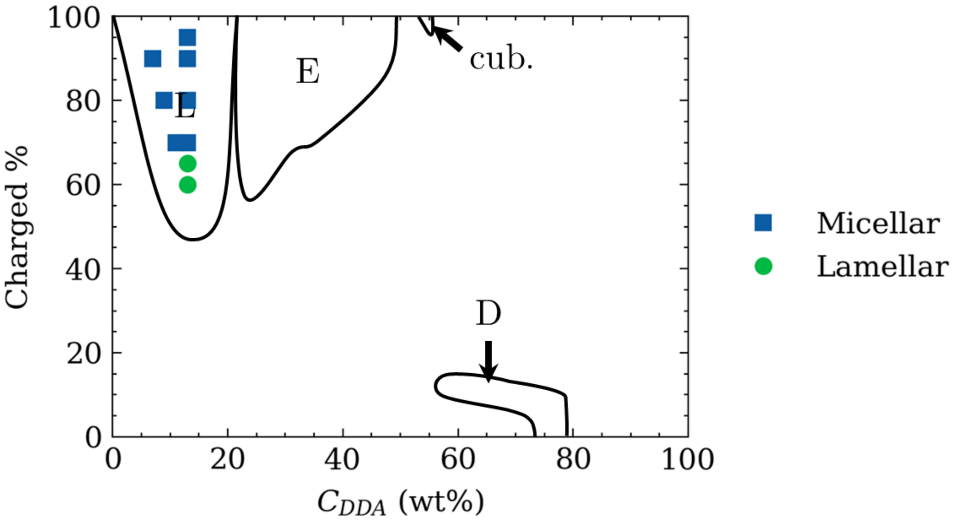

Figure 6.13: Experimental phase diagram for ternary DDA/water/silica dimer systems, dependent on DDA concentration and proportion of charged DDA species with simulation observations plotted. Labels on the diagram which correspond to experimental observations are the same as in Figure 6.2a while observations at points where simulations were carried out are given in the legend.

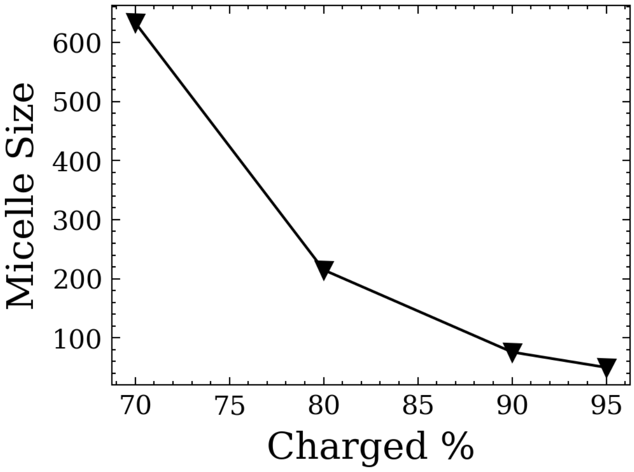

Figure 6.14: DDA micelle size (average number of DDA molecules) for different degrees of charge at 13 wt% DDA in the ternary DDA/water/silica dimer system, as determined by simulation.

Simulations carried out with silica octamers at 13 wt% showed significantly different phase behaviour than simulations with silica dimers at the same points of the phase diagram (see Figure 6.16). At $x_{DDA^+} = 0.6$, while a layered structure resembling a lamellar phase also forms, the curvature of the phase is significantly increased versus the phase observed with silica dimers present. At $x_{DDA^+} = 0.8$, instead of long, worm-like micelles, a lamellar phase forms, with the surfactant phase fully separated from the aqueous phase. At $x_{DDA^+} = 0.95$, the surfactant phase remains separated from the aqueous phase, in contrast to the system with silica dimers which formed dispersed micelles. In this concentrated phase, the surfactant is arranged as disordered rods.

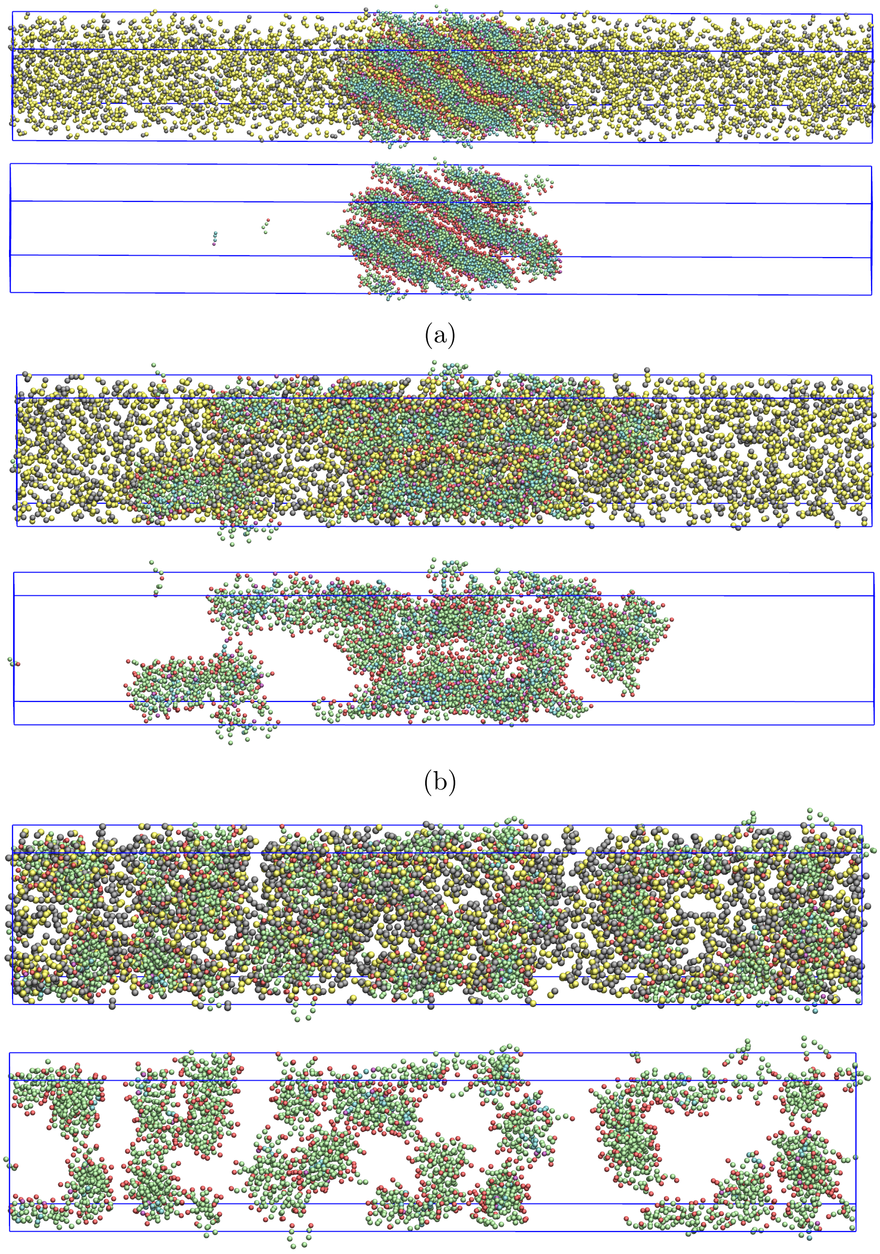
(a)

(b)

(c)

Figure 6.15: Simulations snapshots of the final configurations for DDA/silica dimer self-assembly simulations at 13 wt % of DDA at different proportions of chaged DDA and silica species, $x_{DDA^+} = 0.6$ (a), $x_{DDA^+} = 0.8$ (b) and $x_{DDA^+} = 0.95$ (c). The population of charged silica species is determined by the corresponding pH of the system and is given in Table 6.2. The colour code for DDA species is the same as in Figure 6.6. In the top image, for each value of x_{DDA^+}, charged silica beads are shown in yellow whilst neutral silica beads are shown in grey. In the bottom image, silica species are hidden for increased clarity of the surfactant phase. Water and chloride ions are hidden in all snapshots for clarity.

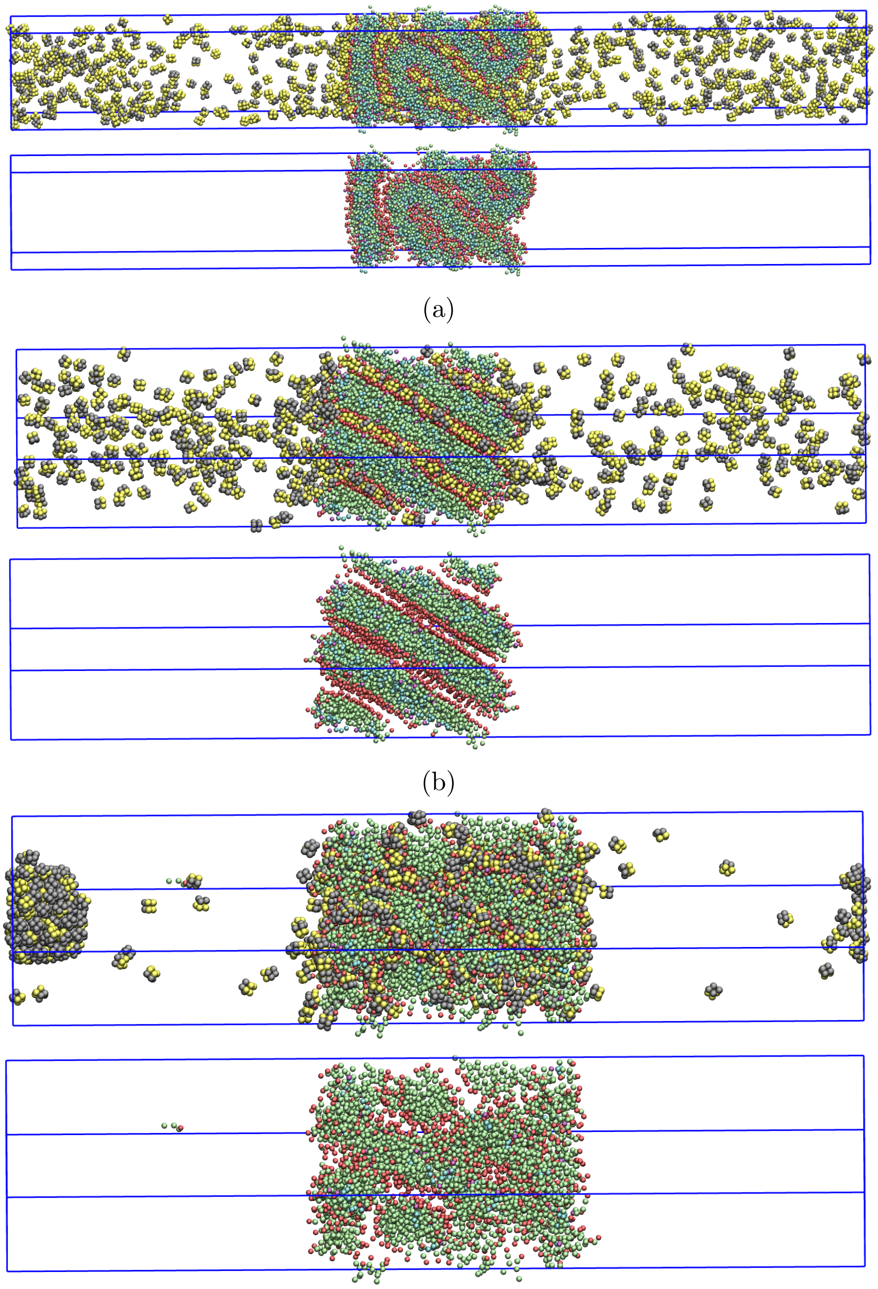

(a)

(b)

(c)

Figure 6.16: Simulations snapshots of the final configurations for DDA/silica octamer self-assembly simulations at 13 wt % of DDA at different proportions of charged DDA and silica species, $x_{DDA^+} = 0.6$ (a), $x_{DDA^+} = 0.8$ (b) and $x_{DDA^+} = 0.95$ (c). The population of charged silica species is determined by the corresponding pH of the system and is given in Table 6.2. The colour code is the same as in Figure 6.15. In the bottom image, silica species are hidden for increased clarity of the surfactant phase. Water and chloride ions are hidden in all snapshots for clarity.

These results clearly show that, similarly to the case with CTAB systems (see Chapter 4), the presence of silica species significantly affects the phase behaviour of DDA, promoting aggregation and separation of the surfactant concentration under conditions where only micelles would form without silica present. The simulations carried out at 13 wt% and $x_{DDA^+} = 0.95$ most closely mimic the experimental conditions under which HMS is synthesised [34], with an initial solution pH of approximately 9.2 according to Centi et al. [11]. The differences between the phases formed in simulations carried out with silica dimers and silica octamers indicate that condensation of silicate species plays an important role in facilitating the formation of the surfactant template for these materials. The range of x_{DDA^+} explored by these simulations corresponds to a pH change in solution from approximately 9.3 (at $x_{DDA^+} = 0.95$) to 10.6 (at $x_{DDA^+} = 0.6$). Throughout this pH range, the relative proportions of fully charged, partially charged and neutral silicate species change significantly. As the proportion of charged silicate species increases, the proportion of charged DDA species decreases. Since this charge-matching behaviour is important to promote self-assembly, as identified by Centi et al. [11], and earlier in this work (Chapter 5), understanding how a correct balance of charge between these two populations of species is established (i.e. by controlling system pH) will be important to achieving ordered structures.

There are several limitations to the approach presented here which make it unlikely that the simulations carried out represent the real experimental system in the synthesis of HMS. As previously mentioned, the calculation used to determine the proportion of charged silica octamer species is only based on the pKa value for dimers, rather than the more detailed method laid out in Chapter 5. Therefore, the population of silica octamers used will not represent an experimentally realistic population under the range of pH values investigated. More critically, as previously mentioned, the effective pH of the solution, based on the proportion of charged DDA species present, is approximately 9.3 to 10.6. Under this pH range, silica species will not remain stable as small oligomers, and will undergo extensive condensation reactions to form larger silica particles [19]. Therefore, neither the simulations with dimers or octamers represent experimentally realistic populations of silica. To obtain a more experimentally realistic system, it would be necessary to develop a reactive model for silicates. However, despite these limitations the results here clearly indicate that both the relative proportions of charged species (both surfactant and silicates), and the degree of condensation of silicates play an important role in directing the phase formation of amine surfactant templated materials.

6.4 Conclusions

In this work, we have demonstrated the effect that the proportion of charged (cationic) versus uncharged (nonionic) surfactant species has on the liquid crystal phase behaviour of an alkylamine surfactant, dodecylamine, at a range of surfactant concentrations in solution. Both micellar and liquid crystal phases with lamellar and hexagonal morphology were observed, in equilibrium with water. The solubility of the surfactant was demonstrated to be strongly dependent on the proportion of charged species present, which can be attributed to the increased hydrophilicity of the protonated headgroup. At low and intermediate surfactant concentrations, the phase behaviour observed in simulations closely agreed with experimental data for a ternary water/DDA/acetic acid system, which is the closest experimental comparison for the binary DDA/water system explored in this work. The differences observed at higher DDA concentrations are discussed in detail. However, these results clearly demonstrate how DDA phase behaviour is altered by protonation/deprotonation of the surfactant headgroup, which may be achieved experimentally through control of the system pH. Understanding of this behaviour is important for many applications, including the synthesis of HMS, where the formation of the templating surfactant phase has been shown to be strongly dependent on system pH [11]. With the inclusion of precursor silica species, developed in previous work (Chapter 4), the phase behaviour was explored within the micellar region of the binary DDA/water phase diagram. This showed that the presence of silica dimers and octamers was capable of significantly altering phase behaviour, with lamellar and disordered regions both observed. While the limitations of the brief investigation presented in this chapter were discussed, this demonstrated the importance of both the degree of condensation of silicate species, and the relative proportions of charged surfactant and silicate species on directing the self-assembly of pH-responsive surfactants. The model could also be applied to study the interactions of surfactant species on solid surfaces at different pH values, which is relevant to flotation applications [203].

Chapter 7

Conclusions and Future Work

7.1 Conclusions

In this thesis, a detailed investigation into the mechanisms governing the self-assembly of surfactant species and silica was presented, with particular focus on the self-assembly of templates for ordered mesoporous silica (OMS) synthesis. Two distinct, but complementary, approaches were applied: experimental synthesis and characterisation, and molecular simulations. Special attention was given to the factors surrouding self-assembly that may influence the degree of structural order in materials obtained through templated synthesis, as understanding these factors is critical to enable production of valuable well-ordered OMS via alternative, greener pathways, without the need for energy intensive and wasteful synthesis processes, a proposition that still remains a significant challenge. Through this work, critical observations are made as to how ordered structures are formed early during OMS synthesis, and what factors may affect this degree of order as synthesis progresses. In particular, charge matching at the silica to surfactant interface is demonstrated to be critical to the initial formation of ordered structures, which occurs as silicates are present as oligomers of silicic acid. This self-assembly behaviour is strongly dependent on the protonation/deprotonation of these oligomers by varying the balance of charge at the silica/surfactant interface. Since the charge state of silica oligomers is most strongly controlled by system pH, the pH under which the initial self-assembly takes place is crucially important. When the pH is lowered during synthesis, silica polycondensation reactions occur rapidly as silica precipitates. These reactions are necessary to obtain OMS, but careful consideration of silica condensation reaction kinetics is required to ensure that the well-ordered phase formed during self-assembly is maintained to effectively provide a template for the resultant material. The results in this work suggest that when these reactions are allowed to proceed rapidly, the well-ordered structures are maintained, whereas, when they proceed slowly, the ordering of the silica/surfactant phase is disrupted leading to less well-ordered silica. This is because the charge balance is disrupted by the change in pH, leading to disordering of the silica/surfactant phase before silica precipitates out of solution.

The first major outcome of this work, which is presented in Chapter 4, was the development of a coarse-grained (CG) model for the self-assembly of OMS, which uses the Martini 3 framework [13]. This model was also extended to include the bio-inspired additives arginine and PEHA, so that their effect on self-assembly behaviour could be observed. Building on methods used to develop previous coarse-grained models for OMS self-assembly, in particular the model of Pérez-Sánchez et al. [75, 77], this model is validated against a more realistic atomistic model for silicate species [12] and is fully compatible with the latest version of Martini, which allows the model to be applied to a broader range of systems owing to the increased versatility of Martini 3. In addition, this work establishes the use of fitting parameters to allow for a rational, quantitative approach for fitting the coarse-grained silica model parameters to atomistic data, in contrast with the purely qualitative approach adopted previously in the literature. This chapter also presented an analysis of the effect of using different box dimensions for self-assembly simulations that utilize CG MD models, and identified that elongated and "half-cubic" box dimensions were particularly effective for simulating liquid crystal phase assembly.

In Chapter 5, an experimental investigation into the synthesis of OMS following a rapid, room temperature synthesis was presented. The incorporation of bio-inspired additives into this synthesis was also investigated. This work, which was carried out following a design of experiments (DOE) approach, identified several key factors that strongly impacted both the synthesis yield and resultant material properties. The synthesis yield was shown to be most strongly impacted by silica precursor concentration and the silica to surfactant ratio. A much greater yield was obtained for samples synthesised at higher silica concentrations (> 100 mM), however, yield was observed to decrease significantly as the silica to surfactant ratio was increased. However, incorporating even small amounts of the bio-inspired additive PEHA into the synthesis results in a marked increase in yield. The yield of synthesis is proposed to be primarily affected by competitive formation of colloidal silica particles outside of the silica-surfactant mesophase. The structure of the materials obtained in this synthesis, most notably the BET surface area and degree of structural ordering of pores, were shown to be affected by several factors, including the silica to surfactant ratio, reaction pH and the presence of certain bio-inspired additives. The effect of silica to surfactant ratio was investigated in CG MD simulations, and it was shown that varying this parameter substantially changed the balance of electrostatic charge at the silica-surfactant interface under the conditions at which self-assembly takes place. Therefore, it was proposed that this balance of charge is critical to achieving a well-ordered hexagonal mesophase which results in more well-ordered OMS. The observed effect of reaction pH and additives was proposed to be the result of the impact these factors had on reaction kinetics. Factors that promoted faster silica condensation reactions, following acid addition, produced more well-ordered materials, suggesting that the well-ordered mesophase formed at high pH was "locked in" as pH is lowered. In particular, in CG MD simulations, PEHA, which promoted more ordered structures, was shown to be present at the silica-surfactant interface prior to acid addition, whereas arginine, which did not promote order, was not. Since the amine groups in PEHA are known to catalyse silica condensation reactions, this supports the hypothesis that rapid reaction following acid addition is essential to producing well-ordered OMS following this method. This finding offers a promising avenue of investigation for rapidly producing well-ordered OMS by maximising silica reaction rate following self-assembly at high pH.

In Chapter 6, a CG MD model was developed for the amine surfactant dodecylamine (DDA), which shows interesting pH responsive behaviour and has been used as a surfactant template in the synthesis of hexagonal mesoporous silica [34]. Surfactants with this pH responsive behaviour have great potential for a synthesis of OMS by methods which are able to extract and recycle the surfactant template by exploting this behaviour. Using this model, the phase behaviour of DDA, following changes in both surfactant concentration and degree of charged surfactant species, was explored, clearly demonstrating how phase behaviour is strongly dependent on the proportion of charged DDA species, which experimentally can be controlled by modifying solution pH. A preliminary investigation into a ternary DDA/water/silica system was presented, showing that the relative proportions of both surfactant and silicate species which are charged strongly influences self-assembly behaviour, as does the speciation of silicate species. This model, and the method presented in this chapter, provide a crucial step towards exploiting pH-responsive surfactants for use in producing well-ordered mesoporous silica, as well as optimizing their use in a variety of other applications.

Through this work, two main mechanistic factors can be highlighted as having profound impact on the degree of order of OMS materials. The first of these, which occurs during the self-assembly process itself, is the balance of charge at the silica-surfactant interface. This factor is controlled by modifying the relative proportions of charged species present in the system, as was clearly demonstrated by thorough simulation studies of modifying silica to surfactant ratio in the case of OMS self-assembly (see Section 5.3.5) or modifying the proportion of charged surfactant species in the case of DDA phase behaviour (see Section 6.3.2). This charge-matching behaviour, which was previously identified by Centi et al. [11], is explored in detail in this work and appears to be the primary drive behind the formation of thermodynamically stable ordered surfactant mesophases which provide the template for OMS materials. Achieving these ordered structures in the early stages of OMS synthesis is essential to achieving ordered structures in the final materials. The second critical factor behind achieving well-ordered mesoporous silica appears to be the optimisation of silica condensation reaction kinetics. Upsetting the conditions under which OMS self-assembly takes place will lead to disordering of the material, as demonstrated by CG MD simulations of the effect of changing system pH (see Section 5.3.5). The traditional synthesis method for OMS relies on hydrothermal treatment to maintain the equilibrium structure of the silica-surfactant mesophase, whilst sufficient silica condensation reactions occur to lock in the porous structure. However, alternative methods that use pH modification to promote rapid silica condensation reactions must pay close consideration to how the rate of these reactions can be maximized to lock in this structure before disordering can occur. By optimizing these two factors, it will be possible to synthesize mesoporous silica with a high degree of order following rapid, low-energy and environmentally friendly methods.

7.2 Future Work

Progression of this work could follow either of the two main mechanistic factors which were identified above. The first is related to understanding and controlling the equilibrium structures that form in the early stage of OMS synthesis. Whilst the model developed in this work is perfectly adequate for describing the self-assembly of a CTAB/silica mesophase at high pH (> 13), which gives rise to MCM-41, the methods employed could also be extended to study precursor solutions of other mesoporous silica materials, such as SBA-15 [6] or HMS [34], to similar effect. One potential avenue of investigation would be to focus on those surfactants that may be more easily removed from the porous silica structure following synthesis, such as pH-responsive amine surfactants which were investigated in this work (see Chapter 6). Another family of surfactants with great potential in this area are amino acid based surfactants, particularly those that possess cleavable amide groups, which may present an alternative approach for template removal [255]. Due to the strong electrostatic interactions that make template removal challenging, milder methods of template removal (compared with calcination) often rely on modification of system pH [37]. Therefore, modelling the pH-responsive behaviour of these surfactants is crucial to understanding how these species can be removed from silica surfaces without destruction of the valuable porous material.

In this work, CG MD simulations were shown to be effective in understanding the way in which bio-inspired additives can complement the synthesis of templated OMS. However, simulations were limited to only two available bio-inspired additives, out of a broad range of potential species [15]. With these methods established, it would be possible to use simulations to screen a large number of potential bio-inspired additives which may assist in identifying candidates for further experimental synthesis studies. Furthermore, this system still has great potential to be further optimized, taking into account the important factors identified in this work such as silica to surfactant ratio, pH, silica concentration and reaction time. Simulation studies could be used to predict optimal conditions for synthesis, allowing for more efficient design of future experiments.

The second mechanistic factor relates to the kinetics of silica condensation, which, as identified in this work, play a crucial role in locking in the ordered equilibrium structures that form. The models presented in this work are non-reactive, that is, silica condensation reactions are not explicity represented, meaning that the speciation of silica oligomers is fixed for any given simulation. True representation of how the kinetics of silica reactions disrupt, or lock in, the structures which form at high pH would require a CG reactive model for silica condensation. Such a model has already been presented by Carvalho et al., compatible with Martini 2 [92]. While the same method could be applied to this Martini 3 model, it is not straightforward to modify the reaction rate of silica species using this method. Since the relative rates of surfactant self-assembly and silica condensation reactions are clearly of great importance to understanding this phenomenon, creation of a model in which the silica reaction rate can be modified is critical. One potential approach would be to adopt the recently published reactive Martini approach of Sami et al. [256], which is compatible with Martini 3. In this approach, energetic barriers can be applied to reactive sites, allowing the reaction rate to be tuned. With this approach, the effect of reaction rate on phase behaviour could be observed, providing additional evidence for the findings presented in this work.

Appendices

Appendix A

Full Experimental Results

Full experimental results for samples synthesised in Chapter 5 are provided in this section. Table A.1 contains sample weights and yields. Table A.2 contains porosity data obtained by gas adsorption and XRD. Figures A.1 through A.4 contain adsorption isotherms. Figures A.5 through A.8 contain pore size distribution plots determined by BJH desorption and XRD patterns.

Table A.1: Sample weights and calculated yields for experimental work.

Sample No.	**Dried Weight (g)**	**Calcined Mass (g)**	**Organics Mass (g)**	**Organics Content (%)**	**Yield (%)**
1-1	0.49	0.019	0.474	96	13
1-2	9.01	0.526	8.479	94	78
1-3	0.00	0.000	0.004	100	0
1-4	1.07	0.565	0.503	47	84
1-5	0.80	0.015	0.788	98	9
1-6	10.54	0.438	10.099	96	57
1-7	0.02	0.008	0.012	61	5
1-8	1.26	0.712	0.547	43	94
1-9	1.40	0.047	1.352	97	29
1-10	10.91	0.489	10.420	96	82
1-11	0.15	0.065	0.090	58	40
1-12	1.26	0.543	0.712	57	81
1-13	1.47	0.048	1.422	97	30
1-14	13.23	0.573	12.655	96	80
1-15	0.14	0.063	0.078	56	39
1-16	0.96	0.440	0.521	54	58
2-1	1.20	0.52	0.68	56	87
2-2	0.57	0.28	0.29	50	47
2-3	0.26	0.10	0.16	63	16
2-4	1.30	0.55	0.75	58	91
2-5	0.47	0.23	0.24	50	39
2-6	0.21	0.10	0.11	51	17
3-1	1.14	0.48	0.66	59	80
3-2	1.20	0.47	0.73	61	78
3-3	1.14	0.44	0.69	61	74
3-4	1.19	0.39	0.80	67	65
3-5	1.16	0.49	0.67	58	81
4-1	0.73	0.39	0.34	47	65
4-2	0.84	0.48	0.36	42	80
4-3	0.78	0.42	0.36	46	69
4-4	0.49	0.25	0.25	50	41
4-5	0.87	0.47	0.40	46	78
4-6	0.88	0.51	0.37	42	86
4-7	0.64	0.34	0.30	47	57

Table A.2: Summary of the porosity data for all samples that were characterized by N_2 adsorption and XRD. The variables are fully described in Section 5.2.3. Comparison is made to available material properties for MCM-41 samples from literature (Samples A, B and C).

Sample No.	**Primary Isotherm Type**	$S_{\mathbf{BET}}$ **($\mathbf{m^2\ g^{-1}}$)**	$V_{\mathbf{pore}}$ **($\mathbf{cm^3\ g^{-1}}$)**	$d_{\mathbf{pore}}$ **(nm)**	$d_{\mathbf{100}}$ **(nm)**	$a_{\mathbf{0}}$ **(nm)**	$t_{\mathbf{wall}}$ **(nm)**	$I_{\mathbf{200}}$ **/$\mathbf{I_{110}}$**
A [5, 26]	IV(a)	1040	0.79	4.00	3.98	4.60	0.60	0.62
B [146]	-	-	-	-	3.48	4.02	-	0.65
C [191]	IV(a)	1312	0.86	3.14	3.05	3.52	0.38	0.00
1-2	IV(a)	1120	0.906	2.48	4.03	4.65	2.17	0.00
1-4	IV(a)	1005	0.828	2.45	3.88	4.48	2.03	0.28
1-6	IV(a)	970	0.721	2.51	3.98	4.60	2.09	0.00
1-8	IV(a)	1030	0.839	2.30	3.81	4.40	2.10	0.27
1-10	IV(a)	1181	0.966	2.63	3.80	4.39	1.76	0.00
1-12	IV(b)	1259	0.834	2.12	3.50	4.04	1.92	0.06
1-14	IV(a)	1217	1.003	2.55	3.82	4.41	1.86	0.04
1-16	IV(b)	1210	0.850	2.14	3.68	4.25	2.11	0.08
2-1	IV(b)	1259	0.971	2.31	3.56	4.11	1.80	0.12
2-2	IV(b)	1165	0.841	2.15	3.40	3.93	1.78	0.46
2-3	IV(a)	1159	0.843	2.13	3.44	3.97	1.84	-
2-4	IV(a)	1193	0.857	2.22	3.52	4.06	1.84	0.11
2-5	IV(b)	1144	0.824	2.14	3.43	3.96	1.82	0.50
2-6	IV(a)	1194	0.898	2.25	3.47	4.01	1.76	0.07
3-1	IV(b)	1149	0.789	2.18	3.39	3.91	1.73	0.06
3-2	IV(b)	1203	0.835	2.17	3.38	3.90	1.73	0.00
3-3	IV(b)	1218	0.938	2.40	3.63	4.19	1.79	0.28
3-4	IV(a)	1273	0.969	2.35	-	-	-	0.00
3-5	IV(b)	1218	0.911	2.24	3.50	4.04	1.80	0.20
4-1	IV(b)	983	0.706	2.20	3.55	4.10	1.90	0.52
4-2	IV(b)	961	0.736	2.27	3.68	4.25	1.98	0.49
4-3	IV(b)	926	0.679	2.24	3.67	4.24	1.94	0.00
4-4	IV(b)	1186	0.830	2.09	3.44	3.97	1.88	0.18
4-5	IV(a)	783	0.608	2.80	-	-	-	0.00
4-6	IV(a)	878	0.686	2.74	-	-	-	0.00
4-7	IV(b)	1142	0.841	2.10	3.40	3.93	1.83	0.29

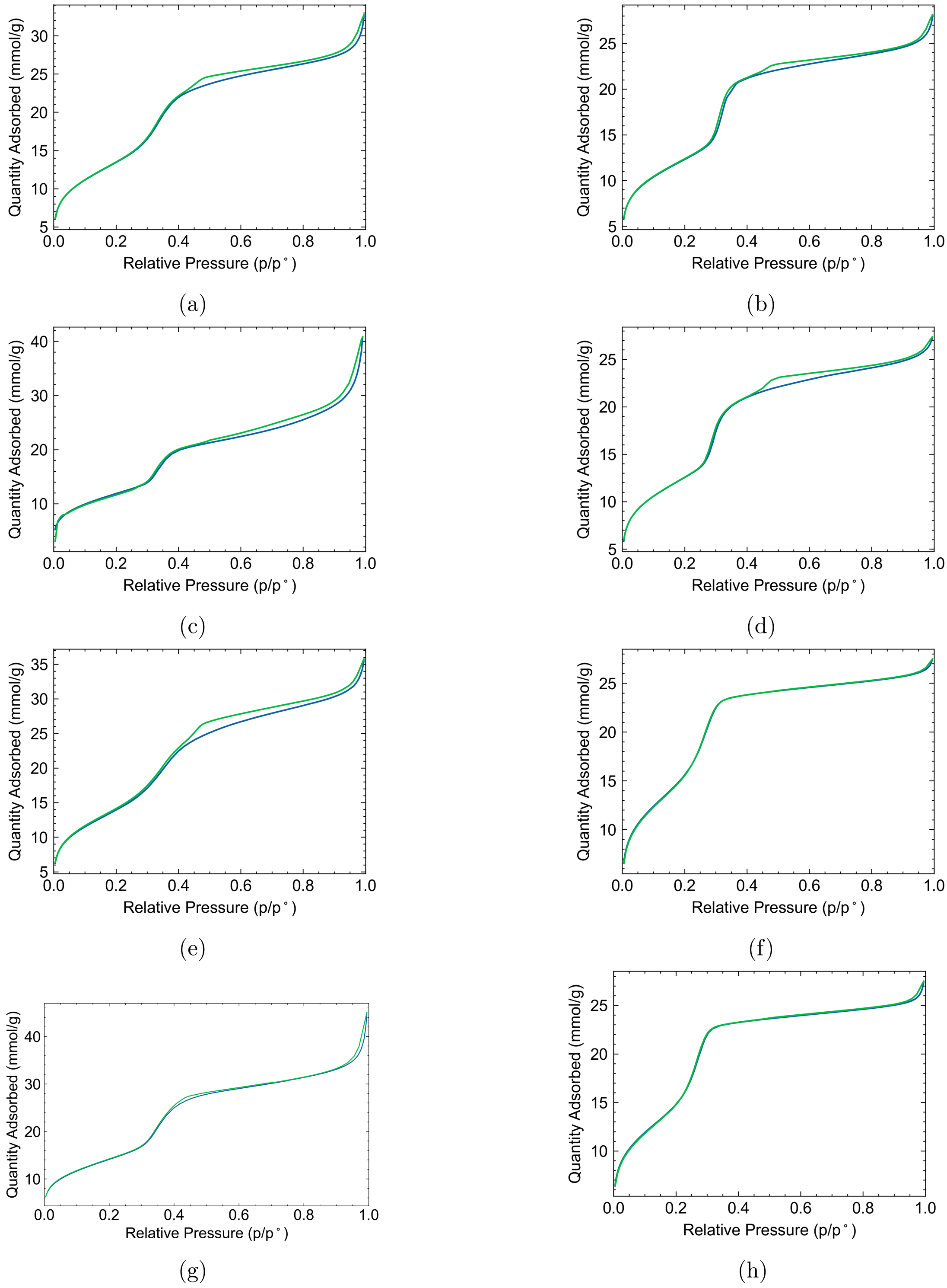

(a) (b) (c) (d) (e) (f) (g) (h)

Figure A.1: N_2 adsorption isotherms for two-level four-factor screening samples. Letters a-h represent samples 1-2, 1-4, 1-6, 1-8, 1-10, 1-12, 1-14 and 1-16, sequentially. The blue line indicates adsorption while the green line indicates desorption.

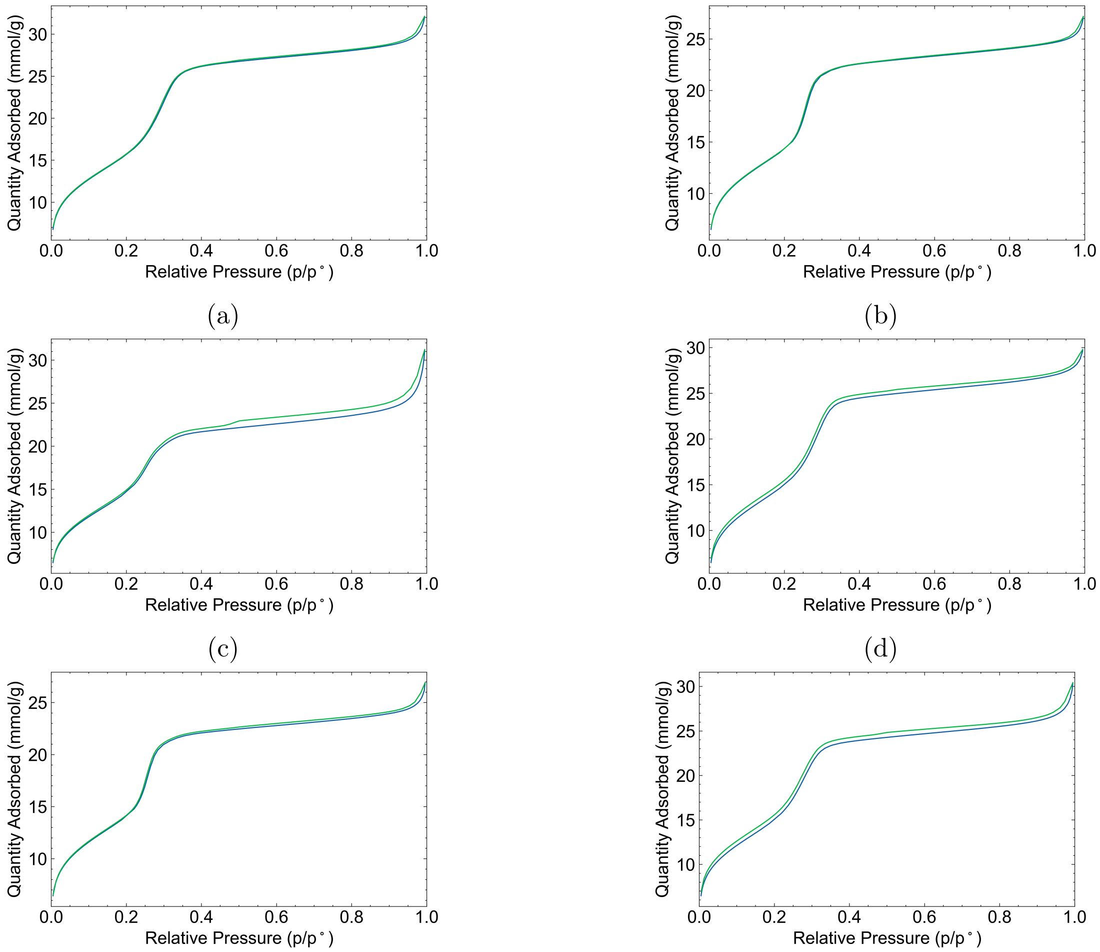

(a) (b) (c) (d) (e) (f)

Figure A.2: N_2 adsorption isotherms for component ratio investigation samples. Letters at to f represent samples 2-1 to 2-6, sequentially. The blue line indicates adsorption while the green line indicates desorption.

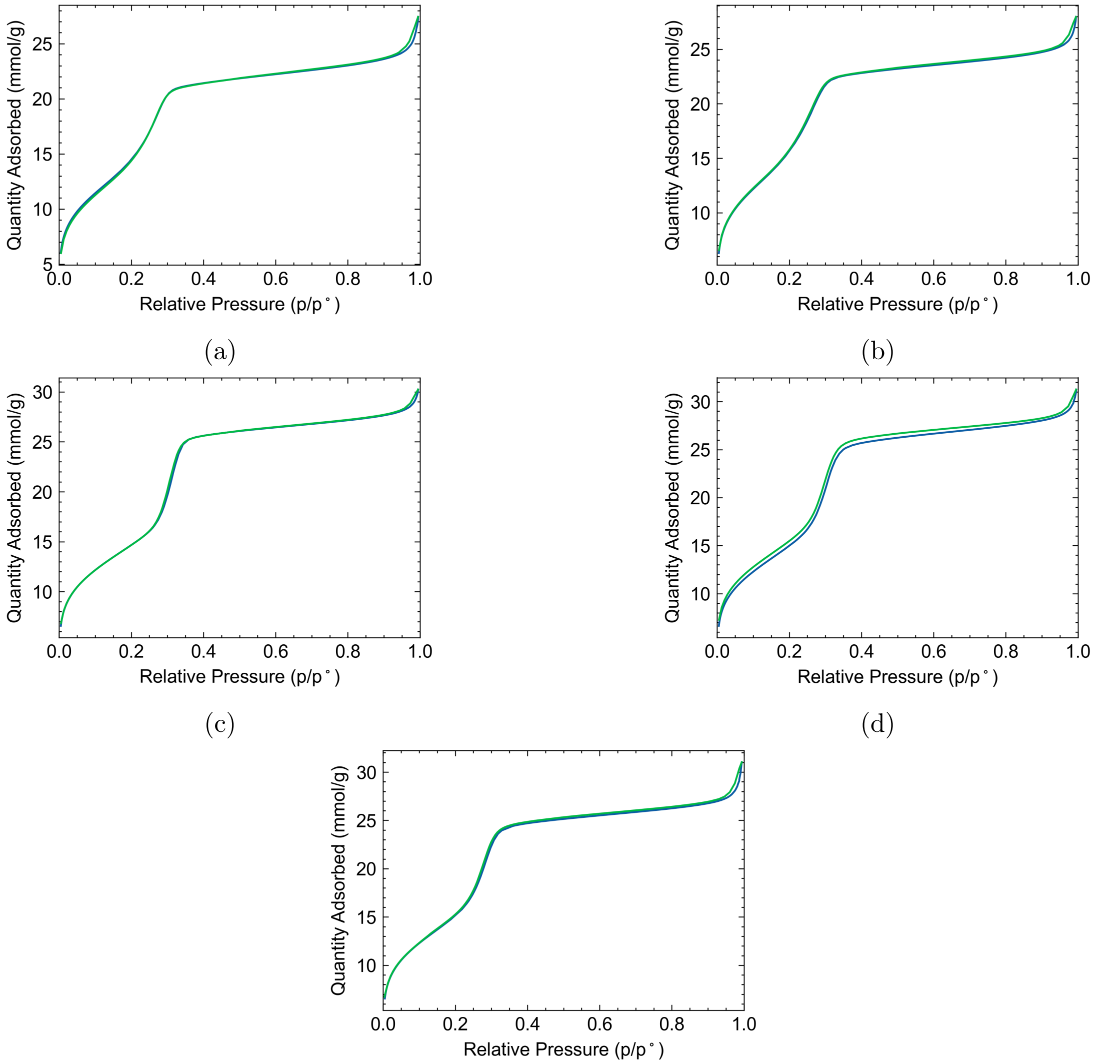

(a)

(b)

(c)

(d)

(e)

Figure A.3: N_2 adsorption isotherms for additive investigation samples with different additives: (a) L-arginine, (b) ammonia, (c) PEHA, (d) propylamine, (e) no additive.

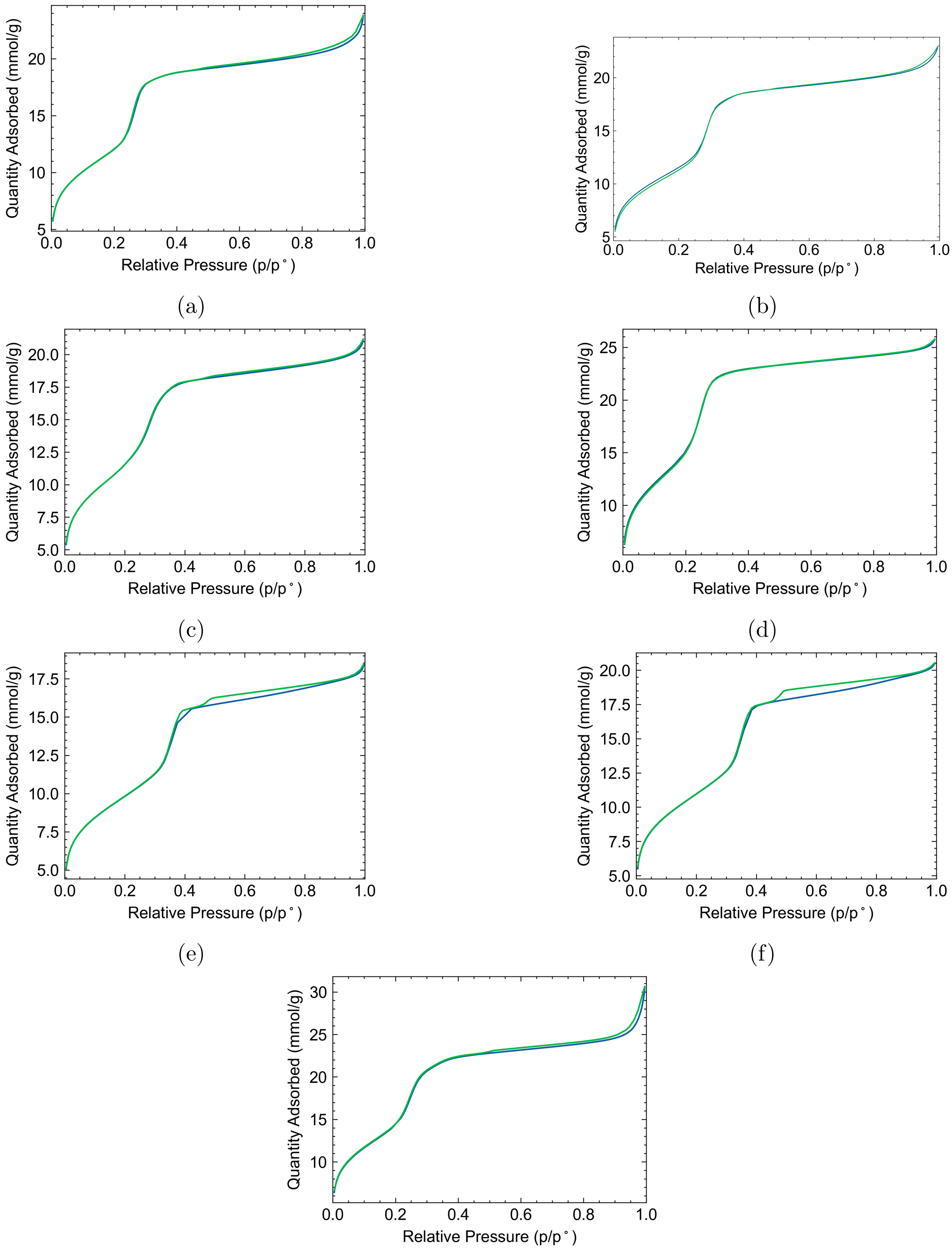

(a)

(b)

(c)

(d)

(e)

(f)

(g)

Figure A.4: N_2 adsorption isotherms for ordered mesoporous silica samples using PEHA as an additive in synthesis. Letters a to g represent samples 4-1 to 4-7, sequentially.

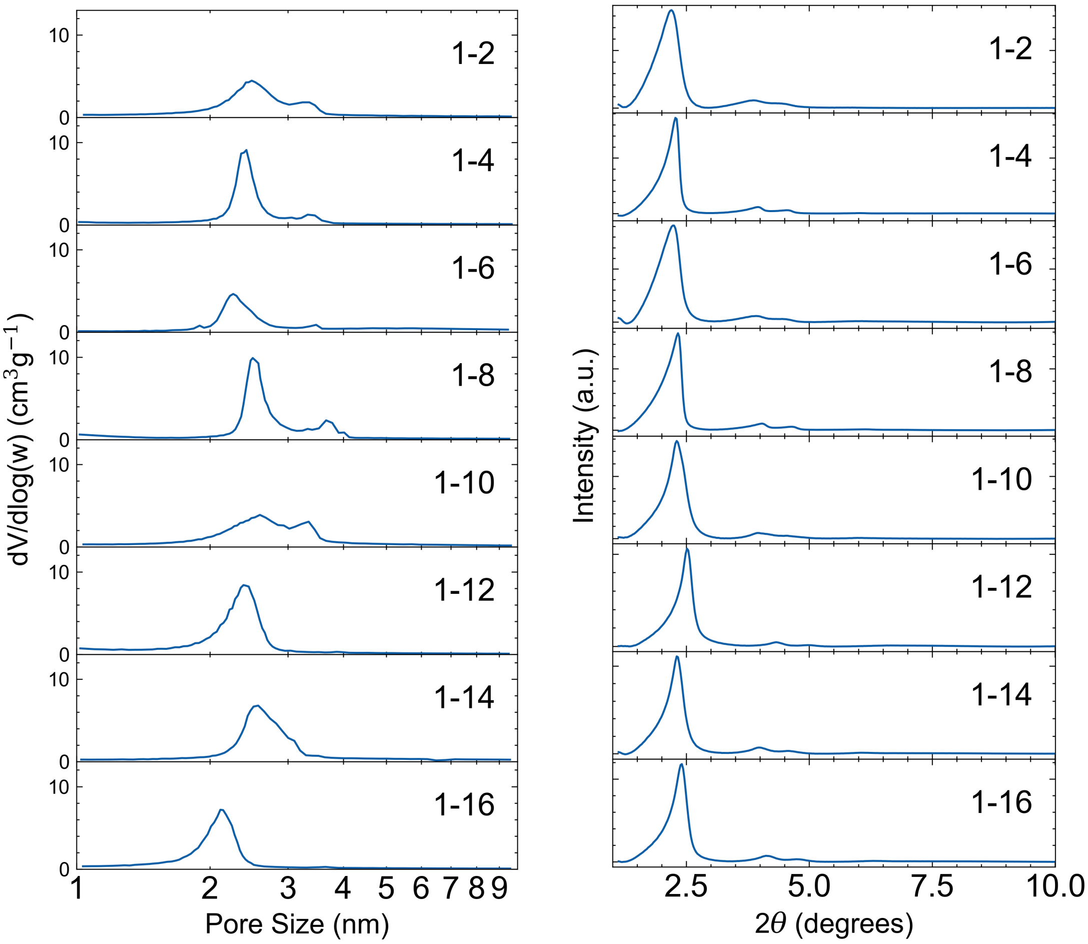

Figure A.5: Pore size distributions (left) and XRD data (right) for two-level four-factor screening samples. For XRD data, baseline intensity was removed manually to allow for easier comparison between peaks.

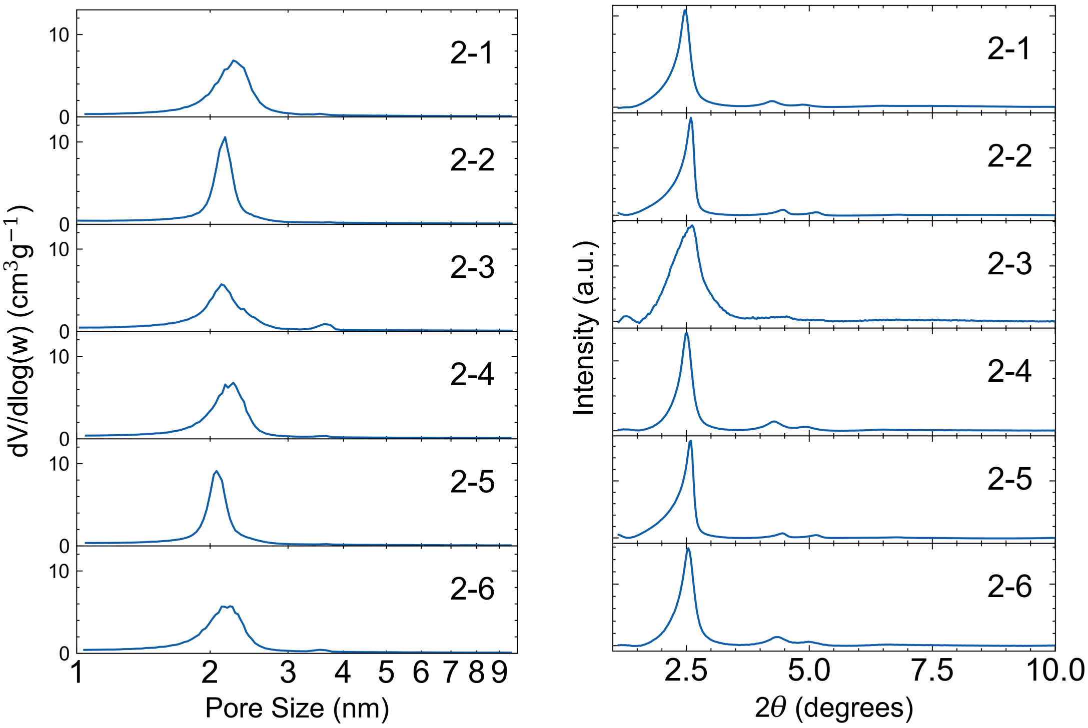

Figure A.6: Pore size distributions (left) and XRD data (right) for component ratio investigation samples. For XRD data, baseline intensity was removed manually to allow for easier comparison between peaks.

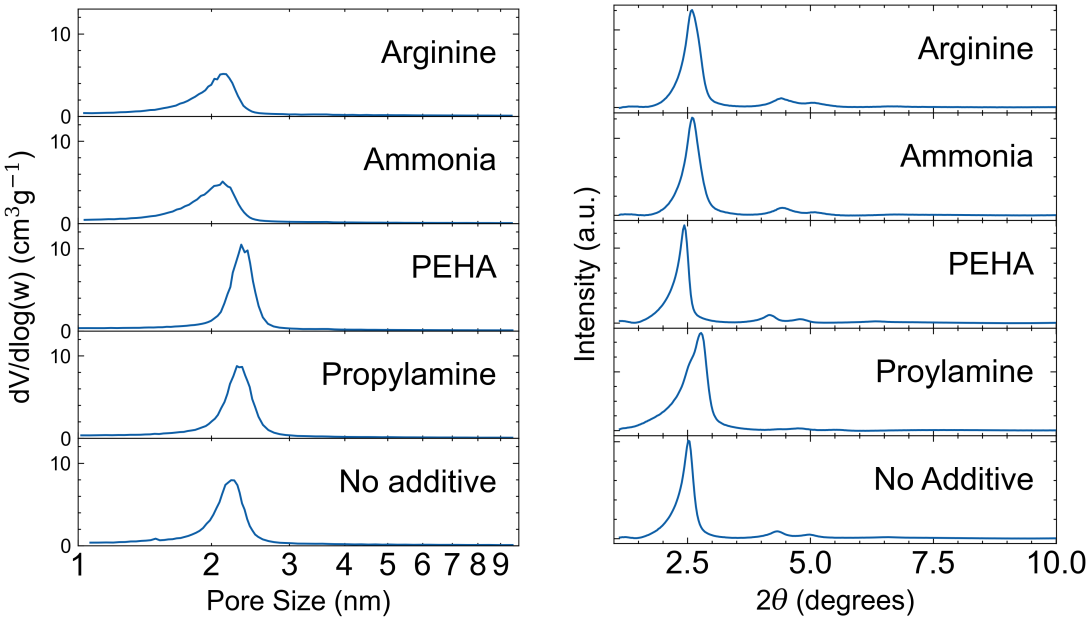

Figure A.7: Pore size distributions (left) and XRD data (right) for investigation with different additives. For XRD data, baseline intensity was removed manually to allow for easier comparison between peaks.

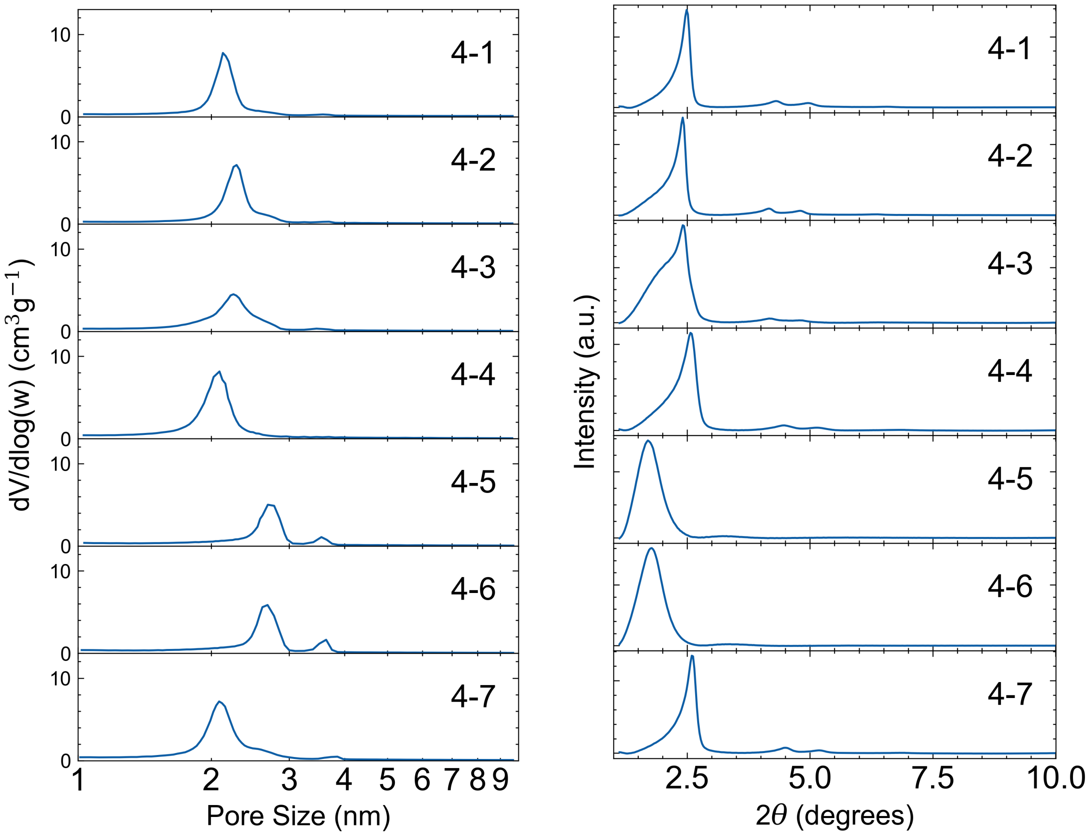

Figure A.8: Pore size distributions (left) and XRD data (right) for samples using PEHA as an additive in synthesis. For XRD data, baseline intensity was removed manually to allow for easier comparison between peaks.

Data Availability

All data underpinning this thesis is openly available from the University of Strathclyde KnowledgeBase at `https://doi.org/10.15129/bea3ae03-cf04-42ca-8804-52af416b2289`.

Bibliography

[1] T. Stavert, S. V. Patwardhan, R. Pilling, M. Jorge, "Unlocking the holy grail of sustainable and scalable mesoporous silica using computational modelling", *RSC Sustainability* **2023**, *1*, 432–438.

[2] T. Stavert, S. V. Patwardhan, M. Jorge, "Development of a coarse—grained model for the early stages of ordered mesoporous silica formation", *Molecular Simulation* **2025**, *51*, 188–205.

[3] T. Stavert, C. Brambila, S. V. Patwardhan, M. Jorge, "Computer—Aided Development of Bio—Inspired Routes to Highly Ordered Green Mesoporous Silica", Submitted.

[4] T. Stavert, M. Jorge, "Understanding the pH—responsive behaviour of alkylamine surfactants", *Journal of Molecular Liquids* **2025**, *431*, 127656.

[5] J. S. Beck et al., "A new family of mesoporous molecular sieves prepared with liquid crystal templates", *Journal of the American Chemical Society* **1992**, *114*, 10834–10843.

[6] D. Zhao, Q. Huo, J. Feng, B. F. Chmelka, G. D. Stucky, "Nonionic Triblock and Star Diblock Copolymer and Oligomeric Surfactant Syntheses of Highly Ordered, Hydrothermally Stable, Mesoporous Silica Structures", *Journal of the American Chemical Society* **1998**, *120*, 6024–6036.

[7] C. Brambila et al., "A Comparison of Environmental Impact of Various Silicas Using a Green Chemistry Evaluator", *ACS Sustainable Chemistry & Engineering* **2022**, *10*, 5288–5298.

[8] S. V. Patwardhan, J. R. H. Manning, M. Chiacchia, "Bioinspired synthesis as a potential green method for the preparation of nanomaterials: Opportunities and challenges", *Current Opinion in Green and Sustainable Chemistry*, Green and Sustainable Nanotechnology / Selected papers from the ACS Symposium on Green chemistry synthesis of nanomaterials and manufacturing **2018**, *12*, 110–116.

[9] M. Jorge, A. W. Milne, O. N. Sobek, A. Centi, G. Pérez-Sánchez, J. R. B. Gomes, "Modelling the self—assembly of silica—based mesoporous materials", *Molecular Simulation* **2018**, *44*, 435–452.

[10] A. Centi, M. Jorge, "Molecular Simulation Study of the Early Stages of Formation of Bioinspired Mesoporous Silica Materials", *Langmuir* **2016**, *32*, 7228–7240.

[11] A. Centi, J. R. H. Manning, V. Srivastava, S. van Meurs, S. V. Patwardhan, M. Jorge, "The role of charge—matching in nanoporous materials formation", *Materials Horizons* **2019**, *6*, 1027–1033.

[12] M. Jorge, A. W. Milne, M. C. Barrera, J. R. B. Gomes, "New Force—Field for Organosilicon Molecules in the Liquid Phase", *ACS Physical Chemistry Au* **2021**, *1*, 54–69.

[13] P. C. T. Souza et al., "Martini 3: a general purpose force field for coarse—grained molecular dynamics", *Nature Methods* **2021**, *18*, 382–388.

[14] S. V. Patwardhan, S. S. Staniland in *Green Nanomaterials*, 2053-2563, IOP Publishing, **2019**, 9–1 to 9–25.

[15] J. R. H. Manning, C. Brambila, S. V. Patwardhan, "Unified mechanistic interpretation of amine—assisted silica synthesis methods to enable design of more complex materials", *Molecular Systems Design & Engineering* **2021**, *6*, 170–196.

[16] D. J. Belton, O. Deschaume, C. C. Perry, "An overview of the fundamentals of the chemistry of silica with relevance to biosilicification and technological advances", *The FEBS Journal* **2012**, *279*, 1710–1720.

[17] J. Šefčík, A. V. McCormick, "Thermochemistry of aqueous silicate solution precursors to ceramics", *AIChE Journal* **1997**, *43*, 2773–2784.

[18] S. Sjöberg, "Silica in aqueous environments", *Journal of Non-Crystalline Solids* **1996**, *196*, 51–57.

[19] R. K. Iler, *The Chemistry of Silica: Solubility, Polymerization, Colloid and Surface Properties and Biochemistry of Silica*, Wiley, **1979**, 904 pp.

[20] J. N. Israelachvili in *Intermolecular and Surface Forces (Third Edition)*, (Ed.: J. N. Israelachvili), Academic Press, San Diego, **2011**, pp. 503–534.

[21] R. Nagarajan, E. Ruckenstein, "Theory of surfactant self—assembly: a predictive molecular thermodynamic approach", *Langmuir* **1991**, *7*, 2934–2969.

[22] Y. Wan, D. Zhao, "On the Controllable Soft—Templating Approach to Mesoporous Silicates", *Chemical Reviews* **2007**, *107*, 2821–2860.

[23] C. A. Dreiss, "Wormlike micelles: where do we stand? Recent developments, linear rheology and scattering techniques", *Soft Matter* **2007**, *3*, 956–970.

[24] R. A. Khalil, F. J. Hammad, "Critical Intermolecular Forces: A New Physical Insight for the Formation of Wormlike Micelles", *Journal of The Chemical Society of Pakistan* **2014**, *36*, 211.

[25] N. K. Raman, M. T. Anderson, C. J. Brinker, "Template—Based Approaches to the Preparation of Amorphous, Nanoporous Silicas", *Chemistry of Materials* **1996**, *8*, 1682–1701.

[26] C. T. Kresge, M. E. Leonowicz, W. J. Roth, J. C. Vartuli, J. S. Beck, "Ordered mesoporous molecular sieves synthesized by a liquid—crystal template mechanism", *Nature* **1992**, *359*, 710–712.

[27] S. Inagaki, Y. Fukushima, K. Kuroda, "Synthesis of highly ordered mesoporous materials from a layered polysilicate", *Journal of the Chemical Society Chemical Communications* **1993**, 680–682.

[28] C. T. Kresge, W. J. Roth, "The discovery of mesoporous molecular sieves from the twenty year perspective", *Chemical Society Reviews* **2013**, *42*, 3663–3670.

[29] M. E. Leonowicz, J. A. Lawton, S. L. Lawton, M. K. Rubin, “MCM—22: A Molecular Sieve with Two Independent Multidimensional Channel Systems”, *Science* **1994**, *264*, 1910–1913.

[30] C. T. Kresge, J. C. Vartuli, W. J. Roth, M. E. Leonowicz in *Studies in Surface Science and Catalysis*, (Ed.: O. Terasaki), Mesoporous Crystals and Related Nano-Structured Materials, Elsevier, **2004**, pp. 53–72.

[31] J. C. Vartuli et al., “Effect of Surfactant/Silica Molar Ratios on the Formation of Mesoporous Molecular Sieves: Inorganic Mimicry of Surfactant Liquid—Crystal Phases and Mechanistic Implications”, *Chemistry of Materials* **1994**, *6*, 2317–2326.

[32] Y. Sakamoto et al., “Direct imaging of the pores and cages of three—dimensional mesoporous materials”, *Nature* **2000**, *408*, 449–453.

[33] G. S. Attard, J. C. Glyde, C. G. Göltner, “Liquid—crystalline phases as templates for the synthesis of mesoporous silica”, *Nature* **1995**, *378*, 366–368.

[34] P. T. Tanev, T. J. Pinnavaia, “A Neutral Templating Route to Mesoporous Molecular Sieves”, *Science* **1995**, *267*, 865–867.

[35] D. Pan et al., “New Understanding and Simple Approach to Synthesize Highly Hydrothermally Stable and Ordered Mesoporous Materials”, *Chemistry of Materials* **2009**, *21*, 5413–5425.

[36] C. Gérardin, J. Reboul, M. Bonne, B. Lebeau, “Ecodesign of ordered mesoporous silica materials”, *Chemical Society Reviews* **2013**, *42*, 4217–4255.

[37] J. R. H. Manning, T. W. S. Yip, A. Centi, M. Jorge, S. V. Patwardhan, “An Eco—Friendly, Tunable and Scalable Method for Producing Porous Functional Nanomaterials Designed Using Molecular Interactions”, *ChemSusChem* **2017**, *10*, 1683–1691.

[38] A. Shimojima, K. Kuroda, “Direct Formation of Mesostructured Silica—Based Hybrids from Novel Siloxane Oligomers with Long Alkyl Chains”, *Angewandte Chemie International Edition* **2003**, *42*, 4057–4060.

[39] A. Shimojima, Z. Liu, T. Ohsuna, O. Terasaki, K. Kuroda, "Self—Assembly of Designed Oligomeric Siloxanes with Alkyl Chains into Silica—Based Hybrid Mesostructures", *Journal of the American Chemical Society* **2005**, *127*, 14108–14116.

[40] Q. Huo et al., "Generalized synthesis of periodic surfactant/inorganic composite materials", *Nature* **1994**, *368*, 317–321.

[41] Q. Huo, D. I. Margolese, G. D. Stucky, "Surfactant Control of Phases in the Synthesis of Mesoporous Silica—Based Materials", *Chemistry of Materials* **1996**, *8*, 1147–1160.

[42] S. A. Bagshaw, E. Prouzet, T. J. Pinnavaia, "Templating of Mesoporous Molecular Sieves by Nonionic Polyethylene Oxide Surfactants", *Science* **1995**, *269*, 1242–1244.

[43] A. Firouzi, F. Atef, A. G. Oertli, G. D. Stucky, B. F. Chmelka, "Alkaline Lyotropic Silicate−Surfactant Liquid Crystals", *Journal of the American Chemical Society* **1997**, *119*, 3596–3610.

[44] S. V. Patwardhan, S. J. Clarson, "Biological and Bioactive Silicon Systems", *Silicon* **2012**, *4*, 1–3.

[45] S. V. Patwardhan, "Biomimetic and bioinspired silica: recent developments and applications", *Chemical Communications* **2011**, *47*, 7567–7582.

[46] C. Gröger, K. Lutz, E. Brunner, "Biomolecular Self—assembly and its Relevance in Silica Biomineralization", *Cell Biochemistry and Biophysics* **2008**, *50*, 23–39.

[47] N. Kröger, R. Deutzmann, C. Bergsdorf, M. Sumper, "Species—specific polyamines from diatoms control silica morphology", *Proceedings of the National Academy of Sciences* **2000**, *97*, 14133–14138.

[48] N. Kröger, R. Deutzmann, M. Sumper, "Polycationic Peptides from Diatom Biosilica That Direct Silica Nanosphere Formation", *Science* **1999**, *286*, 1129–1132.

[49] N. Kröger, R. Deutzmann, M. Sumper, “Silica—precipitating Peptides from Diatoms: The Chemical Structure of Silaffin—1A from Cylindrotheca Fusiforms”, *Journal of Biological Chemistry* **2001**, *276*, 26066–26070.

[50] N. Poulsen, N. Kröger, “Silica Morphogenesis by Alternative Processing of Silaffins in the Diatom Thalassiosira pseudonana*”, *Journal of Biological Chemistry* **2004**, *279*, 42993–42999.

[51] S. Wenzl, R. Deutzmann, R. Hett, E. Hochmuth, M. Sumper, “Quaternary Ammonium Groups in Silica—Associated Proteins”, *Angewandte Chemie* **2004**, *116*, 6059–6062.

[52] T. Mizutani, H. Nagase, N. Fujiwara, H. Ogoshi, “Silicic Acid Polymerization Catalyzed by Amines and Polyamines”, *Bulletin of the Chemical Society of Japan* **1998**, *71*, 2017–2022.

[53] W. E. G. Müller, M. Rothenberger, A. Boreiko, W. Tremel, A. Reiber, H. C. Schröder, “Formation of siliceous spicules in the marine demosponge Suberites domuncula”, *Cell and Tissue Research* **2005**, *321*, 285–297.

[54] S. V. Patwardhan, S. J. Clarson, C. C. Perry, “On the role(s) of additives in bioinspired silicification”, *Chemical Communications* **2005**, 1113–1121.

[55] S. V. Patwardhan, N. Mukherjee, S. J. Clarson, “The Use of Poly—L—Lysine to Form Novel Silica Morphologies and the Role of Polypeptides in Biosilicification”, *Journal of Inorganic and Organometallic Polymers* **2001**, *11*, 193–198.

[56] S. V. Patwardhan, N. Mukherjee, S. J. Clarson, “Effect of process parameters on the polymer mediated synthesis of silica at neutral pH”, *Silicon Chemistry* **2002**, *1*, 47–54.

[57] D. J. Belton, S. V. Patwardhan, V. V. Annenkov, E. N. Danilovtseva, C. C. Perry, “From biosilicification to tailored materials: Optimizing hydrophobic domains and resistance to protonation of polyamines”, *Proceedings of the National Academy of Sciences* **2008**, *105*, 5963–5968.

[58] T. Coradin, C. Roux, J. Livage, “Biomimetic self—activated formation of multi—scale porous silica in the presence of arginine—based surfactants”, *Journal of Materials Chemistry* **2002**, *12*, 1242–1244.

[59] Q. Sun, T. P. M. Beelen, R. A. van Santen, S. Hazelaar, E. G. Vrieling, W. W. C. Gieskes, “PEG—Mediated Silica Pore Formation Monitored in Situ by USAXS and SAXS: Systems with Properties Resembling Diatomaceous Silica”, *The Journal of Physical Chemistry B* **2002**, *106*, 11539–11548.

[60] J. Li, L. Xu, B. Yang, Z. Bao, W. Pan, S. Li, “Biomimetic synthesized chiral mesoporous silica: Structures and controlled release functions as drug carrier”, *Materials Science and Engineering: C* **2015**, *55*, 367–372.

[61] J.-J. Yuan, P.-X. Zhu, N. Fukazawa, R.-H. Jin, “Synthesis of Nanofiber—Based Silica Networks Mediated by Organized Poly(ethylene imine): Structure, Properties, and Mechanism”, *Advanced Functional Materials* **2006**, *16*, 2205–2212.

[62] J.-J. Yuan, O. O. Mykhaylyk, A. J. Ryan, S. P. Armes, “Cross—Linking of Cationic Block Copolymer Micelles by Silica Deposition”, *Journal of the American Chemical Society* **2007**, *129*, 1717–1723.

[63] O. V. Gorbunova, O. N. Baklanova, T. I. Gulyaeva, “Porous structure of PEG—mediated silica controlled by solution pH”, *Microporous and Mesoporous Materials* **2020**, *307*, 110468.

[64] S. M. Auerbach, W. Fan, P. A. Monson, “Modelling the assembly of nanoporous silica materials”, *International Reviews in Physical Chemistry* **2015**, *34*, 35–70.

[65] F. R. Siperstein, K. E. Gubbins, “Synthesis and Characterization of Templated Mesoporous Materials Using Molecular Simulation”, *Molecular Simulation* **2001**, *27*, 339–352.

[66] F. R. Siperstein, K. E. Gubbins, “Phase Separation and Liquid Crystal Self—Assembly in Surfactant—Inorganic—Solvent Systems”, *Langmuir* **2003**, *19*, 2049–2057.

[67] A. Patti, A. D. Mackie, F. R. Siperstein, “Monte Carlo Simulation of Self—Assembled Ordered Hybrid Materials”, *Langmuir* **2007**, *23*, 6771–6780.

[68] A. Patti, F. R. Siperstein, A. D. Mackie, “Phase Behavior of Model Surfactants in the Presence of Hybrid Particles”, *The Journal of Physical Chemistry C* **2007**, *111*, 16035–16044.

[69] A. Patti, A. D. Mackie, F. R. Siperstein, “Monte Carlo simulations of self—assembling hexagonal and cage—like bifunctional periodic mesoporous materials”, *Journal of Materials Chemistry* **2009**, *19*, 7848–7855.

[70] A. Patti, A. D. Mackie, V. Zelenak, F. R. Siperstein, “One—pot synthesis of amino functionalized mesoporous silica materials: using simulations to understand transitions between different structures”, *Journal of Materials Chemistry* **2009**, *19*, 724–732.

[71] S. Bhattacharya, K. E. Gubbins, “Modeling triblock surfactant—templated mesostructured cellular foams”, *The Journal of Chemical Physics* **2005**, *123*, 134907.

[72] S. Bhattacharya, B. Coasne, F. R. Hung, K. E. Gubbins, “Modeling Micelle—Templated Mesoporous Material SBA—15: Atomistic Model and Gas Adsorption Studies”, *Langmuir* **2009**, *25*, 5802–5813.

[73] L. Jin, S. M. Auerbach, P. A. Monson, “Simulating the Formation of Surfactant—Templated Mesoporous Silica Materials: A Model with Both Surfactant Self—Assembly and Silica Polymerization”, *Langmuir* **2013**, *29*, 766–780.

[74] M. Jorge, J. R. B. Gomes, M. N. D. S. Cordeiro, N. A. Seaton, “Molecular Simulation of Silica/Surfactant Self—Assembly in the Synthesis of Periodic Mesoporous Silicas”, *Journal of the American Chemical Society* **2007**, *129*, 15414–15415.

[75] G. Pérez-Sánchez, J. R. B. Gomes, M. Jorge, “Modeling Self—Assembly of Silica/Surfactant Mesostructures in the Templated Synthesis of Nanoporous Solids”, *Langmuir* **2013**, *29*, 2387–2396.

[76] S. J. Marrink, H. J. Risselada, S. Yefimov, D. P. Tieleman, A. H. d. Vries, "The MARTINI Force Field: Coarse Grained Model for Biomolecular Simulations", *The Journal of Physical Chemistry B* **2007**, *111*, 7812–7824.

[77] G. Pérez-Sánchez et al., "Multiscale Model for the Templated Synthesis of Mesoporous Silica: The Essential Role of Silica Oligomers", *Chemistry of Materials* **2016**, *28*, 2715–2727.

[78] S.-C. Chien et al., "Molecular Simulations of the Synthesis of Periodic Mesoporous Silica Phases at High Surfactant Concentrations", *The Journal of Physical Chemistry C* **2017**, *121*, 4564–4575.

[79] B. P. Feuston, S. H. Garofalini, "Empirical three-body potential for vitreous silica", *The Journal of Chemical Physics* **1988**, *89*, 5818–5824.

[80] G. J. McIntosh, "Theoretical investigations into the nucleation of silica growth in basic solution part II – derivation and benchmarking of a first principles kinetic model of solution chemistry", *Physical Chemistry Chemical Physics* **2013**, *15*, 17496–17509.

[81] X.-Q. Zhang, T. T. Trinh, R. A. van Santen, A. P. J. Jansen, "Structure—Directing Role of Counterions in the Initial Stage of Zeolite Synthesis", *The Journal of Physical Chemistry C* **2011**, *115*, 9561–9567.

[82] X.-Q. Zhang, R. A. v. Santen, A. P. J. Jansen, "Kinetic Monte Carlo modeling of silicate oligomerization and early gelation†", *Physical Chemistry Chemical Physics* **2012**, *14*, 11969–11973.

[83] M. G. Wu, M. W. Deem, "Monte Carlo study of the nucleation process during zeolite synthesis", *The Journal of Chemical Physics* **2002**, *116*, 2125–2137.

[84] Z. Jing, L. Xin, H. Sun, "Replica exchange reactive molecular dynamics simulations of initial reactions in zeolite synthesis", *Physical Chemistry Chemical Physics* **2015**, *17*, 25421–25428.

[85] N. Z. Rao, L. D. Gelb, “Molecular Dynamics Simulations of the Polymerization of Aqueous Silicic Acid and Analysis of the Effects of Concentration on Silica Polymorph Distributions, Growth Mechanisms, and Reaction Kinetics”, *The Journal of Physical Chemistry B* **2004**, *108*, 12418–12428.

[86] A. Malani, S. M. Auerbach, P. A. Monson, “Probing the Mechanism of Silica Polymerization at Ambient Temperatures using Monte Carlo Simulations”, *The Journal of Physical Chemistry Letters* **2010**, *1*, 3219–3224.

[87] A. Malani, S. M. Auerbach, P. A. Monson, “Monte Carlo Simulations of Silica Polymerization and Network Formation”, *The Journal of Physical Chemistry C* **2011**, *115*, 15988–16000.

[88] V. M. Burlakov, G. A. D. Briggs, A. P. Sutton, Y. Tsukahara, “Monte Carlo Simulation of Growth of Porous SiOx by Vapor Deposition”, *Physical Review Letters* **2001**, *86*, 3052–3055.

[89] Y. Tu, J. Tersoff, “Structure and Energetics of the Si—SiO2 Interface”, *Physical Review Letters* **2000**, *84*, 4393–4396.

[90] C. Schumacher, J. Gonzalez, P. A. Wright, N. A. Seaton, “Generation of Atomistic Models of Periodic Mesoporous Silica by Kinetic Monte Carlo Simulation of the Synthesis of the Material”, *The Journal of Physical Chemistry B* **2006**, *110*, 319–333.

[91] C. A. Ferreiro-Rangel, M. M. Lozinska, P. A. Wright, N. A. Seaton, T. Düren, “Kinetic Monte Carlo Simulation of the Synthesis of Periodic Mesoporous Silicas SBA—2 and STAC—1: Generation of Realistic Atomistic Models”, *The Journal of Physical Chemistry C* **2012**, *116*, 20966–20974.

[92] A. P. Carvalho, S. M. Santos, G. Pérez-Sánchez, J. D. Gouveia, J. R. B. Gomes, M. Jorge, “Sticky—MARTINI as a reactive coarse—grained model for molecular dynamics simulations of silica polymerization”, *npj Computational Materials* **2022**, *8*, 1–13.

[93] L. Lenoci, P. J. Camp, "Self—Assembly of Peptide Scaffolds in Biosilica Formation: Computer Simulations of a Coarse—Grained Model", *Journal of the American Chemical Society* **2006**, *128*, 10111–10117.

[94] H. Eckert, M. Montagna, A. Dianat, R. Gutierrez, M. Bobeth, G. Cuniberti, "Exploring the organic–inorganic interface in biosilica: atomistic modeling of polyamine and silica precursors aggregation behavior", *BMC Materials* **2020**, *2*, 6.

[95] H. A. Scheraga, M. Khalili, A. Liwo, "Protein—folding dynamics: overview of molecular simulation techniques", *Annual Review of Physical Chemistry* **2007**, *58*, 57–83.

[96] T. Taddese, R. L. Anderson, D. J. Bray, P. B. Warren, "Recent advances in particle—based simulation of surfactants", *Current Opinion in Colloid & Interface Science*, Formulations and Cosmetics **2020**, *48*, 137–148.

[97] J. Meisner, X. Zhu, T. J. Martínez, "Computational Discovery of the Origins of Life", *ACS Central Science* **2019**, *5*, 1493–1495.

[98] M. P. Allen, D. J. Tildesley in *Computer Simulation of Liquids*, (Eds.: M. P. Allen, D. J. Tildesley), Oxford University Press, **2017**, p. 0.

[99] R. A. Buckingham, J. E. Lennard-Jones, "The classical equation of state of gaseous helium, neon and argon", *Proceedings of the Royal Society of London. Series A. Mathematical and Physical Sciences* **1938**, *168*, 264–283.

[100] C. Murthy, S. O'Shea, I. McDonald, "Electrostatic interactions in molecular crystals: Lattice dynamics of solid nitrogen and carbon dioxide", *Molecular Physics* **1983**, *50*, 531–541.

[101] H. S. Antila, E. Salonen, "Polarizable force fields", *Methods in Molecular Biology (Clifton N.J.)* **2013**, *924*, 215–241.

[102] S. W. Rick, S. J. Stuart in *Reviews in Computational Chemistry*, John Wiley & Sons, Ltd, **2002**, pp. 89–146.

[103] B. Hess, H. Bekker, H. J. C. Berendsen, J. G. E. M. Fraaije, “LINCS: A linear constraint solver for molecular simulations”, *Journal of Computational Chemistry* **1997**, *18*, 1463–1472.

[104] J.-P. Ryckaert, G. Ciccotti, H. J. C. Berendsen, “Numerical integration of the cartesian equations of motion of a system with constraints: molecular dynamics of *n*—alkanes”, *Journal of Computational Physics* **1977**, *23*, 327–341.

[105] S. Miyamoto, P. A. Kollman, “Settle: An analytical version of the SHAKE and RATTLE algorithm for rigid water models”, *Journal of Computational Chemistry* **1992**, *13*, 952–962.

[106] W. L. Jorgensen, D. S. Maxwell, J. Tirado-Rives, “Development and Testing of the OPLS All—Atom Force Field on Conformational Energetics and Properties of Organic Liquids”, *Journal of the American Chemical Society* **1996**, *118*, 11225–11236.

[107] R. Salomon-Ferrer, D. A. Case, R. C. Walker, “An overview of the Amber biomolecular simulation package”, *WIREs Computational Molecular Science* **2013**, *3*, 198–210.

[108] A. D. J. MacKerell et al., “All—Atom Empirical Potential for Molecular Modeling and Dynamics Studies of Proteins”, *The Journal of Physical Chemistry B* **1998**, *102*, 3586–3616.

[109] W. C. Swope, H. C. Andersen, P. H. Berens, K. R. Wilson, “A computer simulation method for the calculation of equilibrium constants for the formation of physical clusters of molecules: Application to small water clusters”, *The Journal of Chemical Physics* **1982**, *76*, 637–649.

[110] L. Verlet, “Computer "Experiments" on Classical Fluids. I. Thermodynamical Properties of Lennard—Jones Molecules”, *Physical Review* **1967**, *159*, 98–103.

[111] R. W. Hockney, S. P. Goel, J. W. Eastwood, “Quiet high—resolution computer models of a plasma”, *Journal of Computational Physics* **1974**, *14*, 148–158.

[112] P. P. Ewald, "Die Berechnung optischer und elektrostatischer Gitterpotentiale", *Annalen der Physik* **1921**, *369*, 253–287.

[113] T. Darden, D. York, L. Pedersen, "Particle mesh Ewald: An N·log(N) method for Ewald sums in large systems", *The Journal of Chemical Physics* **1993**, *98*, 10089–10092.

[114] H. J. C. Berendsen, J. P. M. Postma, W. F. van Gunsteren, A. DiNola, J. R. Haak, "Molecular dynamics with coupling to an external bath", *The Journal of Chemical Physics* **1984**, *81*, 3684–3690.

[115] G. Bussi, D. Donadio, M. Parrinello, "Canonical sampling through velocity rescaling", *The Journal of Chemical Physics* **2007**, *126*, 014101.

[116] S. Nosé, "A molecular dynamics method for simulations in the canonical ensemble", *Molecular Physics* **1984**, *52*, 255–268.

[117] W. G. Hoover, "Canonical dynamics: Equilibrium phase—space distributions", *Physical Review A* **1985**, *31*, 1695–1697.

[118] G. J. Martyna, M. L. Klein, M. Tuckerman, "Nosé–Hoover chains: The canonical ensemble via continuous dynamics", *The Journal of Chemical Physics* **1992**, *97*, 2635–2643.

[119] B. Cooke, S. C. Schmidler, "Preserving the Boltzmann ensemble in replica—exchange molecular dynamics", *The Journal of Chemical Physics* **2008**, *129*, 164112.

[120] M. Parrinello, A. Rahman, "Polymorphic transitions in single crystals: A new molecular dynamics method", *Journal of Applied Physics* **1981**, *52*, 7182–7190.

[121] S. Nosé, M. L. Klein, "Constant pressure molecular dynamics for molecular systems", *Molecular Physics* **2006**.

[122] W. G. Noid, "Perspective: Advances, Challenges, and Insight for Predictive Coarse—Grained Models", *The Journal of Physical Chemistry B* **2023**, *127*, 4174–4207.

[123] F. Schmid, "Toy amphiphiles on the computer: What can we learn from generic models?", *Macromolecular Rapid Communications* **2009**, *30*, 741–751.

[124] J.-W. Shen, C. Li, N. F. van der Vegt, C. Peter, "Transferability of Coarse Grained Potentials: Implicit Solvent Models for Hydrated Ions", *Journal of Chemical Theory and Computation* **2011**, *7*, 1916–1927.

[125] S. O. Yesylevskyy, L. V. Schäfer, D. Sengupta, S. J. Marrink, "Polarizable Water Model for the Coarse—Grained MARTINI Force Field", *PLOS Computational Biology* **2010**, *6*, e1000810.

[126] S. J. Marrink, A. H. de Vries, A. E. Mark, "Coarse Grained Model for Semiquantitative Lipid Simulations", *The Journal of Physical Chemistry B* **2004**, *108*, 750–760.

[127] L. Monticelli, S. K. Kandasamy, X. Periole, R. G. Larson, D. P. Tieleman, S.-J. Marrink, "The MARTINI Coarse—Grained Force Field: Extension to Proteins", *Journal of Chemical Theory and Computation* **2008**, *4*, 819–834.

[128] J. J. Uusitalo, H. I. Ingólfsson, P. Akhshi, D. P. Tieleman, S. J. Marrink, "Martini Coarse—Grained Force Field: Extension to DNA", *Journal of Chemical Theory and Computation* **2015**, *11*, 3932–3945.

[129] Z. Jiang et al., "Subnanometre ligand—shell asymmetry leads to Janus—like nanoparticle membranes", *Nature Materials* **2015**, *14*, 912–917.

[130] P. W. J. M. Frederix et al., "Exploring the sequence space for (tri—)peptide self—assembly to design and discover new hydrogels", *Nature Chemistry* **2015**, *7*, 30–37.

[131] R. Alessandri, P. C. T. Souza, S. Thallmair, M. N. Melo, A. H. de Vries, S. J. Marrink, "Pitfalls of the Martini Model", *Journal of Chemical Theory and Computation* **2019**, *15*, 5448–5460.

[132] R. Mee, *A Comprehensive Guide to Factorial Two—Level Experimentation*, Springer, New York, NY, **2009**.

[133] M. Thommes et al., "Physisorption of gases, with special reference to the evaluation of surface area and pore size distribution (IUPAC Technical Report)", *Pure and Applied Chemistry* **2015**, *87*, 1051–1069.

[134] S. Brunauer, P. H. Emmett, E. Teller, “Adsorption of Gases in Multimolecular Layers”, *Journal of the American Chemical Society* **1938**, *60*, 309–319.

[135] J. Rouquerol, P. Llewellyn, F. Rouquerol in *Studies in Surface Science and Catalysis*, (Eds.: P. L. Llewellyn, F. Rodriquez-Reinoso, J. Rouqerol, N. Seaton), Characterization of Porous Solids VII, Elsevier, **2007**, pp. 49–56.

[136] E. P. Barrett, L. G. Joyner, P. P. Halenda, “The Determination of Pore Volume and Area Distributions in Porous Substances. I. Computations from Nitrogen Isotherms”, *Journal of the American Chemical Society* **1951**, *73*, 373–380.

[137] P. I. Ravikovitch, G. L. Haller, A. V. Neimark, “Density functional theory model for calculating pore size distributions: pore structure of nanoporous catalysts”, *Advances in Colloid and Interface Science* **1998**, *76-77*, 203–226.

[138] G. Horváth, K. Kawazoe, “Method for the Calculation of Effective Pore Size Distribution in Molecular Sieve Carbon”, *Journal of Chemical Engineering of Japan* **1983**, *16*, 470–475.

[139] J. Landers, G. Y. Gor, A. V. Neimark, “Density functional theory methods for characterization of porous materials”, *Colloids and Surfaces A: Physicochemical and Engineering Aspects*, Characterization of Porous Materials: From Angstroms to Millimeters A Collection of Selected Papers Presented at the 6th International Workshop, CPM-6 April 30 – May 2nd, 2012, Delray Beach, FL, USA Co-sponsored by Quantachrome Instruments **2013**, *437*, 3–32.

[140] S. J. Gregg, K. S. W. Sing, H. W. Salzberg, “Adsorption Surface Area and Porosity”, *Journal of The Electrochemical Society* **1967**, *114*, 279Ca.

[141] G. Halsey, “Physical Adsorption on Non-Uniform Surfaces”, *The Journal of Chemical Physics* **1948**, *16*, 931–937.

[142] G. Jura, W. D. Harkins, “A New Adsorption Isotherm Which Is Valid Over a Very Wide Range of Pressure”, *The Journal of Chemical Physics* **1943**, *11*, 430–431.

[143] J. C. P. Broekhoff, J. H. de Boer, “Studies on pore systems in catalysts: IX. Calculation of pore distributions from the adsorption branch of nitrogen sorption isotherms in the case of open cylindrical pores A. Fundamental equations”, *Journal of Catalysis* **1967**, *9*, 8–14.

[144] S. R. Stock, *Elements of X—Ray Diffraction: Pearson New International Edition PDF eBook*, Pearson Higher Ed, **2013**, 654 pp.

[145] J. Epp in *Materials Characterization Using Nondestructive Evaluation (NDE) Methods*, (Eds.: G. Hübschen, I. Altpeter, R. Tschuncky, H.-G. Herrmann), Woodhead Publishing, **2016**, pp. 81–124.

[146] Q. Cai, W.-Y. Lin, F.-S. Xiao, W.-Q. Pang, X.-H. Chen, B.-S. Zou, “The preparation of highly ordered MCM—41 with extremely low surfactant concentration”, *Microporous and Mesoporous Materials* **1999**, *32*, 1–15.

[147] J. L. Blin, M. Impéror-Clerc, “Mechanism of self—assembly in the synthesis of silica mesoporous materials: in situ studies by X—ray and neutron scattering”, *Chemical Society Reviews* **2013**, *42*, 4071–4082.

[148] M. Jorge, J. R. B. Gomes, M. N. D. S. Cordeiro, N. A. Seaton, “Molecular Dynamics Simulation of the Early Stages of the Synthesis of Periodic Mesoporous Silica”, *The Journal of Physical Chemistry B* **2009**, *113*, 708–718.

[149] J. C. G. Pereira, C. R. A. Catlow, G. D. Price, “Molecular Dynamics Simulation of Methanolic and Ethanolic Silica—Based Sol−Gel Solutions at Ambient Temperature and Pressure”, *The Journal of Physical Chemistry A* **2002**, *106*, 130–148.

[150] J. R. B. Gomes, M. N. D. S. Cordeiro, M. Jorge, “Gas—phase molecular structure and energetics of anionic silicates”, *Geochimica et Cosmochimica Acta* **2008**, *72*, 4421–4439.

[151] M. Jorge, “Predicting hydrophobic solvation by molecular simulation: 2. New united—atom model for alkanes, alkenes, and alkynes”, *Journal of Computational Chemistry* **2017**, *38*, 359–369.

[152] M. C. Barrera, M. Jorge, “A Polarization—Consistent Model for Alcohols to Predict Solvation Free Energies”, *Journal of Chemical Information and Modeling* **2020**, *60*, 1352–1367.

[153] Y. Wang, L. Jiang, Q. Shen, J. Shen, Y. Han, H. Zhang, “Investigation on the self—assembled behaviors of C 18 unsaturated fatty acids in arginine aqueous solution”, *RSC Adv.* **2017**, *7*, 41561–41572.

[154] E. J. Shepherd, J. A. Kitchener, “474. The ionization of ethyleneimine and polyethyleneimine”, *Journal of the Chemical Society (Resumed)* **1956**, 2448–2452.

[155] J. A. Graham, J. W. Essex, S. Khalid, “PyCGTOOL: Automated Generation of Coarse—Grained Molecular Dynamics Models from Atomistic Trajectories”, *Journal of Chemical Information and Modeling* **2017**, *57*, 650–656.

[156] G. A. Kaminski, R. A. Friesner, J. Tirado-Rives, W. L. Jorgensen, “Evaluation and Reparametrization of the OPLS—AA Force Field for Proteins via Comparison with Accurate Quantum Chemical Calculations on Peptides”, *The Journal of Physical Chemistry B* **2001**, *105*, 6474–6487.

[157] E. K. Watkins, W. L. Jorgensen, “Perfluoroalkanes: Conformational Analysis and Liquid—State Properties from ab Initio and Monte Carlo Calculations”, *The Journal of Physical Chemistry A* **2001**, *105*, 4118–4125.

[158] M. L. P. Price, D. Ostrovsky, W. L. Jorgensen, “Gas—phase and liquid—state properties of esters, nitriles, and nitro compounds with the OPLS—AA force field”, *Journal of Computational Chemistry* **2001**, *22*, 1340–1352.

[159] R. C. Rizzo, W. L. Jorgensen, “OPLS All—Atom Model for Amines: Resolution of the Amine Hydration Problem”, *Journal of the American Chemical Society* **1999**, *121*, 4827–4836.

[160] W. L. Jorgensen, N. A. McDonald, “Development of an all—atom force field for heterocycles. Properties of liquid pyridine and diazenes”, *Journal of Molecular Structure: THEOCHEM* **1998**, *424*, 145–155.

[161] L. S. Dodda, J. Z. Vilseck, J. Tirado-Rives, W. L. Jorgensen, “1.14*CM1A—LBCC: Localized Bond—Charge Corrected CM1A Charges for Condensed—Phase Simulations”, *The Journal of Physical Chemistry B* **2017**, *121*, 3864–3870.

[162] W. L. Jorgensen, J. Tirado-Rives, “Potential energy functions for atomic—level simulations of water and organic and biomolecular systems”, *Proceedings of the National Academy of Sciences* **2005**, *102*, 6665–6670.

[163] L. S. Dodda, I. Cabeza de Vaca, J. Tirado-Rives, W. L. Jorgensen, “LigParGen web server: an automatic OPLS—AA parameter generator for organic ligands”, *Nucleic Acids Research* **2017**, *45*, W331–W336.

[164] H. J. C. Berendsen, D. van der Spoel, R. van Drunen, “GROMACS: A message—passing parallel molecular dynamics implementation”, *Computer Physics Communications* **1995**, *91*, 43–56.

[165] Lindahl, Abraham, Hess, v. d. Spoel, *GROMACS 2021.5 Source code*, **2022**.

[166] G. Van Rossum, F. L. Drake, *Python 3 Reference Manual*, CreateSpace, Scotts Valley, CA, **2009**.

[167] N. Michaud-Agrawal, E. J. Denning, T. B. Woolf, O. Beckstein, “MDAnalysis: A toolkit for the analysis of molecular dynamics simulations”, *Journal of Computational Chemistry* **2011**, *32*, 2319–2327.

[168] R. J. Gowers et al., “MDAnalysis: A Python Package for the Rapid Analysis of Molecular Dynamics Simulations”, *Proceedings of the 15th Python in Science Conference* **2016**, 98–105.

[169] J. D. Hunter, “Matplotlib: A 2D graphics environment”, *Computing in Science & Engineering* **2007**, *9*, 90–95.

[170] U. Essmann, L. Perera, M. Berkowitz, T. Darden, H. Lee, L. Pedersen, “A Smooth Particle Mesh Ewald Method”, *J. Chem. Phys.* **1995**, *103*, 8577.

[171] H. J. C. Berendsen, J. R. Grigera, T. P. Straatsma, “The missing term in effective pair potentials”, *The Journal of Physical Chemistry* **1987**, *91*, 6269–6271.

[172] C. H. Bennett, "Efficient estimation of free energy differences from Monte Carlo data", *Journal of Computational Physics* **1976**, *22*, 245–268.

[173] T. C. Beutler, A. E. Mark, R. C. van Schaik, P. R. Gerber, W. F. van Gunsteren, "Avoiding singularities and numerical instabilities in free energy calculations based on molecular simulations", *Chemical Physics Letters* **1994**, *222*, 529–539.

[174] P. Hansson, B. Jönsson, C. Ström, O. Söderman, "Determination of Micellar Aggregation Numbers in Dilute Surfactant Systems with the Fluorescence Quenching Method.", *The Journal of Physical Chemistry B* **2000**, *104*, 3496–3506.

[175] V. K. Aswal, P. S. Goyal, "Role of different counterions and size of micelle in concentration dependence micellar structure of ionic surfactants", *Chemical Physics Letters* **2003**, *368*, 59–65.

[176] M. N. Melo, H. I. Ingólfsson, S. J. Marrink, "Parameters for Martini sterols and hopanoids based on a virtual—site description", *The Journal of Chemical Physics* **2015**, *143*, 243152.

[177] F. E. Thomasen, T. Skaalum, A. Kumar, S. Srinivasan, S. Vanni, K. Lindorff-Larsen, "Rescaling protein—protein interactions improves Martini 3 for flexible proteins in solution", *Nature Communications* **2024**, *15*, 6645.

[178] R. Wolfenden, L. Andersson, P. M. Cullis, C. C. B. Southgate, "Affinities of amino acid side chains for solvent water", *Biochemistry* **1981**, *20*, 849–855.

[179] A. Radzicka, R. Wolfenden, "Comparing the polarities of the amino acids: side—chain distribution coefficients between the vapor phase, cyclohexane, 1—octanol, and neutral aqueous solution", *Biochemistry* **1988**, *27*, 1664–1670.

[180] S. Berr, R. R. M. Jones, J. S. Johnson, "Effect of counterion on the size and charge of alkyltrimethylammonium halide micelles as a function of chain length and concentration as determined by small—angle neutron scattering", *The Journal of Physical Chemistry* **1992**, *96*, 5611–5614.

[181] F. Quirion, L. J. Magid, “Growth and counterion binding of cetyltrimethylammonium bromide aggregates at 25.degree.C: a neutron and light scattering study”, *The Journal of Physical Chemistry* **1986**, *90*, 5435–5441.

[182] A. M. J. Ležaić, N. Pejić, J. Goronja, L. Pavun, D. Đikanović, A. Malenović, “Micellar properties of cetyltrimethylammonium bromide in an acetonitrile–water mixture: Conductometric and fluorescence studies”, *Macedonian Journal of Chemistry and Chemical Engineering* **2021**, *40*, 277–287.

[183] R. K. Banjare, M. K. Banjare, K. Behera, M. Tandon, S. Pandey, K. K. Ghosh, “Deep eutectic solvents as modulator on the micellization behaviour of cationic surfactants and potential application in human serum albumin aggregation”, *Journal of Molecular Liquids* **2021**, *344*, 117864.

[184] R. K. Banjare, M. K. Banjare, S. Panda, “Effect of Acetonitrile on the Colloidal Behavior of Conventional Cationic Surfactants: A Combined Conductivity, Surface Tension, Fluorescence and FTIR Study”, *Journal of Solution Chemistry* **2020**, *49*, 34–51.

[185] P. Lianos, R. Zana, “Fluorescence probe studies of the effect of concentration on the state of aggregation of surfactants in aqueous solution”, *Journal of Colloid and Interface Science* **1981**, *84*, 100–107.

[186] P. Ekwall, L. Mandell, P. Solyom, “The aqueous cetyl trimethylammonium bromide solutions”, *Journal of Colloid and Interface Science* **1971**, *35*, 519–528.

[187] S. Tiwari, C. Mall, P. P. Solanki, “CMC studies of CTAB, SLS & tween 80 by spectral and conductivity methodology to explore its potential in photogalvanic cell”, *Surfaces and Interfaces* **2020**, *18*, 100427.

[188] *Encyclopedia of Surface and Colloid Science, 2004 Update Supplement*, (Ed.: P. Somasundaran), CRC Press, Boca Raton, **2004**, 704 pp.

[189] R. Pilling, S. V. Patwardhan, “Recent Advances in Enabling Green Manufacture of Functional Nanomaterials: A Case Study of Bioinspired Silica”, *ACS Sustainable Chemistry & Engineering* **2022**, *10*, 12048–12064.

[190] H. P. Lin, S. Cheng, C.-Y. Mou, “Synthesis of Thermally Stable MCM—41 at Ambient Temperature”, *Journal of the Chinese Chemical Society* **1996**, *43*, 375–378.

[191] E. V. Vyshegorodtseva, Y. Larichev, G. V. Mamontov, “The influence of CTAB/Si ratio on the textural properties of MCM—41 prepared from sodium silicate”, *Journal of Sol-Gel Science and Technology* **2019**, *92*, 496–505.

[192] T. Yokoi, Y. Sakamoto, O. Terasaki, Y. Kubota, T. Okubo, T. Tatsumi, “Periodic Arrangement of Silica Nanospheres Assisted by Amino Acids”, *Journal of the American Chemical Society* **2006**, *128*, 13664–13665.

[193] J. C. Eriksson, “Thermodynamics of surface phase systems: V. Contribution to the thermodynamics of the solid—gas interface”, *Surface Science* **1969**, *14*, 221–246.

[194] P. Schneider, “Adsorption isotherms of microporous—mesoporous solids revisited”, *Applied Catalysis A: General* **1995**, *129*, 157–165.

[195] N. La-Salvia, J. J. Lovón-Quintana, A. S. P. Lovón, G. P. Valença, “Influence of Aluminum Addition in the Framework of MCM—41 Mesoporous Molecular Sieve Synthesized by Non—Hydrothermal Method in an Alkali—Free System”, *Materials Research* **2017**, *20*, 1461–1469.

[196] G. Ren, L. Wang, Q. Chen, Z. Xu, J. Xu, D. Sun, “pH Switchable Emulsions Based on Dynamic Covalent Surfactants”, *Langmuir* **2017**, *33*, 3040–3046.

[197] L. Zhao et al., “Light—switchable emulsions: From reversible emulsification—demulsification to controllable microreactors”, *Journal of Molecular Liquids* **2023**, *372*, 121166.

[198] S. Dowlati, R. Mokhtari, L. Hohl, R. Miller, M. Kraume, “Advances in CO2—switchable surfactants towards the fabrication and application of responsive colloids”, *Advances in Colloid and Interface Science* **2023**, *315*, 102907.

[199] P. Brown, T. Alan Hatton, J. Eastoe, “Magnetic surfactants”, *Current Opinion in Colloid & Interface Science* **2015**, *20*, 140–150.

[200] C. I. Fowler et al., "Emulsion Polymerization of Styrene and Methyl Methacrylate Using Cationic Switchable Surfactants", *Macromolecules* **2011**, *44*, 2501–2509.

[201] M. Zhang, Y. Nan, Y. Lu, Q. You, Z. Jin, "CO2—responsive surfactant for oil—in—water emulsification and demulsification from molecular perspectives", *Fuel* **2023**, *331*, 125773.

[202] C. Liang et al., "Use of CO2—Triggered Switchable Surfactants for the Stabilization of Oil—in—Water Emulsions", *Energy & Fuels* **2012**, *26*, 488–494.

[203] W. Yuhua, R. Jianwei, "The flotation of quartz from iron minerals with a combined quaternary ammonium salt", *International Journal of Mineral Processing* **2005**, *77*, 116–122.

[204] X. Zhang, X. Gu, Y. Han, N. Parra-Álvarez, V. Claremboux, S. K. Kawatra, "Flotation of Iron Ores: A Review", *Mineral Processing and Extractive Metallurgy Review* **2021**, *42*, 184–212.

[205] Y. Ao et al., "Influence of Different Types of Surfactants on the Flotation of Natural Quartz by Dodecylamine", *Molecules* **2024**, *29*, 2256.

[206] S.-Y. Ju, M. Utz, F. Papadimitrakopoulos, "Enrichment Mechanism of Semiconducting Single—Walled Carbon Nanotubes by Surfactant Amines", *Journal of the American Chemical Society* **2009**, *131*, 6775–6784.

[207] Y. Shi, H. Li, L. Chen, X. Huang, "Obtaining ultra—long copper nanowires via a hydrothermal process", *Science and Technology of Advanced Materials* **2005**, *6*, 761–765.

[208] X. Zhou, Y. H. Tan, J. A. Finch, "Effect of pH and time on hydrodynamic properties of dodecylamine", *Physicochemical Problems of Mineral Processing* **2018**, *54*, 1237–1244.

[209] A. Firouzi et al., "Cooperative Organization of Inorganic—Surfactant and Biomimetic Assemblies", *Science* **1995**, *267*, 1138–1143.

[210] W. Zhang, T. R. Pauly, T. J. Pinnavaia, “Tailoring the Framework and Textural Mesopores of HMS Molecular Sieves through an Electrically Neutral (S°I°) Assembly Pathway”, *Chemistry of Materials* **1997**, *9*, 2491–2498.

[211] H. Caldararu, A. Caragheorgheopol, F. Savonea, D. J. Macquarrie, B. C. Gilbert, “A Spin Probe Study of Mesoporous Silica Formation via a Neutral Templating Route”, *The Journal of Physical Chemistry B* **2003**, *107*, 6032–6038.

[212] A. Galarneau, F. Sartori, M. Cangiotti, T. Mineva, F. D. Renzo, M. F. Ottaviani, “Sponge Mesoporous Silica Formation Using Disordered Phospholipid Bilayers as Template”, *The Journal of Physical Chemistry B* **2010**, *114*, 2140–2152.

[213] S. Backlund, S. Karlsson, J. Sjöblom, “Phase Equilibria in Aqueous Low Molecular Catanionic Surfactant Systems”, *Journal of Dispersion Science and Technology* **1994**, *15*, 561–573.

[214] S. Karlsson, S. Backlund, R. Friman, “Complexation in the heptanoic acid–heptylamine system”, *Colloid and Polymer Science* **2000**, *278*, 8–14.

[215] R. Mokaya in *Encyclopedia of Physical Science and Technology (Third Edition)*, (Ed.: R. A. Meyers), Academic Press, New York, **2003**, pp. 369–381.

[216] S. Karlsson, R. Friman, M. Björkqvist, B. Lindström, S. Backlund, “Phase Behavior and Characterization of the System Acetic Acid−Dodecylamine−Water”, *Langmuir* **2001**, *17*, 3573–3578.

[217] P. C. Hartmann, P. Dieudonné, R. D. Sanderson, “Self—assembly and influence of the organic counterion in the ternary systems dodecylamine/acrylic acid/water and dodecylamine/methacrylic acid/water”, *Journal of Colloid and Interface Science* **2005**, *284*, 289–297.

[218] S. Kawada, M. Komori, K. Fujimoto, N. Yoshii, S. Okazaki, “Molecular dynamics study of the formation mechanisms of ionic SDS and nonionic C12E8 micelles and *n*—dodecane droplets”, *Chemical Physics Letters* **2016**, *646*, 36–40.

[219] K. Fujimoto, Y. Kubo, S. Kawada, N. Yoshii, S. Okazaki, “Molecular dynamics study of the aggregation rate for zwitterionic dodecyldimethylamine oxide and cationic dodecyltrimethylammonium chloride micelles”, *Molecular Simulation* **2017**, *43*, 1331–1337.

[220] M. Jorge, “Molecular Dynamics Simulation of Self—Assembly of n—Decyltrimethylammonium Bromide Micelles”, *Langmuir* **2008**, *24*, 5714–5725.

[221] S. Kawada, K. Fujimoto, N. Yoshii, S. Okazaki, “Molecular dynamics study of the potential of mean force of SDS aggregates”, *The Journal of Chemical Physics* **2017**, *147*, 084903.

[222] R. D. Groot, P. B. Warren, “Dissipative particle dynamics: Bridging the gap between atomistic and mesoscopic simulation”, *The Journal of Chemical Physics* **1997**, *107*, 4423–4435.

[223] H. Eslami, M. Khani, F. Müller-Plathe, “Gaussian Charge Distributions for Incorporation of Electrostatic Interactions in Dissipative Particle Dynamics: Application to Self—Assembly of Surfactants”, *Journal of Chemical Theory and Computation* **2019**, *15*, 4197–4207.

[224] M. Panoukidou, C. R. Wand, A. Del Regno, R. L. Anderson, P. Carbone, “Constructing the phase diagram of sodium laurylethoxysulfate using dissipative particle dynamics”, *Journal of Colloid and Interface Science* **2019**, *557*, 34–44.

[225] R. L. Anderson, D. S. D. Gunn, T. Taddese, E. Lavagnini, P. B. Warren, D. J. Bray, “Phase Behavior of Alkyl Ethoxylate Surfactants in a Dissipative Particle Dynamics Model”, *The Journal of Physical Chemistry B* **2023**, *127*, 1674–1687.

[226] W. Shinoda, R. DeVane, M. L. Klein, “Multi—property fitting and parameterization of a coarse grained model for aqueous surfactants”, *Molecular Simulation* **2007**, *33*, 27–36.

[227] W. Shinoda, R. DeVane, M. L. Klein, “Coarse—grained molecular modeling of non—ionic surfactant self—assembly”, *Soft Matter* **2008**, *4*, 2454–2462.

[228] H. Chen, A. Z. Panagiotopoulos, “Molecular Modeling of Surfactant Micellization Using Solvent—Accessible Surface Area”, *Langmuir* **2019**, *35*, 2443–2450.

[229] S. Wang, R. G. Larson, “A Coarse—Grained Implicit Solvent Model for Poly(ethylene oxide), CnEm Surfactants, and Hydrophobically End—Capped Poly(ethylene oxide) and Its Application to Micelle Self—Assembly and Phase Behavior”, *Macromolecules* **2015**, *48*, 7709–7718.

[230] A. Jusufi, A.-P. Hynninen, A. Z. Panagiotopoulos, “Implicit solvent models for micellization of ionic surfactants”, *The Journal of Physical Chemistry. B* **2008**, *112*, 13783–13792.

[231] R. G. Larson, “Self-assembly of surfactant liquid crystalline phases by Monte Carlo simulation”, *The Journal of Chemical Physics* **1989**, *91*, 2479–2488.

[232] A. D. Mackie, A. Z. Panagiotopoulos, I. Szleifer, “Aggregation Behavior of a Lattice Model for Amphiphiles”, *Langmuir* **1997**, *13*, 5022–5031.

[233] P. H. Nelson, G. C. Rutledge, T. A. Hatton, “On the size and shape of self—assembled micelles”, *The Journal of Chemical Physics* **1997**, *107*, 10777–10781.

[234] D. W. Cheong, A. Z. Panagiotopoulos, “Monte Carlo Simulations of Micellization in Model Ionic Surfactants: Application to Sodium Dodecyl Sulfate”, *Langmuir* **2006**, *22*, 4076–4083.

[235] M. S. Minkara et al., “Probing Additive Loading in the Lamellar Phase of a Nonionic Surfactant: Gibbs Ensemble Monte Carlo Simulations Using the SDK Force Field”, *Langmuir* **2018**, *34*, 8245–8254.

[236] M. S. Minkara et al., “Nonane and Hexanol Adsorption in the Lamellar Phase of a Nonionic Surfactant: Molecular Simulations and Comparison to Ideal Adsorbed Solution Theory”, *The Journal of Physical Chemistry B* **2022**, *126*, 3940–3949.

[237] A. A. Louis, P. G. Bolhuis, J. P. Hansen, “Mean—field fluid behavior of the Gaussian core model”, *Physical Review E* **2000**, *62*, 7961–7972.

[238] C. M. Wijmans, B. Smit, R. D. Groot, "Phase behavior of monomeric mixtures and polymer solutions with soft interaction potentials", *The Journal of Chemical Physics* **2001**, *114*, 7644–7654.

[239] R. L. Anderson, D. J. Bray, A. Del Regno, M. A. Seaton, A. S. Ferrante, P. B. Warren, "Micelle Formation in Alkyl Sulfate Surfactants Using Dissipative Particle Dynamics", *Journal of Chemical Theory and Computation* **2018**, *14*, 2633–2643.

[240] J. C. R. Thacker, D. J. Bray, P. B. Warren, R. L. Anderson, "Can Machine Learning Predict the Phase Behavior of Surfactants?", *The Journal of Physical Chemistry B* **2023**, *127*, 3711–3727.

[241] M. Velinova, D. Sengupta, A. V. Tadjer, S.-J. Marrink, "Sphere—to—Rod Transitions of Nonionic Surfactant Micelles in Aqueous Solution Modeled by Molecular Dynamics Simulations", *Langmuir* **2011**, *27*, 14071–14077.

[242] Y. Ruiz-Morales, A. Romero-Martínez, "Coarse—Grain Molecular Dynamics Simulations To Investigate the Bulk Viscosity and Critical Micelle Concentration of the Ionic Surfactant Sodium Dodecyl Sulfate (SDS) in Aqueous Solution", *The Journal of Physical Chemistry B* **2018**, *122*, 3931–3943.

[243] S. D. Anogiannakis, P. C. Petris, D. N. Theodorou, "Promising Route for the Development of a Computational Framework for Self—Assembly and Phase Behavior Prediction of Ionic Surfactants Using MARTINI", *The Journal of Physical Chemistry B* **2020**, *124*, 556–567.

[244] G. Rossi, P. F. J. Fuchs, J. Barnoud, L. Monticelli, "A Coarse—Grained MARTINI Model of Polyethylene Glycol and of Polyoxyethylene Alkyl Ether Surfactants", *The Journal of Physical Chemistry B* **2012**, *116*, 14353–14362.

[245] D. Patel et al., "Rationalizing the Design of Pluronics–Surfactant Mixed Micelles through Molecular Simulations and Experiments", *Langmuir* **2023**, *39*, 2692–2709.

[246] G. Pérez-Sánchez et al., “Rationalizing the Phase Behavior of Triblock Copolymers through Experiments and Molecular Simulations”, *The Journal of Physical Chemistry C* **2019**, *123*, 21224–21236.

[247] R. Wu, M. Deng, B. Kong, X. Yang, “Coarse—Grained Molecular Dynamics Simulation of Ammonium Surfactant Self—Assemblies: Micelles and Vesicles”, *The Journal of Physical Chemistry B* **2009**, *113*, 15010–15016.

[248] M. J. Abraham et al., “GROMACS: High performance molecular simulations through multi—level parallelism from laptops to supercomputers”, *SoftwareX* **2015**, *1-2*, 19–25.

[249] W. Humphrey, A. Dalke, K. Schulten, “VMD: Visual molecular dynamics”, *Journal of Molecular Graphics* **1996**, *14*, 33–38.

[250] J. Hoshen, R. Kopelman, “Percolation and cluster distribution. I. Cluster multiple labeling technique and critical concentration algorithm”, *Physical Review B* **1976**, *14*, 3438–3445.

[251] A. J. M. Valente, H. D. Burrows, S. M. A. Cruz, R. F. P. Pereira, A. C. F. Ribeiro, V. M. M. Lobo, “Aggregation and micellization of sodium dodecyl sulfate in the presence of Ce(III) at different temperatures: A conductometric study”, *Journal of Colloid and Interface Science* **2008**, *323*, 141–145.

[252] A. Centi, “Computational modelling and design of bioinspired silica materials”, PhD thesis, 2017.

[253] F. K. Broome, C. W. Hoerr, H. J. Harwood, “The Binary Systems of Water with Dodecylammonium Chloride and Its N—Methyl Derivatives1”, *Journal of the American Chemical Society* **1951**, *73*, 3350–3352.

[254] Z. Fojud, E. Szcześniak, S. Jurga, S. Stapf, R. Kimmich, “Molecular dynamics of n—dodecylammonium chloride in aqueous solutions investigated by 2H NMR and 1H NMR relaxometry”, *Solid State Nuclear Magnetic Resonance*, 31st Congress Ampere, Magnetic Resonance and Related Phenomena **2004**, *25*, 200–206.

[255] S. Ghosh, A. Ray, N. Pramanik, “Self—assembly of surfactants: An overview on general aspects of amphiphiles”, *Biophysical Chemistry* **2020**, *265*, 106429.

[256] S. Sami, S. J. Marrink, “Reactive Martini: Chemical Reactions in Coarse—Grained Molecular Dynamics Simulations”, *Journal of Chemical Theory and Computation* **2023**, *19*, 4040–4046.